THE CALCITE-WATER INTERFACE

A Thesis submitted for the Degree of

Doctor of Philosophy in the

University of Oxford

by

Christine A. Narramore

St. John's College

Trinity Term 1994

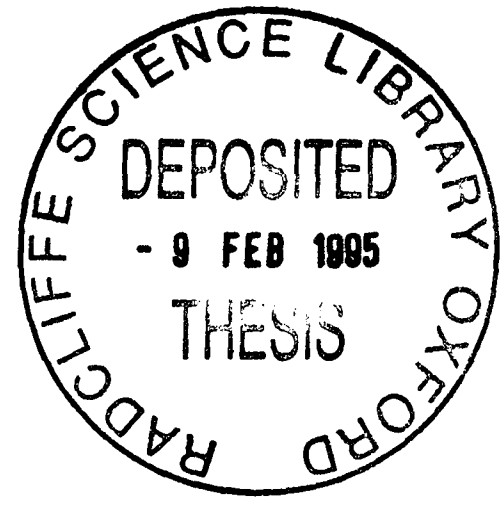

ACKNOWLEDGEMENTS

First I wish to thank my supervisor Dr. Richard Compton for all his help, support and advice during my time at Oxford. Next I have to thank all the members of the 'Compton group', without whom the experience would not have been quite the same. I must thank Chris Brown for both introducing me to the ways of calcite, and guiding me on several enjoyable Sunday pub walks. Also Adrian Fisher for his advice with some of my computer programming and friendship. Lastly I cannot leave out a special mention of Jane Larsen and Roula Barghout, and their girlie lunches.

Acknowledgement also has to be paid to F.M.C. (previously Ciba-Geigy Industrial Additives) for funding this work, and especially to Mike Lees for his interest, ideas and support.

I also wish to thank various members of St. John's college for the enrichment of my life in Oxford. Then I also have to thank various members of the department of Geological Science at U.I.C., for both understanding my split time commitments and for some useful comments on my work. In particular I have to thank Deborah Leowenherz-Lawrence for her friendship and support.

Finally I have to thank my long suffering husband, David King, for his love and support for me, beyond the call of duty; specifically in making coffee, photocopying and proof-reading.

To my late mother, Pamela J. Narramore.

CONTENTS

CHAPTER 1

INTRODUCTION

1.1 Introduction

The aim of the work reported in this thesis is to elucidate the reaction kinetics of calcite dissolution. The kinetics will be investigated at both low pH (< 4.5) and high pH (> 7.0). At low pH the dissolution reaction is dominated by the reaction between $CaCO_3$ and H^+, whereas at high pH the dominant reaction is that involving H_2O, and the precipitation back reaction also becomes relevant.

Having studied the general dissolution processes, it is of value to then investigate the effect of inhibitors on calcite dissolution. Both monomeric inhibitors and the effect of a polymeric inhibitor (polyacrylic acid) at both low and high pH will be considered. Polyacrylic acid is of particular importance as it is one of the two major industrial scale inhibitors sold to inhibit the precipitation of calcite, the other being polymaleic acid.[1] Study at high pH is particular importance as it is closer to the actual conditions in which the inhibitor is used commercially. Whilst study at low pH is of particular use in allowing some comparison with previous work on polymaleic acid [2].

In order to investigate the kinetics of dissolution thoroughly, this study will use a hydrodynamically well defined experimental method, namely one based on the channel flow-cell, as is further discussed in section 1.6 and theoretically in Chapter 2.

This chapter outlines the wide variety reasons for studying the dissolution kinetics of calcite. It then continues to discuss some basic principles of reactions at the solid liquid interface, together with the principles of crystal growth and the Burton Cabrera

Frank model. Subsequently the chapter reviews previous studies on calcite dissolution, which use a variety of experimental techniques and investigate the kinetics at both low and high pH. Finally, the conclusion will explain why previous investigations have been inadequate and why the channel flow cell provides a suitable methodology to probe the interfacial kinetics.

1.2 Reason for Study

Calcite is one of the most widespread and common rock-forming minerals. It is the most thermodynamically stable form of calcium carbonate under normal conditions [3], the other major form being aragonite. As one would expect there has been considerable interest in the kinetics of such a widespread mineral, and the kinetics of its dissolution and precipitation have been studied for over a century [4,5,6,7,8].

The dissolution/precipitation of calcium carbonate is of interest in a variety of fields. Details of the relevance of the kinetics of calcite in various specific areas is given below.

1.2.1 Environmental and Geological Reasons

Environmentally and geologically, calcite and calcium carbonate dissolution and precipitation reactions and their associated reaction kinetics are of significance in a number of areas including limnology, oceanography, and sedimentology [9-14]. Pure geological applications of the importance of calcite dissolution/precipitation range from cave formation in carbonate platforms[15], to Karst scenery formation[16,17], and stalagmite and stalactite growth. In the case of stalagmites, they are formed by the precipitation of calcium carbonate when pressure or temperature changes cause the

water flowing in caves to become supersaturated, or alternatively by the evaporation of cave water saturated by calcium carbonate. Therefore kinetics of calcite precipitation are of great relevance to an understanding of their formation. Some of the specific relevance of calcite dissolution kinetics in such systems is outlined in the section on Karst scenery later.

In limnology examples of the relevance of the dissolution kinetics include the buffering of freshwater systems, both under 'natural' conditions and when perturbed such as in the case of 'acid rain' [9,18-21]. In both situations the dissolution of calcium carbonate minerals as water is percolating through soil and rock to reach the freshwater system, and from sediments in lakes, regulate the pH and ion-speciation in the water system. This has great consequences on the whole freshwater ecosystem as discussed later in the section on 'acid rain'.

In oceanography and sedimentology the kinetics are important to understand carbonate mineral formation, and the incorporation of carbonate minerals into sediments. This has particular relevance to the possibility of the oceans as long term CO_2 sinks and therefore importance in the study of global warming [9,21-27],as discussed in the relevant section below.

1.2.1.1 *Karst Scenery*

Karst scenery gets its name from the Karst region of former Yugoslavia; such landscape shows a characteristic pattern of denudation of limestone and dolomite rocks. The latter have calcite as an important primary component mineral. The topography is not produced by normal surface run-off, but by the percolating of ground waters and underground streams. This can occur either through down-cutting of a stream through

other sediments into limestone, or by the uplift of a limestone surface upon which normal drainage has commenced.

In order to understand the processes which form such features there needs to be a detailed knowledge of the calcite dissolution kinetics [16,17], and in particular, their understanding under a variety of conditions, including variations in temperature and pressure. Both systems equilibrated with atmospheric carbon dioxide and closed systems need to be considered.

1.2.1.2 *Freshwater Acidification*

Another area where understanding calcite dissolution is of importance is in freshwater acidification, particularly the effects of 'acid rain'. This is where rain that is highly acidic, due to dissolved sulphur dioxide and other industrial emissions falls on poor soils overwhelming the 'buffering' capacity of the soil, so acidifying ground water and streams. A further consequence is that under such acidic conditions, aluminium is soluble and leached from the soil further harming fish and other lifeforms in rivers and lakes. Also at times of heavy precipitation the rainfall can be so high that most of the water reaches the aquifers by surface run-off thereby not allowing any buffering by the soil. This is a huge problem affecting thousands of lakes in Scandinavia and North America which have critical pH's for at least part of the year [28,29].

Interest in calcite dissolution in these circumstances is two-fold. First calcium species in soil provide natural buffering raising the pH of the water, that percolates through the soil profile, from that of rain which can be as low as pH 3.5 [19,30]. Also calcium carbonate is often used to counteract the effects of freshwater acidification. Usually this is carried out by adding lime to acid lakes. Although in the case of the Loch

Fleet project powdered lime was instead added to the catchment [19,31]. The aim is to raise the pH of the water, and to precipitate out aluminium, so that the water system becomes biologically non-toxic.

Estimates of amount of lime and the relative particle sizes necessary are often made on the basis that calcite dissolution is a transport limited reaction [33,34], and assume that all the powder will dissolve before being incorporated in the sediment at the base of the river or lake. Study of calcite kinetics has put doubt on this assumption [33], as it can be shown that calcite dissolution may not be transport controlled even at low pH as discussed later. Therefore by miscalculating the amount of lime needed to control acidification, and indeed applying the lime using inefficient methods, resources can be wasted.

Even the Loch Fleet project, where solid lime was added to the catchment, a thorough understanding of calcite kinetics is important. Woodin and Skita [31] have shown that adding lime to the catchment can have major ecological consequences. In particular adding lime to the catchment can drastically affect the plant speciation. For example sphagnum moss is very sensitive to calcium and will not have recovered even a year after liming. Other acid loving plants species are also killed. This is of particular importance in flushes, springs and bogs. These very wet areas have diverse vegetation and provide crucial environmental niches for invertebrates, so providing food for the birdlife. In liming such areas (as are targeted by such projects as the Loch Fleet project) the vegetation natural to them can be killed, and other plant species colonise the areas. There is also the possibility that in killing the mosses the peat underlying will begin to erode, further affecting the upland ecosystem.

From the above it is evident that it is desirable to minimize the amount of lime used in counteracting the effects of acid rain, and to maximise its effectiveness in buffering freshwater. A through understanding of dissolution of limestone, and the effects of any natural inhibitors is essential.

1.2.1.3 *The Global Carbon Cycle*

Another crucial environmental role played by calcite is as part of the global carbon cycle [35]. Calcium carbonate is an important constituent of deep-sea sediment; its dissolution and burial rates are very important. The ultimate sink for anthropological CO_2 is thought to be the deep oceans.

The dominant source for deep ocean calcium carbonate is biogenic, derived from the shells and skeletons of small organisms near the surface. Most calcium carbonate produced in the open ocean (between 75% to 95%) is dissolved before it is able to be incorporated into the sediment. This dissolution is thought to occur mainly near the sediment-water interface.

The balance between calcium carbonate production and dissolution is the major buffering mechanism of the seawater over periods of thousands of years. The atmospheric carbon dioxide reservoir is less than 2% of the seawater reservoir, and there is exchange between these two reservoirs at the air-water interface [26]. This could have important consequences on the so called 'greenhouse effect' and global warming. Global warming is predicted to occur as carbon dioxide builds up in the atmosphere, trapping infra-red radiation from the earths surface [36] and thus increasing the ambient surface temperature. Hence it is of importance to predict accurately the carbon cycle, in order to forecast the changes likely, the ability of the earth to self regulate and absorb excess

carbon dioxide, and the existence of any positive feed-back systems. In this aim the dissolution/precipitation kinetics of calcite are essential. As discussed previously the sea provides a great reservoir of carbon dioxide, and a long-term sink, so an understanding of calcite dissolution/precipitation is necessary to understand this essential part of the global carbon cycle.

As well as needing to measure the *in situ* dissolution *rates* [22,26] it is also necessary to understand the *mechanisms* controlling dissolution [23-26] so as to be able to predict how changes in atmospheric CO_2 levels and other conditions would affect this dissolution/precipitation.

Ideally one would not only understand the present contribution of calcite dissolution/precipitation to the global carbon cycle, but additionally be able to predict how an increase in carbon dioxide levels will affect the whole cycle itself. Then it would be desirable to predict the extent of any changes in atmospheric conditions due to increased emissions of carbon dioxide. For example would the rate of weathering of carbonate rocks increase as the ambient surface temperature increases, and how large would any increase in rate be. So overall the calcite dissolution/precipitation kinetics are of great relevance to global warming, and any aims to predict both quantitatively and qualitatively any changes that result from an increase in carbon dioxide released into the atmosphere.

1.2.2 Industrial relevance

Industrially calcite is of relevance in a number of industries such as water softening, and problems of scaling in a number of industries, and the pharmaceutical industry in such uses as the dissolution of antacids[37].

Calcium and Magnesium ions are the most common metals associated with hardness in water. $CaCO_3$ and $Mg(OH)_2$ are formed in water softening treatments in order to remove these ions. However frequently the processes designed allow insufficient time for complete crystallisation[10,38-39,]. This can lead to encrustation of sand particles in sand filters and the formation of lime deposits in the pipes of water reticulation systems. A greater understanding of calcite formation kinetics and the application of the kinetics to water softening treatment design could therefore be profitable.

The problem of scaling is of major industrial relevance. This ranges from the scaling of boilers to the scaling of heat exchangers in desalination plants [10,24,39-46]. The scaling of pipes in the petroleum industry [47] is a particular problem. Scale is deposited lime, which is precipitated by solutions becoming supersaturated by a variety of means, from pressure and temperature changes in pipe, boilers and heat exchangers, to concentration increases in desalination plants. Calcium carbonate is one of the major dissolved species to be precipitated in scale, and calcite is the dominant mineral form. Particular problems with scaling occur in the petroleum industry as petroleum deposits are found in limestone rocks [47]. Problems occur with the decrease in pressure that occurs as oil is brought up from depth. Desalination plants also suffer particular problems with the concentration effected in reverse osmosis [44].

Industrially much use is made of inhibitors to prevent scaling especially in desalination plants [45]. The study of inhibitors and their exact operation is therefore of great relevance. Commercially an inhibitor is desired both to be effective and to be able to be regenerated so as to have reasonable lifetime in use. Such inhibitors frequently act by preventing the calcite particles from reaching the critical size at which they precipitate. Understanding of the action of inhibitors on calcite dissolution/precipitation is useful both in deciding the best means of use, and in designing new commercial inhibitors [2,45].

For these reasons the study of calcite dissolution/precipitation, and the action of inhibitors is of widespread industrial interest.

1.3 Reactions at the Solid-Liquid Interface

Reactions which occur between a liquid and a solid surface involve a number of elementary steps. These are summarised in Figure 2.1, in which reactants are brought to the reaction site, (a kink, step, ledge etc.) and products are removed. Reactant species are conveyed to the Outer Helmholtz Plane by one or more of the mass transport processes to be detailed in Section 2.2. Once there, the reactant can be adsorbed onto the reactive surface with a possible reduction in solvation. This adsorbed species may then undergo surface diffusion to a reaction site where it is converted to products. The product species can then follow the reverse process of desorption followed by mass transport away into bulk solution. For any particular solid-liquid interface under investigation any one of these elementary steps could be the rate determining process.

When the surface reactions are very fast, if the rate of transport of reactants to the surface is relatively slow, the reactants are consumed faster than they can be

transported to the surface, in which case the reaction is said to be transport controlled. Alternatively transport control can also occur when the rate of transport of products away from the surface is slow enough to control the overall rate of reaction. For kinetic control the limiting step could be the rate of adsorption of reactants, the rate of migration to reactive sites, or the rate of desorption of products, as well as the rate of the surface reaction itself. Finally a complex mixed reaction occurs when more than one of these steps 'controls' the reaction, ie. more than one kinetic step or a combination of a kinetic step and transport control. This occurs when none of the processes is so slow with respect to the other steps as to totally dominate the overall reaction rate.

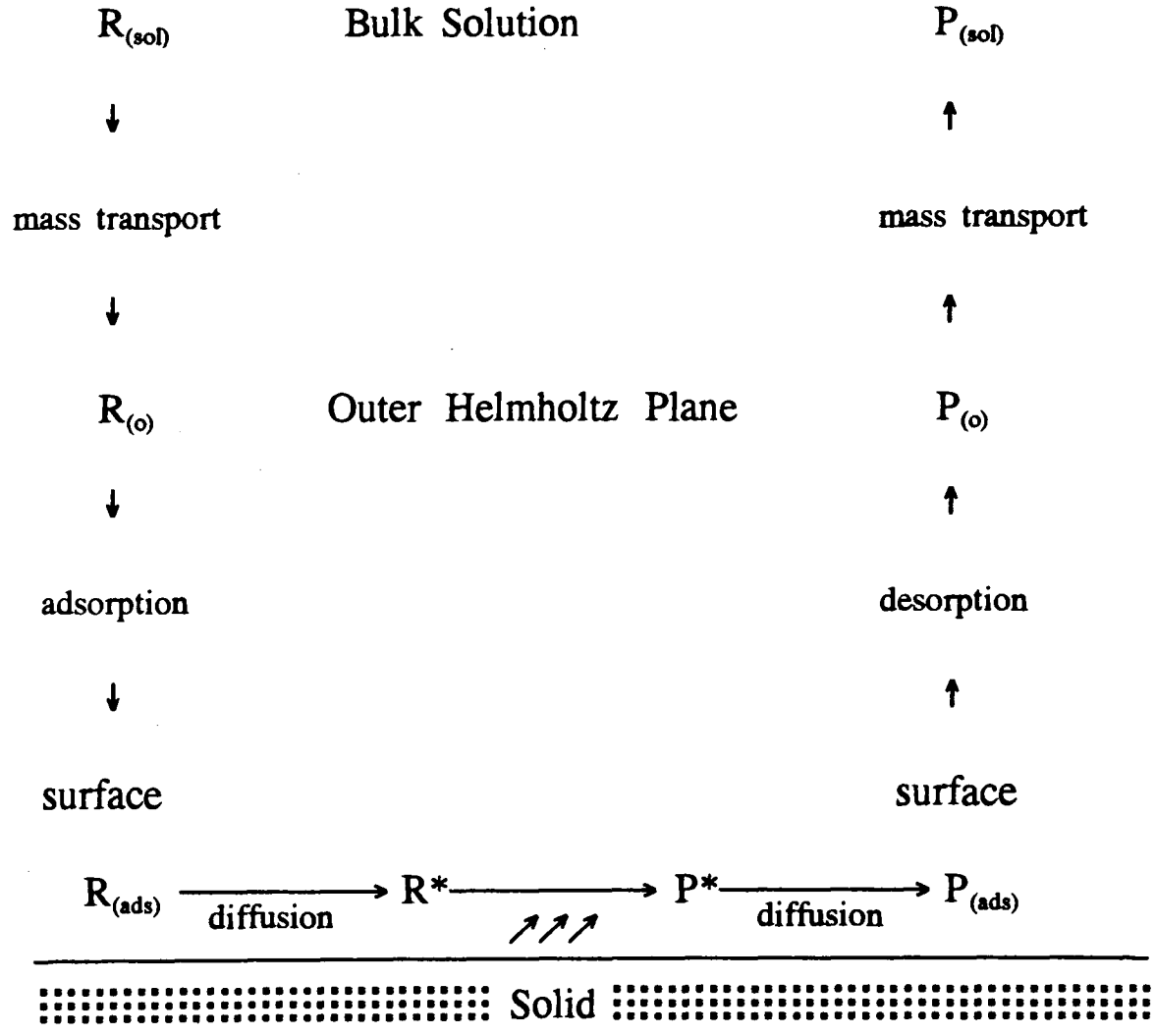

Figure 1.1. Elementary steps that occur in reactions at the solid-liquid interface, where R *represents the reactant species and* P *the products. The asterisked species represent those adsorbed at reaction sites.*

In order to fully understand the kinetics of any solid-liquid reaction it is desirable to be able to identify which of these processes control the rate of reaction. For this it is necessary to have well-defined mass transport of reactants to the surface and of products from the surface. Under such circumstances it is possible to identify accurately if and when the reaction rate is limited by the rate of transport. If the rate of transport is fast enough, then even fast kinetics may be 'out run', and the reaction will be kinetically controlled.

A boundary or diffusion layer (see Chapter 2) can be defined as that area adjacent to the surface, where the species although not adsorbed have concentrations which reflect the surface reactions. Then a heterogeneous rate law can be written of the general form

$$J\ /\mathrm{mol\,cm^{-2}s^{-1}} = k[\mathrm{R}]_o^n \qquad (1.1)$$

where J is the flux of reactant reaching the reactive surface, the subscript o denotes a concentration in the surface, k is a rate constant and n is the reaction order. When the reaction occurs at a metal-solution interface the flux can be directly measured from the electrode current, I, since

$$I = nFAJ \qquad (1.2)$$

where n is the number of electrons transferred, F is the Faraday constant and A is the area of the electrode. However, when the reaction is occurring at an insulator-liquid interface no direct analogue of the electrode current exists, so the investigation is more complex. Instead the concentration of a reactant or product species must be monitored as close to the reaction site as possible in order to measure the flux J. Also it is desirable to be able to predict how the concentration of species will vary between those at the surface and those measured at the detector. For this reason it is desirable to have

well-defined hydrodynamics which as shown in Chapter 2 enable the prediction of the variation in concentration.

When the hydrodynamics are well-defined it is possible to investigate the processes with a high degree of mechanistic sensitivity. Measurement of bulk concentrations provide less information about the surface reaction mechanism because of the remote nature of the detection. Even in the case of well defined hydrodynamics they will be less sensitive to small variations in surface concentrations, and so are less precise in distinguishing between mechanisms.

1.4 Crystal Growth BCF theory.

The Burton, Cabrera and Frank (BCF) model of crystal growth has been widely used[48,49]. This introduces the concept of steps on surfaces and kinks within steps as shown in Figure 1.2 below.

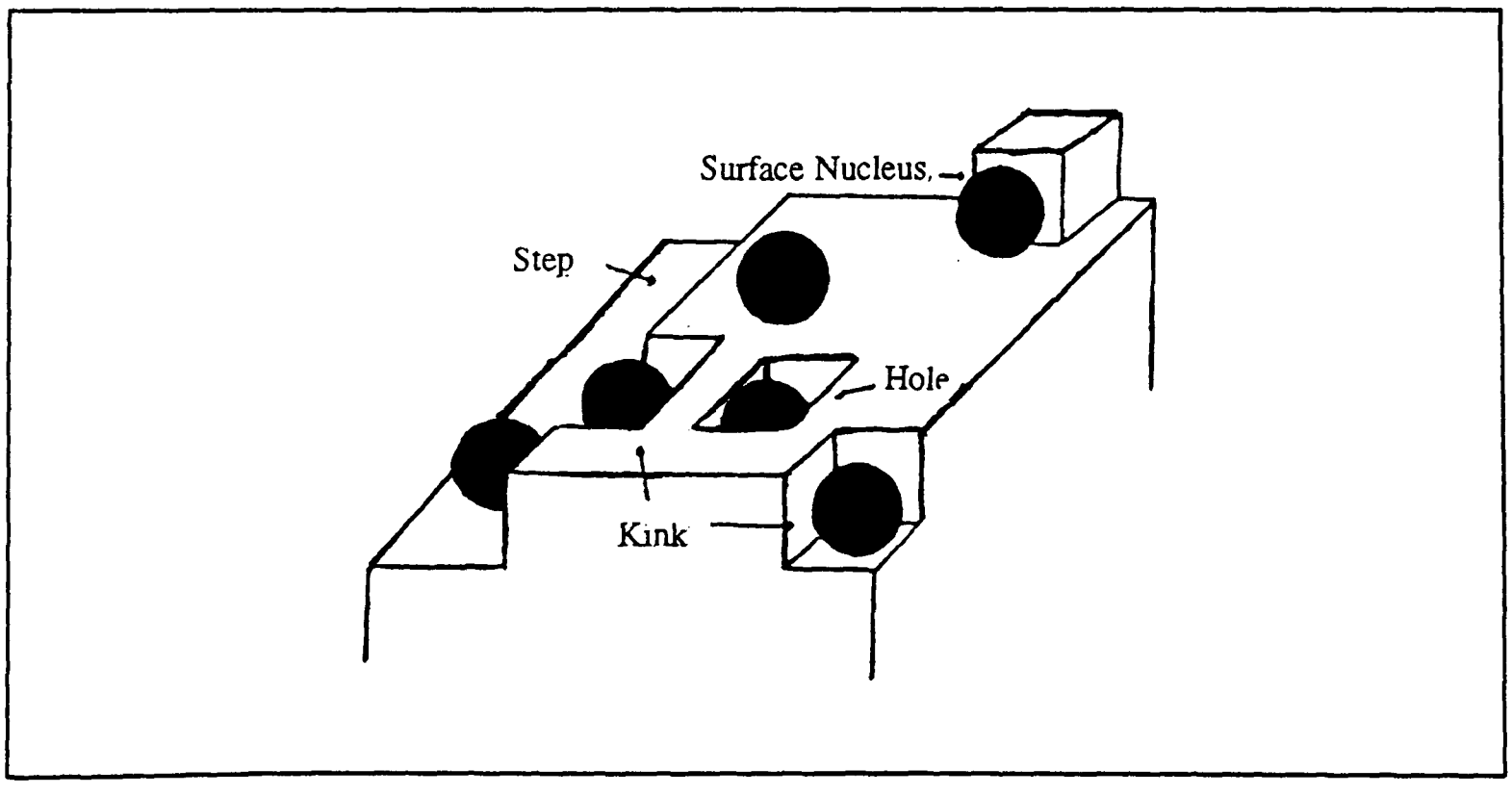

Figure 1.2 A schematic diagram of the crystal surface according to the BCF model of crystal growth, showing kinks, steps, and terraces, together with adsorbed ions shown in black.

Below a certain critical temperature for a crystal T_R, the surface of the crystal is essentially flat on an atomic scale as there is an energy barrier to build a step, and such defects are formed only rarely by statistical fluctuations [48]. Above this temperature the edge free-energy vanishes and the crystal faces becomes rough.

The important point for this study is how these surface defects affect the rate of reaction. Adsorbed surface species at these defect sites interact with a larger number of atoms than otherwise. The species interacts with more atoms so it experiences greater forces, which will trap it for longer than non-defect sites allowing more time for reaction to occur. Also it is possible that greater coloumbic interactions overcome the loss of favourable solvation energy. Both these factors can favour the surface reaction since such sites are more exposed and reactive than general sites at the crystal surface. Thus they are thought to be where the majority of dissolution, precipitation, and inhibition occurs. In the case of crystal growth, once the species of growth has been transported near the surface, adsorption may occur, possibly involving a dehydration step. Then there may be diffusion across the surface to a step, followed by incorporation into a kink on the step, possibly involving further dehydration. Thus kinks are the crucial sites for crystal growth. The number of such 'reactive sites' can be rate determining as has been shown experimentally by a number of methods including comparing the rates of reaction of different crystal form of the same mineral and showing that rate varies with defect density [50].

1.5 Previous Studies

This section will attempt to review the most relevant and important of the vast body of work previously performed on calcite dissolution and precipitation kinetics. The wide variety of experimental techniques adopted will be considered. The details will be given of the conclusions drawn for calcite dissolution in general and then separately for both high pH and low pH dissolution. Finally some recent work will be reviewed which uses modern techniques to probe the surface itself, directly.

1.5.1 Experimental strategies

An ideal experimental design would give:

i) Well defined transport of reactants to the calcite surface.

ii) Well defined transport of products to the detector.

iii) Control of the surface topography of the crystal and so to have reproducible surface defect densities (see section 1.4).

Also if the interfacial reaction rate is fast it is desirable to be able to use high rates of mass transport so as to 'outrun' the kinetics, so enabling measurement of the latter.

Previous work on calcium carbonate dissolution can be divided into two basic categories; free drift or pH/chem-stat methods. For free drift methods, the pH of the solution is allowed to vary as dissolution proceeds. In fact this variation in pH is used to monitor the progress of the reaction[10,14,43,51-57]. On the other hand in the pH-stat method the pH is kept constant by the addition of titrant [18,52,55-60].The chem-stat method is a variation on pH-stat and involves keeping the levels of *all* reactants constant, not just the H^+ ions. The advantage of chem or pH-stat methods are that the reaction can be kept in a state of disequilibrium which helps in the probing of the kinetics. For

example the back precipitation reaction could be eliminated simplifying the reaction scheme under investigation, as only the forward reaction rate is measured[57].

The reaction can be followed in a number of ways. For free drift methods following the change in solution pH is usually the chosen method. For the pH-stat the reaction can be followed from a knowledge of the addition of titrant with time. Other methods used include the removal of samples to be analyzed for calcium, usually by atomic absorption spectrometry[10,17,24,43,58],or titration with EDTA in the presence of an indicator [21,61].

As well as investigations of dissolution there have been studies on crystal growth and precipitation rates. These studies involve the forced precipitation from a supersaturated solution with the growth occurring on seed crystals [21,24,25,38,43,55,57,60,62,63]The experiments are performed either under free drift or pH-stat conditions. Seed crystals of known origin and surface preparation are added to a reaction vessel containing a mixture of super-saturated solution. Precipitation can be forced by the outgassing of CO_2 by bubbling N_2 gas through the solutions [62]. The solids formed can be examined, for example by SEM, to verify that it is indeed calcite which is formed [10,43].

In most of the methods above convection is forced by stirring. In some cases the effects of stirring on dissolution rate have been measured with varying conclusions. However as Sjöberg [54] has stated if 'there is no measured stirring rate dependence it does not necessarily mean that there is no effect of hydrodynamics on the system; it could mean that the hydrodynamics just do not change significantly with the variation in stirring'. This is a problem of systems where hydrodynamics (see Chapter 2) are ill-defined. In order to counteract this the rotating disc has been employed in the

dissolution of calcite [14,54,63-65]. This either involves the use of a cylinder of calcite, or a disc of calcite embedded in an unreactive cylinder. The rotating disc has well defined hydrodynamics so reliable studies of the effects of stirring rate on dissolution can be performed [14,53,54,63,64]. The detector itself is remote from the rotating disc apparatus and measures changes in bulk concentration. So although the rotating disc gives good hydrodynamics of reactants to the crystal the transport of products to detector are again ill-defined.

There is a need to consider the materials used in the various experimental strategies, and the preparation treatments used, as these factors could affect surface defect densities and thence the measured reaction rate (see section 1.4). These vary between calcium carbonate powder [56,66],seed crystals [28,38],and samples of carrara marble [63,64] or iceland spar crystals [15,17,18,53,55,63]. Carrara marble is a polycrystaline form of pure calcite, which has a number of crystal planes exposed and ready for reaction at its surface. This contrasts with Iceland Spar where the surface studied can either be the cleavage plane or a plane at an angle to the cleavage plane, but can be defined precisely.

A variety of preparation techniques are also employed. Washing the seed crystals or surface of the crystal with dilute HCl is common in order to remove surface impurities and to remove the outermost, 'strained' surface of calcite discs [57,63,64]. In the case of rotating disc experiments this can be followed by polishing and washes. These surface preparation techniques can also affect the nature of the surface and hence the rate of reaction.

Other studies have either tried to measure *in situ* kinetics in various geological environments or to more closely model actual geological situations [27,54]. One study

measured the calcite dissolution kinetics of *in situ* sediment cores in the ocean [57], measuring the pH with microelctrodes. In another study suspended calcite samples were positioned in the deep ocean then subsequently recovered for analysis [26].

Overall it can be seen that a variety of techniques have been used in the studies further discussed here. Short comings of these techniques include ill-defined hydrodynamics. Also the detection is remote from the actual surface and surface kinetics have to be modelled from data produced by measuring bulk changes. The latter is insensitive to small variations in surface concentrations. In these circumstances it is hard to probe very fast kinetics when the changes in surface concentrations may only differ in a small way between those for true mass transport control, and those for kinetic control. These problems will be later shown to be overcome by the channel flow cell technique adopted in this work.

1.5.2 The conclusions of previous studies: an overview

Calcite dissolution can be considered to occur via the reactions [55]

$$CaCO_3 + H^+_{(o)} \rightleftharpoons Ca^{2+}_{(s)} + HCO^-_{3\,(s)} \tag{1.2}$$

$$CaCO_3 + H_2CO_{3\,(o)} \rightleftharpoons Ca^{2+}_{(s)} + 2HCO^-_{3\,(s)} \tag{1.4}$$

$$CaCO_3 + H_2O_{(o)} \rightleftharpoons Ca^{2+}_{(s)} + HCO^-_{3\,(s)} + OH^-_{(s)} \tag{1.5}$$

with associated back reactions

$$\left|Ca^{2+} + HCO_3^-\right|^+_{(o)} + CO^{2-}_{3\,(s)} \rightleftharpoons CaCO_3 + H^+_{(s)} + CO^{2-}_{3\,(s)} \tag{1.5}$$

$$\left|Ca^{2+} + HCO_3^-\right|^+_{(o)} + HCO^-_{3\,(s)} \rightleftharpoons CaCO_3 + H_2CO_{3\,(s)} \tag{1.6}$$

$$\left|Ca^{2+} + HCO_3^-\right|^+_{(o)} + OH^-_{(s)} \rightleftharpoons CaCO_3 + H_2O_{(s)} \tag{1.7}$$

where the subscripts (o) and (s) represent the surface layer and the adsorbed layer, respectively. The $| Ca^{2+} + HCO_3^- |^+$ terms in the above equations occur as there is no distinction made here between free Ca^{2+} and HCO_3^- ions and the ion pair $CaHCO_3^+$.

Three distinct pH regions of the reactions have often been identified empirically [14,55,66]:

i) Low pH (< 4) where there is little dependence of the dissolution rate on the partial pressure of CO_2 (P_{CO2}) , and the rate depends on the concentration of H^+ in the bulk solution. Equation (1.2) predominates in the mechanistic scheme above.

ii) An intermediate region in which the dissolution rate depends on both pH and P_{CO2}.

iii) High pH (> 7) where the rate becomes independent of bulk pH, and at CO_2 partial pressures below 1 to 3 percent the rate is independent of P_{CO2}.

The boundaries between the regions are dependent on pH and P_{CO2} occurring at higher pH as P_{CO2} decreases [55,57,66].

1.5.3 Calcite dissolution / precipitation at low and intermediate pH

Based on the considerations outlined in the previous section Plummer *et al* [68] have deduced the following empirical rate equation for dissolution :

$$rate\ /\ \mathrm{mmol\,cm^{-2}s^{-1}} = k_1 a_{H^+} + k_2 a_{H_2CO_3^*} + k_3 a_{H_2O} - k_4 a_{Ca^{2+}} a_{HCO_3^-} \qquad (1.9)$$

where a_i is the activity for species i, and the activity of species H_2CO_3* is equivalent to the total of the activities for both H_2CO_3 and CO_2. All the terms relate to activities in bulk solution. In this equation the dissolution rate is dependent on each of the forward

reactions ((1.2), (1.4), and (1.5)), and the overall backward precipitation rate from the combined reactions ((1.5), (1.6), and (1.7)).

Plummer *et al.* [55] used this equation to explain the kinetics of dissolution in experiments using stirred Iceland Spar powders utilizing both free drift and pH-stat methods at 25°C. The value of k_1 was found to be proportional to stirring rate, whilst k_2 and k_3 were not. They obtained the following values $k_1 = 0.051$ cm s^{-1} (for stirring rates of 1800 to 2300 rpm), $k_2 = 3.5 \times 10^{-5}$ cm s^{-1} and $k_3 = 1.2 \times 10^{-7}$ cm s^{-1}. In order to explain k_4 mechanistically Plummer [55,57] proposed the back reaction equations ((1.5), (1.6) and (1.7)). Reaction (1.2) was assumed to be mass transport controlled. Given these assumptions, the mechanism agreed with the empirical rate law (1.9) and defined k_4 as

$$k_4 = \frac{K_{a2}}{K_{sp}}\left\{k_1 + \frac{1}{a_{H^+_{(s)}}}\left(k_2 a_{H_2CO_{3(s)}} + k_3 a_{H_2O_{(s)}}\right)\right\} \qquad (1.10)$$

where K_{a2} is the second dissociation constant of carbonic acid, and K_{sp} is the solubility product for calcite. In this case the solubilities are written in terms of surface activities. The values for the surface speciation were derived via the use of thermodynamic models of the aqueous phase. However it was very difficult to assess the surface activity of H^+. In the high partial pressures of CO_2 used in Plummer's experiments it was assumed that P_{CO2} and the activity of water were close to the bulk values. Surface pH was then determined from the calcite equilibrium owing to the rapid reaction with H^+.

The version of the Plummer equation above applies to all pH ranges. However at low pH the reactions between $CaCO_3$ and CO_2 and between $CaCO_3$ and H_2O can be ignored as being insignificant as compared to the H^+ reaction. The latter is much faster

and totally dominates [54,55]. The Plummer equation at low pH can be simplified to:

$$rate/\text{m mol cm}^{-2}\ \text{s}^{-1} = k_1 a_{H^+} \tag{1.11}$$

The work of Plummer [57] and various other workers [27,52,56-58,65,69,70]have agreed that the low pH calcite dissolution reaction is mass transport controlled and that the order of the reaction with respect to H^+ concentration, n is unity. Alternatively Sjöberg [14,54,56,63,64]has suggested that n=0.9. This was explained in terms of formation of aqueous CO_2 and the consequent disturbance of purely Fickian H^+ gradient throughout the boundary layer [63].

One indication that the reaction at low pH is transport rather than kinetically controlled is that several experiments [63,64]have failed to observe any difference in the rate of dissolution between Carrara Marble and Iceland Spar crystals. As Carrara Marble is polycrystalline it has a much larger number of crystal surfaces on any given exposed surface, and hence a larger number of reactive sites, than Iceland Spar which is monocrystalline. A faster rate of dissolution with Carrara Marble than with the Iceland Spar cleavage plane would therefore be expected [50,53].

An equation very similar to the Plummer equation (1.9) was derived by Chou et al [66] using the fluidized-bed method, when they carried out experiments over a wide pH range (pH 4 to pH 10). This method involves pumping solution through bed of carbonate material. In this method a steady state is reached and the composition of the fluid phase is dependent only on the composition of the input material and the input rate so it is in fact a pH-stat method. However unlike some pH-stat methods it cannot fix the partial pressure of carbon dioxide (P_{CO2}) of the system. This is not considered to

be a disadvantage by Chou et al because of the slow response of pH-stat devices as compared to the relatively fast dissolution of carbonates. This method did have high turbulence, so the hydrodynamics of the system were ill-defined and a problem. Their dissolution rate law was very similar to the Plummer equation but the precipitation rate decreased with $a_{Ca}a_{HCO3}$ in contradiction with the Plummer results which predicted an increase with this activity product. Instead the precipitation rate was found to increase with the product $a_{Ca}a_{CO3}$. This corresponds to the precipitation reaction being

$$Ca^{2+} + CO_3^{2-} \longrightarrow CaCO_3 \qquad (1.12)$$

giving a net dissolution rate equation:

$$J_{net} = k_1 a_{H^+} + k_2 a_{H_2CO_3^*} + k_3 a_{H_2O} - k_4 a_{Ca^{2+}} a_{CO_3^{2-}} \qquad (1.13)$$

k_1, k_2, k_3 were deduced as 0.089 cm s^{-1}, 5.0 x 10^{-5} cm s^{-1}, 6.5 x 10^{-8} cm s^{-1} respectively which are comparable with those obtained by Plummer et al above (section 1.5.2) and k_4 as 1.9 cm s^{-1}.

In order to obtain better defined hydrodynamics Compton and Daly[65,71,72] used the rotating disc method and again obtained a Plummer type equation (1.9). They performed their experiments in the pH region 3.0-6.2 and the reaction was monitored by the use of a Ca^{2+} ion selective electrode. The dissolution of Iceland spar crystals was found to obey the following equation

$$J_{Ca^{2+}} = k_1[H^+] + k_2[H_2CO_3] + k_3 \qquad (1.14)$$

The value of k_3 was shown to be dependent on the surface morphology of the calcite surface. When the surface was well polished and rinsed in 10^{-3} M HCl; k_3 was found to be 2.1×10^{-9} mol cm^{-2} s^{-1} which is comparable to the value obtained by Plummer *et al* (1.2×10^{-10} mol $cm^{-2}s^{-1}$). However increasing the surface roughness increased k_3; as the number of surface defects increased so did k_3 thereby increasing the rate of the reaction. Also if the crystal was polished at an angle to the {100} cleavage plane the dissolution rate was enhanced, which was explained in terms of an increased number of kinks [55].

Previously Dorange and Guetchidjan [71] had derived another empirical reaction equation, when they investigated the dissolution of marble in the presence of a known CO_2-N_2 atmosphere for bulk pH's of pH 4.5-6.7. They determined the P_{CO2} in the reaction vessel spectroscopically, and measured the extent of the reaction by monitoring the pH variation. They obtained the following rate equation.

$$\frac{d[Ca^{2+}]}{dt} = k([Ca^{2+}]_{eq} - [Ca^{2+}]_o) \qquad (1.15)$$

where $[Ca^{2+}]_{eq}$ represents the concentration of Ca^{2+} at equilibrium for the pH concerned, and $[Ca^{2+}]_o$ is the concentration of Ca^{2+} at the surface. Therefore the rate as defined by the variation in Ca^{2+} concentration is related to the difference between this concentration of Ca^{2+} and that predicted when the system has reached equilibrium.

Most of the studies at low pH discussed here have simply reflected the mass transport rates in whichever reaction vessels the calcite dissolution was studied. A few involved rotating disc experiments [14,54,63,65,71,72]but even in these cases the rate

was measured in terms of bulk changes. So all these experiments suffered from some lack of hydrodynamic control; even rotating disc experiments the transport of products to the detector is uncertain. Nor have previous experiments accessed the very fast rates of transport necessary to investigate fast interfacial kinetics, and so differentiate between true transport controlled processes and those which are controlled by very fast interfacial kinetics. This was in part because they measured bulk properties which are relatively insensitive to surface differences. In practice describing a reaction as transport controlled may only mean that the experimental design is unable to provide fast enough rates of transport in supplying reactants, or removing products, to probe the interfacial kinetics. As will be shown later the channel flow cell overcomes these problems and, at low pH the dissolution of calcite can be shown not to be transport controlled.

1.5.4 Dissolution of calcite at High pH

At high pH the reaction between calcite and H_2O dominates the dissolution kinetics. A number of kinetic schemes for the reaction at high pH have been proposed, as are discussed in this section.

The work of Plummer et al [55] as above has been used in the high pH range. If their results are compared with previous rate equation studies [55] then it is found that most dissolution rates agreed within a factor of 10 and many within a factor of 2 or less. Worse agreement was found with precipitation data, with growth rates being between 4 and 68 times those observed. The problem was identified as the need to quantify the mass transport, and reaction site density (see section 1.4).

Another rate law was proposed by Sjöberg and Rickard, who extensively studied both calcite powders and crystals. Early work by Sjöberg [73] involved the study of the dissolution of calcite powders by a free drift method. These experiments were performed at ionic strength 0.7 M KCl, with initial pH 8, and under an O_2 free N_2 atmosphere. $CaCl_2$ was added to the solutions in order to measure the effect of calcium on dissolution rate. The dissolution rate of the $CaCO_3$ obeyed the following law:

$$\frac{d[Ca^{2+}]}{dt} = kA\left(\sqrt{K_{sp}} - \sqrt{[Ca^{2+}][CO_3^{2-}]}\right) \qquad (1.16)$$

where k is a constant, A is the surface area and K_{sp} is the calcite solubility product. The dissolution rate was however found to be dependent on stirring rate.

Later work by Sjöberg and Rickard [51,54] had a greatly improved design which incorporated a calcite crystal in rotating disc apparatus (see also Compton and Daly 1.5.3). This gives well defined hydrodynamics so mass transport to the surface could be calculated. However the rate was still monitored by measuring bulk pH and thus was insensitive to surface processes. In the high pH region (pH > 5.5) using a pH-stat method they found [56] that the dissolution rate was independent of pH, but that it did depend on the nature of the calcite crystal, Carrara marble dissolving faster than Iceland spar. This is as would be expected as explained previously.

In order to model their results they derived the following mechanism, in which it was argued that dissolution in neutral and alkaline solutions was controlled by mixed kinetics, i.e. a combination of chemical and transport processes. They considered concentration in terms of c the concentration of $CaCO_3$. Transport across the diffusion

layer thickness was given by

$$\frac{dc}{dt} = \frac{k_T A(c_o - c_{bulk})}{V} \tag{1.17}$$

where k_T was a transport rate constant, V the volume of solution, the concentration at the surface c_o, and in the bulk c_{bulk}. Implicit in equation (1.17) are the assumptions that the species concerned is not involved in homogeneous reactions [68]. The rate of the chemical reaction was said to be a function of the chemical potential difference between the concentration of the dissolving $CaCO_3$ at the surface c_0 and the concentration at equilibrium, c_{eq}

$$\left.\frac{dc}{dt}\right|_C = \frac{k_C A(c_{eq} - c_o)^n}{V} \tag{1.18}$$

where k_C was a chemical reaction rate constant. Equating equations (1.17) and (1.18), which assumes that the species is not involved in homogeneous reactions within the diffusion layer [68], gave the following rate law for $n = 1$

$$\frac{dc}{dt} = \frac{k_T k_C}{(k_T + k_C)} \frac{A(c_{eq} - c_{bulk})}{V} \tag{1.19}$$

The empirical rate equation (1.16) was shown to be equivalent to this rate law [48]. Using this model the initial dissolution rate was written in terms of the diffusion layer thickness for a rotating disc and this gave

$$\frac{1}{rate} = \frac{1.61 \nu^{1/6}}{D^{2/3} c_{eq} \omega^{1/2}} + \frac{1}{c_{eq} k_C} \tag{1.20}$$

where ν was the kinematic viscosity of the solution, D the diffusion coefficient and ω the rotational velocity of the rotating disc. Experiments [48] gave linear plots of $1/rate$ against $1/\omega^{1/2}$ from which it was concluded that equation (1.19) gave an accurate description of the kinetics.

In this model as outlined above it was proposed that only Ca^{2+}, CO_3^{2-} and H_2O were present in the diffusion layer and rapid protonation of the carbonate ion occurred at the diffusion layer boundary. The onset of H^+-dependent kinetics was argued to occur when H^+ penetrated the diffusion layer and reached the calcite surface. This was said to only occur when the rate of transport of H^+ across the diffusion layer is at least equal to the rate of calcite dissolution, otherwise all the H^+ in this region will react with carbonate formed in the dissolution, and the effective surface concentration will be zero. This means that there is a pH above which the surface concentration of H^+ will be zero, this pH being in the range of pH 4.5-4.9 depending on experimental conditions. Their chemical step rate constant, k_C, was shown [14] to be independent of added bulk calcium ion concentrations up to 0.2 mM. It was concluded that the reduction in dissolution rate on adding Ca^{2+} ions was purely due to a reduction in diffusion rate and not due to inhibition of the chemical step, as concluded earlier by the same authors [56]. The rotating disc method was also used to investigate the temperature dependence of the dissolution rate with an Arrhenius activation energy for k_C being 46 ± 4 kJ mol^{-1} for Iceland Spar [64].

An equation similar to that of Rickard and Sjöberg (1.16) was derived by Buhmann and Dreybrodt [16-17,74],who tried to closely model the precise circumstances of dissolution of calcite in Karst systems. They modelled both laminar and turbulent flow, in both open (in contact with the atmosphere) and closed systems. The open systems model those circumstances when pore water is in contact with the atmosphere and maintains equilibrium concentrations of CO_2, this was obtained by allowing the reaction solution to maintain and equilibrate with an atmosphere of known CO_2 content.

Closed systems are more common, such as deep within pores when the solution has no chance to equilibrate with the atmosphere. This was modelled by two calcite surfaces being held apart by teflon dividers, modelling a pore. With CO_2 being excluded from the experiment. Both turbulent and laminar flow conditions were used, as both conditions can occur naturally in geological situations. They found three rate determining steps, which were treated simultaneously; the surface-controlled dissolution or precipitation at the $CaCO_3$ surface, the slow conversion of CO_2 to H_2CO_3, and the mass transport of dissolved species to and from the surface. The precipitation or dissolution rates in all cases were described by an equation similar to that of Rickard and Sjöberg (1.16)

1.5.5 Precipitation of calcite at high pH

Nancollas and Reddy [24,58] proposed a rate law for calcite precipitation from experiments utilizing a free drift method of calcite growth, using seed crystal. Precipitation rate was measured by monitoring pH and $[Ca^{2+}]$ then taking samples and analysing by means of ^{45}Ca isotope exchange or atomic adsorption spectroscopy. After an initial surge the rate was found to be independent of stirring and to follow a second order rate law:

$$\frac{d[Ca^{2+}]}{dt} = -kA\left([Ca^{2+}][CO_3^{2-}] - \frac{K_{sp}}{\gamma_{\pm}^2}\right) \qquad (1.21)$$

where $\gamma_{\pm}$ is the divalent ion activity coefficient. The activation energy was calculated as 46 ± 4 kJ mol^{-1} in good agreement with later values of Weichers et al [28] of 43.1 ± 3.8 kJ mol^{-1} and Inskeep and Bloom [75] of 48.1 kJ mol^{-1}.

Another rate law for calcite growth was proposed by Reddy [50,51] and Reddy and Nancollas [52] and this time was of the form

$$rate = kA\left([Ca^{2+}] - [Ca^{2+}]_{eq}\right)^2 \tag{1.22}$$

The maximum variation in the equilibrium calcium ion concentration, $[Ca^{2+}]_{eq}$, for the growth experiments utilizing this equation was 10%, whereas the variation in $[Ca^{2+}]_{eq}$ for equation (1.21) was much greater [52].

The Plummer equation (1.9) under conditions of high pH and low P_{CO2} can be reduced to:

$$rate = k_3 a_{H_2O}\left(1 - \frac{a_{H^+}}{a_{H^+_{(e)}}}\Omega\right) \tag{1.23}$$

where Ω is the saturation ratio defined as $a_{Ca}a_{CO3}/K_{SP}$. Which Plummer et al. [55] noted was very similar to the Nancollas and Reddy equation (1.21). The H^+ activity was calculated to be just less than one for low P_{CO2}. Reddy, Plummer and Busenburg [20], investigated the applicability of the Plummer model to calcite precipitation. However analysis of $[Ca^{2+}]$ with time for seeded growth experiments at P_{CO2} between 0.03 and 0.3 atm gave non-linear plots for log *rate* versus log Ω, log (1-Ω), and log ($[Ca^{2+}] - [Ca^{2+}]_{eq}$). Also though there was agreement within a factor of three between observed and calculated rates using the Plummer model for P_{CO2} between 0.029 and 0.096 atm, at higher P_{CO2} and near equilibrium the precipitation rate was less than expected with a much larger discrepancy. Therefore this model was concluded not to be a satisfactory explanation of calcite precipitation.

Kazmierczak, Tomson and Nancollas [10] used a chem-stat method to keep the concentrations of all reactants constant during crystallisation. They used seed calcite crystals in a supersaturated calcium carbonate solution. From these experiments they concluded precipitation was governed by the rate law

$$\frac{\mathrm{d}[Ca^{2+}]}{\mathrm{d}t} = -kA\left(\sqrt{a_{Ca^{2+}} a_{CO_3^{2-}}} - \sqrt{K_{sp}}\right)^2 \qquad (1.24)$$

where a_i are activities and K_{SP} is the thermodynamic solubility product of calcite. The rate constant k was found to be independent of the ionic strength of the supersaturated solution over a wide range 90.0 to 0.20 $mmol\,dm^{-3}$, when the rate equation was in terms of activities rather than concentrations.

Zhong and Mucci [25] seeded calcite growth in seawater solutions of various salinities using a chem-stat method. They fitted the data to a empirical rate law of the form

$$rate = k(\Omega - 1)^n \qquad (1.25)$$

where the reaction order n was between 2.5 and 3.3. Their method used seed crystals of both calcite and aragonite, the surface areas having been previously characterised. These seed crystals were used in artificially aged seawater solutions of various salinities, with the degree of supersaturation altered by adding varying amounts of carbonate rich solutions. These experiments were carried out in an open system. They found the reaction rate to be 'fairly' independent of salinity. This equation has also been widely used by other people [76-79].

Davies and Jones [80,81] developed another model, initially for the precipitation of silver chloride. The model assumes there is a monolayer of hydrated ions covering the surface, and that hydration or dehydration of ions at the surface precedes dissolution or precipitation respectively. Following these assumptions, based on the double layer model with Boltzman distributions of surface concentrations

$$[Ca^{2+}]_{(s)} = [Ca^{2+}]_{Bulk} \exp\left(-\frac{2F\phi}{RT}\right) \tag{1.26}$$

$$[CO_3^{2-}]_{(s)} = [CO_3^{2-}]_{Bulk} \exp\left(\frac{2F\phi}{RT}\right) \tag{1.27}$$

where Φ is the electrical potential.

Assuming the surface concentrations of Ca^{2+} and CO_3^{2-} are equal

$$[Ca^{2+}]_{eq\,(s)} = \frac{K_{sp}^{1/2}}{\gamma_{\pm}} \tag{1.28}$$

and also from equations (1.26) and (1.27)

$$\exp\left(\frac{2F\phi}{RT}\right) = \left(\frac{[Ca^{2+}]}{[CO_3^{2-}]}\right)^{1/2} \tag{1.29}$$

The rate of growth was assumed to be proportional to the amount of Ca^{2+} and CO_3^{2-} available for growth, i.e.

$$rate = k\gamma_{\pm}^2\left\{[Ca^{2+}]_{(s)} - [Ca^{2+}]_{eq\,(s)}\right\}\left\{[CO_3^{2-}]_{(s)} - [CO_3^{2-}]_{eq\,(s)}\right\} \tag{1.30}$$

which on substitution gave

$$rate = k\gamma_{\pm}^{2}\left\{\sqrt{[Ca^{2+}][CO_3^{2-}]} - \sqrt{\frac{K_{sp}}{\gamma_{\pm}^{2}}}\right\}^{2} \qquad (1.31)$$

Which is very similar to the Kazmierczak, Tomson and Nancollas equation (1.24) above.

The assumption that the surface concentrations of the cation and anion are equal, however, has been shown to be invalid for calcite [61,82]. So the justification for this equation is built on false assumptions.

Both House [60] and Inskeep and Bloom [75] have investigated a number of these rate laws for seeded crystal growth experiments. In the case of House supersaturated calcium bicarbonate solutions were used, and the course of the reactions monitored via pH and conductivity measurements. He concluded that the equations proposed by Nancollas and Reddy (1.21), and Reddy and Nancollas (1.22), gave poor agreement over the supersaturation range. The Davies Jones (1.31) gave good agreement over a limited range. The Plummer equation (1.9) was however consistent with the data, but a unique growth curve was not obtained.

Inskeep and Bloom [75] used a pH-stat method of seeded crystal growth, for pH 8.25 - 8.70, $P_{CO2} < 0.01$ atm and ionic strengths 0.015 - 0.10 mol dm^{-3}. A form of the Davies Jones equation and the Reddy and Nancollas equation (1.22) did not fit the data. The Davies Jones written in terms of surface potential (1.31) was consistent with the data but was discounted because of the errors associated with its derivation (see above). The

Plummer equation (1.9) was consistent with the data, but broke down if the initial [Ca^{2+}] / [CO_3^{2-}] ratio was altered. Best agreement was found with the Nancollas Reddy equation (1.21) when modified to account of ionic strength differences.

Christoffersen and Christoffersen [68] used a pH-stat seeded crystal growth experiment. They explained the kinetics in terms of a spiral growth mechanism proposed by Nielsen [83,84] in which growth occurs via self propagating spirals. They obtained an overall rate equation of

$$rate\ /\text{mol s}^{-1} = \frac{0.1a\left(\frac{\nu_{in}}{\nu}\right)K_{ad}c_{eq}}{\left(\frac{\gamma}{k_B T}\right)\exp\left(\frac{\gamma}{k_B T}\right)}(S-1)S^{1/2}\ln S \qquad (1.32)$$

where a is the mean lattice ionic diameter, ν_{in} the frequency of a species entering a kink from a neighbouring site, ν the number of ions in a formula unit, K_{ad} an adsorption constant, c_{eq} the equilibrium concentration, γ the edge work and S the supersaturation expressed as $([Ca^{2+}][CO_3^{2-}]/K_{sp})^{1/\nu} = \Omega^{1/\nu}$.

1.5.6 Recent work

Recent advances particularly in spectroscopy have allowed the surface of calcite to be studied directly. *Ex situ* techniques such as LEED (Low Energy Electron Diffraction), XPS (X-ray Photo Spectroscopy), and *in situ* ones such as AFM (Atomic Force Microscopy) have been used. These allow molecular, and atomic information about the surface to be obtained.

i) LEED. In this technique low energy electrons are fired at the crystal; as they are of low energy they only penetrate the surface. The resulting diffraction pattern is the result of surface features rather than the bulk lattice. The pattern is sharp if the surface is well ordered. Diffuse spots indicate either a lack of order or the presence of impurities. Stipp and Hochella [85] applied LEED to a calcite surface, which had been prepared carefully. The calcite crystal was washed several times, soaked in nitric acid, then washed again and dried by in N_2. After this prepreparation the crystal was cleaved with a razor blade. Then either this freshly exposed surface was used in the LEED experiment, or the surface was exposed to aqueous solutions the latter was followed by drying by blowing off the water with steam, and then used in the experiment. The resulting patterns from the LEED showed that the surface was well ordered. This order persisted even after precipitation, thus supporting the assumption often made that the number of hydrated surface sites reflects the density of crystal lattice sites along the crystallographic planes.

ii) XPS. This method uses electrons of a known wavelength to eject electrons from the core and valence atoms near the surface of a solid. Only electrons from within some tens of angstroms of the surface can escape so again the technique providing information on the surface only. By measuring the energy of the electron details of the

oxidation and reduction state of the region it was emitted from is given, so giving information of the bonding characteristic and details of the valence shells of materials. From XPS experiments on Calcite Stipp and Hochella [85] have shown that there is evidence of hydration species $> CaOH^0$ and $> CO_3H^0$ on the surface of calcite, where $>$ represents the mineral lattice. This evidence is seen even after the vacuum pretreatment of the surface necessary for XPS.

iii) AFM. This is an *in situ* technique which uses a very sharp probe (a pyramidal Si_3N_4 tip), to limit the interaction area on the surface being studied. The AFM measures a contact force, typically of van der Waals type in origin between the tip and the sample. The contact forces fall off rapidly with distance from the surface. This keeps the interaction primarily confined to the end of the AFM tip, allowing high resolution images to be obtained. The tip stays in contact with the surface, while a xyz translator moves the sample in a raster pattern. The tip moves up and down in response to surface features; these movements deflect the cantilever and are detected by a laser. These movements are then recorded, and an image of the surface obtained, deflection being related to the height of surface features. Hillner et al. [86] used AFM to look at calcite dissolution and growth processes in real time. They worked at high pH in order to follow the H_2O reaction (1.5) for simplification. Dissolution occurred layer by layer but with the addition of etch pin holes and etch cores (which nucleated rhombic surface voids). These pin holes and cores affected latter growth patterns on the same surface. For growth they used a supersaturated solution prepared by adding $NaHCO_3$ solution slowly to a $CaCl_2$ solution, then titrated to the correct pH with NaOH. A $15 \times 15 \mu m$ region of cleaved calcite was imaged while $CaCO_3$ was grown on it in a series of

dissolution growth episodes. The conclusions were that growth occurred layer by layer, with no evidence of growth islands.

Van Cappellan et al [87] has made use of LEED and XPS, which give direct molecular level information on bonding environments at the carbonate water interface. They have combined such data with a surface complexation model, which sees the surface exposed cations and anions being hydrated. Thus cation and anions may be adsorbed at the surface by exchanging for H^+ or OH^- groups respectively. XPS and LEED have indeed given evidence for such hydrated surfaces. The surface kinetics are deemed very rapid.

1.6 The Channel Flow Cell

In order to investigate calcite kinetics, or any other solid-liquid interface reaction, it is desirable to fulfil a number of criteria. First it is necessary to have well defined and calculable transport of reactants to the surface and products away from it. Second it is useful to have control of the surface topography and third to have chemistatic control of the reactants. In most of the studies present earlier the transport processes are ill-defined. Even in the rotating disc experiments, although there is well defined transport of reactants to the surface, the transport of products to the detector is ill defined. In addition for fast reaction rate, high rates of transport to the interface are needed otherwise the experiment will merely measure the rate of transport in the liquid phase.

In order to fulfil these criteria the channel flow cell was developed as shown in figure 1.3. It has well defined mass transport (as discussed in Chapter 2), and with a detector close downstream to the interface, measures predictable, close to the surface concentrations. Both mass transport of reactants to the surface and products from the

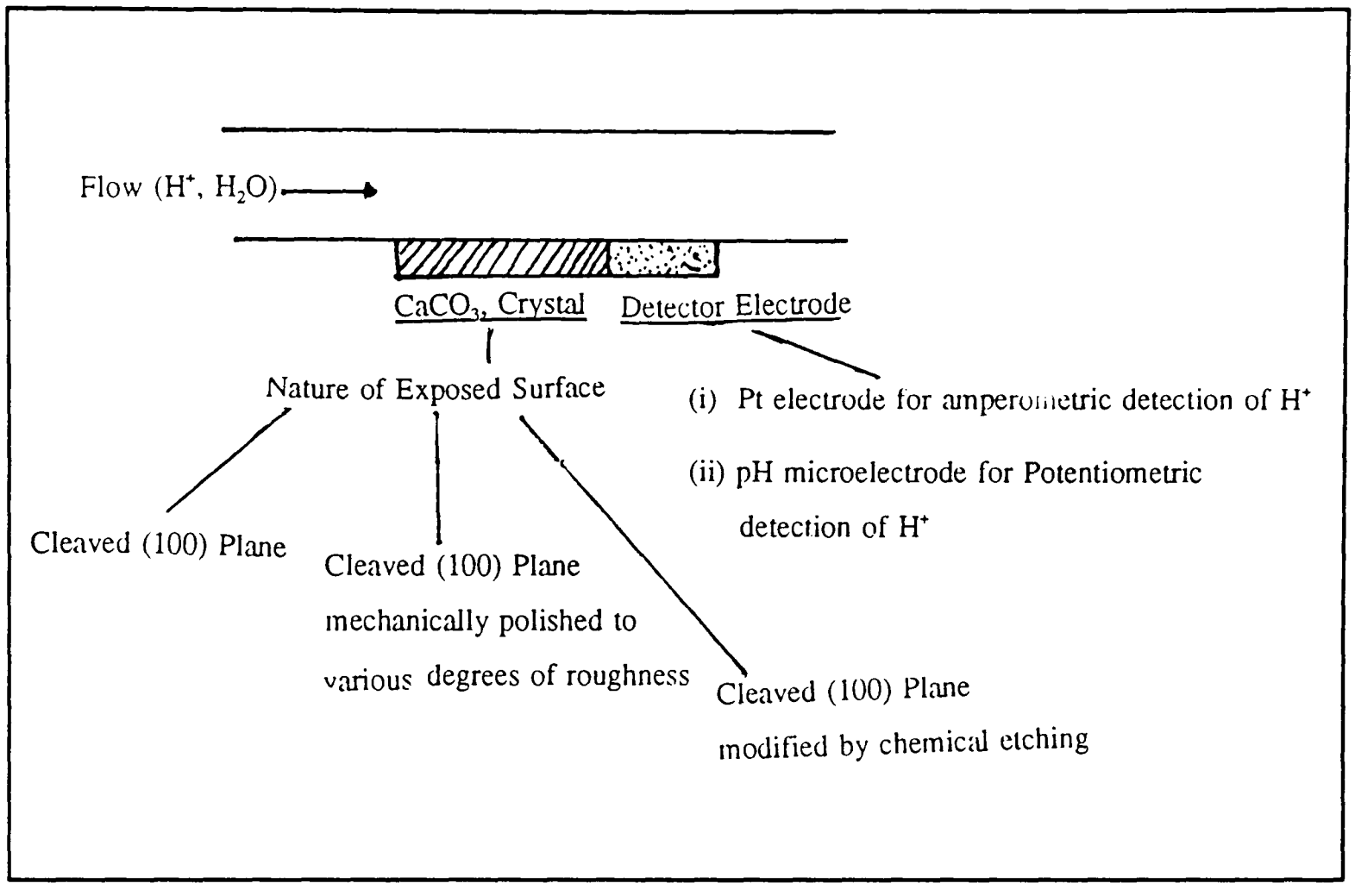

Figure 1.3 The channel flow cell.

surface to the detector are well defined. The surface of the calcite crystal can be etched, freshly cleaved, or polished in some predetermined manner. Thus the surface topography can be defined by the experimental pretreatment. There is precise chemostatic control of the reaction environment, with continual replacement of reactants flowing to the surface, and the products flowing away to waste. In addition the detector measures close to surface concentrations, enabling more accurate probing of small variations resulting from the precise kinetics. So all of the above criteria are fulfilled. This has enabled greater understanding of the calcite dissolution processes.

As stated above most earlier studies assumed that at low pH the reaction was transport limited. However Compton and Unwin [53,88] showed by use of the channel flow cell, that the variation the concentration of H^+ with flow rate is not that which is

expected for a transport controlled reaction. Compton and Unwin derived the following rate equation for the dissolution of calcite (Iceland Spar) at low pH.

$$J_{Ca^{2+}} / \text{mol cm}^{-2}\,\text{s}^{-1} = 0.043[H^+]_o \qquad (1.33)$$

where $[H^+]_0$ is the concentration of H^+ at the surface.

Another study by Compton *et al* [33] investigated the consquences of this kinetic control of low pH calcite dissolution on the liming of lakes. They used this kinetic rate equation together with the methods of estimating mass transport to a dissolving particle as developed by Harriott [79] and Sherwood *et al* [90]. This demonstated that the rate of dissolution of calcite particles under lake liming conditions was much slower than previously thought. This was the case even though the possible inhibition by natural inhibitors, such as humic acids or aluminium, present in lake waters were not taken into consideration in the calculations. So it was concluded that the dissolution of lime added to lakes would take place at significantly slower rates than hitherto considered, and future strategies for liming lakes would need to reflect this particularily in the particle size distributions used for neutralization.

The channel flow cell has also been used to investigate the action of inhibitors on the dissolution of calcite. At low pH small monomeric inhibitors such as, maleic and fumaric acids [91] and various tartaric acids [92]; were studied. From these experiments comparison was made between the inter carboxylic distance and the structure of the calcite etch pit, which lead to a conclusion that these factors were of importance in efficiency of a given inhibitor. Further discussion of these studies will be given in Chapter 4. Also at low pH investigation was made of the effect of polymaleic acid [93].

The inhibition slowly increased with time, and again this study will be further discussed in Chapter 4.

Investigation has also been carried out on the effects of inhibitors at high pH, by Brown [95] utilizing the channel flow cell methodology. Inhibitors which have been studied include succinic acid, phthalic acid, 2-sulphobutanedioic acid trianion, maleic acid, aspartic acid, and Mg^{2+}. Further detail of and comparision of the results of some these studies will be discussed in Chapter 6.

Compton *et al* [94] used the channel flow cell to investigate the dissolution of Carrera Marble, Portland Stone, and various other limestones. In these experiments the calcite crystal in the flow cell was replaced by a sample of the relevant calcium carbonate containing rock. The results showed that Carrera Marble had a faster rate of dissolution than Iceland Spar, as would be expected due to surface defect density. In other limestone cases the rates measured were so fast that they were mass transport controlled. For Portland Stone the dissolution rate was slower than Iceland Spar, but in this case the sample had significant quantities of Al^{3+}. Abbeytown limestone and Connemara marble both contained significant amounts of acid insoluble material, in the first case leading to a relatively slow rate constant, and in the second to highly irreproducible results.

1.7 Aims

The work presented in this thesis will lead to an enhanced understanding of the dissolution kinetics of calcite at high pH. It will utilize the channel flow cell, so that the hydrodynamics are well defined and the species concentrations measured are close those to the dissolution surface, and all of the other criteria mentioned in the previous section as desirable for accurate probing of surface kinetics are achieved. The surface

topography can also be controlled; in this work the surface choosen is a calcite cleavage plane which has undergone some initial etching by HCl (see Chapter 3 for full detail). A wide range of flow rates, initial bulk pHs and Ca^{2+} ion concentrations are used in the channel flow cell experiments. Using the numerical methods introduced in Chapter 2 it is possible to compare the experimental results with those predicted by a number of existing rate laws for high pH dissolution. As none of these rate laws will be shown to adequately fit over the whole range of conditions used a new mechanistically rational rate equation is derived. This mechanism is based on surface reaction/molecular integration model of Chang and Donohue [95] for crystal growth in which growth is considered to occur via adsorption of ions on the surface followed by formation of $CaCO_3$ and subsequent incorporation into the crystal lattice. Dissolution proceeds via the reverse of this process, and the overall net dissolution rate is the balance between the dissolution rate and the growth rate. The rate equation derived from this model is shown by the work described in this thesis to fit the experimental data over the whole range of flow rates, pHs, and Ca^{2+} concentrations studied. Further evidence from literature which supports this model is also presented.

Additionally the work considers the effect of inhibitors on the dissolution of calcite at high pH. In particular attention is paid to the action of the polymeric inhibitor, polyacrylic acid. The inhibitor is shown to act by adsorption on the surface, so preventing the dissolution (or growth). It is deduced that a complex is formed between the polymer and Ca^{2+} and that this adsorbs in a langmuirian manner, so causing inhibition by blocking the crystal growth sites.

The inhibiting effects of polyacrylic acid at low pH are reported under conditions of low pH. Polymers of a variety of molecular weights (2,000, 5,000 and 15,000) are

studied (Chapter 4). It is shown that full inhibition by this polyacrylic acid is rapidly established. So any conformational change necessary for adsorption is rapid, due to the flexible nature of the polymer. This contrasts with polymaleic acid [93], a fairly rigid polymer, in which case the strength of the inhibition varied over time needing half an hour or more to reach full inhibition. Flow cell measurements again show that it is a complex of polyacrylic acid and a divalent cation which is the surface active adsorption.

In addition two small dissolution inhibitors namely phthalic and homophthalic acids are studied at low pH (Chapter 4). The study of these molecules enables comparison of the efficiency of the polymer with these molecular inhibitors on a weight for weight basis.

CHAPTER 2

MASS TRANSPORT AND THE SOLID LIQUID INTERFACE

2.1 Introduction

This chapter introduces some basic concepts about mass transport. Then the hydrodynamics of the channel flow cell are explained and shown to be well defined. The hydrodynamics are then used to generate an approximate analytical solution for the limiting current within a channel electrode. Then the limitations of such analytical approaches are made evident. Following this the backwards implicit finite difference method is introduced. This is a powerful numerical method for the general solution of mass transport equations in the channel flow cell geometry. This latter approach provides the basis for modelling all of the experimental work presented in this thesis.

2.2 Mass Transport

Initially it is necessary to understand the basic concepts of mass transport at a surface. If the amount of a species transported to a surface of unit area, in a unit time is the flux, J, with units of mol cm^{-2} s^{-1}, then to quantify this flux it is necessary to understand the mechanisms by which reactants are brought from bulk solution to the surface. Three mechanisms operate by which reactants can be brought from bulk solution to the solid-liquid interface or conversely, by which products may be removed

from it into bulk solution. These are migration, diffusion and convection.

a) Migration is the movement of charged particles in an electric field. The force on the particle is proportional to the electrical potential gradient, and the charge of the particle.

b) Diffusion is the process by which particles move from a region of high concentration to one of lower concentration so as to maximise entropy.

c) Convection is a process in which solution as a whole is mechanically moved so that both solvent and solute are moved, unlike the case with migration and diffusion where the solute alone moves.

2.2.1 Migration

Migration of charged species occurs when a potential gradient exists. If the local potential ϕ varies along the x-axis then there is an electrostatic force acting on the ions in the x-direction which is opposed by viscous forces. This results [96] in the ions having a velocity v:

$$\mathbf{v} = -\frac{zu}{|z|}\frac{\partial \phi}{\partial x} \tag{2.1}$$

where u is the mobility of the ions with charge number z. This can be transformed into the migratory flux.

$$J(x,t) = -\frac{zuc(x,t)}{|z|}\frac{\partial \phi}{\partial x} \tag{2.2}$$

Transport due to migration can be made negligible by the addition of an excess of an inert supporting electrolyte, as described in section 2.3.

2.2.2 Diffusion

Diffusion is the movement of species "down" a concentration gradient and was shown experimentally by Fick [97,98] to be proportional to this gradient:

$$J(x,t) = -D\frac{\partial c(x,t)}{\partial x} \tag{2.3}$$

where D is the diffusion coefficient. This equation is known as Fick's first law. The concentration gradient is altered with time by diffusion. Conserving mass with planar diffusion gives Fick's second law [97,98]:

$$\frac{\partial c(x,t)}{\partial t} = D\frac{\partial^2 c(x,t)}{\partial x^2} \tag{2.4}$$

2.2.3 Convection

Convection is movement which arises as a result of a pressure gradient which exists in the fluid. The flux, J, can be related to the average velocity, v, of the species in the direction normal to this surface, and also the concentration, c, of the species. This can be related to velocity and the concentration (at the same time and distance) as shown below

$$J(x,t) = vc(x,t) \tag{2.5}$$

It is important in this study to understand how convection influences the movement of reaction species to and product species from, the surface of interest. The surface is in this study usually a calcite crystal, but might also be an electrode. For example electrodes are utilized in some rotating disc measurements, and for amperometric detection in the channel flow cell. Convection takes two forms: forced and natural. Forced convection is when motion is deliberately introduced into the system

by stirring or pumping, for example. This is can be irreproducible unless care is taken to set up the forced convection in a controlled and quantifiable way. Examples of forced convection range from simple stirring of solution, to the rotating disc electrode and the channel flow cell. In the case of simple stirring the convection patterns produced are ill defined and complex. In contrast for both the rotating disc electrode and channel flow cell the convection patterns are well defined and understood. The patterns are as shown in figure 2.1 for the rotating disc electrode and in figure 2.6 for the channel flow cell.

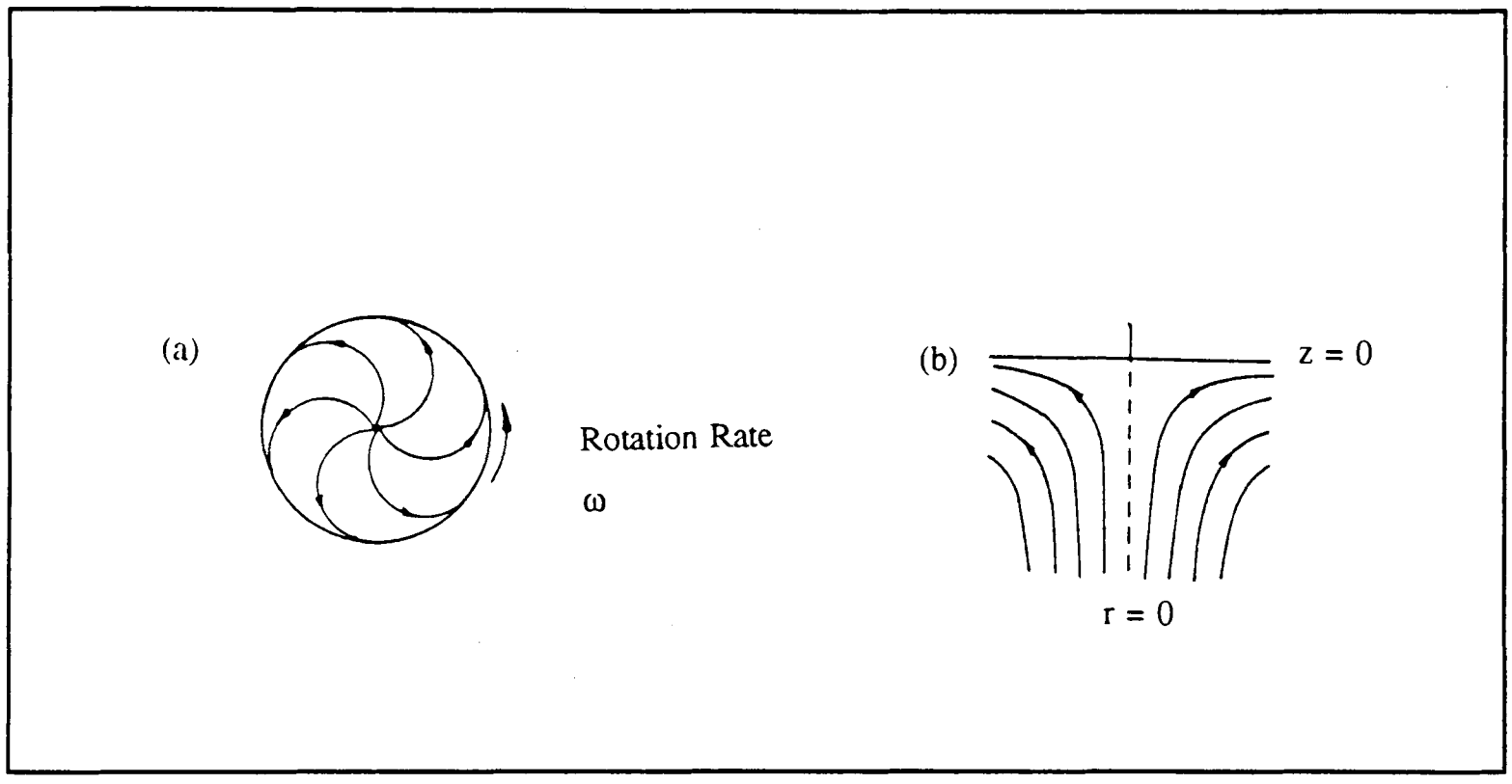

Figure 2.1 The flow patterns created by the rotating disc electrode, a) solution flow close to the electrode surface as viewed from above, b) view from the side showing how the solution is pumped towards the disc then thrown outwards.

When a rotating disc electrode is rotated, the electrode acts as a pump, pulling the solution vertically upwards towards the disc then throwing it outwards. If the volume of solution is large enough, so that the vessel walls do not interfere, then as can be seen in the above diagram the flow follows certain patterns, or 'streamlines'. By investigating these streamlines it can be seen first that the rotational movement of the solution is strongest at the surface, but drops off rapidly with the distance from the surface. The centrifugal motion is zero at the surface and also in the bulk, but goes through a broad

maximum a short distance away from the surface. Provided the radius of the electrode is small with respect to the sheath, then there will be a uniform supply of material to the disc. Because of this the rotating disc electrode is said to be uniformly accessible.

In the case of the channel flow cell the electrode under laminar flow, when it can be considered that the solution advances down the channel in non-mixing layers or elements in a highly organised manner, with only diffusion moving species between these 'layers'. Therefore not all the solution has equal access to the electrode, with only the solution at the walls accessing the electrode. So the channel flow cell is non-uniformly accessible. In the case of an electrode this leads to the current density varying over the surface.

Natural convection can result from reactions at the surface. If the reaction changes the amount of solute, the density of the solution may alter slightly in the locality of the reaction site. As a consequence regions of solution near the interface will tend to rise or fall under gravity, setting up natural convection. As this natural convection is difficult to eliminate, normally it is better to make its effect negligible by employing forcing convection of a much greater magnitude.

2.2.4 Conclusions

The flux of a species *i* due to all three modes of transport can be summarised by a general mass transport equation [99] where

$$J_i = c_i \mathbf{v}(x,t) - D_i \frac{\partial c_i(x,t)}{\partial x} - \frac{z_i u_i c_i(x,t)}{|z_i|} \frac{\partial \phi}{\partial x} \qquad (2.6)$$

convection *diffusion* *migration*

In order to investigate the kinetics at the solid-liquid interface it is thus necessary to have well defined and quantifiable mass transport for each of these processes, if the experimental results are to be capable of theoretical interpretation and modelling.

2.3 Supporting Electrolyte

Supporting, or background, electrolyte is often used to eliminate the effect of migration on transport. How supporting electrolyte effects transport can be illustrated by the example of the electrolysis between two parallel plates with the cathode above the anode (see figure 2.2).

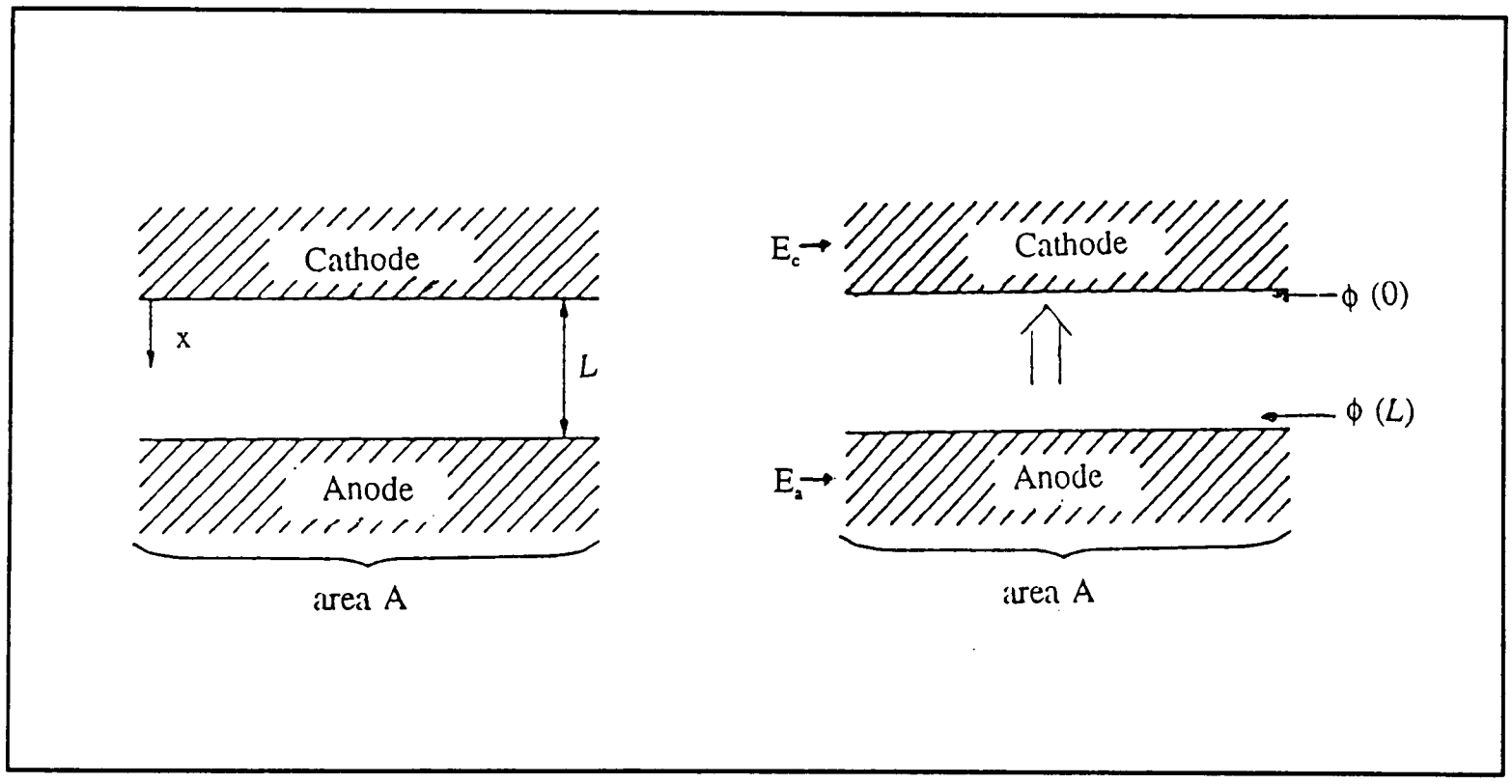

Figure 2.2 Electrolysis between two parallel plates, with the cathode (O) above the anode (L), and x is the distance from the cathode.

At the anode the electrode is dissolving

$$M(s) - ne^-(M) \longrightarrow M^{n+}(sol) \qquad (2.7)$$

and at the cathode ions are being replated:

$$M^{n+}(sol) + ne^-(M) \longrightarrow M(s) \qquad (2.8)$$

When the only ions in solution are the electroactive cation and its associated anion the steady state concentration profile for the two ions is as shown in Figure 2.3 [100]. As there is electroneutrality:

$$z_1 c_1 (x,t) + z_2 c_2 (x,t) = 0 \tag{2.8}$$

where z_i is the charge on ion i and c_i is the concentration of ion i.

At steady-state the flux of any ion is constant across cell so for ion 2, the electroinactive ion

$$-D_2 \frac{d}{d} x c_2(x) + u_2 c_2 \frac{d}{d} x \phi(x) = J_2(x) = 0 \tag{2.9}$$

where u_2 is the potential of ion 2. So that the diffusive and migratory fluxes are equal and opposite, throughout the cell.

Hence

$$D_2 \frac{dc_2(x)}{c_2(x)} = u_2 d\phi(x) \tag{2.11}$$

which integrates to

$$D_2 \ln c_2(x) = u_2 \phi(x) + \text{constant} \tag{2.12}$$

If this integration is done with reference to conditions at the cathode, ie. $x = 0$, then

$$D_2 \ln \frac{c_2(x)}{c_2(0)} = u_2 [\phi(x) - \phi(0)] \tag{2.13}$$

which can be converted to

$$c_2 = c_2(0) \exp\left\{\frac{u_2}{D_2}[\phi(x) - \phi(0)]\right\} \tag{2.14}$$

This describes the equilibrium distribution of the electroinactive ion in an electric field.

Equating the exponent in equation (2.14) with that in the Boltzman distribution:

$$c_2(x) = c_2(0)\exp\left\{-\frac{N_A\epsilon(0\rightarrow x)}{RT}\right\} \tag{2.15}$$

where R is the gas constant, T is temperature and ϵ (0 → x) is the energy required to carry an ion from $x=0$ to $x=x$. Leading to the following on combining the two exponents

$$\frac{u_2}{D_2} = -\frac{N_A\epsilon(0\rightarrow x)}{RT[\phi(x)-\phi(0)]} = -\frac{N_A z_2 q^\circ}{RT} = -\frac{z_2 F}{RT} = \frac{|z_2|F}{RT} \tag{2.16}$$

where q° is the unit charge which is equal to F/N_A, and where F is the Faraday constant. This is a general relationship, the Nernst-Einstein relationship, this is applied to the exponential then

$$\frac{\partial}{\partial x}c_j(x) + \frac{z_j F}{RT}c_j(x)\frac{\partial}{\partial x}\phi(x) = -\frac{J_j}{D_j} \tag{2.17}$$

where J_j(x) has been replaced by J_j because of the constancy of this term. This can be written first for the electroinactive ion

$$\frac{\partial}{\partial x}c_1(x) + \frac{z_1 F}{RT}c_1(x)\frac{\partial}{\partial x}\phi(x) = -\frac{J_1}{D_1} = \frac{i}{z_1 A F D_1} \tag{2.18}$$

for the electroinactive ion

$$\frac{\partial}{\partial x}c_2(x) + \frac{z_2 F}{RT}c_2(x)\frac{\partial}{\partial x}\phi(x) = -\frac{J_2}{D_2} = 0 \tag{2.19}$$

These two equations can be summed at steady state; since the flux of any ion is constant across the cell (equation (2.9)), giving

$$\frac{\partial}{\partial x}[c_1(x)+c_2(x)] = \frac{i}{z_1 A F D_1} \tag{2.20}$$

This relationship gives rise to the concentration profile of the ions shown in figure (2.3) below.

If we consider the potential drop inside the cell (not across the electrode) we obtain

$$\phi(L)-\phi(0) = \frac{RT}{|z_2|F}\ln\frac{c_2(L)}{c_2(0)} \tag{2.21}$$

where c_2(L), and c_2(0)are the concentrations of ion 2 at the anode and cathode respectively. If the electrode reactions are rapid so that Nernst's equation is obeyed, the interelectrode potential difference with respect to distance is

$$E_a - E_c = \frac{RT}{z_1 F}\ln\frac{c_1(L)}{c_1(0)} + \phi(L) - \phi(0) \tag{2.22}$$

ignoring double layer effects. If $z_1 = z_2$ then half of E_a -E_c arises from the thermodynamic Nernstian effect, and the other half from the potential difference created in the solution from the passage of current. The later is colloquially known as the 'ohmic drop'.

This situation is altered on the addition of an inert 'supporting' electrolyte. The <u>total</u> cation and anion concentration profile is still the same linear function of distance as in Figure 2.3, but this is not any longer the case for the concentration profiles of the individual ionic species, as shown in Figure 2.4. [101,102].

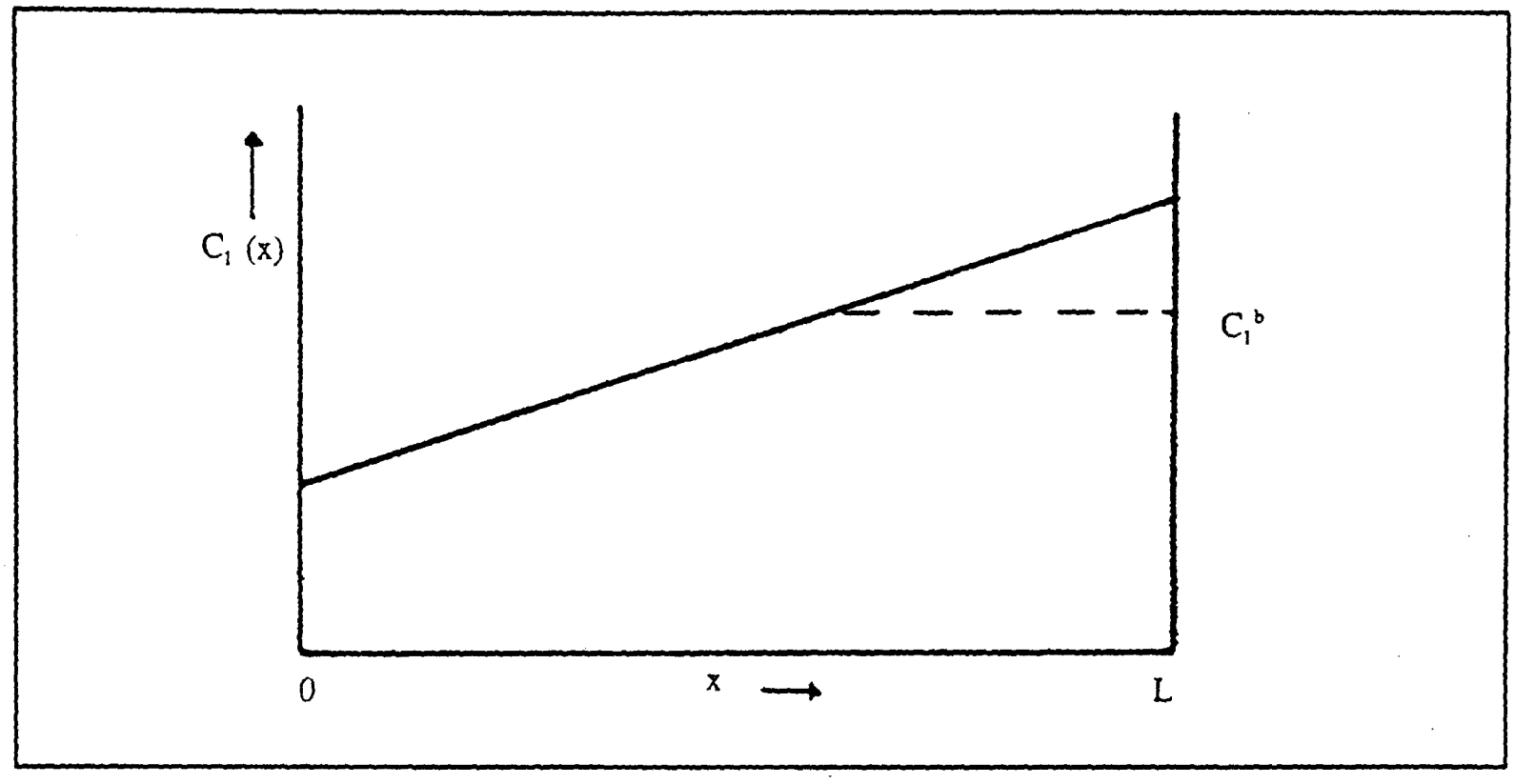

Figure 2.3 Concentration of ions as a function of distance between two electrodes, a distance L apart. Only the electroactive cation and its anion are present.

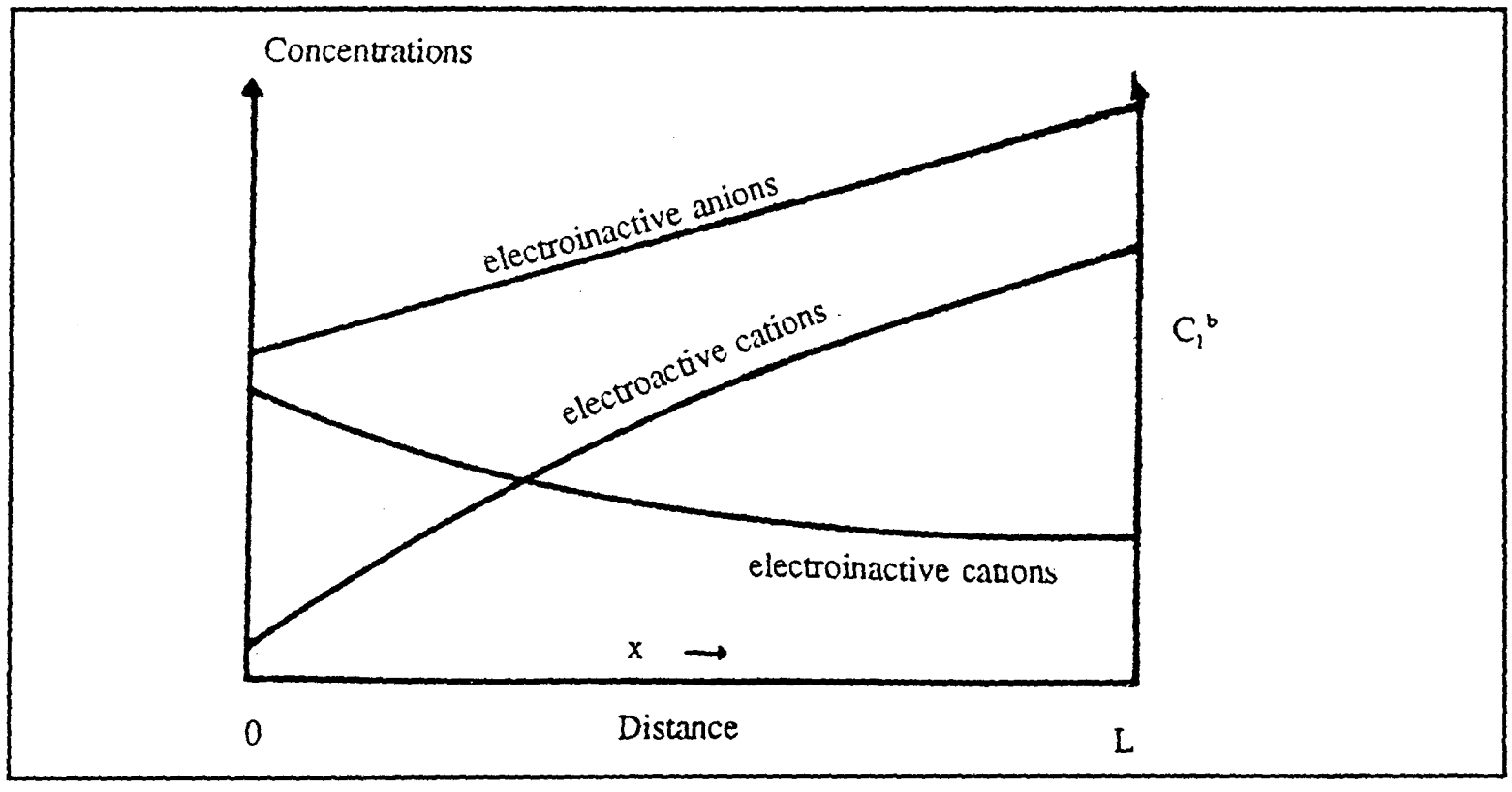

Figure 2.4 Concentration of ions as a function of distance between two electrodes, a distance L apart. In the case where there is a supporting electrolyte.

The migration of the electroactive species is reduced by the addition of supporting electrolyte. When the supporting electrolyte is in an infinite excess the limiting current is exactly twice that in the unsupported case [102]. This is because in the unsupported

case, the flux due to migration is equal to the diffusion flux, but in the former case mass transport due to migration is eliminated and only the mass transport due to diffusion remains. In order to reduce the migratory component to 1% of the diffusive component in the homovalent case, a 33-fold excess of the supporting electrolyte is required [103].

The suppression of migration to negligible levels with supporting electrolyte is often said to occur since 'the current is largely carried by the supporting ions' [101]. This however is not the case. The electroactive ions carry all the current and the other ions are effectively immobile at steady state. A more accurate explanation is that the electroinactive ions redistribute themselves in the solution, so that any potential gradient within the solution is eliminated. As there is no potential gradient to drive migration, diffusion becomes dominant.

Migration may be of great importance when dealing with ionic species and with charged surfaces or electrodes. However by the addition of an excess of supporting electrolyte it can be experimentally rendered a negligible transport process, thus simplifying the theoretical interpretation of experimental data.

2.4 The Convective-Diffusion Equation

The use of diffusion alone to transport reactants to the surface, is not very reproducible due to the possibility of natural convection occurring. As it is very difficult to eliminate natural convection and the smallest alteration in conditions can have a large effect on this convection, forced convection is required. The contribution to mass transport from forced convection will be much greater than that by natural convection, allowing the later to be ignored.

The introduction of convective processes into the mass transport of species to and from a reactive surface requires knowledge of the velocity profile of the system, if the mass transport is to be quantifiable. Hence it is necessary to have a system in which the flow patterns are well defined and quantifiable, such as the rotating disc or channel flow cell.

Migration can be neglected for solutions containing an excess of supporting electrolyte, so that the general mass transport equation (2.6) becomes

$$J_i = vc_i(x,t) - D_i\frac{\partial c_i(x,t)}{\partial x} \tag{2.23}$$

In terms of vectors this equation can be rewritten and generalised to three dimensions:

$$\underline{J}_i = c_i\underline{v} - D_i\underline{\nabla}c_i \tag{2.24}$$

The variation of c with time is given by

$$\frac{\partial c_i}{\partial t} = -\underline{\nabla}.\underline{J}_i = -\underline{div}\,\underline{J}_i \tag{2.25}$$

Combining equations (2.24) and (2.25) yields the general convective-diffusion equation

$$\frac{\partial c_i}{\partial t} = D_i\nabla^2 c_i - \underline{v}.\underline{\nabla}c_i \tag{2.26}$$

where it has been assumed that D is not a function of spacial position. In three-dimensional Cartesian coordinates, substituting for the Laplacian operator, ∇^2, and for the scalar product of the velocity and grad c, leads to:

$$\frac{\partial c_i}{\partial t} = D_i\left(\frac{\partial^2 c_i}{\partial x^2} + \frac{\partial^2 c_i}{\partial y^2} + \frac{\partial^2 c_i}{\partial z^2}\right) - \left(v_x\frac{\partial c_i}{\partial x} + v_y\frac{\partial c_i}{\partial y} + v_z\frac{\partial c_i}{\partial z}\right) \tag{2.27}$$

Expressions are thus required for the velocity profile, $\underline{v}(x,y,z)$, before the convective-diffusion equation can be solved for the concentration profile, $c(x,y,z)$.

The velocity profile for an incompressible fluid is obtained from the solution of two equations:

(i) the continuity equation:

$$\frac{\partial \rho}{\partial t} = -\underline{\nabla}.(\rho \underline{v}) = 0 \tag{2.28}$$

and

(ii) the Navier-Stokes equation [102]:

$$\rho \frac{\partial \underline{v}}{\partial t} = -\underline{\nabla} P + \eta \nabla^2 \underline{v} + f \tag{2.29}$$

which is Newton's second law applied to fluids. The left-hand side of equation (2.29) represents the rate of change of momentum of a volume element, P is the pressure, ρ is the density, η is the viscosity and f is the gravitational force acting on a unit volume of fluid. The Navier-Stokes equation is normally rewritten in terms of kinematic viscosity $\nu = \eta/\rho$

$$\frac{\partial \underline{v}}{\partial t} = -\frac{1}{\rho}\underline{\nabla} P + \nu \nabla^2 \underline{v} + \frac{f}{\rho} \tag{2.30}$$

The first term represents the change in velocity due to the pressure acting on the fluid, the second represents the frictional forces, and the final term represents the effect of natural convection due to density gradients. For most cases the forced convection is constant and $\partial \underline{v}/\partial t$ is zero.

If the Navier-Stokes equation can be solved, the mass transport of species in a hydrodynamic system can be calculated from the convective-diffusion equation (2.26).

2.5 The Diffusion Layer

A useful concept in hydrodynamic flow systems is that of the diffusion layer. The diffusion layer is the zone in which the concentration is reduced or enhanced due to the surface reaction. Its boundary marks the border between where the species has its bulk concentration and this altered region (see Figure 2.5). Therefore as there is depletion of reactants and generation of products at the surface, a concentration gradient is formed in this region. This gives rise to diffusion. Outside the diffusion layer convection is strong enough for all species to be held at their bulk concentrations. However, inside the diffusion layer diffusion is the dominant transport process, although convection can still be significant.

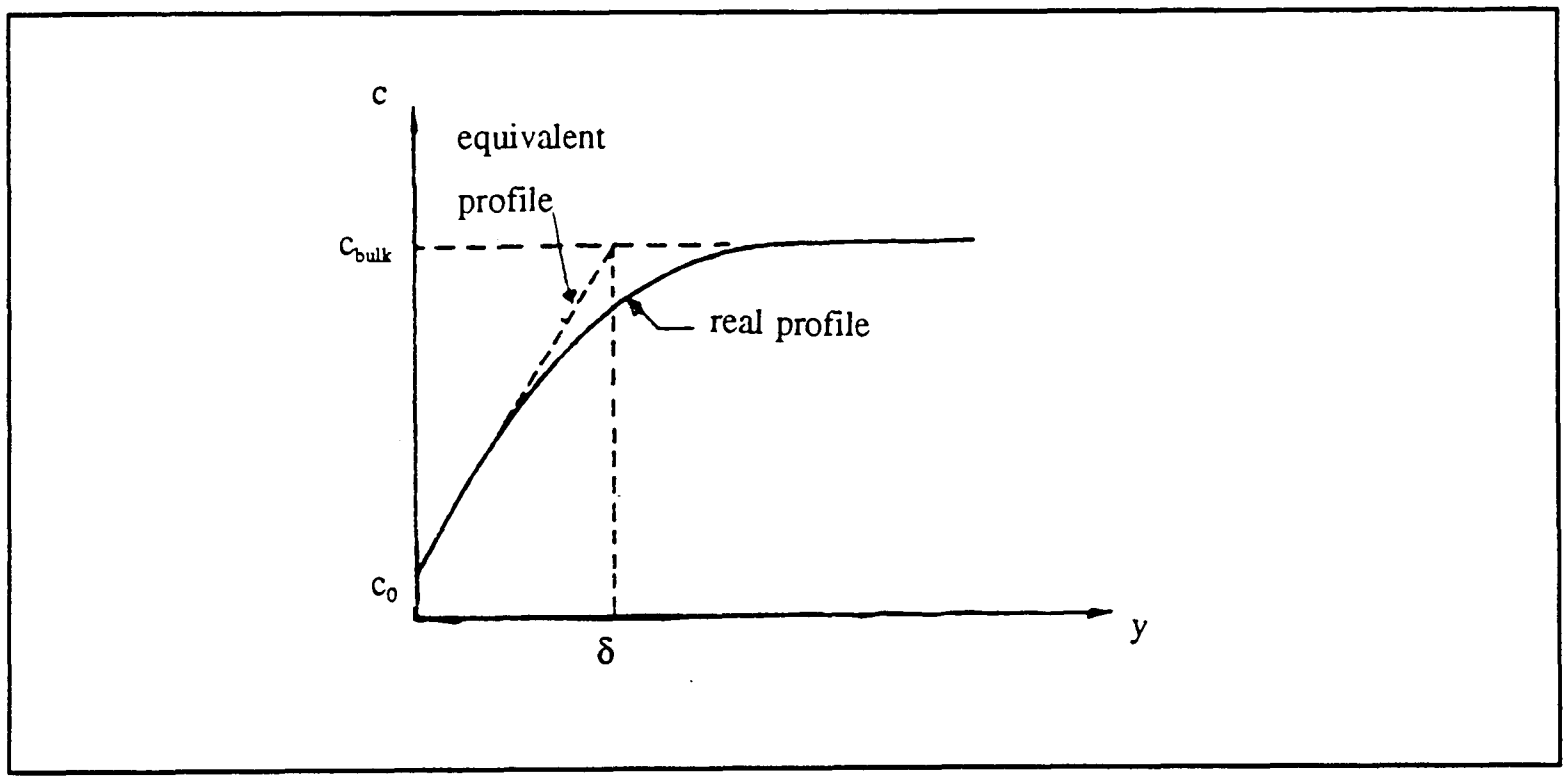

Figure 2.5 The variation of reactant concentration on distance from the reactive surface, which gives rise to the concept of a diffusion layer.

Assuming the concentration gradient is linear then the flux J, at the electrode is given by:

$$J = D\frac{\partial c}{\partial y} = D\frac{(c_{bulk} - c_o)}{\delta} \tag{2.31}$$

where δ is the thickness of the diffusion layer and c_o and c_{bulk} are the concentrations at the surface and in bulk solution respectively. The diffusion limited flux occurs when all the reactant reaching the interface reacts, so that $c_o = 0$, in which case:

$$J_{lim} = \frac{D c_{bulk}}{\delta} \tag{2.32}$$

The diffusion layer in part reflects the efficiency of convection in maintaining bulk concentration at its boundary. It follows that δ depends on the nature and extent of the convection processes. At low rates of convection the diffusion layer will be thicker, so the concentration gradient within the diffusion layer will be smaller and thus the diffusion of species will be slow. Conversely at fast convection rates the diffusion layer is thin giving rise to faster diffusion. In the case of the rotating disc convection rate is controlled by the rotation speed, and for the channel flow cell flow rate.

2.6 Hydrodynamics of the Channel Cell (CFC)

The channel flow cell will now be examined in detail. The channel flow cell has the reactive surface (such as a calcite crystal) embedded in one wall of a rectangular duct, through which solution flows. A detector electrode is located flush to the channel wall immediately downstream of the reactive interface. This is shown in Figure 2.6, along with the co-ordinate system used and some of the cell parameters.

The nature of the fluid flow is described by the Reynolds number [104]

$$Re = \frac{v_o h}{\nu} \tag{2.33}$$

where v_o is the solution velocity at the centre of the channel, h is the half-height of the channel and ν the kinematic viscosity of the solution. Below a critical value of

Re = 2000 [104-106] the flow is laminar; above this, flow is turbulent. Under the practical conditions used in the work described in this thesis, flow was always laminar and therefore this will be assumed henceforth.

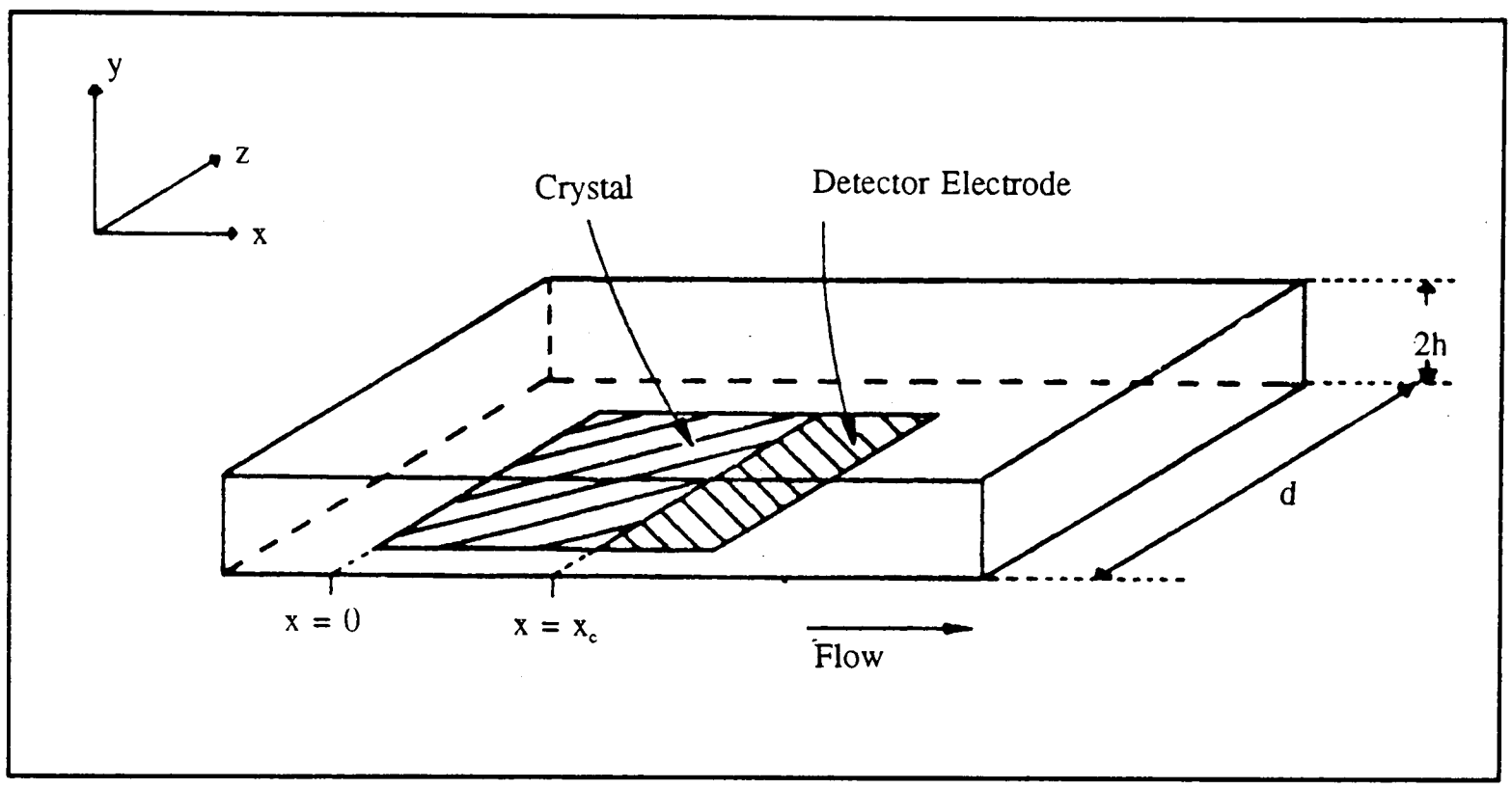

Figure 2.6. Schematic diagram of the channel flow cell.

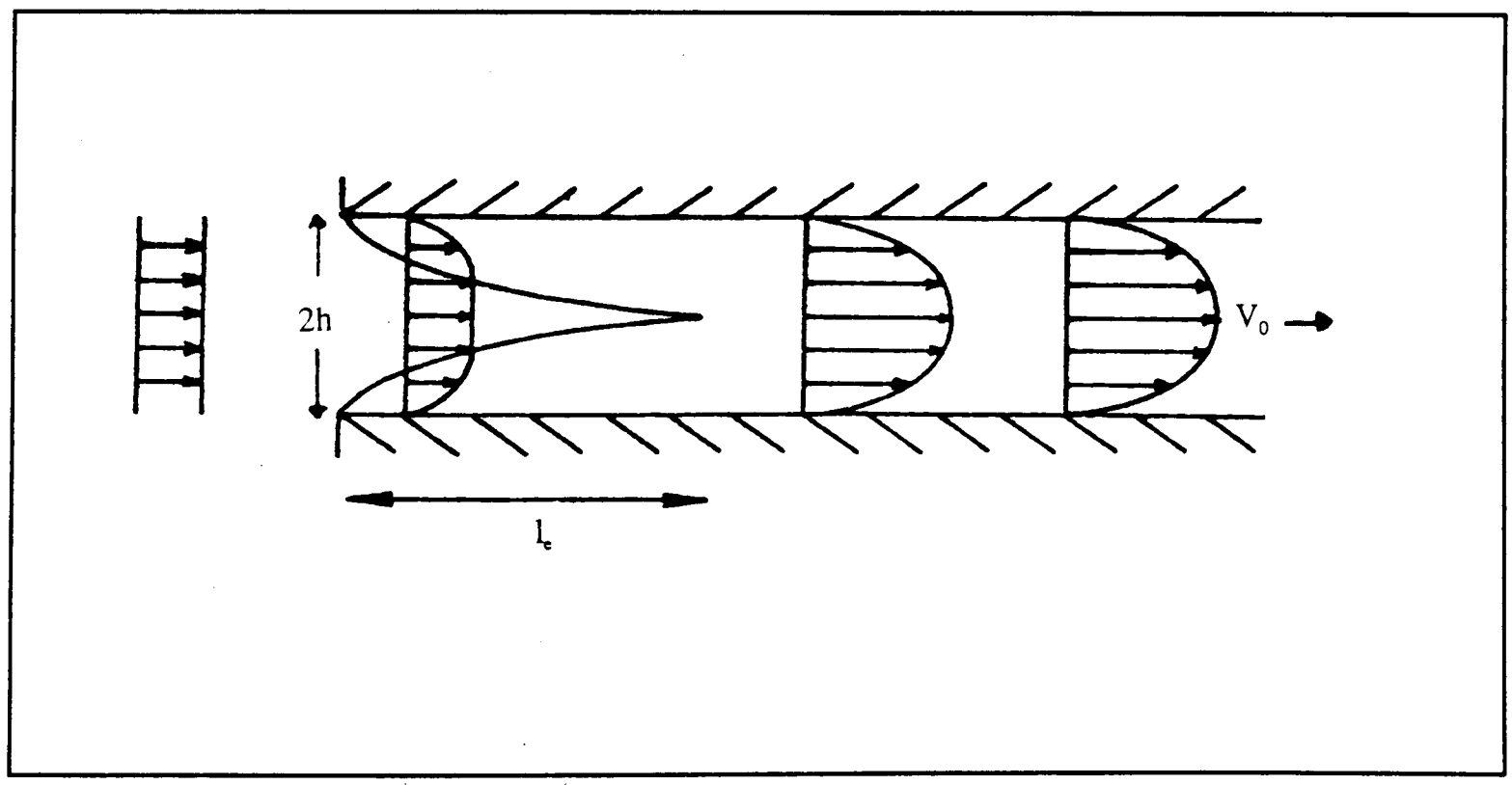

Figure 2.7 Hydrodynamic flow in the channel cell under laminar conditions. Parabolic Poiseuille flow is established after a lead-in length.

As solution flows through the channel, friction at the walls retards the flow at the edges of the channel. The boundary at which the flow rate is retarded as compared to the initial value moves towards the centre of the channel as the flow proceeds, due to viscous forces, as shown in Figure 2.7.

After an entry length, l_e, given approximately by [107]:

$$l_e = 0.1\,hRe \tag{2.34}$$

fully developed Poiseuille flow is established. In this regime the laminar flow is parabolic in shape and the velocities along the Cartesian axes are:

$$v_x = v_o\left(1 - \frac{(h-y)^2}{h^2}\right) \tag{2.35}$$

and

$$v_y = 0\,; \quad v_z = 0 \tag{2.36}$$

Mass transport of species in a hydrodynamic system, as discussed earlier (section 2.4), is described by the following general differential equation containing diffusion and convection terms.

$$\frac{\partial c_i}{\partial t} = D_i \nabla^2 c_i - \left(v_x \frac{\partial c_i}{\partial x} + v_y \frac{\partial c_i}{\partial y} + v_z \frac{\partial c_i}{\partial z}\right) \tag{2.37}$$

assuming no homogeneous chemical reactions. Assuming that axial diffusion is small compared to axial convection and neglecting lateral diffusion.[67,109-111],the convective-diffusion equation (2.37) can be rewritten given equation (2.36),

$$\frac{\partial c}{\partial t} = D\frac{\partial^2 c}{\partial y^2} - v_x \frac{\partial c}{\partial x} \tag{2.38}$$

The following boundary conditions can be derived from these assumptions, for the case

where the species undergoes amperometric detection at the electrode

$$
\begin{aligned}
x=0 \ (all\ y), \qquad & [C]=[C]^{\infty} \\
0 < x \le x_c \ (y=0), \qquad & D_C \partial[C]/\partial y = k_n [C]^n \\
0 < x \le x_{c+e} \ (y \to 2h), \qquad & \partial[C]/y = 0 \\
x_c < x \le x_{c+e} \ (y=0), \qquad & [C]=0
\end{aligned}
\tag{2.39}
$$

where [C] replaces c_i. At the very edge of the crystal (x = 0) the concentration of the species is equal to that introduced in the bulk solution, at all positions through the channel flow cell (all distances y out from the surface). Over the crystal (where the distance x along the flow cell is between that at the upstream edge of the crystal, x=0, and the downstream edge, x_c), at the crystal surface (y=0) the concentration of the species is governed by the relevant reaction equation. For all distances from the edge of the crystal (x=0) to the edge of the detector (x_{c+e}) at the far wall (y=2h) the flux of species equals zero. Then finally over the electrode (from the end of the crystal, x_c, to the end of the electrode, x_{c+e}) the concentration of the species is zero, as all of the species at the electrode undergoes the electrode reaction at the limiting current.

Note that in the case of calcite dissolution there are also additional homogeneous reactions, for simplicity here the case without homogeneous reactions will be discussed. Later chapters will modify the convection diffusion equation as required to account for homogeneous kinetics.

2.7 Analytical Solution of the Channel Cell Convective-Diffusion Equation

Full understanding of the hydrodynamics of the channel cell is desirable, as only then can the kinetics of the reactions at the reactive surface be modelled adequately. In order to fully characterise the hydrodynamics of a system it is necessary to solve equation (2.38). An approximate solution was developed by Levich [111] who applied the Lévêque approximation [112] which linearises the parabolic velocity profile.

$$v_x \approx 2v_0\left(1 - \frac{h-y}{h}\right) \tag{2.40}$$

This approximation is valid close to the channel walls[113], where $y=0$ or $y=2h$. The assumptions underlining this will be discussed later in this section. Under steady-state conditions, together with the Lévêque approximation, the convective-diffusion equation (2.38) becomes

$$D\frac{\partial^2 c}{\partial y^2} = \frac{2v_0 y}{h}\frac{\partial c}{\partial x} \tag{2.41}$$

The substitution

$$\eta = \left(\frac{v_0}{xh}\right)^{1/3} y \tag{2.42}$$

leads to the following second-order differential equation

$$\frac{d^2 c}{d\eta^2} + \frac{2\eta^2}{3d}\frac{dc}{d\eta} = 0 \tag{2.43}$$

Applying the boundary conditions for a simple transport-limited heterogeneous reaction:

$$0 \le x \le l\,, \quad y = 0\,; \qquad [c] = 0$$
$$x < 0 \quad \text{or} \quad y \to \infty\,; \qquad [c] = [c]_{bulk} \tag{2.44}$$

and the substitution

$$p = \frac{\partial c}{\partial \eta} \tag{2.45}$$

in equation (2.43), leads to

$$\frac{1}{p}\frac{\partial p}{\partial \eta} + \frac{2}{9d\eta^2} = 0 \tag{2.46}$$

thus

$$\frac{c}{c_{bulk}} = \frac{\int_0^{\eta} \exp(-2\eta^3/9D)\,d\eta}{\int_0^{\infty} \exp(-2\eta^3/9D)\,d\eta} \tag{2.47}$$

The diffusional flux to the channel electrode is given by

$$J = \int_0^1 D\frac{\partial c}{\partial y}\bigg|_{y=0} d(x/l) \tag{2.48}$$

This can be evaluated by expanding the indefinite integral in equation (2.47) as a power series in η and integrating term by term. This results in

$$J = \int_0^l \left\{ Dc_{bulk}\left(\frac{v_0}{Dhx}\right)\left[\int_0^{\infty} \exp\left(-\frac{2\eta^3}{9D}\right)d\eta\right]^{-1}\right\} d(x/l) \tag{2.49}$$

which can after rearrangement and substitution, yield the final expression for J [114]

$$J = \int_0^l 0.067\, c_{bulk} D^{2/3}\left(\frac{v_0}{hx}\right)^{1/3} d(x/l) \tag{2.50}$$

Comparison with equation (2.32), gives the diffusion layer thickness, δ, as [111,115]:

$$\delta = \frac{1}{0.67}\left(\frac{Dhl}{v_o}\right)^{1/3} \tag{2.51}$$

The total mass transport limited flux to the interface is:

$$J_{lim} = 0.925 c_{bulk}\left(\frac{D^2 V_f}{h^2 ld}\right)^{1/3} \tag{2.52}$$

where c_{bulk} is the bulk concentration of the electroactive species (mol cm^{-3}), l the length of the reactive surface (cm) and V_f the volume flow rate (cm^3 s^{-1}).

In the specific case where the reactive surface is an electrode, equation (2.52) can be rewritten using equation (2.2) to give the transport limited current for a simple n electron reduction or oxidation reaction. This is the Levich equation for the channel electrode [111]

$$I_{lim} = 0.925 nFw c_{bulk}\left(\frac{x_e^2 D^2 V_f}{h^2 d}\right)^{1/3} \tag{2.53}$$

where I_{lim} is the transport-limited current (Ampere), n is the number of electrons transferred in the reaction, F is Faraday's constant (C mol^{-1}), w the electrode width (cm), x_e the electrode length (cm) and d the channel width (cm).

The validity of the Levich equation with its associated assumptions will next be discussed. The Lévêque approximation, as stated above, only applies close to the electrode. When the diffusion layer thickness becomes comparable to the channel height this approximation breaks down. In this case (the "thin layer" limit) the limiting current is given by [116]:

$$I_{lim} = nFV_f c_{bulk} \tag{2.54}$$

According to the expression for the diffusion layer thickness, equation (2.51), the thin layer limit only occurs with very low flow rates or long electrodes. Specifically it is possible that the Levich equation may breakdown over the relatively long distances such as between the calcite crystal and electrode, which are encountered in the work presented in this thesis.

The second assumption is that axial diffusion is negligible compared to convection. Flanagan and Marcoux [109] solved equation (2.38) numerically using a simple explicit method and demonstrated that this assumption was valid essentially under the same conditions as the Lévêque approximation, for electrodes sizes and channel flow dimensions as used in the work reported in this thesis. This assumption breaks down for microelectrodes although the Lévêque approximation is usually valid, when diffusion parallel to the electrode surface is not negligible and gives rise to 'edge effects' [117], causing larger limiting currents than would otherwise be expected. Such phenomena only occur for short electrodes ($< 10\ \mu m$), 'microelectrodes', or very low flow rates and have been examined analytically by Oldham [117] and numerically by Amatore [119].

For the cell geometries, electrode sizes and flow rates used in this work these assumptions are justified. However for greater generality and in order to retain detail of the full parabolic velocity profile, it is necessary to use a numerical method, which allows a wide range of kinetic equations to be considered. For this reason and the possible break down of the 'thin layer' limit due to the gap between the crystal and electrode as discussed above, the section 2.9 will deal with a numerical solution which is capable of handling the kinetics needed in this study.

2.8 The Rotating Disc Electrode

The majority of experiments described in this thesis deal with the channel flow cell; however the rotating disc electrode is used in a number of preliminary investigations of the electrochemical behaviour of new chemicals before they are used in the channel flow cell. Therefore it is important to have a solution of the convection diffusion equation for the rotating disc electrode.

The mass transport equation for the RDE was solved by Levich [108], who re-wrote the convective-diffusion equation (2.37) in cylindrical polar co-ordinates (Figure 2.8) because of the geometry of the problem. Thus

$$\frac{\partial c}{\partial t} = D\left(\frac{\partial^2 c}{\partial z^2} + \frac{\partial^2 c}{\partial r^2} + \frac{1}{r}\frac{\partial c}{\partial r} + \frac{1}{r^2}\frac{\partial^2 c}{\partial \theta^2}\right) - \left(v_r\frac{\partial c}{\partial r} + \frac{v_\theta}{r}\frac{\partial c}{\partial \theta} + v_z\frac{\partial c}{\partial z}\right) \qquad (2.55)$$

This can be simplified considerably. Due to the symmetry of the system, c is independent of θ so

$$\frac{\partial c}{\partial \theta} = \frac{\partial^2 c}{\partial \theta^2} = 0 \qquad (2.56)$$

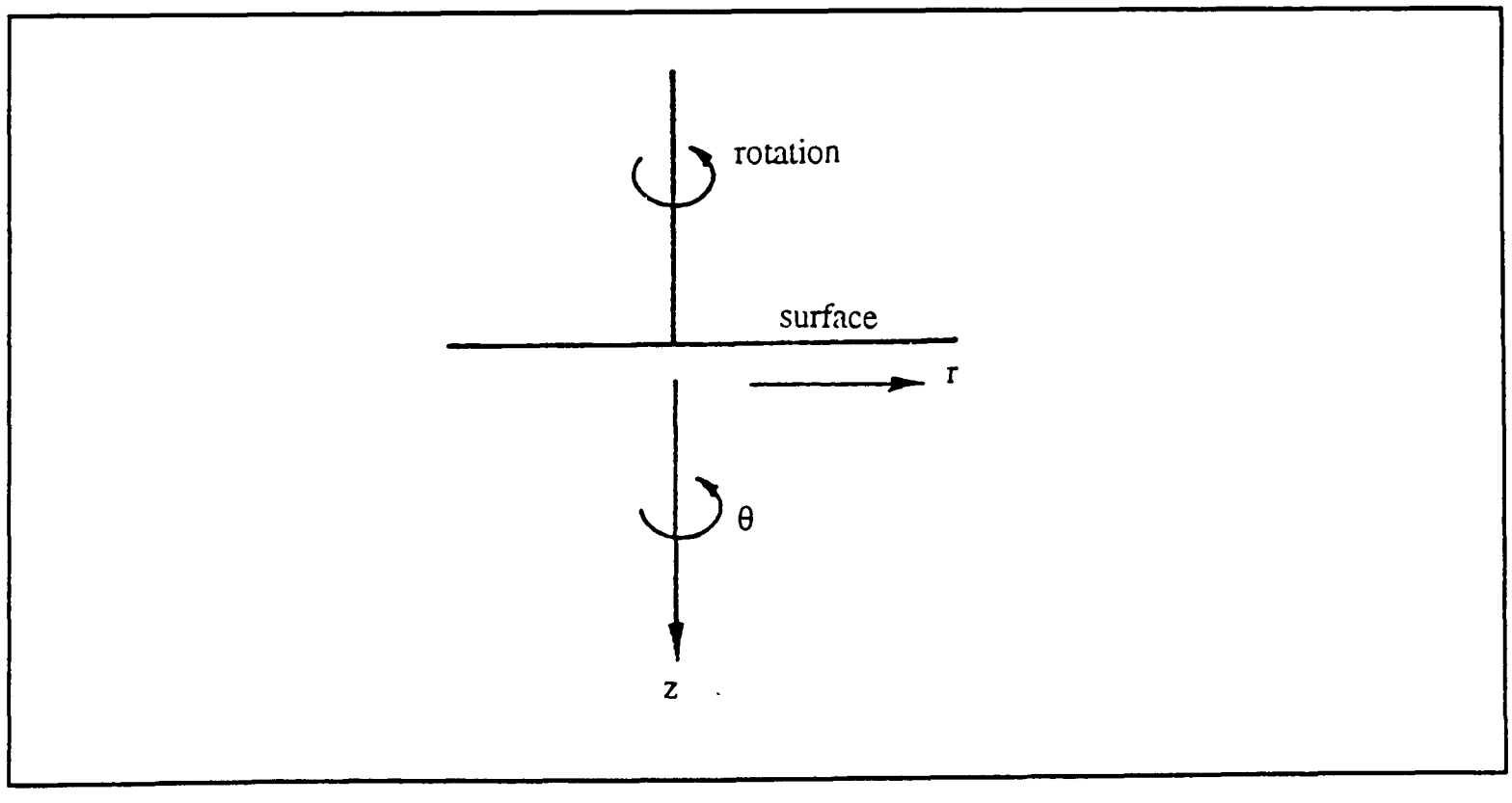

Figure 2.8 Cylindrical coordinates used for solving the convective-diffusion equation at the rotating disc electrode.

Provided the radius of the sheath is much greater than that of the electrode, v_z will be independent of r, and at $z = 0$ $(\partial c/\partial r) = 0$, hence across the electrode face

$$\frac{\partial c}{\partial r} = \frac{\partial^2 c}{\partial r^2} = 0 \tag{2.57}$$

Applying these simplifications at steady state, equation (2.55) becomes

$$v_z \frac{\partial c}{\partial z} = D \frac{\partial^2 c}{\partial z^2} \tag{2.58}$$

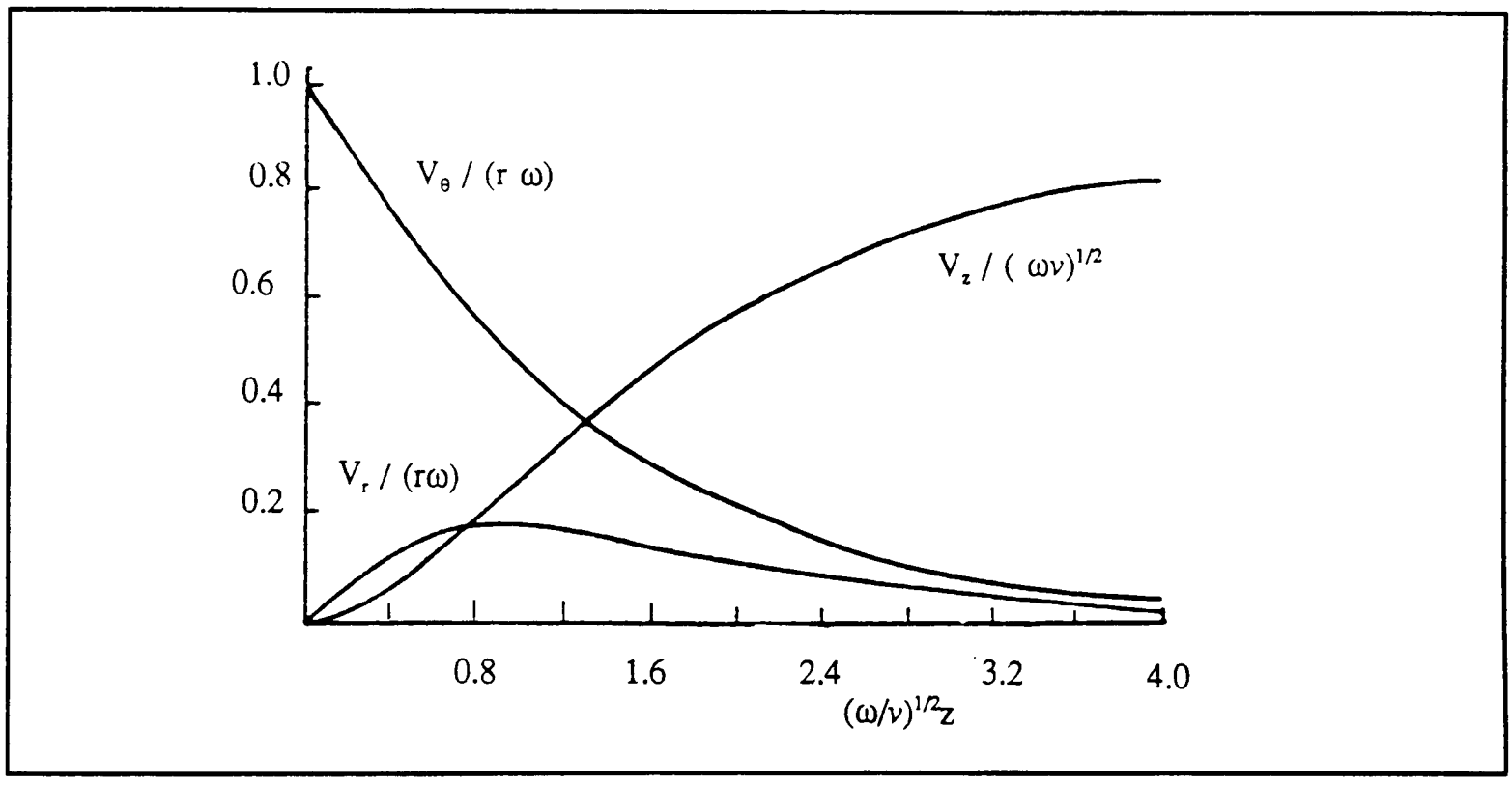

Figure 2.9 Velocity components as a function of distance along the three cylindrical coordinates for the rotating disc electrode. The functions as plotted are dimensionless.

The velocity profile for the RDE as a function of z is shown in Figure 2.9. Using an expression for v_z [105] and applying the appropriate boundary conditions, equation (2.58)

can be solved [99, 105] to give the Levich equation;

$$I_{lim}/A = 0.62048 n F A c_{bulk} D^{\frac{2}{3}} \nu^{-\frac{1}{6}} \omega^{\frac{1}{2}} \tag{2.59}$$

or

$$I_{lim}/A = 1.5553 n F A c_{bulk} D^{\frac{2}{3}} \nu^{-\frac{1}{6}} f^{\frac{1}{2}} \tag{2.60}$$

where A is the electrode area (cm^2), c_{bulk} the bulk concentration (mol cm^{-3}) of the electroactive species, ω is the angular velocity (rad s^{-1}) and f is the frequency of rotation (rev s^{-1} or Hz) of the RDE. This compares with the Levich equation for the channel (equation 2.53).

2.9 Numerical Solution of the Channel Cell Convective-Diffusion Equation

In Section (2.7) the mass transport equation for the channel cell was solved analytically using the Lévêque approximation, for the specific problem of the limiting current at an electrode. Alternatively numerical methods are particularly useful under conditions where the assumptions made in the analytical solution are no longer valid or complex kinetic processes make analytical solution difficult or impossible. In addition they make full use of the parabolic velocity profile which enables differentiation between small differences in flux caused by surface mechanisms. In the case of this work it is the complexity of the kinetic processes, with necessity to consider several different kinetic rate equations and possible rate controlling steps that necessitates the use of a numerical method.

There are several different numerical approaches which have been used to solve mass transport equations [122]. All the methods involve solution of a two dimensional problem with a finite difference grid. Anderson and Moldoveanu [116] explored three

such methods. These were the simple explicit (SE) method, the Crank-Nicolson implicit (CNI) method [123] and the backward implicit (BI) finite difference method. They found the BI finite difference method superior, with excellent agreement with theoretical [124] and semi-empirical [125] results. The BI method was first developed by Laasonen [126] and has been extensively used to study mechanistic electrochemistry at the channel electrode [i.e.113,116,128-130].

The advantages of the BI approach are:

(a) The surface concentration suddenly changes at the upstream edge of the electrode making it a point of discontinuity. This causes uncertainty over what concentration value to use at this point in the boundary conditions (whether bulk concentration or that correspond to the active surface). With the SE method in the case of limiting current simulation, the result depends on the value chosen for this point and on the size of the grid used. The CNI approach also requires knowledge of this although it seems to have no influence on the computed results. Only the BI calculation does not need knowledge of the concentrations at this discontinuity point [113].

(b) The BI method requires at least 100 times fewer grid points in the x-direction, as it uses simple vector calculations to obtain convergence, than for SE, so is computationally less expensive [113].

(c) The CNI method offers no computational advantage over the BI approach, and is more complex to implement [113].

Overall the merits of the BI method is that it deals with vector calculations rather than matrix calculations, which makes it much faster and cheaper in computational terms.

2.9.1 Backwards Implicit Finite Difference Solution of the Channel Cell Convective-Diffusion Equation

The application of the BI approach to a simple heterogeneous reaction has been considered [113] where a species A undergoes a mass transport limited reaction at a reactive surface in the channel. The reaction in question could be a one electron redox reaction at a channel electrode or equally a fast heterogeneous reaction between species A and an insulator surface. This example is illustrated below.

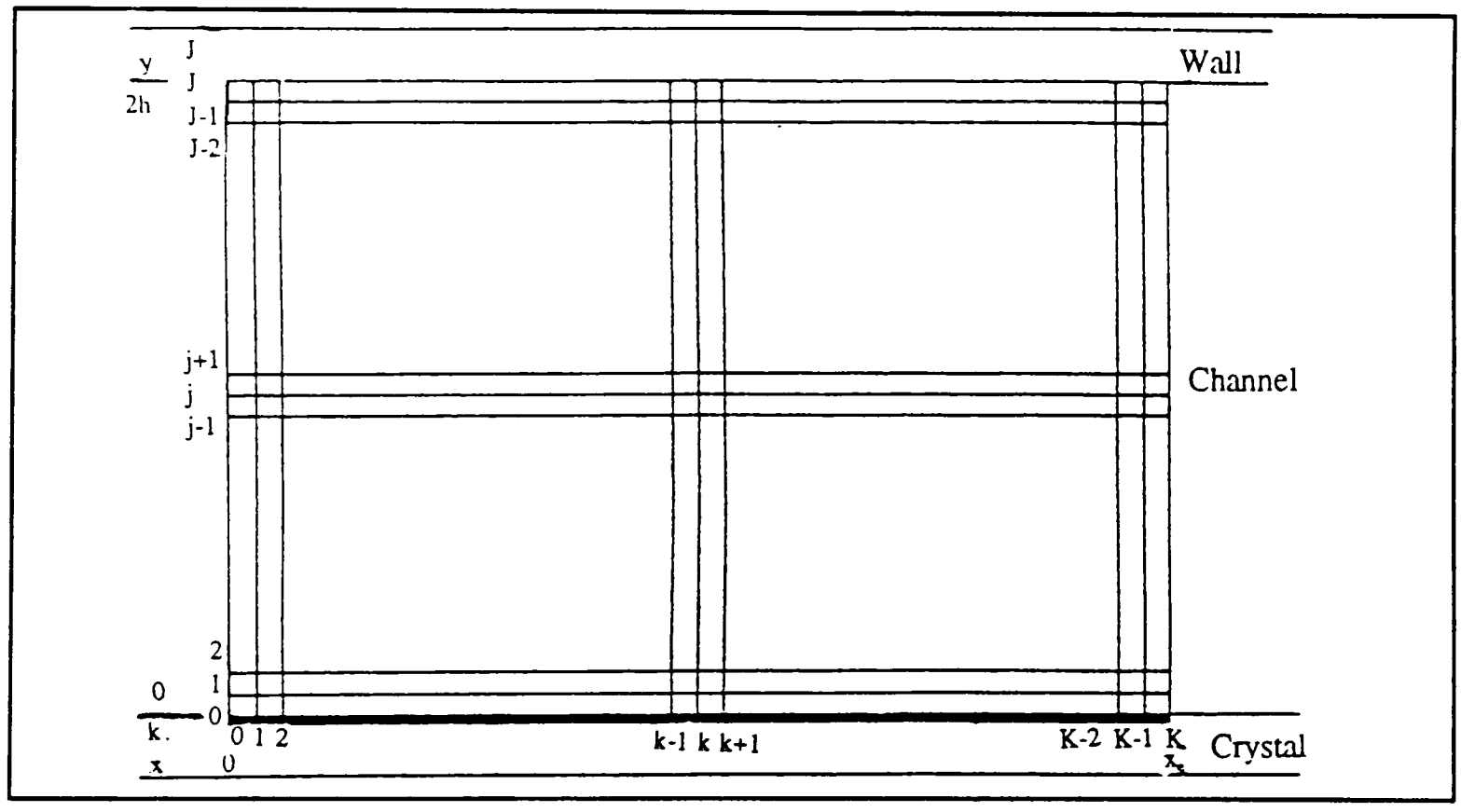

Figure 2.10. Finite difference grid.

The steady-state transport equation for species A is

$$D\frac{\partial^2[A]}{\partial y^2} = v_o\left(1 - \frac{(y-h)^2}{h^2}\right)\frac{\partial[A]}{\partial x} \qquad (2.61)$$

The xy-plane is covered with a two-dimensional finite-difference grid, (Figure 2.10) in order to apply the BI method. Increments in the x-direction are Δx and in the y-direction, Δy. The co-ordinates of a point (x_k,y_j) in the channel are given by

$$y_j = j\Delta y \quad j = 0, 1.... J \quad \text{where} \quad \Delta y = \frac{2h}{J} \tag{2.62}$$

$$x_k = k\Delta x \quad k = 0, 1... K \quad \text{where} \quad \Delta x = \frac{x_e}{K} \tag{2.63}$$

The derivatives in equation (2.61) are approximated to

$$\frac{\partial g^A}{\partial x} = \frac{g^A_{j,k+1} - g^A_{j,k}}{\Delta x} \tag{2.64}$$

where g^A is the normalised concentration of species A ($g^A = a/a_0$, a_0 is the bulk concentration of species A), and

$$\frac{\partial^2 g^A}{\partial y^2} = \frac{g^A_{j-1,k+1} - 2g^A_{j,k+1} + g^A_{j+1,k+1}}{(\Delta y)^2} \tag{2.65}$$

Combining equations (2.61), (2.64) and (2.65) results in

$$\left(\frac{D}{(\Delta y)^2}\right)\left\{g^A_{j-1,k+1} - 2g^A_{j,k+1} + g^A_{j+1,k+1}\right\} = \left\{g^A_{j,k+1} - g^A_{j,k}\right\}\left(\frac{D}{\lambda_j(\Delta y)^2}\right) \tag{2.66}$$

where

$$\lambda_j = \frac{D\Delta x(2h)^3 d}{6V_f j(\Delta y)^3(2h - j\Delta y)} \tag{2.67}$$

In this equation, V_f is the volume flow rate, where:

$$V_f = \frac{4}{3}v_o hd \tag{2.68}$$

The appropriate boundary conditions for the calculation of the transport-limited regime are:

$$x = 0 \; ; \quad [A]_o = [A]_{bulk} \; ; \quad g^{A}_{j,0} = [A]_{bulk} \tag{2.69}$$

$$y = 0 \; ; \quad [A]_o = 0 \; ; \quad g^{A}_{0,k} = 0 \tag{2.70}$$

$$y = 2h \; ; \quad \frac{\partial [A]}{\partial y} = 0 \; ; \quad g^{A}_{J,k} = g^{A}_{J-1,k} \tag{2.71}$$

Thus equation (2.66) simplifies to

$$g^{A}_{1,k} = (2\lambda_1 + 1) g^{A}_{1,k+1} - \lambda_1 g^{A}_{2,k+1} \tag{2.72}$$

$$g^{A}_{j,k} = -\lambda_j g^{A}_{j-1,k+1} + (2\lambda_j + 1) g^{A}_{j,k+1} - \lambda_j g^{A}_{j+1,k+1} \qquad j = 2,3..J\text{-}2 \tag{2.73}$$

$$g^{A}_{J-1,k} = -\lambda_{J-1} g^{A}_{J-2,k+1} + (\lambda_{J-1} + 1) g^{A}_{J-1,k+1} \tag{2.74}$$

These (J-1) simultaneous equations may be expressed as a (J-1) x (J-1) matrix equation

$$\{d\} = [T]\{u\} \tag{2.75}$$

i.e.

$$\begin{bmatrix} d_1 \\ d_2 \\ \vdots \\ \vdots \\ \vdots \\ d_j \\ \vdots \\ \vdots \\ \vdots \\ d_{J-2} \\ d_{J-1} \end{bmatrix} = \begin{bmatrix} b_1 & c_1 & 0 & & & & & & \\ a_2 & b_2 & c_2 & 0 & & & & & \\ & \ddots & \ddots & \ddots & & & & & \\ & & \ddots & \ddots & \ddots & & & & \\ & & 0 & a_j & b_j & c_j & 0 & & \\ & & & & \ddots & \ddots & \ddots & & \\ & & & & & \ddots & \ddots & \ddots & \\ & & & & & & a_{J-2} & b_{J-2} & c_{J-2} \\ & & & & & & 0 & a_{J-1} & b_{J-1} \end{bmatrix} \begin{bmatrix} u_1 \\ u_2 \\ \vdots \\ \vdots \\ \vdots \\ u_j \\ \vdots \\ \vdots \\ \vdots \\ u_{J-2} \\ u_{J-1} \end{bmatrix} \tag{2.76}$$

where:

$$d_j = g^{A}_{j,k} \qquad j = 1,2..J\text{-}1 \qquad (2.77)$$

$$u_j = g^{A}_{j,k+1} \qquad j = 1,2..J\text{-}1 \qquad (2.78)$$

$$a_j = -\lambda_j \qquad j = 2,3..J\text{-}1 \qquad (2.79)$$

$$b_j = 2\lambda_j + 1 \qquad j = 1,2..J\text{-}2 \qquad (2.80)$$

$$b_{J-1} = \lambda_{J-1} + 1 \qquad (2.81)$$

$$c_j = -\lambda_j \qquad j = 1,2..J\text{-}2 \qquad (2.82)$$

The matrix [T] is of tridiagonal form which allows the use of the Thomas algorithm [131] (see Appendix 2), to calculate $\{u\}_k$ from $\{d\}_k$. The boundary condition $g^{A}_{j,0} = [A]_{bulk}$ supplies the vector $\{d\}_0$ from which $\{u\}_0$ is calculated. In the absence of homogeneous chemical complications, $\{d\}_{k+1} = \{u\}_k$, so $\{u\}_1$ is calculated from $\{d\}_1$ ($= \{u\}_0$) and so on until $\{u\}_K$ is obtained. Thus all the values $g^{A}_{j,k}$ ($j = 1,2...J\text{-}1$, $k = 1,2...K$) are evaluated. Using the theory outlined, concentration profiles can be calculated for the species of interest using FORTRAN 77 programs.

In the case where the reactive surface is an electrode the redox current at the electrode can be calculated using Fick's first law.

$$I = FwD\sum_{k=1}^{K}\left(\frac{g^{A}_{1,k} - g^{A}_{0,k}}{\Delta y}\right)\Delta x \qquad (2.83)$$

Under mass transport limiting conditions this reduces to the numerical equivalent to the Levich equation (2.53).

$$I_{lim} = \frac{FDw\Delta x}{\Delta y}\sum_{k=1}^{K} g^{A}_{1,k} \qquad (2.84)$$

For cases where the reactive surface is not an electrode equations (2.83) and (2.84) are not applicable. In these cases the solution to the matrix equation (2.76) has

already given the concentration profile of species A and the flux can be calculated from equations similar to equation (2.83), for the region of the channel over the reactive interface.

Then the BI calculations need to be continued 'downstream' over the detector electrode with modified boundary conditions as follows. If the detector itself acts potentiometrically, so does not affect the species concentration in the solution, then this area can be treated like the far wall leading to a no flux condition (2.71). If the detector is an amperometric detector, for instance a platinum electrode measuring H^+ reduction, then it itself can be considered as a reactive surface with the boundary conditions ((2.69),(2.70),and (2.71)), and equations ((2.83) and (2.84)) are applicable. The no flux condition for electroinactive species and potentiomentric determination (equation (2.71)) is replaced by the following:

$$y = 0 \; ; \quad \frac{\partial [A]}{\partial y} = 0 \; ; \quad g^{A}_{0,k} = g^{A}_{1,k} \tag{2.85}$$

thus equation (2.72) is replaced by:

$$g^{A}_{1,k} = (\lambda_1 + 1) g^{A}_{1,k+1} - \lambda_1 g^{A}_{2,k+1} \tag{2.86}$$

Solving the appropriately modified matrix equation produces the concentrations at the surface of the detector electrode. From which the detector response can be calculated. The detector response calculated will vary with flow rate and the way in which this happens depends on the precise kinetics occurring at the surface. It is this variation of detector signal with flow rate which is used in the experiments described in the work presented in this thesis, to differentiate between different possible surface reaction schemes.

Later chapters discuss the specific application of the channel cell method and BI when the reactive surface of interest is a calcite crystal. Both the cases where the detector electrode is either a pH electrode, and an amperometric detector, are dealt with at low and high pH respectively.

CHAPTER 3

EXPERIMENTAL DETAILS

3.1 Introduction

This chapter deals with experimental aspects of the work described in this thesis. In particular it deals with the channel flow cell strategies for both high pH calcite dissolution and low pH dissolution.

3.2 Flow Cell

The channel flow cell was made up of two parts - the channel and coverplate, as shown in Figure 3.1. The channel has a rectangular groove cut into a block of Perspex.

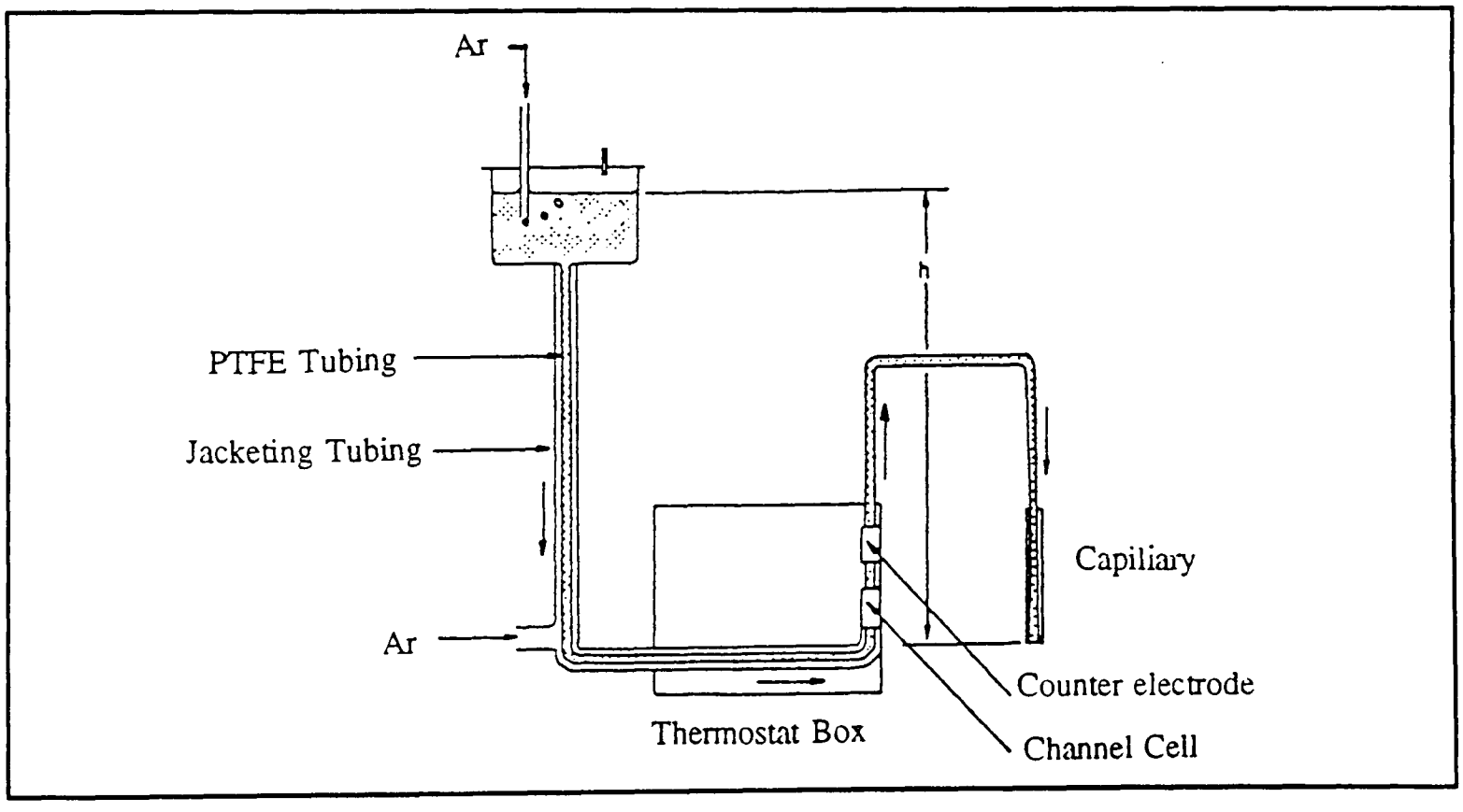

Figure 3.1 The channel flow cell configuration. (see figures 3.2 and 3.3 for specific flow cells for high and low pH).

The inlet and outlet pipes fed into a deeper duct at either end of the groove so as to even out the flow of the solution into the channel. The fourth side of the channel is formed by a coverplate which includes an embedded calcite crystal (the fabrication of

which is explained in section 3.3). An O-ring between the Perspex block and the coverplate formed an airtight seal when pressure was applied to the coverplate by means of a pressure plate and six bolts. The coverplate was positioned in such a way that the crystal was a distance greater than the necessary lead-in length away from the beginning of the channel to ensure Poiseuille flow had been obtained. For the typical channel dimensions used this was less than a few millimetres at all flow rates used (equation (2.34)).

Downstream of the crystal is the detector electrode. At high pH this is a flat membrane pH, and at low pH a platinum electrode linked to a potentiostat is used. Care is taken to ensure that the detector electrode is flush with the surface. For a platinum electrode this is achieved by smoothing the electrode after being glued to the surface. In the case of a flat membrane pH electrode, the electrode is manipulated until flush with the surface, and then secured in this position with wax (Wax-a-Way; Vychem Ltd, Poole, Dorset).

The solution under investigation was held in a 500 cm^3 reservoir. Argon gas (British Oxygen Company Limited, Guildford, Surrey) was bubbled through the solution to remove dissolved CO_2. From the reservoir the solution flowed through a 1.5 mm bore PTFE tube (Altex; Anachem, Luton), then after flowing through the flow cell itself, through a capillary to waste. The whole system up to and including the channel flow cell, was jacketed in argon to prevent the ingress of CO_2, through the channel cell, At least 1 m of the PTFE tubing upstream of the channel was situated in the thermostatted box to ensure that the solution was at constant temperature. The thermostatted box consisted of a perspex box which contained a heater under thermostatic control and a fan to ensure even heating. The capillaries were also held inside the box to maintain

constant flow. The rate of flow of solution through the channel was varied by changing the bore of the capillary and by altering the height of the reservoir relative to the outlet tube. This resulted in flow rates ranging from 1×10^{-3} to 3.5×10^{-1} cm^3s^{-1}.

3.2.1 The Potentiostat

The potentiostat was used in all amperometric detection, and in initial rotating disc investigations of inhibitors. The potentiostat is a device which actively maintains the potential difference between the working (WE) and reference (RE) electrodes at a given value by altering the voltage between the working and counter (CE) electrodes as necessary. In other words it forces whatever current is necessary through the CE so that the required potential is achieved. The potentiostat used was an Oxford Electrodes Potentiostat (Oxford). A description of the circuit design of the potentiostat is given in Appendix 3.

3.3 Surface Preparation

The coverplate is made by pouring freshly mixed Araldite (Resin CY219, Hardener HY219, Accelerator DY219; Ciba-Geigy, Duxford, Cambs.) into a mould in which a cleaved calcite crystal (Roger Tayler Minerals, Cobham, Surrey) has been previously placed. The cover plate is then left to set. Once set it is removed from the mould and initially polished with sandpaper to remove the Araldite covering the face of the crystal, and then mechanically polished using diamond lapping compounds (Hyprez Sprays; Engis, Maidstone, Kent) with the lapping compounds gradually being replaced by finer grits down to 1μm spray (further details of the surface preparation will be outlined in the next section).

Then the coverplate is thoroughly rinsed with ultra high purity water, which is followed by a rinse with millimolar hydrochloric acid for a minute to remove any organic species. For the surface at high pH the crystal was then etched by flowing 0.5 M KCl (pH > 7) over the surface in the channel for at least 100 minutes to achieve an equilibrated surface morphology. At low pH this is not necessary as the H^+ in solution etches the surface very rapidly, so quickly establishing an equilibrated surface.

3.4 Calibration

3.4.1 Capillary

A variety of capillaries were used so as to gain the full range of flow rates as outlined in section 3.2. Each one used was calibrated by measuring the amount of water flowing through to waste in a given time. For every one the mass of water collected over a known time was measured for several 'solution heights' (i.e. the height of the reservoir above the outlet). Using the density of water ($\rho = 0.99707\ g\ cm^{-3}$ at 25°C, $\rho = 0.99823\ g\ cm^{-3}$ at 20°C [132]) a mean capillary constant of flow rate per unit height of solution ($cm^3\ s^{-1}\ cm^{-1}$) was determined for each capillary. During an experiment the flow rate was simply calculated from the product of this capillary constant and the solution height.

3.4.2 Channel Dimensions

The channel width d, crystal length x_c, crystal to detector electrode (pH sensor or platinum electrode) separation and electrode dimension (for pH sensor the diameter and for platinum electrode the length) were all measured using a travelling microscope (Unicam Instruments, Cambridge) capable of measuring to 10^{-3} cm.

Overall some dimensions vary more than others, with channel width and height being the most constant. However as various different crystals and detectors were used over the whole range of the experiments the detector and crystal dimensions are far more variable.

Typical dimensions of the cell parameters were as follows,

Channel height, $2h$	0.104 ± 0.006 cm
Channel width, d	0.600 ± 0.003 cm
Crystal length, x_c	1.033 to 0.783 cm

for high pH,

Crystal - sensor separation	0.049 to 0.200 cm

(This is as measured from the edge of the crystal to the edge of the 'active' part of the pH sensor, i.e. inside the outer glass wall.)

'active' pH electrode diameter	0.134 to 0.314 cm

for low pH,

detector/monitor electrode width	0.140 to 0.300 cm

(This is the length of 'active', i.e. non masked, electrode across the channel flow cell.)

detector/monitor electrode length	0.150 to 0.250 cm

(This is the length of the electrode in the direction of the flow.)

The final cell dimension required to interpret results was the channel half-height *h*. This was determined by measuring the transport limiting current for a simple one electron reduction or oxidation of a species with a known diffusion coefficient over a range of solution flow rates. To observe this the flow cell was used in an amperometric mode (as figure 3.2 but with a monitor electrode unused). The electroactive species used was the ferricyanide anion which undergoes a one electron reduction to the ferrocyanide anion and has a diffusion coefficient of 7.6×10^{-6} cm^2 s^{-1} [133].

$$Fe(CN)_6^{3-} + e^- \rightleftharpoons Fe(CN)_6^{4-} \qquad (3.1)$$

This determination of cell height was performed each time the cell was assembled. When high pH determinations were being performed a Perspex coverplate was used (for low pH the normal coverplate could be used) on which was attached a 2 mm (approx.) strip of 25 μm thick silver foil (Goodfellow, Cambridge) with Evo-stik (Evode Ltd, Stafford). A coating of AgCl was formed on this by making the foil the anode in 0.1 M aqueous HCl and passing 0.4 mA cm^{-2} for 30 minutes [134]. This Ag/AgCl electrode acted as the reference electrode. Downstream of the reference electrode a 1 mm (approx.) strip of rolled 12.5 μm thick platinum foil (Goodfellow, Cambridge) was attached in a similar manner to act as the working electrode. The edges of the platinum foil were masked off using thin PTFE tape in such a way that approximately 1 mm of the coverplate between the channel edge wall and the working electrode was covered. This was to minimise any edge effects. The counter electrode was a piece of platinum gauze (whose area was much larger than that of the working electrode) which was coiled and inserted into a glass tube. This was plumbed into the flow system immediately downstream of the channel flow cell. The three electrodes were connected to an Oxford

Electrode Potentiostat, which controlled the potential applied to the working electrode relative to the reference electrode (see Appendix 3).

The solution used for channel height determinations was 1mM $K_3Fe(CN)_6$ adjusted to pH 13 with KOH and with 0.5 M KCl as background electrolyte. By using the potentiatstat to ramp the potential from +0.5 V to 0 V, with respect to Ag/AgCl, when the half-wave potential is +0.205 V on platinum [43], this was done slowly enough to ensure that all the Fe^{3+} was reduced at the electrode. From the voltamogram the limiting current (I_{lim}) was measured, as I_{Lim} is the difference between the baseline current obtained before the reduction and that current measured when all the Fe^{3+} was reduced. A Levich plot of I_{lim} versus $V_f^{1/3}$ (flow rate see 2.53) was then drawn. The gradient of this yielded the channel half-height h.

4.4.3 pH Electrodes

The bulk pH of solutions was measured using a glass combination pH electrode (GelPlas pH electrode, BDH, Poole.) connected to a Jenway 3030 pH meter. This was calibrated using BDH Colourkey buffer solutions of pH 4.00 ($\pm$0.02) and pH 7.00 or pH 7.00 and pH 10.00 depending on whether the determinations were to be performed at low pH or high pH respectively.

4.5 Low pH Dissolution

At low pH the H^+ is detected amperometrically, by the reduction of H^+ at the platinum electrode:

$$H^+ + e^- \rightarrow \frac{1}{2} H_2 \qquad (3.2)$$

with the half-wave potential being at -0.4 V against calomel [43].

The experimental arrangement for calcite dissolution at low pH was as shown in figure 3.2. This is very similar to the arrangement used to determine channel height with ferricyanide as described above; there is a platinum detector electrode downstream of the calcite crystal, a silver foil detector electrode, and a counter electrode further downstream. In this case a monitor electrode is used, to measure current upstream of the calcite crystal, this should give the behaviour expected for the full bulk concentration of H^+ unreacted with calcite. If the monitor electrode did not give the expected behaviour then the experiments were declared invalid and repeated with a new cell assembly. Thus the monitor electrode provided an check on the validity of the measurements.

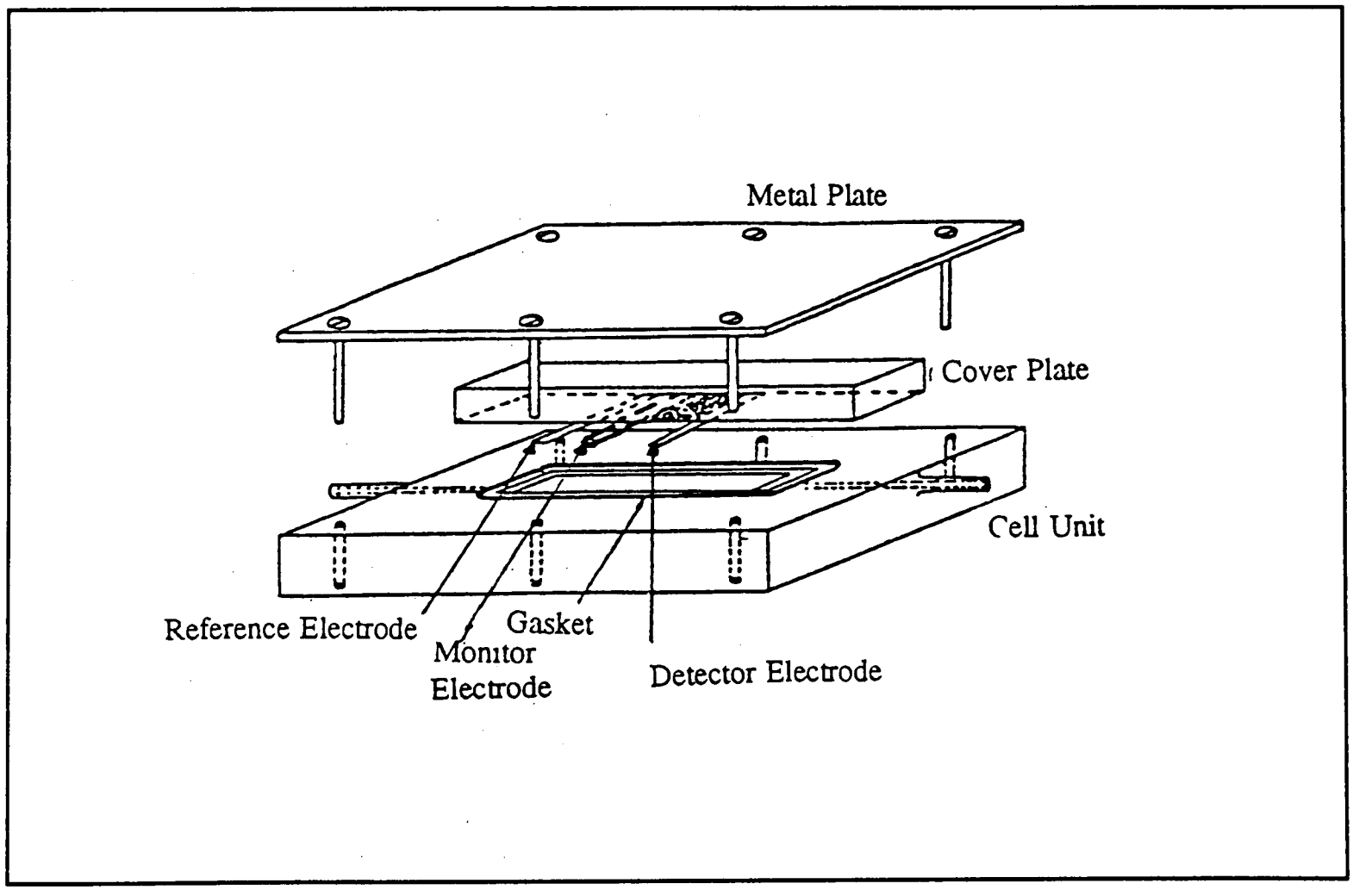

Figure 3.2 The experimental arrangement of the channel flow cell at low pH.

It has been noted before [136-137] that reduction of H^+ at the platinum electrode becomes progressively less reversible unless the electrode is periodically 'activated' by taking the electrode to positive potential (+1300 mV against Ag/AgCl) for a few seconds.[67, 139-143] At least some of this effect is due to the 'pseudo-CO_2' reduction on platinum, which occurs at approximately the same potential as the H^+ reduction. This pseudo reduction occurs via a catalysed electrochemical reaction between CO_2 and H_2 adsorbed on the electrode [136-138]. The CO_2 at the surface comes from dissolved CO_2 in solution, which exists in equilibrium with carbonic acid ie.

$$CO_2 + H_2O \rightleftharpoons H_2CO_3 \tag{3.3}$$

Therefore in order to minimise these effects, CO_2 was rigorously excluded as well as degassed, by lagging the channel itself by a jacket of argon so stopping atmospheric CO_2 leaking into the solution whilst in the flowing towards the flow cell. The normal degassing expels dissolved CO_2, and also pushes the equilibrium from towards CO_2 and H_2O, so gets rid of all this source of CO_2. Also the electrode was periodically 'electrochemically cleaned' of adsorbed H^+ by the method stated above. In this way reproducible curves were obtained. The validity of the H^+ reduction waves could be checked by comparison with the reduction of potassium ferricyanide in the same cell. If the H^+ waves measured are uncontaminated then the Levich equation will be valid. Hence plotting:

$$I_{lim} \quad \text{vs} \quad w c_{bulk} \left(\frac{x_e V_f D^2}{h^2 d} \right)^{1/3} \tag{3.4}$$

as obtained from the Levich equation (2.53) where c is the concentration of the species (H^+ or $Fe(CN)_6^{4-}$), w is the electrode width, x_e is the electrode length,, V_f is the flow

$Fe(CN)_6^{4-}$ and H^+, should superimpose for the two species, so providing another check on the accuracy of the experimental measurements.

3.6 High pH

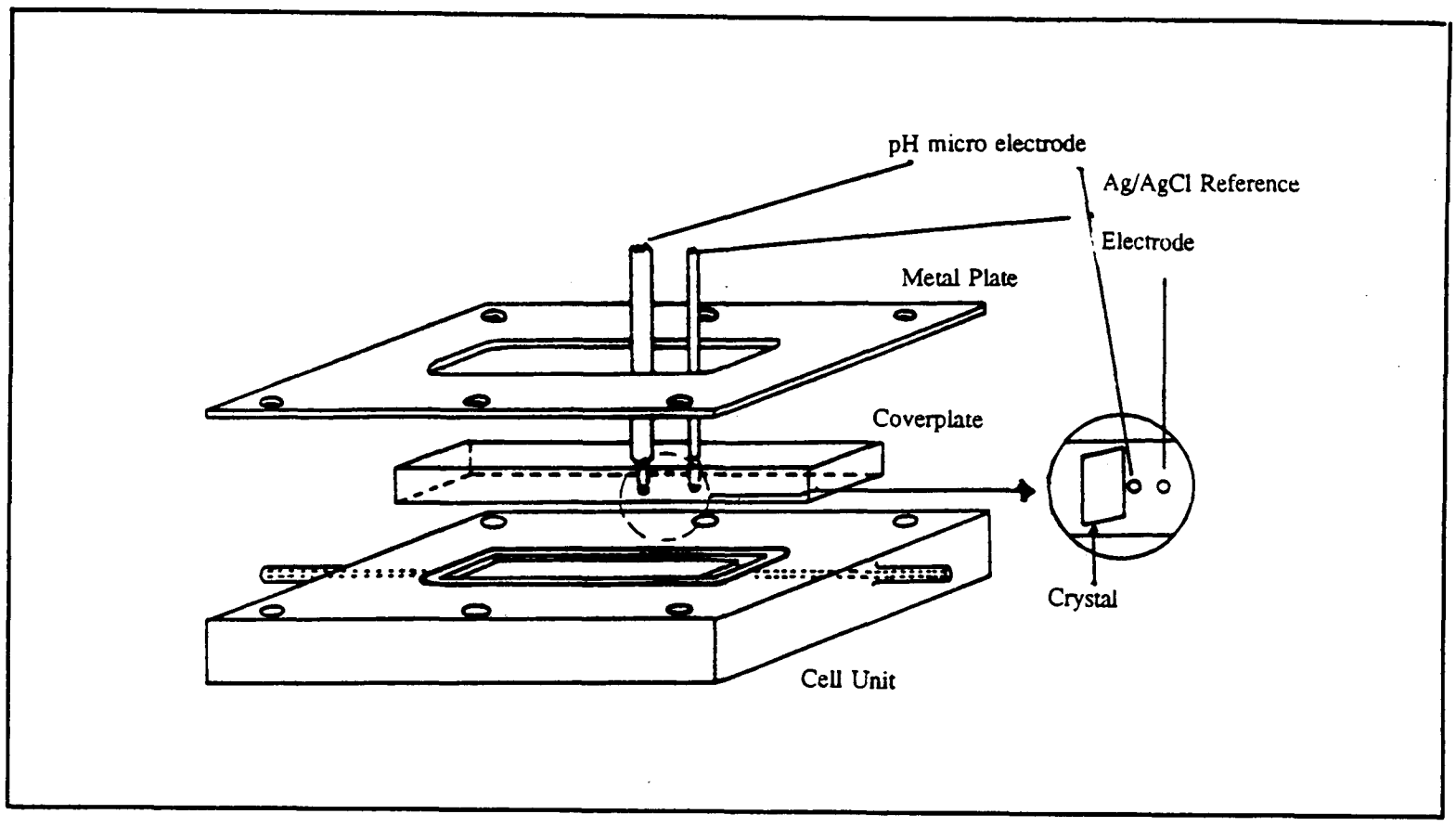

Figure 3.3 The experimental arrangement of the channel flow cell at high pH.

The configuration of the channel flow cell for high pH dissolution of calcite is as show in figure 3.3. The detector for high pH dissolution is a flat membrane glass pH electrode (GS-Glass series, Reagecon Electrodes,Shannon, Eire). This sensor was inserted into a hole 2.5 to 3.0 mm in diameter, which is drilled in the coverplate immediately downstream of the crystal. The hole is positioned in the centre of the channel (width-wise), in order to minimise any 'edge effects' (see Chapter 2). Care was taken to ensure that the glass electrode lay absolutely flush with the coverplate surface. The Ag/AgCl reference electrode (Microelectrodes Inc, Londonderry, New Hampshire, USA MI-401) as necessary for pH detection was inserted into another hole in the coverplate further downstream. Electrodes were held in place by PTFE tape, and low

temperature melting and inert wax (Wax-a-Way; Vychem Ltd, Poole, Dorset) which ensured an airtight seal of the cell. The flow cell was mounted in a thermostatted air bath held at 25 $\pm$ 0.5°C (see section 3.2).

The channel cell is constructed as described above. The solutions under investigation are degassed with Argon. The micro pH and reference electrodes were connected to a Jenway pH meter as described above, and the mV scale on the pH meter was used to monitor the pH variation. This scale is used both to calibrate the electrodes at both the beginning and end of each set of experiments, and to measure the pH variation with flow rate. Calibration with buffers as described in section (3.43) were performed at the beginning and end of each set of experiments using standard buffers as described previously for the combination electrode, noting the mV reading for each buffer.

3.7 Computing

Computer programs for the Backwards Implicit calculations were written in FORTRAN 77 and executed on the Oxford University VAX/VMS (DEC 6000/620). Examples of the programs used are in Appendix 4.

3.8 Chemicals

The source and purity of the chemicals used are summarised in Table 3.1. The calcite single crystals were semi-optical grade Iceland Spar crystals which originated from Chihuahua, Mexico. Chemical analysis of this was carried out by Ciba-Geigy and the results are shown in Table 3.2. Water was purified using an Elgastat UHQ II (Elga Ltd.,

Table 3.1. Source and Purity of Chemicals used.

Chemical	Purity	Supplier
Iceland spar (single crystals)	Semi-Optical Grade (see Table 3.2)	Roger Tayler minerals, Cobham, Surrey
Calcium Chloride	AnalaR	BDH Ltd., Poole, Dorset
Colourkey Buffer Solutions: pH 4.00, pH 7.00 & pH 10.00	Laboratory Reagent	BDH Ltd., Poole, Dorset
Hydrochloric Acid	AnalaR	BDH Ltd., Poole, Dorset
Potassium Chloride	AnalaR, Aristar	BDH Ltd., Poole, Dorset
Potassium Ferricyanide	AnalaR	BDH Ltd., Poole, Dorset
Potassium Hydroxide	AnalaR	East Anglia Chemicals, Ipswich
Phthalic Acid	puriss	Fluka, Switzerland
Homophthalic acid	Laboratory Reagent	Aldrich, Gillingham, Dorset
Polyacrylic acid (PAA) (MW 2000)	Laboratory Reagent (details in Chapter 4)	Aldrich, Gillingham, Dorset
Narlex (PAA MW 14000)	Industrial sample (see Chapter 4)	FMC, Trafford Park, Manchester
Antiprex (PAA MW 5000)	Industrial sample (see Chapter 4)	FMC, Trafford Park, Manchester
Magnesium Chloride	AnalaR	BDH Ltd., Poole, Dorset
Barium Chloride	AnalaR	BDH Ltd., Poole, Dorset

Where the molecular weight of polymers is quoted it is the weight average molecular weight (MW).

Table 3.2. Chemical analysis of Iceland Spar

Element	Concentration /ppm
Cd	< 5
Cu	< 5
Fe	< 10
Mn	< 5
Na	< 10
P	< 50
Sb	< 20
Zn	< 5

CHAPTER 4

THE EFFECT OF INHIBITORS ON CALCITE DISSOLUTION AT LOW pH (<4)

4.1 Introduction

This chapter describes the effect of polyacrylic acid and two molecular inhibitors on the dissolution of calcite at low pH. These latter are phthalic - $C_6H_4(COOH)_2$ and homo-phthalic acids - $C_6H_4(COOH)CH_2COOH$, and their structures are shown in figure 4.8. The potency of these inhibitors is then compared, and contrasted, with that of other known small molecular inhibitors (maleic, fumaric, and tartaric acids) and that of polymaleic acid.

Initially the general experimental strategy for studying the dissolution of calcite at low pH is described. A basic theoretical description of dissolution at low pH is then presented. Next discussion continues to the specific case of dissolution in the presence of phthalic or homo-phthalic acids. The inhibition caused by these monomers is then demonstrated to proceed via Langmuirian adsorption of the dianions of the acids. The strength of the inhibition is compared with previously studied species [144 and 145]. This is followed by a rationalisation of the relative inhibitory strengths.

Next the inhibition of calcite dissolution by polyacrylic acid inhibition is examined. It is seen that simple Langmuirian adsorption cannot be used to explain the results in this case. The nature of the inhibition is probed by adding background calcium ions, Ca^{2+}. It is shown that, although added Ca^{2+} has no effect on low pH dissolution of calcite by itself, in combination with polyacrylic acid in solution, there is an effect which increases the inhibitory power of the polymer at low concentrations. It is proposed that this occurs due to a calcium - polyacrylic acid complex forming, and that this complex

adsorbs on the calcite surface blocking the dissolution. This theory is verified by means of channel flow cell experiments, and a stoichiometry for the complex is deduced. Experiments using polyacrylic acid polymers of different molecular weights are subsequently reported. These had the aim of identifying any chain length effect on inhibition. Two other divalent cations, Ba^{2+} and Mg^{2+} were investigated as alternatives to Ca^{2+}.

Finally conclusions are drawn about the relative power of different polyacrylic acid polymers as inhibitors. Comparison is then made between polyacrylic acid and other inhibitors, in order to attempt to achieve some quantitative basis as to which inhibitors are most effective on a 'per gram' basis.

4.2 General Experimental Approach for Low pH Dissolution

In order to investigate calcite dissolution at low pH, the channel flow cell is used as outlined in Chapter 3. Solution is flowed through a rectangular duct under laminar flow conditions via a gravity feed, and over the surface of a calcite crystal (Iceland Spar) which is flush with the wall of the channel. Immediately downstream of the crystal is an electrochemical detector. In this case the latter is an electrode formed from a platinum foil. Upstream of the calcite crystal is a reference electrode. Adjacent to the crystal, but upstream of it is a monitor electrode which can be used to monitor the H^+ concentration reaching the crystal surface. Downstream of the detector electrode is a counter electrode. These electrodes (detector or monitor) are connected via a potentiostat (Appendix 3) with a potential applied across the working and reference electrodes. In this configuration the H^+ concentration can be determined by measuring the limiting

current for the reduction of H^+ as described in Chapter 3. The typical values for the dimensions of the cell for low pH dissolution are outlined in Chapter 3.

As the flow for the channel flow cell is well defined this permits modelling of the convection/diffusion process within the cell (Chapter 2). The backwards implicit finite difference method can be used to compute the solution profiles of H^+, Ca^{2+} and other solution species, and the deviation from these profiles at the dissolving surface. This allows investigation of the surface processes governing the dissolution of H^+ at low pH.

4.3 Theory

In this section the general kinetics of calcite dissolution in acidic conditions will be introduced. This is followed by an account of the computational modelling of low pH dissolution in the absence of inhibition. Then there is a brief overview of the existing conclusions from experiments with the channel flow cell for low pH dissolution are presented.

4.3.1 Kinetics

The overall reaction defining the dissolution of calcite in aqueous solution is described by the following equations.

$$H^+ + CaCO_3 \xrightarrow{k_1} Ca^{2+} + HCO_3^- \tag{4.1}$$

$$CaCO_3 + H_2CO_3 \xrightarrow{k_2} Ca^{2+} + 2HCO_3^- \tag{4.2}$$

$$CaCO_3 + H_2O \xrightarrow{k_3} Ca^{2+} + HCO_3^- + OH^- \tag{4.3}$$

At low pH the reaction with H^+ totally dominates the reaction with water. Also in the work presented here CO_2 is rigorously excluded so that equation (4.2) can be ignored. In the solution the following homogeneous reactions also occur:

$$H^+ + HCO_3^- \overset{K_{H_2CO_3}}{\rightleftharpoons} H_2CO_3 \tag{4.4}$$

$$H_2CO_3 \overset{k_{H_2CO_3}}{\rightarrow} H_2O + CO_2 \tag{4.5}$$

These equations it can be rearranged to show that under homogeneous conditions:

$$\frac{d[HCO_3^-]}{dt} = \frac{d[H^+]}{dt} = -\frac{k_{H_2CO_3}[H^+][HCO_3]}{K_{H_2CO_3} + [H^+] + [HCO_3^-]} \tag{4.6}$$

From these kinetic equations it is possible to model the dissolution of calcite in the presence of mineral acid. In order to do this it is necessary to utilize the Backwards Implicit finite difference method as introduced in chapter 2 if the relevant matrix elements are derived for this case. Once the numerical modelling has been done it is possible to differentiate between different explanations of the surface processes governing the dissolution of calcite at low pH. For example in this work attention will be paid to whether the dissolution is kinetically or transport controlled. In the former case all H^+ which reaches the electrode reacts immediately, hence it can be modelled in terms of a sufficiently large k_1 in equation (4.1), so that the concentration of H^+ ions at the calcite surface is effectively zero.

4.3.2 Derivation of the Matrix Elements

In deriving the matrix elements it is assumed that the surface kinetics are dominated by equation (4.1) [27,52,53,56-57]. So to describe the dissolution of calcite at low pH the following equation can be derived [53]:

$$Rate = D_{H^+}\frac{\partial[H^+]}{\partial y} = k_1[H^+]_{surface} = -D_{HCO_3^-}\frac{\partial[HCO_3^-]}{\partial y} \tag{4.7}$$

where k_1 is the heterogeneous rate constant for the dissolution of calcite with H^+.

The steady state convective-diffusion equation describing the distribution of the species R in the channel flow cell in the absence of any homogeneous kinetics is

$$\frac{\partial[R]}{\partial t} = 0 = D_R\frac{\partial^2[R]}{\partial y^2} - v_x\frac{\partial[R]}{\partial x} \tag{4.8}$$

where D_R is the diffusion coefficient of species R, x and y are the coordinates in the channel flow cell (as defined in Chapter 2 2.6), and v_x is the solution in the x-direction. This last term is given by

$$v_x = v_o(1-(h-y)^2/h^2) \tag{4.9}$$

where v_o is the solution velocity in the centre of the channel and h is the channel half-height.

If we take into account the homogeneous kinetics as described in section (4.2.1) above the convective diffusion equation for H^+ becomes:

$$0 = D_{H^+}\frac{\partial^2[H^+]}{\partial y^2} - v_x\frac{\partial[H^+]}{\partial x} - \frac{k_{H_2CO_3}[H+][HCO_3^-]}{K_{H_2CO_3}+[H+]+[HCO_3^-]} \tag{4.10}$$

and for HCO_3^-:

$$0 = D_{HCO_3^-}\frac{\partial^2[HCO_3^-]}{\partial y^2} - v_x\frac{\partial[HCO_3^-]}{\partial x} - \frac{k_{H_2CO_3}[H+][HCO_3^-]}{K_{H_2CO_3}+[H+]+[HCO_3^-]} \tag{4.11}$$

In order to derive the matrix elements from these equations the boundary conditions first have to be defined.

4.3.2.1*Boundary Conditions*

The boundary conditions are as follows:

(i) *Upstream of the Crystal*

The concentration of all species are equal to that present in the bulk solution entering the flow cell:

$$x = 0, \quad 0 < y < 2h, \quad [H^+] = [H^+]_{bulk} \;\; \& \;\; [HCO_3^-] = [HCO_3^-]_{bulk} = 0 \tag{4.12}$$

(ii) *Zone of the Crystal*

At the surface of the crystal the flux is given by the rate law for dissolution of calcite.

$$0 < x \le x_c, \quad y = 0, \quad D_{H^+}\frac{\partial[H^+]}{\partial y} = k_1[H^+]_{y=0} \tag{4.13}$$

$$\& \quad D_{HCO_3^-}\frac{\partial[HCO_3^-]}{\partial y} = -k_1[H^+]_{y=0}$$

where x_c is x coordinate at the end of the crystal.

(iii) *At the Far Wall*

Additionally at the channel wall opposite the crystal, there is no flux so:

$$0 < x \le x_{c+e}, \quad y = 2h, \quad \frac{\partial[H^+]}{\partial y} = 0 \;\; \& \;\; \frac{\partial[HCO_3^-]}{\partial y} = 0 \tag{4.14}$$

where x_{c+e} is the x coordinate at the end of the detector electrode.

(iv) *Downstream of the Crystal*

The detector is assumed to start immediately downstream of the crystal, and at the surface of the electrode the concentration of H^+ is zero if the electrode is held at a potential corresponding to the transport limited reduction of H^+ on platinum

$$x_c < x \leq x_{c+e}, \quad y=0, \quad [H^+] = 0 \tag{4.15}$$

On the far wall there is again a no flux situation so the boundary condition is as defined in section (ii) above. Additionally for HCO_3^- at the electrode surface a no flux condition applies so:

$$x_c < x \leq x_{c+e}, \quad y = 0, \quad \frac{\partial[HCO_3^-]}{\partial y} = 0 \tag{4.16}$$

4.3.2.2*Matrix Elements for the low pH Dissolution of Calcite in the Absence of Inhibitor.*

From the above equations the matrix elements for the dissolution of calcite at low pH can be derived.

Let g^H be the normalized concentration of H^+,

$$g^H = \frac{[H^+]}{[H^+]_{bulk}} \tag{4.17}$$

where $[H^+]_{bulk}$ is the initial bulk concentration of H^+. Similarly for HCO_3^-:

$$g^B = \frac{[HCO_3^-]}{[H^+]_{bulk}} \tag{4.18}$$

where $B=[HCO_3^-]$.

(i) *The Matrix Elements in Solution*

Now applying the equation (4.10) above to equation (2.73), the following general equation describing the H^+ concentration in the centre of the channel can be formed:

$$g^{H}_{j,k} = -\lambda^{H}_{j} g^{H}_{j-1,k+1} + (2\lambda^{H}_{j} + 1) g^{H}_{j,k+1} - \lambda^{H}_{j} g^{H}_{j+1,k+1} - \frac{\lambda^{H}_{j} k_{H_2CO_3} (\Delta y)^2 g^{H}_{j,k} g^{B}_{j,k}}{\frac{K_{H_2CO_3}}{[H^+]_{bulk}} + g^{H}_{j,k} + g^{B}_{j,k}} \qquad j = 2,3..J\text{-}2 \quad (4.19)$$

where the subscripts j,k refer to the position in the finite difference grid as shown previously in figure 2.10. This can be written as an equation of the form:

$$d^{H}_{j} = a^{H}_{j} g^{H}_{j-1,k+1} + b^{H}_{j} g^{H}_{j,k+1} + c^{H}_{j} g^{H}_{j+1,k+1} \quad (4.20)$$

where

$$d^{H}_{j} = g^{H}_{j,k} - \frac{\lambda^{H}_{j} k_{H_2CO_3} (\Delta y)^2 g^{H}_{j,k} g^{B}_{j,k}}{\frac{K_{H_2CO_3}}{[H^+]} + g^{H}_{j,k} + g^{B}_{j,k}} \qquad j=2,3,\ldots J\text{-}2 \quad (4.21)$$

$$a^{H}_{j} = -\lambda a^{H}_{j} \qquad j=2,3,\ldots J\text{-}2 \quad (4.22)$$

$$b^{H}_{j} = 2\lambda^{H}_{j} + 1 \qquad j=2,3,\ldots J\text{-}2 \quad (4.23)$$

$$c^{H}_{j} = -\lambda^{H}_{j} \qquad j=2,3,\ldots J\text{-}2 \quad (4.24)$$

Similarly matrix elements can be derived for HCO_3^-:

$$d_j^B = g_{j,k}^B - \frac{\lambda_j^B k_{H_2CO_3} (\Delta y)^2 g_{j,k}^H g_{j,k}^B}{\frac{K_{H_2CO_3}}{[H^+]} + g_{j,k}^H + g_{j,k}^B} \qquad j=2,3,\ldots J\text{-}2 \quad (4.25)$$

$$a_j^B = -\lambda a_j^B \qquad j=2,3,\ldots J\text{-}2 \quad (4.26)$$

$$b_j^H = 2\lambda_j^H + 1 \qquad j=2,3,\ldots J\text{-}2 \quad (4.27)$$

$$c_j^B = -\lambda_j^B \qquad j=2,3,\ldots J\text{-}2 \quad (4.28)$$

where B represents HCO_3^-.

(ii) *Matrix Elements at the Crystal Surface*

For the surface of the crystal the flux of H^+ and HCO_3^- species, as shown in the boundary conditions above, are governed by the interfacial kinetics. The surface boundary condition for H^+ can be written as in terms of g^H as:

$$D_{H^+} \frac{\partial [H^+]}{\partial y} = D_{H^+} \frac{(g_{1,k+1}^H - g_{0,k+1}^H)}{\Delta y} = k_1 g_{0,k}^H \qquad (4.29)$$

Which can be rearranged to give:

$$g_{0,k+1}^H = g_{1,k+1}^H \left(1 + \frac{\Delta y k_1 g_{o,k}^H}{D_{H^+}} \right)^{-1} \qquad (4.30)$$

At the crystal surface equation (4.19) becomes:

$$g^{H}_{1,k} = -\lambda^{H}_{1} g_{1,k+1}\left(1 + \frac{\Delta y k_1 g^{H}_{0,k+1}}{D_H}\right) + \left(2\lambda^{H}_{1} + 1\right) g^{H}_{1,k+1} - \lambda^{H}_{1} g^{H}_{2,k+1} - \frac{(\Delta y)^2 \lambda^{H}_{1} k_{H_2CO_3} g^{H}_{1,k} g^{B}_{1,k}}{D_{H^+}\left(\frac{K_{H_2CO_3}}{[H^+]_{bulk}} + g^{H}_{1,k} + g^{B}_{1,k}\right)} \quad (4.31)$$

Again this can be written in the form of equation (4.20) where c_1 and d_1 are as for the centre of the channel but:

$$a^{H}_{1} = 0 \qquad j=1 \quad (4.32)$$

$$b^{H}_{1} = \lambda^{H}_{1} + 1 + \frac{\lambda^{H}_{1} \Delta y k_1 g^{H}_{0,k+1}}{D_H}$$

HCO_3^- again has similar matrix elements, which are derived here, but in this case the flux equation is:

$$D_{HCO_3^-} \frac{\partial [HCO_3^-]}{\partial y} = D_{HCO_3^-} \frac{(g^{B}_{1,k+1} - g^{B}_{0,k+1})}{\Delta y} = -k_1 g^{H}_{0,k} \quad (4.33)$$

which can be rearranged to give:

$$g^{B}_{0,k+1} = g^{B}_{1,k+1}\left(1 - \frac{\Delta y k_1 g^{H}_{o,k}}{D_{HCO_3^-}}\right)^{-1} \quad (4.34)$$

At the crystal surface equation (4.19) becomes:

$$g^{B}_{1,k} = -\lambda^{B}_{1} g^{B}_{1,k+1}\left(1 - \frac{\Delta y k_1 g^{H}_{0,k+1}}{D_B}\right) + \left(2\lambda^{B}_{1} + 1\right) g^{B}_{1,k+1} - \lambda^{B}_{1} g^{B}_{2,k+1} - \frac{(\Delta y)^2 \lambda^{B}_{1} k_{H_2CO_3} g^{H}_{1,k} g^{B}_{1,k}}{D_{HCO_3^-}\left(\frac{K_{H_2CO_3}}{[H^+]_{bulk}} + g^{H}_{1,k} + g^{B}_{1,k}\right)} \tag{4.35}$$

Again c_1 and d_1 have the same form as for the centre of the channel but:

$$a^{B}_{1} = 0 \qquad j=1 \tag{4.36}$$

$$b^{B}_{1} = \lambda^{B}_{1} + 1 - \frac{\lambda^{B}_{1} \Delta y\, k_1 g^{H}_{0,k}}{D_{HCO_3^-}}$$

(iii) *Matrix Elements for the Far Wall of the Channel.*

At the far wall to the reactive surface (electrode or calcite crystal) the flux of any species is zero. This modifies some of the matrix elements. The expressions for the terms a_J and d_J are not altered from the terms for the centre of the channel given above, but the terms b_J and c_J are modified to:

$$b^{R}_{J} = \lambda^{R}_{J} + 1 \tag{4.37}$$

$$c^{R}_{J} = 0$$

where R represents either H or B.

(iv) *Matrix Elements over the Detector Electrode Surface.*

For the species HCO_3^- a no flux condition exists at the electrode since HCO_3^- is electroinactive. The matrix elements are identical to those at the crystal surface except for b_1^B :

$$b_1^B = \lambda_1^B + 1 \tag{4.38}$$

However H^+ is consumed at the electrode. This means that in this case whilst the expressions for a_1^H, c_1^H and d_1^H are the same as at the crystal surface, b_1^H:

$$b_1 = 2\lambda_1^H + 1 \tag{4.39}$$

4.3.3 Conclusions on the Dissolution of Calcite at Low pH.

Utilizing the BI method it is possible to predict the detector response under different flow and pH conditions for a value of k_1. It is possible to investigate if experimental behaviour is transport or kinetically controlled, as if k_1 is large the interfacial processes will appear to be transport controlled. Therefore it is necessary to compare the behaviour expected with a large value of k_1 with that observed experimentally. If this does not fit well there must be partial or full control of the kinetics by the interfacial reaction of H^+ and $CaCO_3$. The two possible rate determining steps can be distinguished by measuring and modelling experimental data for the flow cell over a wide range of flow rates, [53]. In addition if the behaviour is not transport controlled then the line predicted by the BI method which best fits the experimental data will give a numerical value for k_1.

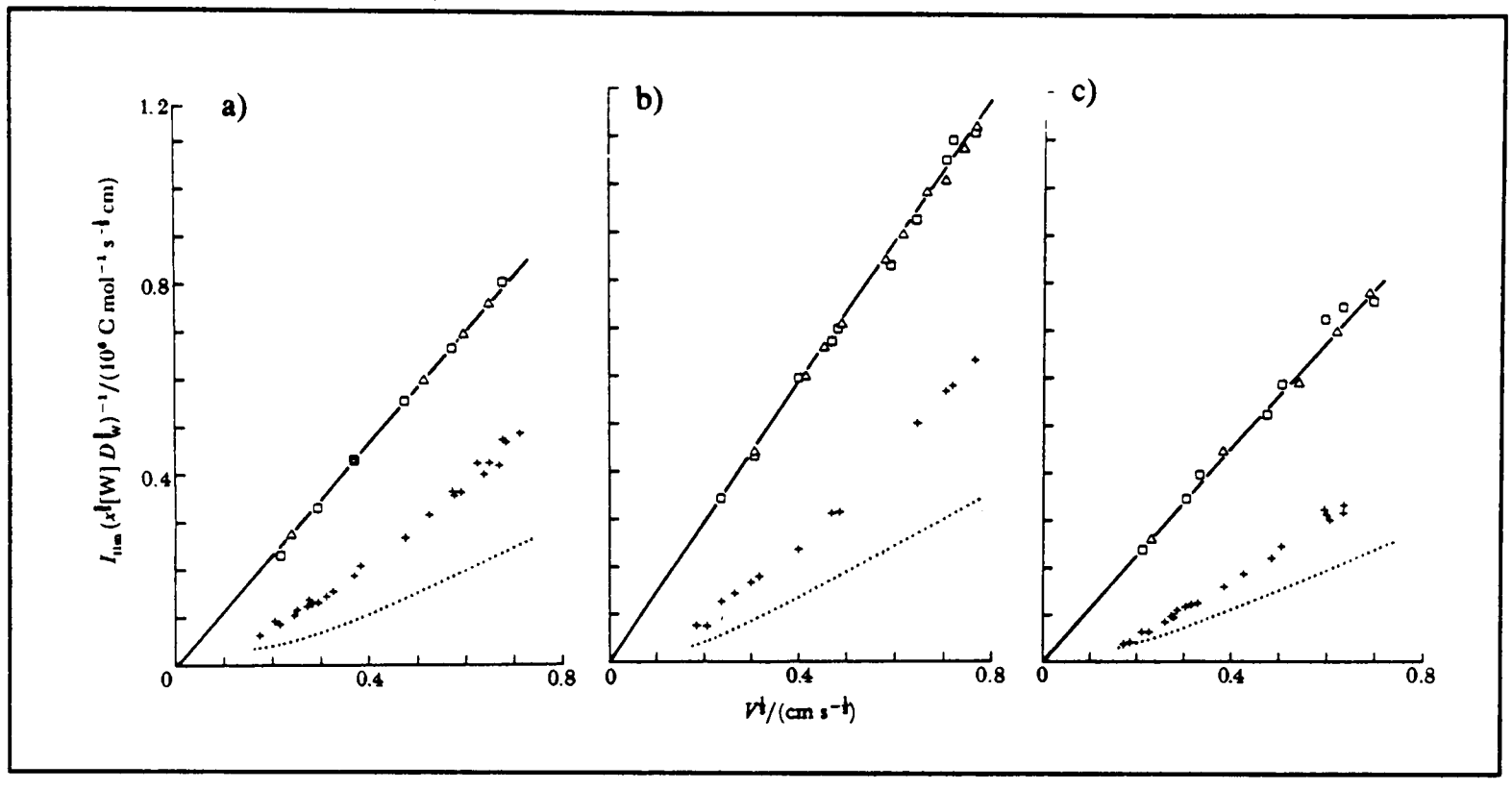

Figure 4.1: Transport limited current-flow rate behaviour for the reduction of H^+ at the monitor electrode □; H^+ at the detector electrode +; $Fe(CN)_6^{3-}$ at the detector electrode Δ 9; for $[H^+]$ a) 1 × 10^{-6} mol cm^{-3} (b)5 × 10^{-7} mol cm^{-3} and (c)2.5 × 10^{-7} mol cm^{-3}. The dotted lines show the predicted behaviour for H^+ reduction at the detector electrode if the reaction between calcite and H^+ was transport controlled. [53]

In this way Compton and Unwin [53] were able to show that the surface reaction is kinetically controlled. They derived an overall interfacial equation for the dissolution of calcite:

$$Rate/\text{mol cm}^{-2}\,\text{s}^{-1} = 0.043/\text{cm s}^{-1}\,[\text{H}^+]_{\text{surface}} \qquad (4.40)$$

Thus the channel flow cell has revealed the surface kinetics of calcite dissolution for the first time. The heterogeneous rate constant which appears in equation (4.40) can be used in our further investigation of calcite dissolution, so enabling us to quantify the effect of inhibitors.

4.4 Molecular Inhibitors

4.4.1 Introduction

The effect of a wide variety of inhibitors on calcite dissolution and precipitation have previously been studied, by a wide range of methods [i.e. 18, 25, 46, 56, 76-79, 91, 92]. The results of some of these investigations made prior to the channel flow cell development are outlined in Appendix 1. The understanding of the action of inhibitors is of great importance, both industrially in the design of new commercial scale inhibitors, and in the understanding of calcite dissolution in natural systems.

As discussed briefly in Chapter 1 (1.6) the channel flow cell methodology was used by Compton and Unwin [53,144,145]offers a great advantage to previous methods. It enables accurate knowledge of the flow of both reactants to the surface and of products any to the detector electrode. Further it allows reproducible surface preparation, and precise chemistatic control of reactants. Most importantly, the detector is measuring near surface concentrations and so can recognise the small concentration effects predicted for differing possible kinetic mechanisms.

The channel flow cell method was used by Compton and Unwin [144,145]to study a variety of small molecular dissolution at low pH. It is thought the inhibitors may adsorb to the sites from which dissolution takes place so slowing or even stopping dissolution.

The experiments by Compton and Unwin [144,145]also investigated whether it was the acid itself or its mono-anion, or dianion which caused inhibition. For example maleic acid can be considered to be in equilibrium with its mono- and di-anion, and give an

equation such:

$$H_2Mal \rightleftharpoons HMal^- + H^+ \rightleftharpoons Mal^{2-} + 2H^+ \quad (4.41)$$

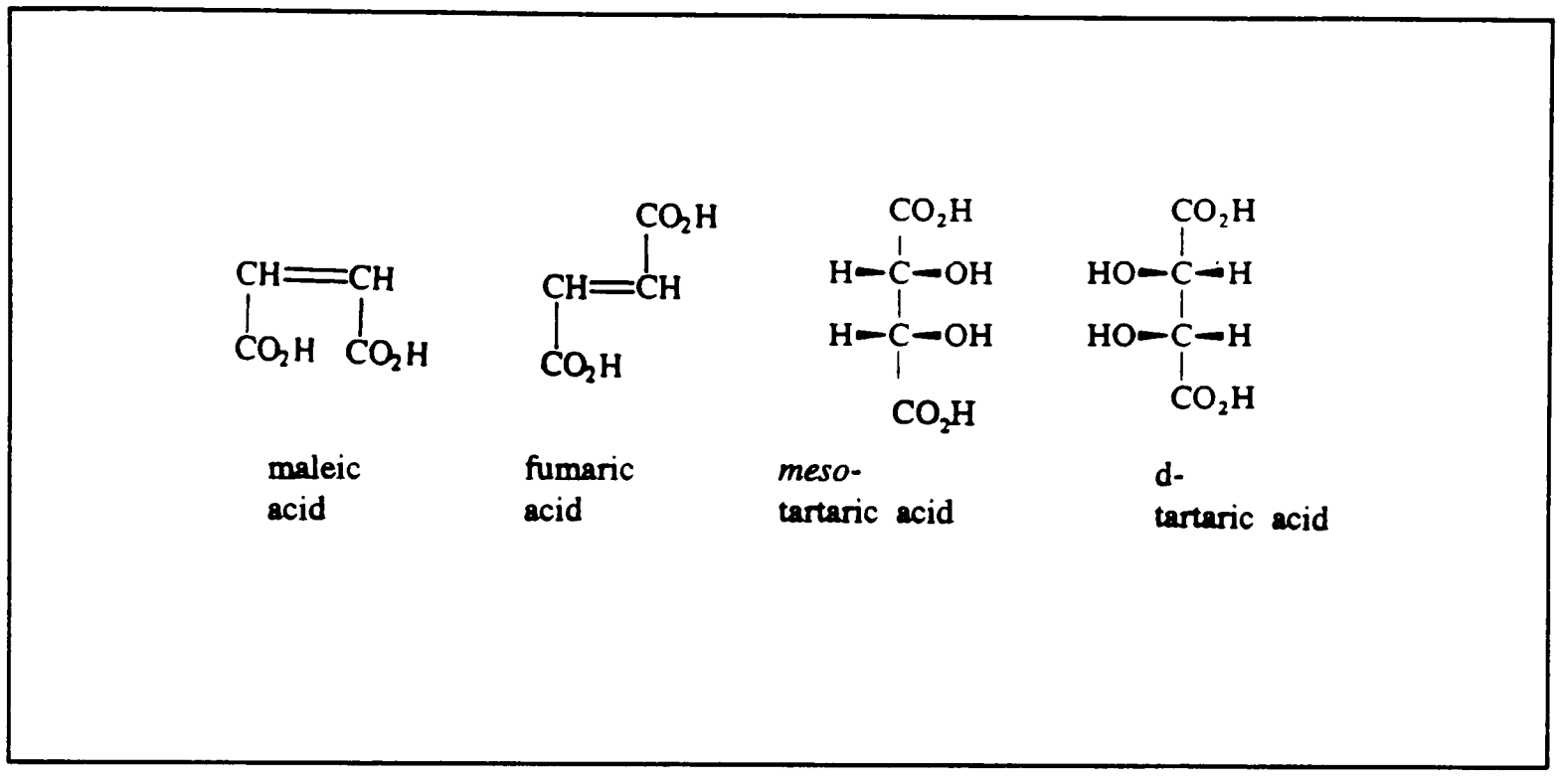

*Figure 4.2: The molecular structures of maleic acid, meso tartaric acid, d-tartaric acid, and fumaric acid. (l-tartaric acid being the **optical** isomer of d-tartaric acid.)*

They showed from experiments in which the pH was controlled thus fixing the extent to which the reactions proceeded to the left, that it is the di-anion Mal^{2-} only which adsorbs on the $CaCO_3$ surface [144].

By use of the Backwards Implicit finite difference method the dissolution reactions were modelled, and an effective rate constant was obtained. This rate constant k_1' was linked to the rate constant k_1 for the reaction in when there is no inhibition:

$$k_1' = k_1(1-\theta) \quad (4.42)$$

when θ is the surface coverage of Mal^{2-}.

Assuming that adsorption is Langmuirian, then for the example of Mal^{2-}:

$$\theta_{Mal^{2-}} = \frac{K_L[Mal^{2-}]}{1 + K_L[Mal^{2-}]} \quad (4.43)$$

From these two relationships it is possible to relate k_1' to the concentration of Mal^{2-}:

$$\frac{1}{k_1'} = \frac{1}{k_1} + \frac{K_L[Mal^{2-}]}{k_1} \tag{4.44}$$

Then plotting $1/k_1'$ against [Mal2-] enables the verification of the validity of the assumption that adsorption is Langmuirian. If valid the line will be linear with an intercept of $1/k_1$. Also the slope will yield K_L, thus enabling comparison of the effectiveness of different inhibitors.

The conclusions drawn from this previous work on molecular inhibitors of calcite [144,145] gives an inhibition order:

maleic acid > >*meso*-tartaric acid > >*d*- and *l*- tartaric acids > > fumaric acid.

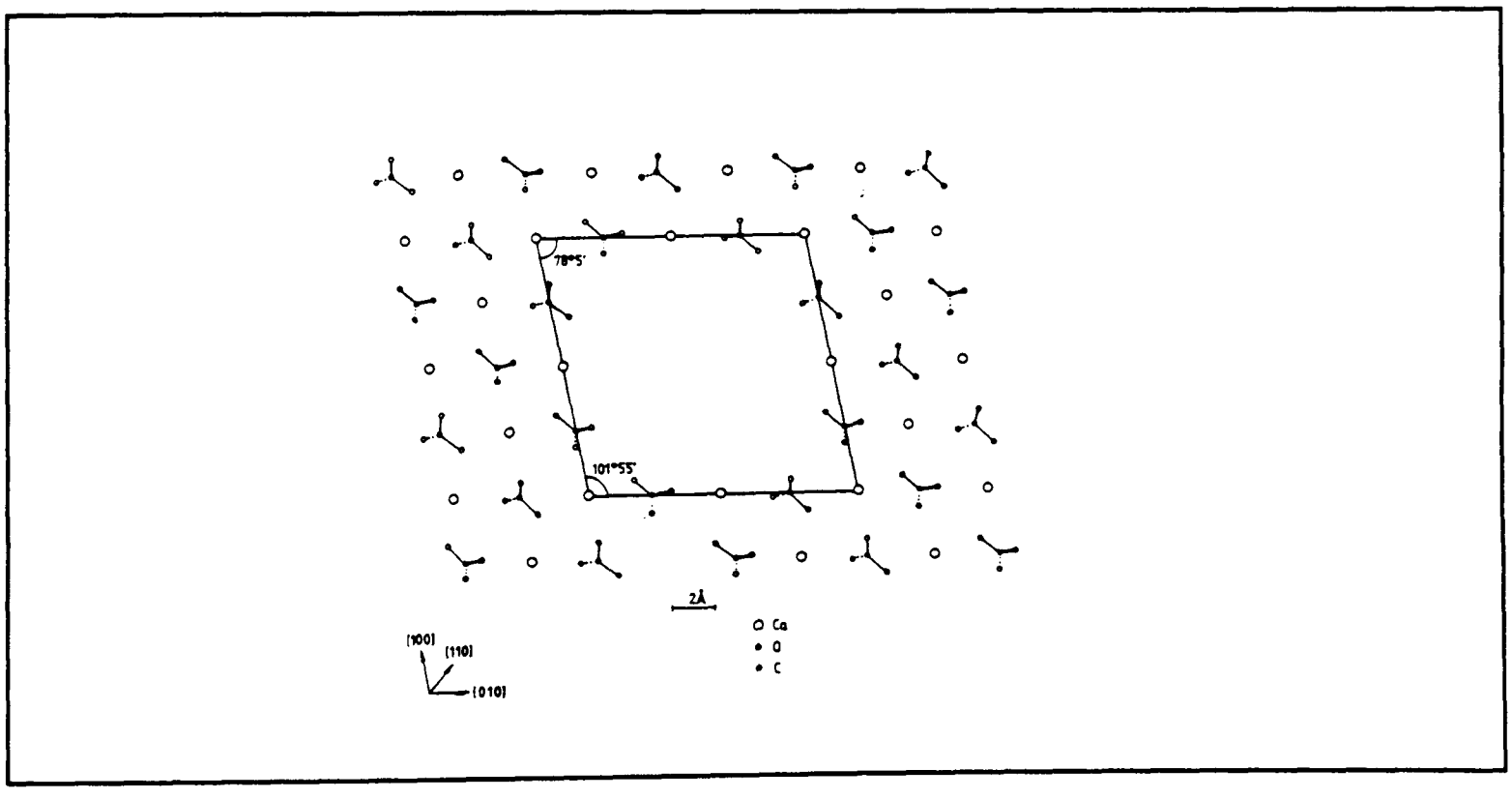

Figure 4.3: A schematic representation of the shape of the etch pits (obtained by exposing the calcite crystal (100) surface to a 1 × 10^{-3} mol dm^{-3} solution of HCl) relative to the geometry of this crystal plane.

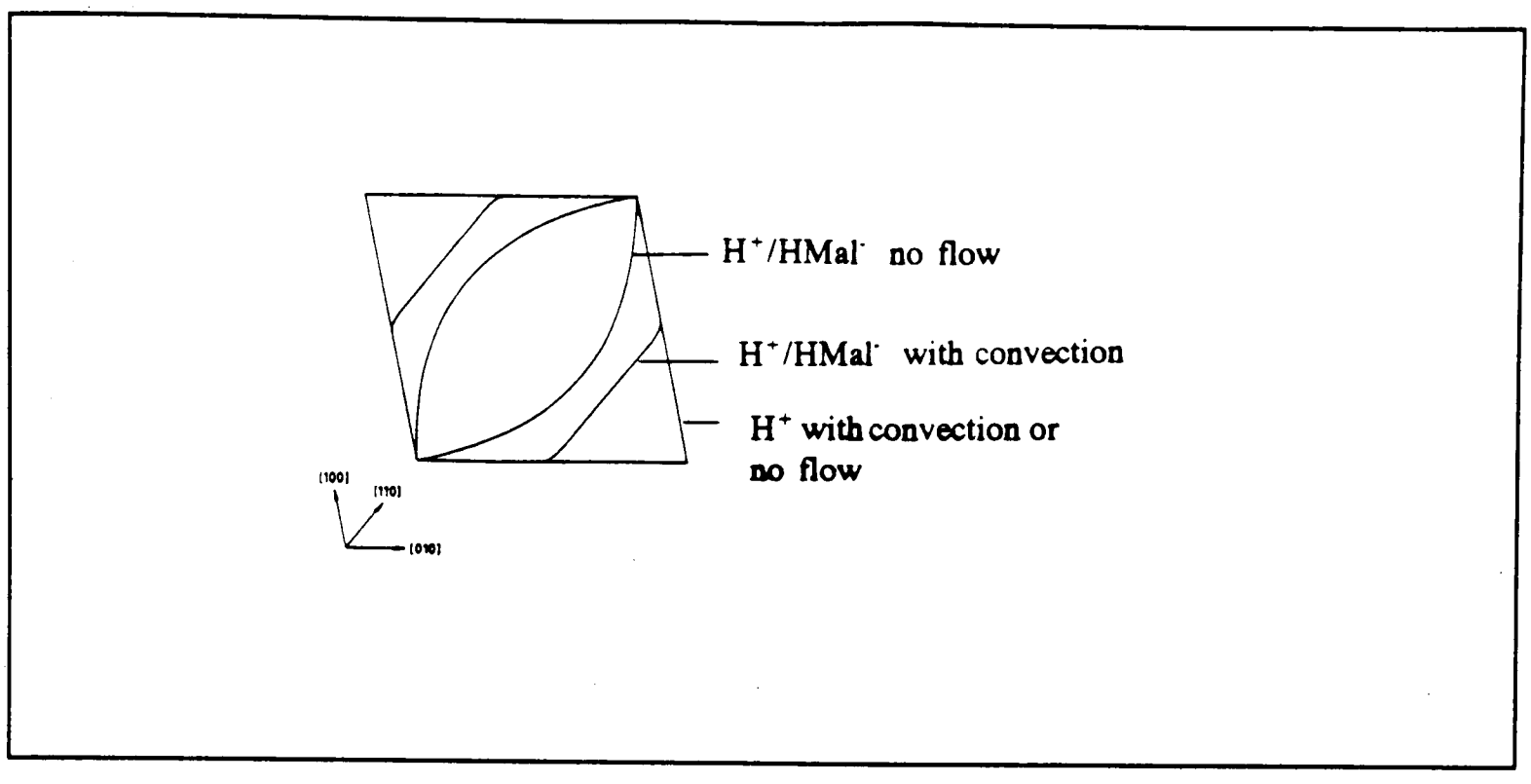

Figure 4.4: Comparison of the calcite etch pit as formed in the presence of mineral acid, with those formed with HMal⁻ under differing flow conditions.

As calcite dissolves pits are formed on the surface, these have a characteristic shape, which varies in the presence on an inhibitor [53,145]. In attempting to understand the above relative inhibition order attention was paid to the etch pit shape and size, in

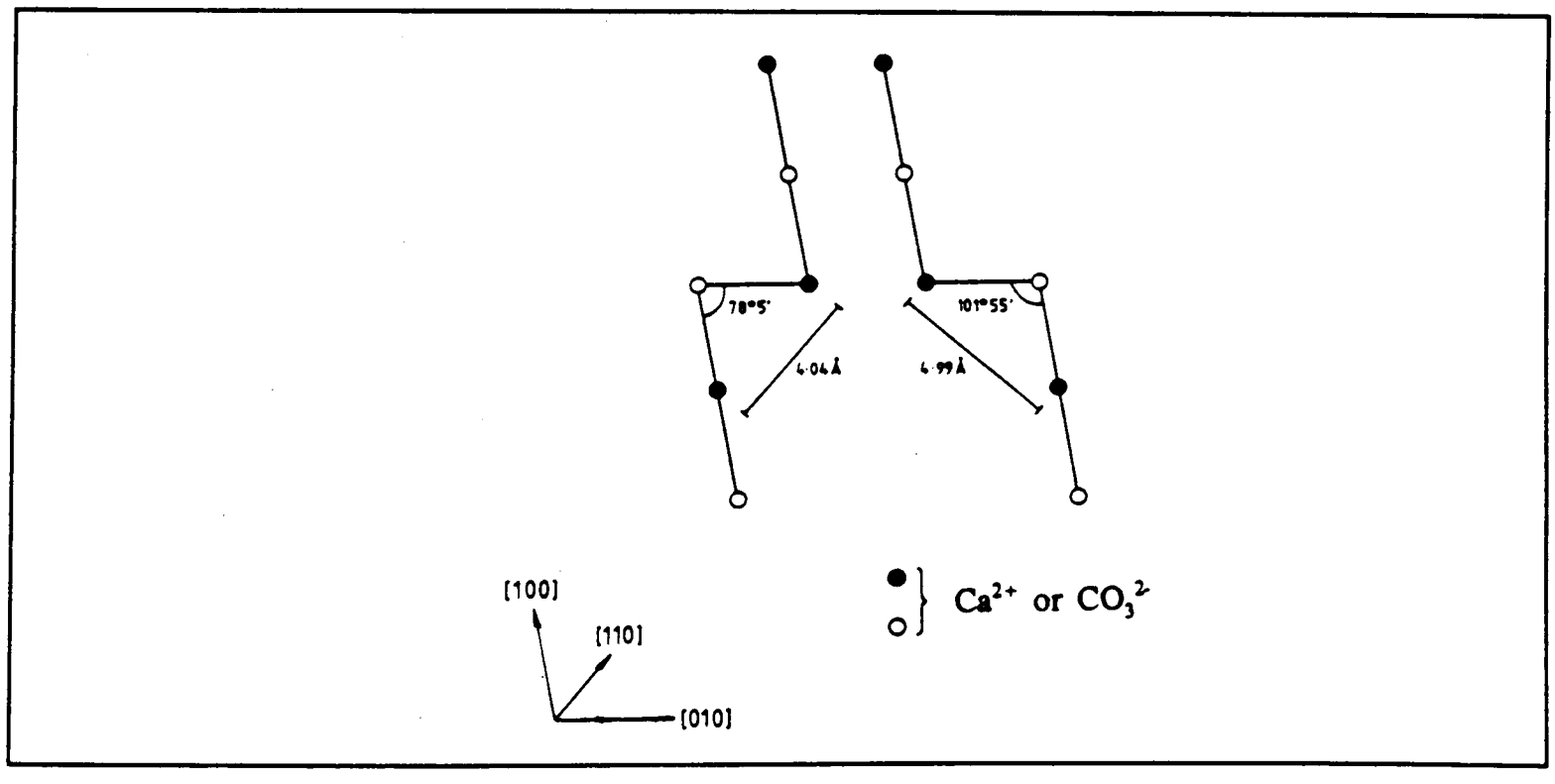

Figure 4.5: The two different kink sites which can be formed in the calcite (100) plane ● and ○ denote Ca^{2+} or CO_3^{2-} respectively.

particular in relation to the crystal structure as shown in figure 4.3.. If examination is made between the etch pit when etched with maleic acid as compared to a mineral acid (figure 4.4), then it can be inferred that maleic acid seems to inhibit preferentially at the 4.04 Å Ca^{2+} - Ca^{2+} corner. This can be interpreted as the maleic acid di-anion preferentially adsorbing at this corner as compared to the other Ca^{2+}-Ca^{2+} corner.

The inter-carboxylic distance on the Mal^{2-}, ion as determined crystallographically from the disodium salt, when compared to this inter-Ca distance reveals an exact match (see figure 4.5). Therefore it is possible to envisage the Mal^{2-} anion acting as a 'molecular clamp' between the Ca^{2+} ions in a kink site with a 4.04 Å Ca^{2+}-Ca^{2+} distance, and thus stopping dissolution in this direction.

The above interpretation explains the modification in the pit shape caused when etching with maleic acid. As dissolution in one pair of opposite corners is largely stopped whilst dissolution in the other corners may proceed freely, thus leading to the lens shaped etch pits observed. However for fumaric acid the inter-carboxylic distance is much greater and there is no ability for this molecule to deform so as to be able to clamp across either type of kink site. Examination of the etch pits formed with fumaric acid shows little obvious alteration in etch pit shape from that obtained by etching with HCl [53,144].

The intermediate behaviour of the tartaric acids can also be rationalised. All the tartaric acids are capable of rotation about the carbon-carbon bond and so can present different CO_2^- - CO_2^- distances to the surface. However as can be seen in figure 4.6 below, the preferred lowest energy conformation of *meso* tartaric is *gauche* rather than

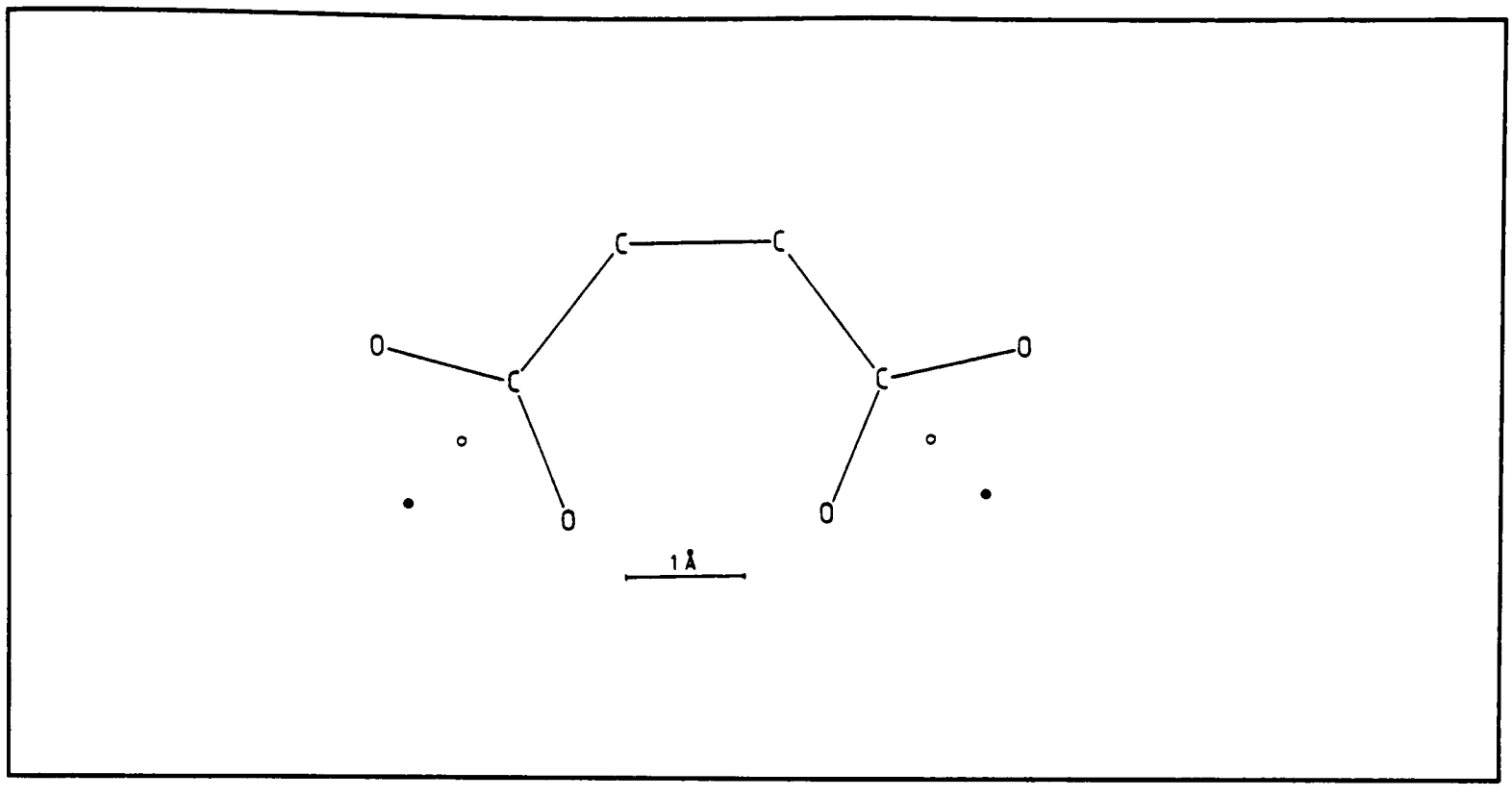

Figure 4.6 The size of the Mal^{2-} anion and the two calcium-calcium separations as represented by ● for the 4.04 Å separation and ○ for the 4.99 Å separation.

anti which is the preferred conformation for both *d*- and *l*- tartaric acids. The *gauche* conformation brings the carboxylic groups much closer, so that the low energy conformer of the molecule is closest in structure to the requirements of clamping across the 4.04 Å Ca^{2+} - Ca^{2+} distance. This may explain the greater inhibitory power of the *meso*-tartaric acid dianion.

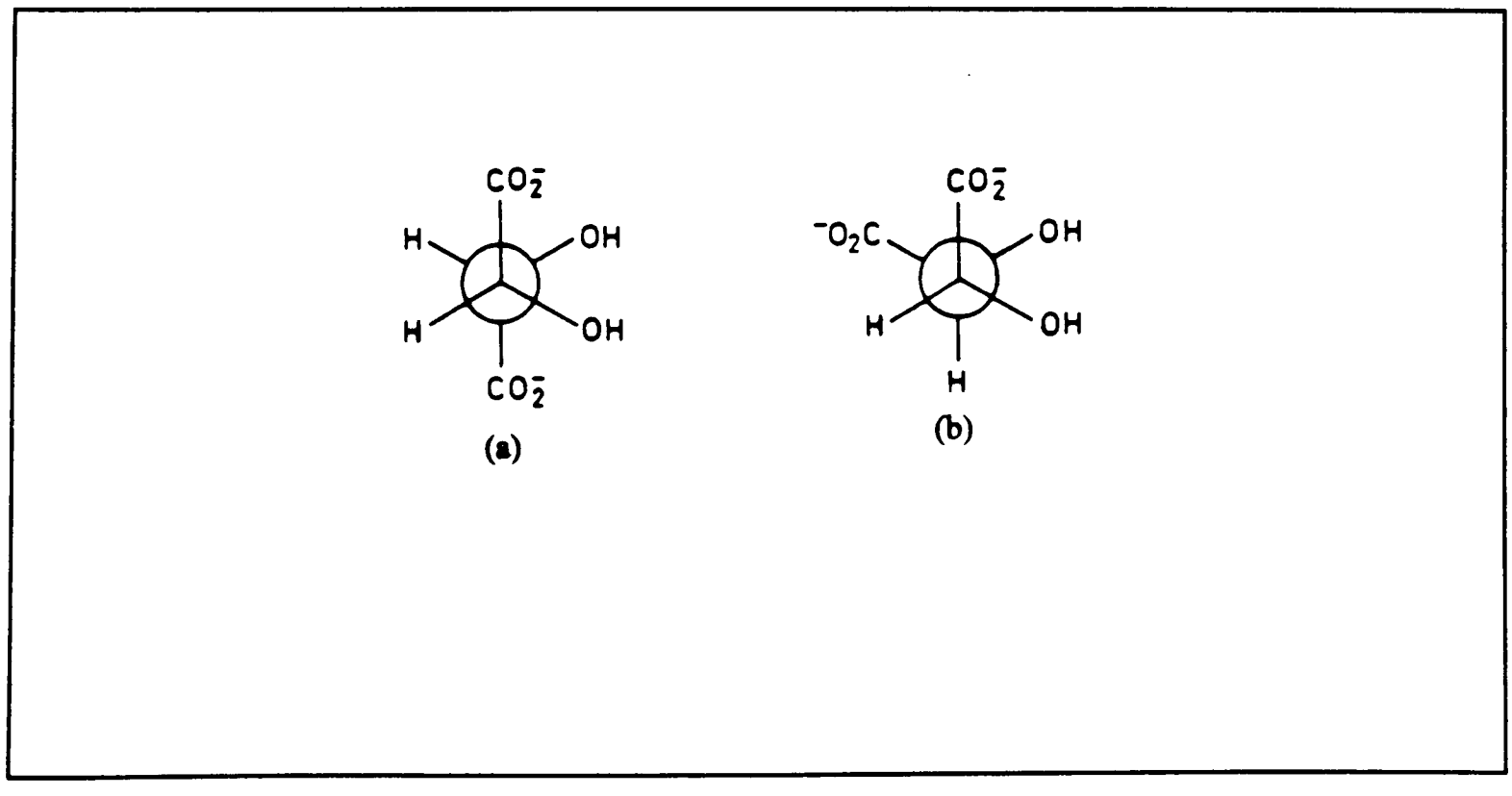

Figure 4.7: The most stable conformations of (a) l-tartaric acid and (b) meso tartaric acid.

In the present study two further small molecular inhibitors, phthalic and homo-phthalic acids are investigated. This enables further verification of this conclusion with respect to the importance of inter-carboxylic distance and the Ca^{2+} - Ca^{2+} distance in the etch pit. Phthalic acid is of additional interest as it has a bulky benzene ring. This ring holds the inter-carboxylic acid distance at 3.74 Å which is close to the short Ca^{2+} - Ca^{2+} distance noted above. Moreover the ring could sterically hinder clamping at this site. Homo-phthalic acid whilst still having a large benzene ring in contrast does have some freedom to alter its inter-carboxylic distance due to the short side chain between the second acid group and the benzene ring. Also its inter-carboxylic acid distance, as measured crystallographically in the disodium salt, is much closer to that of the Ca^{2+} - Ca^{2+} separation at the second site (at 4.99Å). Hence it is possible that either or both of these molecules could clamp across the longer inter Ca^{2+} distance.

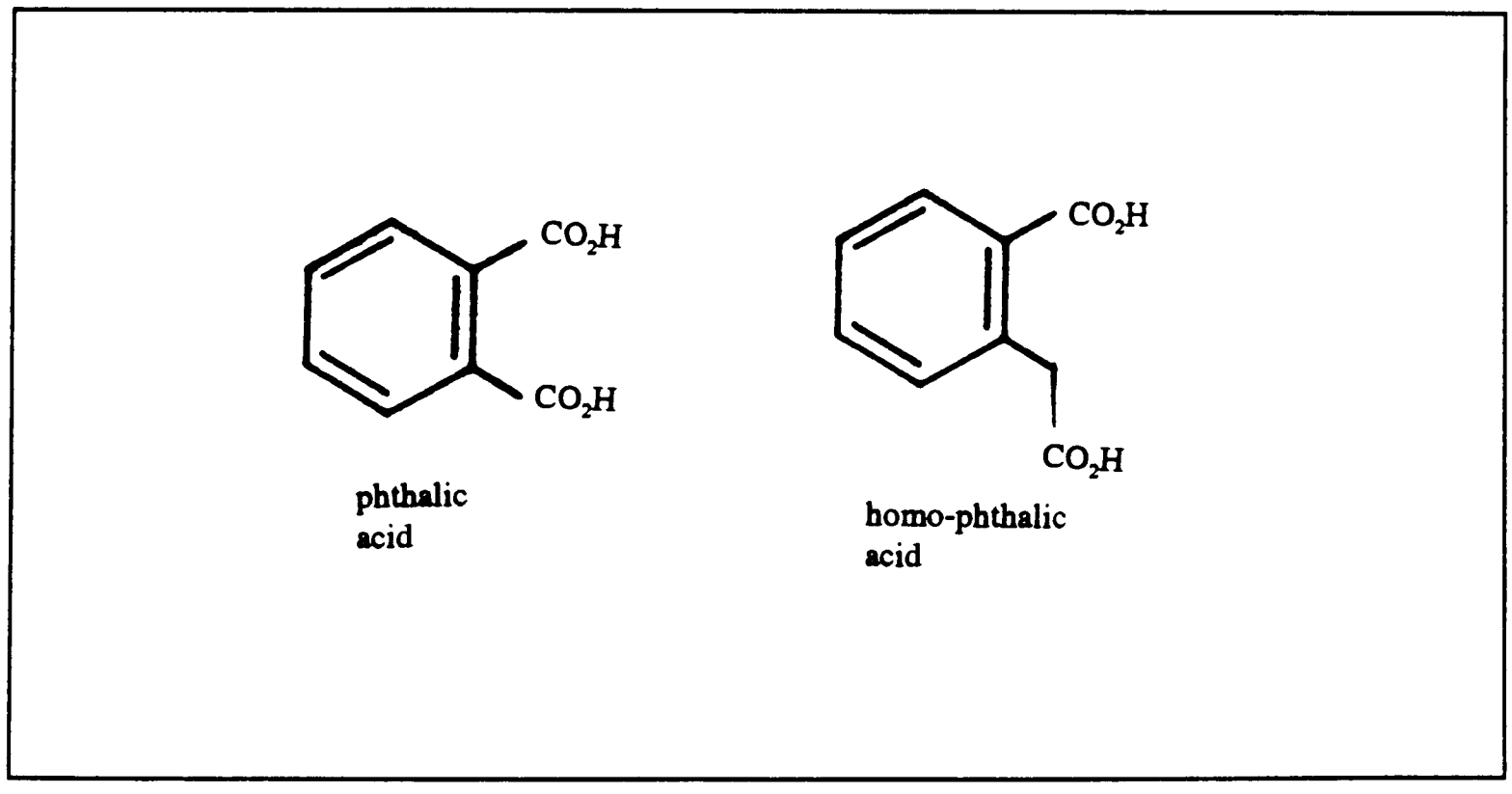

Figure 4.8: The structures of phthalic and homo-phthalic acids.

4.4.2 Experimental Details of the Dissolution of Calcite in the Presence of Phthalic and Homo-phthalic acids.

In this section the precise conditions used for the channel flow cell in the study of calcite inhibition by phthalic and homo-phthalic acids will be described. Also reported are some preliminary experiments which were performed in order to characterise the speciation, diffusion coefficients and electrochemical behaviour of the molecules.

The experimental design of the channel flow cell used was outlined in section 4.2. Experiments were carried out on solutions of 0.5 mol dm^{-3} KCl, with a concentration of phthalic acid between 2.2×10^{-3} mol dm^{-3} and 1.5×10^{-2} mol dm^{-3}, or alternatively homo-phthalic acid between 5.7×10^{-4} mol dm^{-3} and 1.1×10^{-2} mol dm^{-3}.

4.4.2.1 *Preliminary Rotating Disc Experiments*

As a preliminary to using amperometric H^+ detection in the channel flow cell it is necessary to confirm that all the H^+ does react at the electrode surface. That is that both 'free' protons in solution *and* those still bound to undissociated acid, are measured by amperometric detection. This was investigated by measuring the limiting currents for each acid using the rotating disc method. If the dissociation kinetics at the electrode surface are sufficiently fast that all the H^+ is reduced, then a linear Levich plot (see Chapter 2, section 2.7) will be observed.

The limiting current is proportional to the solution concentration of the acid and the singly dissociated anion:

$$I_{LIM} \propto D_{H^+}^{2/3}[H^+] + D^{2/3}\left([HA^-] + 2[H_2A]\right) \tag{4.45}$$

where it is assumed that the diffusion coefficients for both H_2A and HA^- are the same and equal D.

Or in terms of the total acid concentration,

$$I_{LIM} \propto D_{H^+}^{2/3}[H^+] + nD_{H_2A\,tot}[H_2A]_{tot} \qquad (4.46)$$

where n is a measure of the mean number of protons still attached to the acid.

In order to investigate if the basic hypothesis that all the H^+, both that which is 'free' and that which is still bound to the acid, react equally at the electrode it is only necessary to see if the limiting current of that component due to the 'free' H^+ subtracted still behaves linearity in a Levich plot. The observed behaviour for typical experiments with phthalic and homo-phthalic acids is shown in figures 4.9 and 4.10 respectively. The result is a satisfactory Levich plot although there is a larger error arising from the pH reading used to find the 'free' H^+ concentration. The calculation of the actual value of D_{H2A} will be calculated later in section 4.4.2.3.

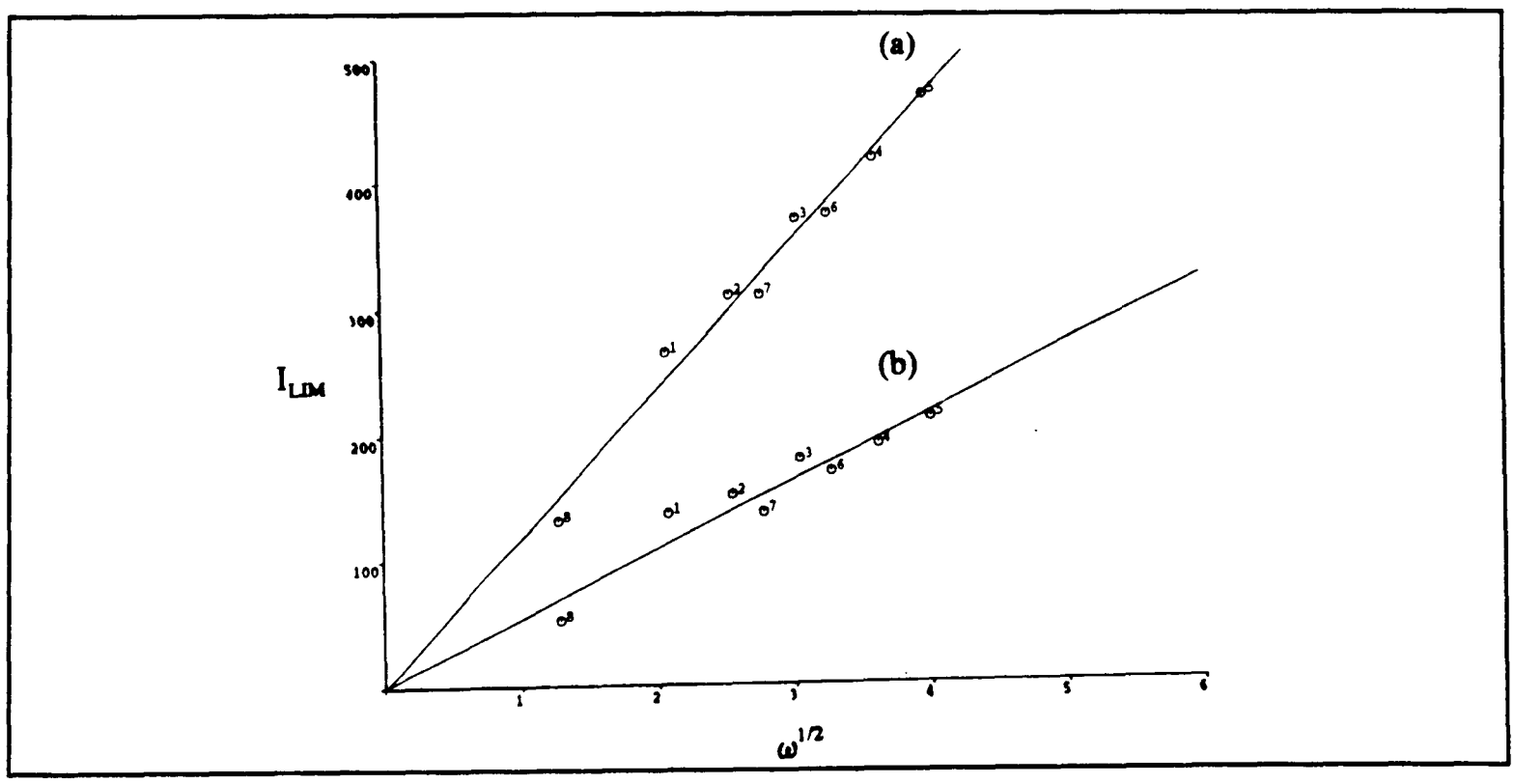

Figure 4.9: A Levich plot of I_{LIM} against $(\omega)^{1/2}$ for phthalic acid of concentration 6.3 × 10^{-4} mol dm^{-3} and pH 3.55, (speciation calculated from pH as described in section 4.4.2.2 is $[PhthH_2]$= 1.25 × 10^{-4}, $[PhthH^-]$=5.07 × 10^{-4}, and $[Phth^{2-}]$=7.02 × 10^{-6} mol dm^{-3}) (a) The total I_{LIM}. (b) I_{LIM} with the contribution due to 'free' H^+ subtracted.

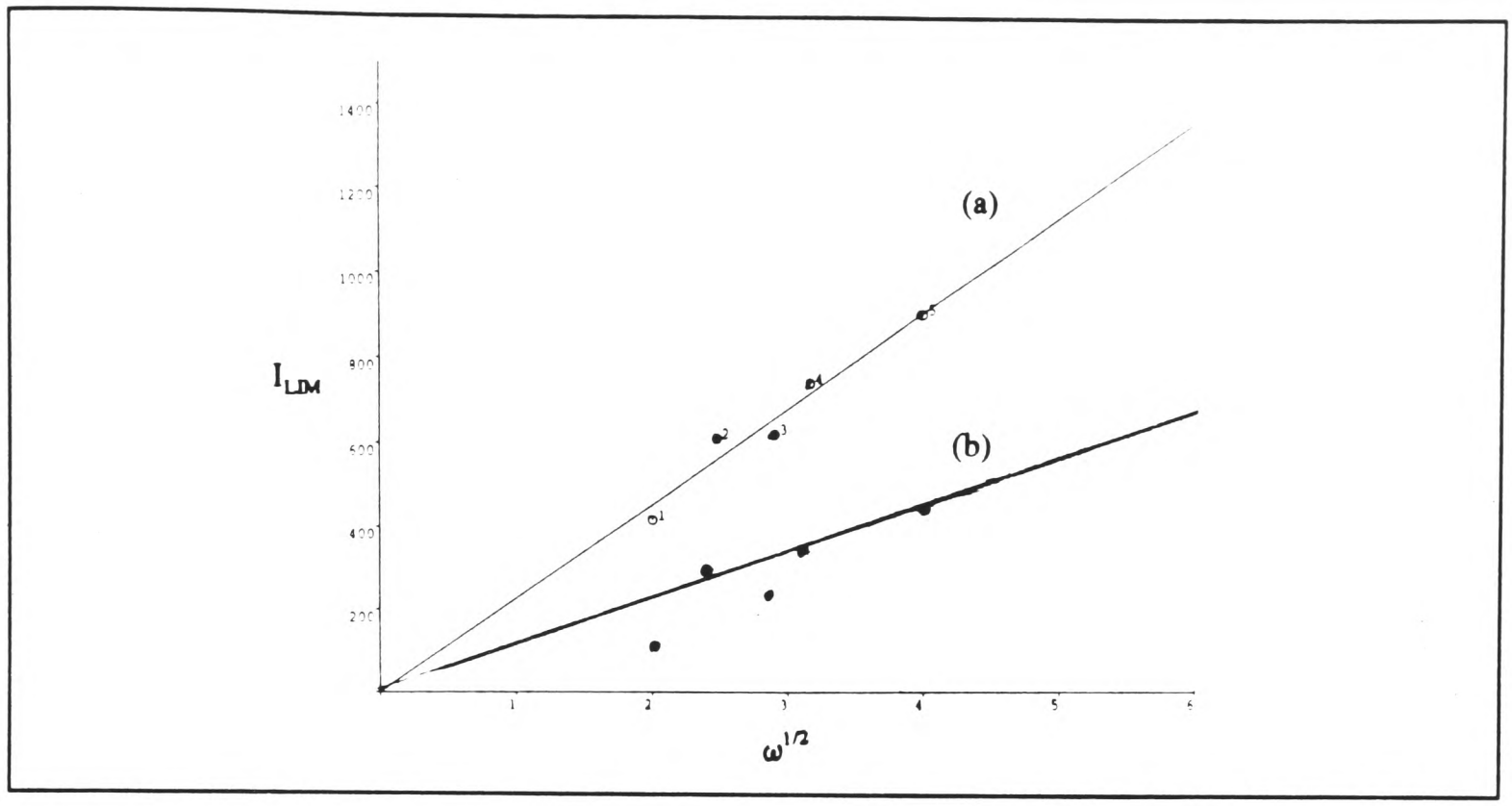

Figure 4.10: A Levich plot of I_{LIM} against $(\omega)^{1/2}$ for homo-phthalic acid of concentration 6.5 × 10^{-4} mol dm^{-3} and pH 3.55, (speciation calculated from pH as described in section 4.4.2.2 [$HomoH_2$] = 6.04 × 10^{-4}, [$HomoH^-$]= 4.38 × 10^{-5}, and [$Homo^{2-}$]=5.78 × 10^{-6} mol dm^{-3}) (a) The total I_{LIM}. (b) I_{LIM} with the contribution due to 'free' H^+ subtracted.

This demonstrates that all H^+ that reaches the electrode whether 'free' or bound to the acid reacts at the electrode rapidly enough for the dissociation kinetics to be treated as very rapid.

4.4.2.2 *Determining the Speciation of Phthalic and Homo-phthalic Acids*

A knowledge of the speciation along with the results of the rotating disc experiments is required to enable a derivation of the mean diffusion coefficient of HA^- and H_2A, for both phthalic and homophthalic acids. In order to determine the speciation the K_a's of the acids under the electrolyte conditions used in this work needs to be known. This was accomplished by performing potentiometric titrations.

The titrations used solutions with background electrolyte concentrations of 0.5 mol dm^{-3} KCl. The solutions were stirred whilst being titrated with a solution of KOH. The concentration of the KOH was 2.8×10^{-3} mol dm^{-3} and 1.48×10^{-3} mol dm^{-3} for phthalic and homo-phthalic acid respectively (as determined by titration with HCl). All titrations were performed with the reaction vessel held at 25°C by a water bath, and with the solution degassed with Argon. The change in pH was followed by the use of a combination pH electrode and a Jenway pH meter as described in Chapter 3. A typical titration for phthalic acid is shown in figure 4.11,and a typical titration for homo-phthalic acid is later shown in figure 4.12.

From this potentiometric titration curve for phthalic acid (4.11), only one end point can be seen. This has two possible explanations, either both end points and K_a's are so close as to be indistinguishable here, *or* one end point has either already occurred at the pH at the start of the titration or one occurs at a higher pH than limit of this titration. By calculating the amount of OH^- used at the end of the titration it is possible

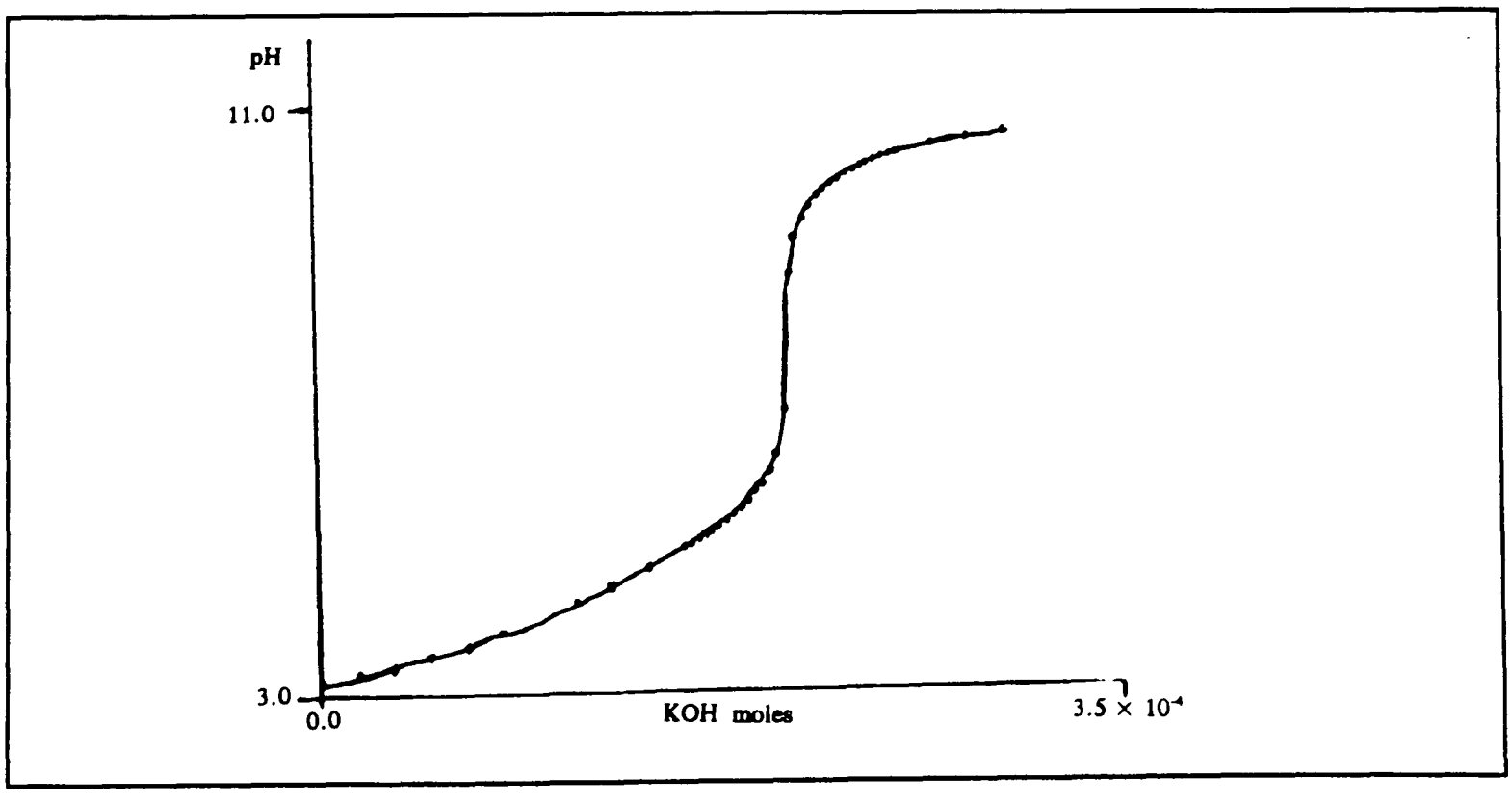

Figure 4.11: A potentiometric titration of 9.6×10^{-4} mol dm^{-3} phthalic acid with 2.8×10^{-3} mol dm^{-3} KOH.

to calculate if all the acid groups are neutralized at the end of the titrations, and this is indeed the case, so both end points have occurred by the end of the titration. In order to decide if the K_a's are close or one has occurred before the start of the titration it is useful to look at any literature values of the K_a's. For phthalic acid the literature values of the K_a's at 25°C are: 1.123×10^{-3} and 3.906×10^{-6} [146], which indicates that one acid group has already dissociated at the start of the titration.

These literature values are stated to have been 'determined at high ionic strength' [146]. These values are in agreement with the potentiometric titrations which were carried out (for example figure 4.11), despite the uncertainty about the precise ionic conditions used in the literature determination. Using these two values for the K_a's would predict that only one end point would be seen in the pH range of the titrations at precisely the point observed. Hence these values are used in the experiments described later .

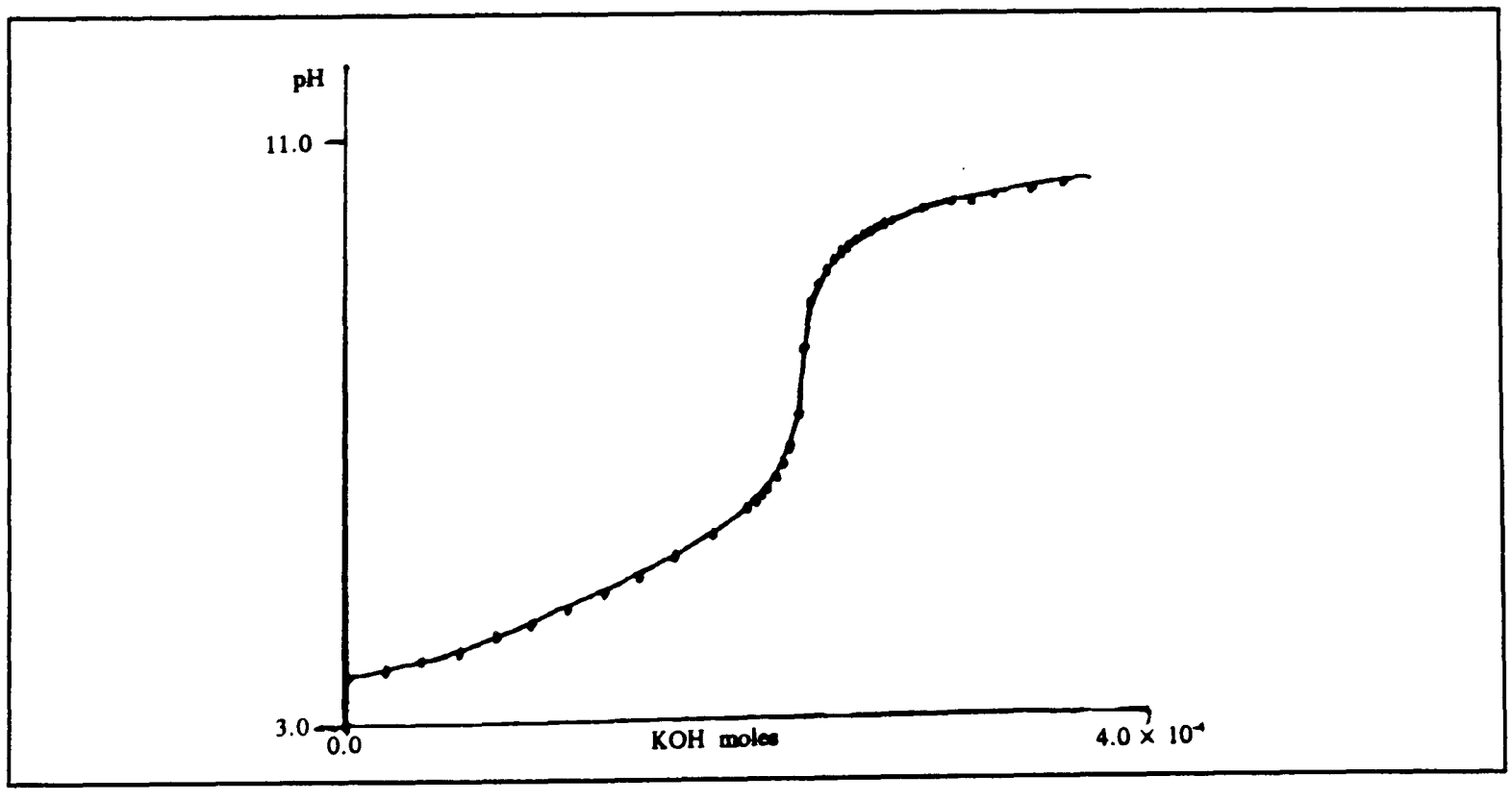

Figure 4.12: A potentiometric titration of 0.55×10^{-3} mol dm^{-3} homo-phthalic acid with 1.48×10^{-3} mol dm^{-3} KOH.

Again in figure 4.12, for the potentiometric titration of homo-phthalic acid, only one end point is seen, and it has been determined that all the acid groups are neutralized by the end of the titration. For homo-phthalic acid the literature values are $K_1 = 1.5 \times 10^{-6}$ and $K_2 = 8.9 \times 10^{-7}$ [147]. This indicates that in this case the single end point can only be accounted for by the closeness of the K_a's.

The precise ionic conditions used for the literature determination were not stated [147]. These literature values are not consistent with the potentiometric titrations reported in this work, as can be seen the combined end point occurs in a different position to that which would be expected from these values (see figure 4.13). This difference is possibly due to the ionic conditions been quite different in this work from those used in the literature determination, as the later were not clearly stated.

Thus it is necessary to derive the K_a's from measured potentiometric titration curves for homo-phthalic acid. The method employed was to predict the expected potentiometric titration curves for homo-phthalic acid solutions of different concentrations, given candidate values for K_1 and K_2, and comparing these with the experimental curves. This can be done by the method of Skoog and West [148]. This derives the titration curve for a polyfunctional acid with an alkali of known strength assuming the values for the equilibrium constants for the two equations:

$$H_2A + H_2O \overset{K_1}{\rightleftharpoons} H_3O^+ + HA^- \tag{4.47}$$

$$HA^- + H_2O \overset{K_2}{\rightleftharpoons} H_3O^+ + A^{2-} \tag{4.48}$$

Then using the method as outlined in Appendix 6 it is possible to determine which dissociation constants give the closest fit to experiment. Figure 4.13 shows an example

of the fit with the two chosen constants ($K_1 = 4.0 \times 10^{-5}$ and $K_2 = 1.9 \times 10^{-5}$) and the

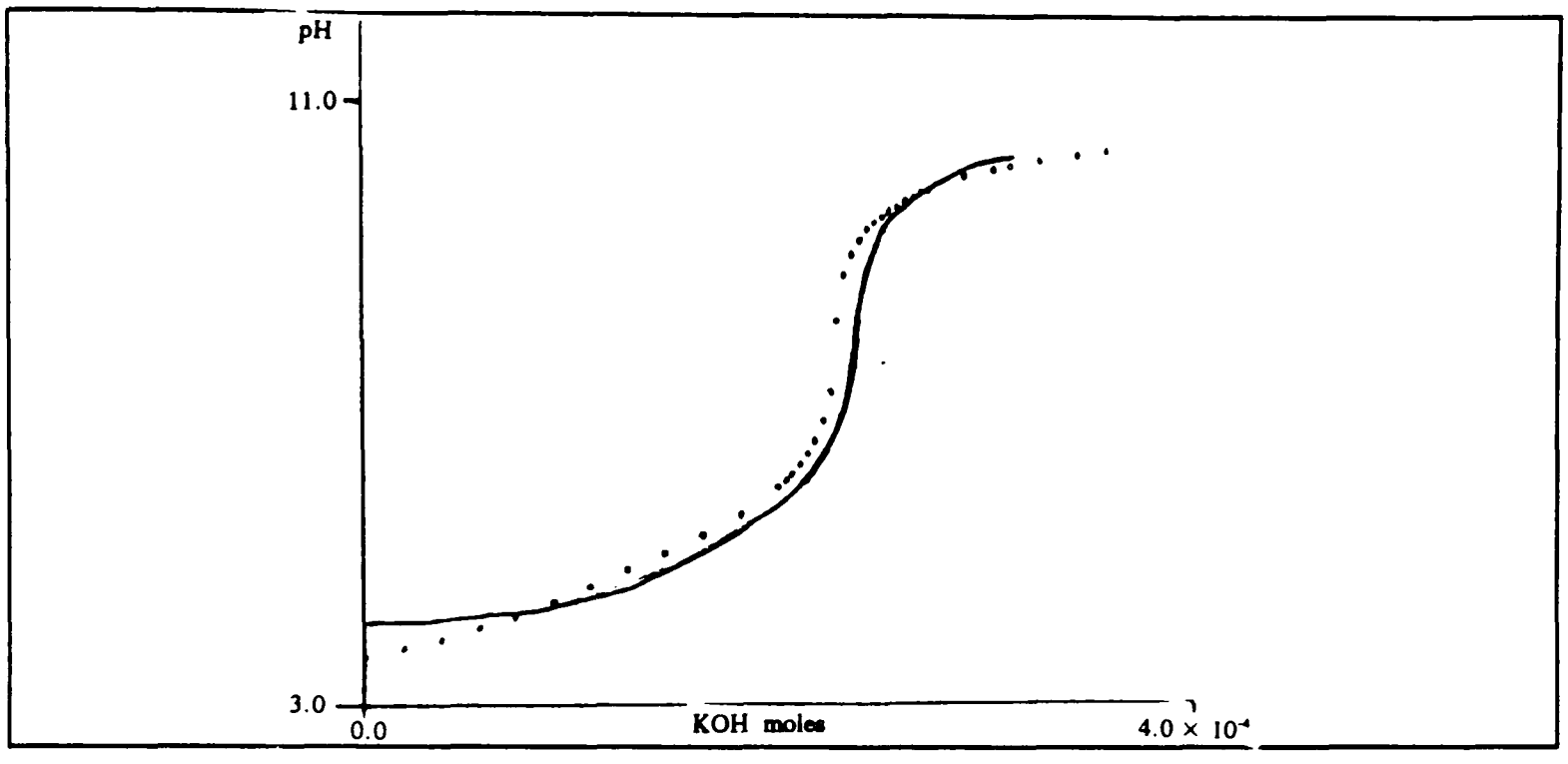

Figure 4.13: A comparison of the experimental data for a potentiometric titration of 0.55 × 10^{-3} mol dm^{-3} homo-phthalic acid, by 1.48 × 10^{-3} mol dm^{-3} KOH; with the titration curve predicted (using the method described in Appendix 6) with K_1 = 4.0 × 10^{-5} and K_2 = 1.9 × 10^{-5} mol dm^{-3}.

comparison with experimental data for a typical potentiometric titration. Whereas figure 4.14 shows the same experimental data fitted with the literature values ($K_1 = 1.5 \times 10^{-6}$ and $K_2 = 8.9 \times 10^{-7}$ mol dm^{-3}).

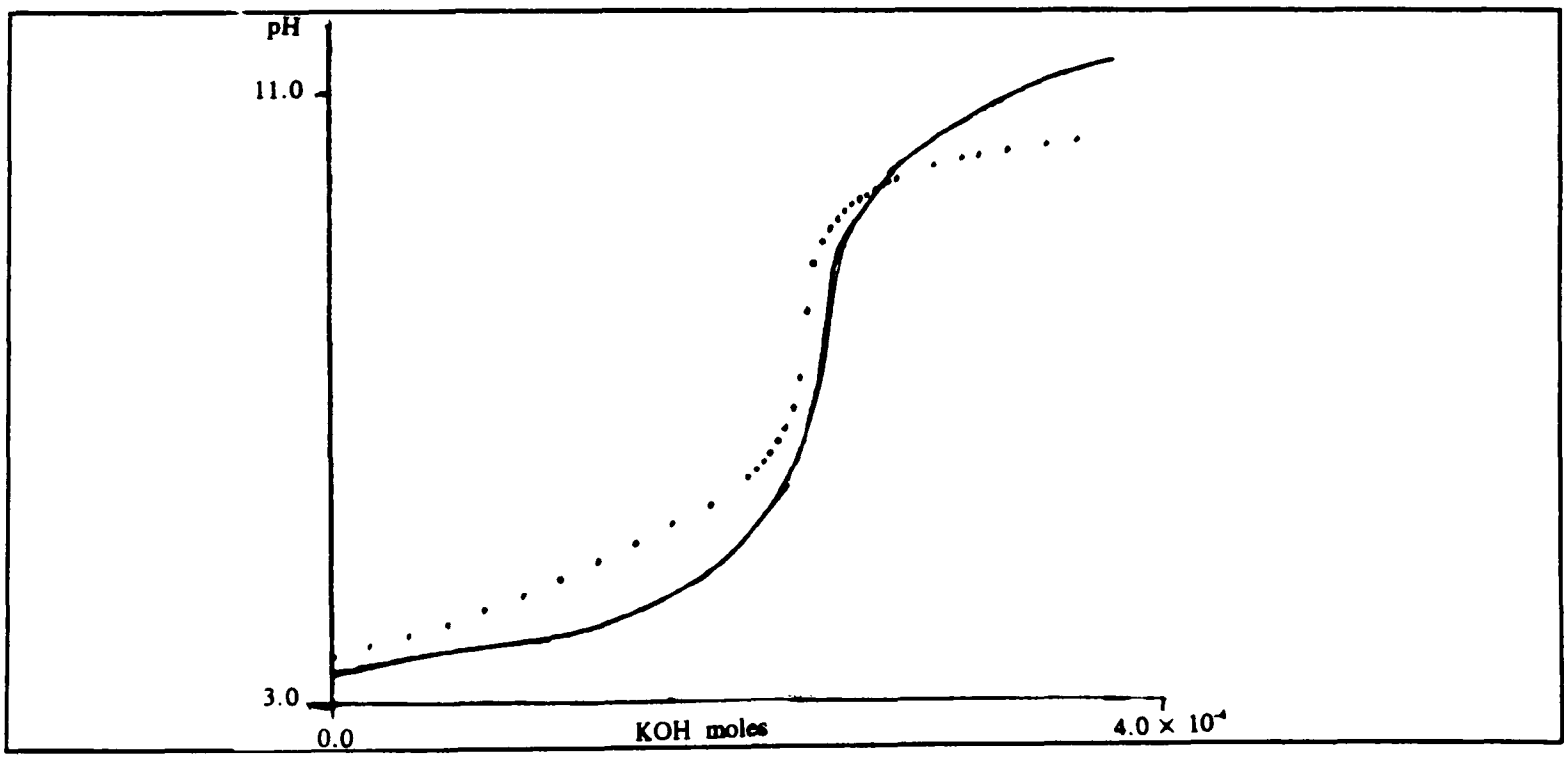

Figure 4.14: A comparison of the experimental data for a potentiometric titration of 0.55 × 10^{-3} mol dm^{-3} homo-phthalic acid, by 1.48 × 10^{-3} mol dm^{-3} KOH; with the titration curve predicted with the literature values, K_1 = 1.5 × 10^{-6} and K_2 = 8.9 × 10^{-7} mol dm^{-3}.

The values as seen in figure 4.13 of $K_1 = 1.9 (\pm 0.2) \times 10^{-5}$ and $K_2 = 4.0 (\pm 0.2) \times 10^{-5}$ mol dm^{-3} are shown to be consistent with the experimental data measured in aqueous 0.5 mol dm^{-3} KCl. These values compare with the literature values of $K_1 = 1.5 \times 10^{-6}$ and $K_2 = 8.9 \times 10^{-7}$ [147].

The values obtained here (for phthalic acid $K_1 = 1.123 \times 10^{-3}$ and $K_2 = 3.906 \times 10^{-6}$ mol dm^{-3}, and for homophthalic acid $K_1 = 1.9 \times 10^{-5}$ and $K_2 = 4.0 \times 10^{-5}$ mol dm^{-3}) are used in subsequent modelling. The knowledge of the K_a's for both homo-phthalic and phthalic acids allows their speciation at any given pH to be known.

4.4.2.3 *Determining the Mean of the Solution Diffusion Coefficient for H_2A and HA^-*

The speciation at the specific pH of the rotating disc experiments can be calculated from the dissociation constants derived above. Using this speciation and the Levich equation for the limiting current with the component due to 'free' H^+ subtracted (see section 4.4.2.1)i.e.:

$$I_{LIM} = 1.554 F \omega^{\frac{1}{2}} \nu^{\frac{-1}{6}} A D^{\frac{2}{3}} (2[H_2A] + [HA^-]) \qquad (4.49)$$

then the mean diffusion coefficient for H_2A and HA^- can be determined. A plot of I_{Lim} against $\omega^{1/2}$ will yield the diffusion coefficient from the slope. The diffusion constant of homo-phthalic acid was measured to be $5.2 (\pm 0.2) \times 10^{-6}$ cm^2 s^{-1}, and for phthalic acid $1.0 (\pm 0.3) \times 10^{-5}$ cm^2 s^{-1}. These values can be compared with those estimated by the Wilkie-Chang [149] equation. This is an empirical method of estimating diffusion

coefficients and is usually correct to within 10%. The correlation is:

$$D = 7.4\times10^{-8}\left|\frac{(\chi M)^{\frac{1}{2}}T}{\eta\,\vartheta}\right| \tag{4.50}$$

where χ is the solvent factor (2.6 for water), M is the molecular weight of the solvent, T is the temperature in Kelvin, η is the solvent viscosity in centipoise (for water 0.893) and ϑ is the molecular volume. The molecular volume is calculated from the factors given for specific functional groups and atomic weights as given in the paper by Wilkie-Chang [149]. The diffusion coefficients of phthalic and homo-phthalic acid are estimated in this way as 7.7×10^{-6} cm^3 s^{-1} and 7.1×10^{-6} cm^3 s^{-1} respectively. The value for homo-phthalic acid is close to that measured by the rotating disc experiments. For phthalic acid there is a literature value for the diffusion coefficient of 8.6×10^{-6} cm^3 s^{-1} [150], which is intermediary between that measured here and that estimated from the Wilkie-Chang equation.

With the values measured by rotating disc for the diffusion coefficients of the two molecules ($D_{PHTH}=5.2 \times 10^{-6}$ cm^3 s^{-1}, and $D_{HOMO}=1.0 \times 10^{-6}$ cm^3 s^{-1}), it is possible to model the transport of these molecules in a channel flow cell, and so study their effect on the dissolution of calcite and its inhibition.

4.4.3Theory for the dissolution of Calcite in the Presence of Phthalic and Homo-phthalic acids at low pH

In section 4.3 the matrix elements required to model the simple dissolution of calcite under acidic conditions were derived. In this section the necessary modifications for the case of inhibition by di-anions derived from weak acids, will be made using phthalic acid as an example. Under the bulk pH range of the experiments (pH 2.5 - 4.0) phthalic acid exists as either the fully protonated form $PhthH_2$ or the singularly deprotonated form $PhthH^-$. Thus as well as free protons (as measured by the pH) reacting at the calcite surface it is also possible that protons transported by the phthalic acid itself will react with the calcite surface.

$$PhthH_2 \rightleftharpoons PhthH^- + H^+ \tag{4.51}$$

$$PhthH^- \rightleftharpoons Phth^{2-} + H^+ \tag{4.52}$$

$$CaCO_3 + H^+ \rightleftharpoons Ca^{2+} + HCO_3^- \tag{4.53}$$

[PHTH] is used to denote the total concentration of phthalic acid.

$$[PHTH] \approx [PhthH_2] + [PhthH^-] \tag{4.54}$$

If it is assumed that these protons react at the same rate as the 'free' protons at the crystal surface, as is shown in section 4.4.2.1to be valid for the case of reaction at an electrode surface, a modified version of the diffusion equation can be written:

$$0 = D_{PHTH}\frac{\partial^2[PHTH]}{\partial y^2} - v_x\frac{\partial[PHTH]}{\partial x} \tag{4.55}$$

In this equation there is no need to include the dissociation equations, as the system will be at equilibrium at almost every point throughout the flow cell.

The boundary condition at the reaction interface is modified to:

$$D_{HCO_3^-}\frac{\partial[HCO_3^-]}{\partial y} = k_1([H^+]+(2-n)[PHTH]) \tag{4.56}$$

where n is the mean number of protons per phthalic acid molecule which are 'free' as calculated from the solution pH.

4.4.3.1 *The Boundary Conditions*

All the boundary conditions are now stated.

(i) *Upstream of the Crystal*

Upstream the total concentration of phthalic acid is the same as the initial bulk concentration.

$$x=0,\quad 0<y<2h,\quad [PHTH]=[PHTH]_{bulk} \tag{4.57}$$

(ii) *At the Surface of the Crystal*

Here the flux is governed by the kinetics as described by the dissolution equation (4.56) as above.

$$0<x<x_c,\quad y=0,\quad -D_{HCO_3^-}\frac{\partial[HCO_3^-]}{\partial y} = k_1([H^+]+(2-n)[PHTH]) \tag{4.58}$$

$$= D_{H^+}\frac{\partial[H^+]}{\partial y} + D_{PHTH}\frac{\partial[PHTH]}{\partial y}$$

(iii) *At the Far Wall*

At the far wall again there is no flux of the phthalic acid.

$$0<x<x_{c+e},\quad y=2h,\quad \frac{\partial[\mathbf{PHTH}]}{\partial y}=0 \tag{4.59}$$

(iv) *Downstream of the Crystal*

If the detector electrode is held at a potential such that the 'free' H^+ is all reduced, then as shown in section 4.4.2.1all the H^+ still bound to phthalic acid is also consumed.

$$x_c<x<x_{c+e},\quad y=0,\quad [\mathbf{PHTH}]=0\ \&\ [H^+]=0 \tag{4.60}$$

4.4.3.2*The Matrix Elements*

From these boundary conditions and the diffusion equation (4.8) it is possible to derive the matrix elements for the dissolution of calcite with phthalic acid. The matrix elements for H^+ are unchanged from those above in section 4.3.2. However those for HCO_3^- are modified and these modified matrix elements will be given below as necessary. The matrix elements for PHTH are derived below using the boundary conditions above.

(i) *The Matrix Elements in Solution.*

Writing PHTH in terms of g^{PHTH}

$$g^{PHTH} = \frac{[PHTH]}{[H^+]_{bulk}} \tag{4.61}$$

Now applying the equation (4.61) above to equation (2.73) from Chapter 2 and the matrix defined there (figure 2.10), the following general equation describing PHTH concentration in the centre of the channel can be established:

$$g_{j,k}^{PHTH} = -\lambda_j^{PHTH} g_{j-1,k+1}^{PHTH} + (2\lambda_j^{PHTH} + 1) g_{j,k+1}^{PHTH} - \lambda_j^{PHTH} g_{j+1,k+1}^{PHTH} \qquad j = 2,3..J\text{-}2 \quad (4.62)$$

This can be written as an equation of the form:

$$d_j^{PHTH} = a_j^{PHTH} g_{j-1,k+1}^{PHTH} + b_j^{PHTH} g_{j,k+1}^{PHTH} + c_j^{PHTH} g_{j+1,k+1}^{PHTH} \tag{4.63}$$

where:

$$d_j^{PHTH} = g_{j,k}^{PHTH} \qquad j=2,3,\ldots J\text{-}2 \quad (4.64)$$

$$a_j^{PHTH} = -\lambda_j^{PHTH} \qquad j=2,3,\ldots J\text{-}2 \quad (4.65)$$

$$b_j^{PHTH} = 2\lambda_j^{PHTH} + 1 \qquad j=2,3,\ldots J\text{-}2 \quad (4.66)$$

$$c_j^{PHTH} = -\lambda_j^{PHTH} \qquad j=2,3,\ldots J\text{-}2 \quad (4.67)$$

The solution matrix elements for H^+ and HCO_3^- are unaltered from those derived in section 4.3.2 earlier.

(ii) *The Matrix Elements at the Crystal Surface.*

At the calcite crystal surface the boundary condition for flux of phthalic acid at the surface of the calcite crystal can be written terms of g^{PHTH} as:

$$D_{PHTH}\frac{\partial[PHTH]}{\partial y} = D_{PHTH}\frac{(g_{1,k+1}^{PHTH} - g_{0,k+1}^{PHTH})}{\Delta y} = k_1(2-n)g_{0,k}^{PHTH} \quad (4.68)$$

which can be rearranged to give:

$$g_{0,k+1}^{PHTH} = g_{1,k+1}^{PHTH}\left(1+\frac{\Delta y\, k_1(2-n)g_{o,k}^{PHTH}}{D_{PHTH}}\right)^{-1} \quad (4.69)$$

On further rearrangment:

$$g_{0,k+1}^{PHTH} = g_{1,k+1}^{PHTH}\left(1+\frac{\Delta y\, k_1(2-n)g_{0,k}^{PHTH}}{D_{PHTH}}\right)^{-1} \quad (4.70)$$

At the crystal surface equation (4.62) becomes:

$$g_{1,k}^{PHTH} = -\lambda_1^{PHTH} g_{1,k+1}\left(1+\frac{\Delta y k_1(2-n)g_{0,k+1}^{PHTH}}{D_{PHTH}}\right) + \left(2\lambda_1^{PHTH}+1\right)g_{1,k+1}^{PHTH} - \lambda_1^{PHTH} g_{2,k+1}^{PHTH} \quad (4.71)$$

Again this can be written in the form of equation (4.20) where c_1 and d_1 are as for the centre of the channel but:

$j=1$ (4.72)

$$a_1^{PHTH} = 0$$

$$b_1^{PHTH} = \lambda_1^{PHTH} + 1 + \frac{\lambda_1^{PHTH}\Delta y\, k_1(2-n)g_{0,k+1}^{PHTH}}{D_{PHTH}}$$

H^+ has the same matrix elements as in section 4.3.3.4.. The flux equation for HCO_3^- is modified as the reaction of both 'free' H^+ and H^+ which is bound to the acid, when it reacts at the calcite surface generates HCO_3^-, so:

$$D_{HCO_3^-}\frac{\partial[HCO_3^-]}{\partial y} = D_{HCO_3^-}\frac{(g^{B}_{1,k+1}g^{B}_{0,k+1})}{\Delta y} = -k_1\left(g^{H}_{0,k} + (2-n)g^{PHTH}_{0,k}\right) \quad (4.73)$$

which can be rearranged to give:

$$g^{B}_{0,k+1} = g^{B}_{1,k+1}\left(1-\frac{\Delta y\, k_1\left(g^{H}_{0,k} + (2-n)g^{PHTH}_{0,k}\right)}{D_{HCO_3^-}}\right)^{-1} \quad (4.74)$$

At the crystal surface equation (4.74) is modified, c_1 and d_1 are as for the centre of the channel but:

$$j=1 \quad (4.75)$$

$$a^{B}_1 = 0$$

$$b^{B}_1 = \lambda^{B}_1 + 1 - \frac{\lambda^{B}_1 \Delta y\left(g^{H}_{0,k} + (2-n)g^{PHTH}_{0,k+1}\right)}{D_{HCO_3^-}}$$

(iii) *The Matrix Elements at the Far Wall of the Channel.*

At the far wall to the reactive surface (electrode or calcite crystal) the flux of any species is zero. This modifies some of the matrix elements. The expressions for the terms a_j and d_j are not altered from the terms for the centre of the channel given above,

but the terms b_J and c_J are modified to:

$$b_J^R = \lambda_J^R + 1 \qquad (4.76)$$

$$c_J^R = 0$$

where R is either PHTH, H^+ or HCO_3^-.

(iv) *The Matrix Elements at the Electrode Surface.*

Over the electrode for both species HCO_3^- and H^+ the matrix elements are as in section 4.3.2.5. However H^+ transported to the detector electrode by PHTH is also consumed when the electrode is held at a potential for the transport controlled reduction of H^+. As a result in the case of PHTH the expressions for c_1 and d_1 are the same as in the centre of the channel, but:

$$a_1^{PHTH} = 0 \qquad (4.77)$$

$$b_1^{PHTH} = 2\lambda_1^{PHTH} + 1$$

4.4.3.3*The Matrix elements for Homo-phthalic Acid.*

Analogous matrix elements can be derived for homo-phthalic acid. These matrix elements are valid for homo-phthalic acid as the pH range of the experiments involving homo-phthalic acid range from 2.8 to 3.5, which is well below the pH required for the dissociation of the acid.

4.4.4 Results

From the proceeding theory it is possible to perform channel flow cell experiments with solutions of various concentrations of phthalic acid or homo-phthalic acid, and to measure the amount of H^+ which reacts at the downstream detector electrode. In addition it is possible to model the expected detector response with flow rate. Initially it can be attempted to fit the experimental data with the rate constant as determined with mineral acid i.e. 0.043/cm s^{-1}. If this does not fit then the results need to be modelled instead in terms of inhibition.

So experiments were performed as described earlier in section 4.4.2. The results for both phthalic and homo-phthalic acid are shown tables 4.1 and 4.2. Figures 4.15 and 4.16 show typical results for both acids, along with the theoretically predicted behaviour

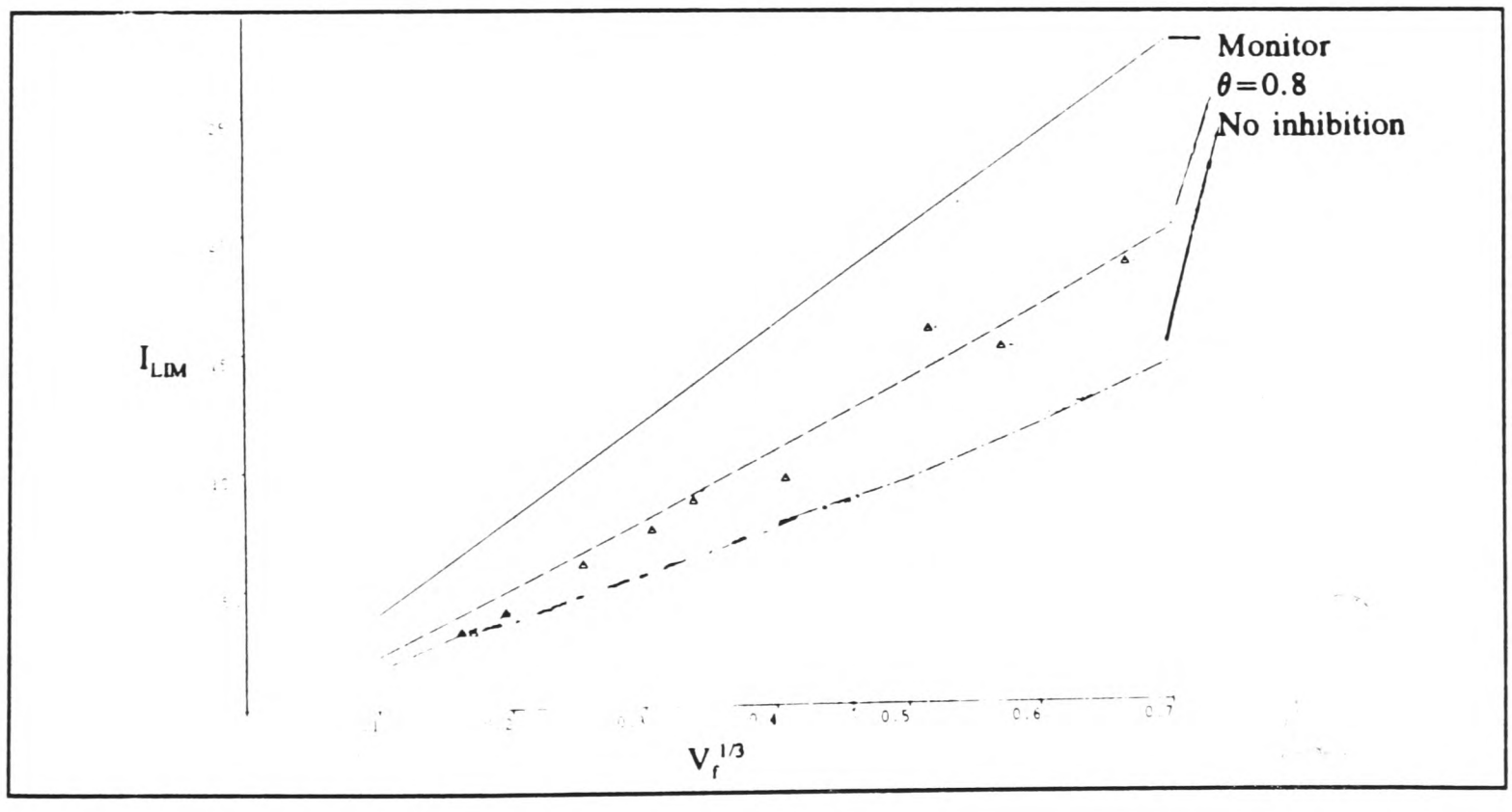

Figure 4.15 The experimental and predicted behaviour (for both monitor and detector electrode) for phthalic acid 5.92 × 10^{-3}mol dm^{-3}, with initial pH 2.56, x_{el}=0.183 cm, x_{crys}=0.766 cm, w=0.123 cm and 2h=0.089 cm.

in the absence of inhibition. These theoretical predictions are calculated using the theory derived above treating phthalic or homo-phthalic acid purely as a source of extra protons at the surface, and setting the surface coverage of the acid (either phthalic acid or homo-phthalic acid), $\theta = 0$.

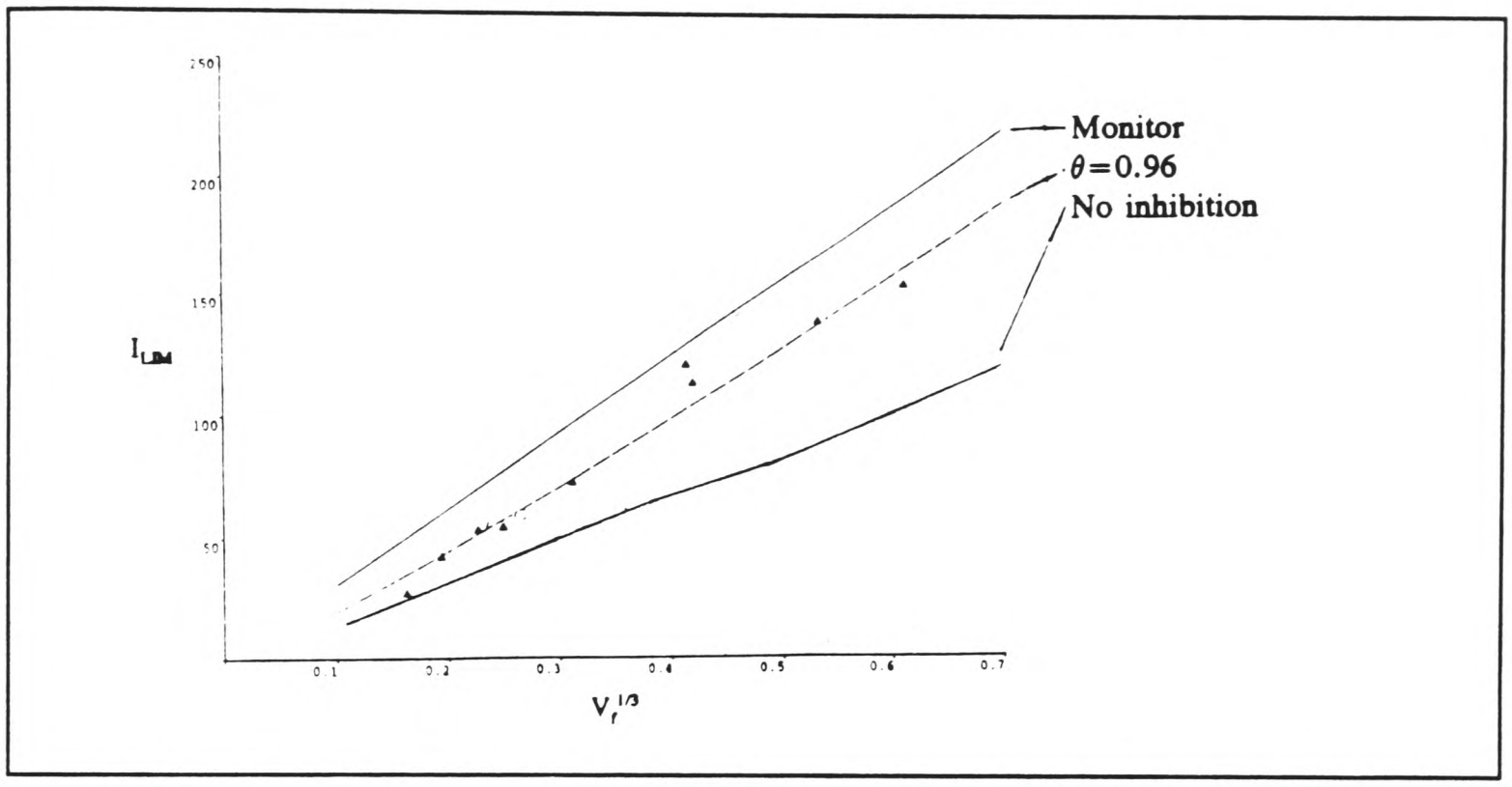

Figure 4.16 The experimental and predicted behaviour (for both monitor and detector electrode) for homo-phthalic acid 1.10 × 10^{-2} mol dm^{-3}, with initial pH 2.53, x_{el}=0.189 cm, x_{crys}=0.694 cm, w=0.243 cm and 2h=0.098 cm.

The monitor electrode in these experiments was merely the detector electrode with the channel flow cell turned around. So it measures the concentration of H^+ before the reaction with calcite. As can be seen the experimental results fall between those predicted for the monitor electrode, and those when all of the H^+ reacts with no inhibition occurring. Thus it can be seen that the acids are inhibiting the dissolution of calcite, although not totally shutting off the dissolution reaction.

Any inhibition can be modelled in terms of an effective rate constant (as in section 4.4.1). This rate constant k_1' was linked to the rate constant k_1 for the reaction

in the absence of inhibitor, by the surface coverage θ of phthalic or homo-phthalic acid respectively as follows:

$$k_1' = k_1(1-\theta) \tag{4.78}$$

where (1-θ) is the number of free surface sites available for dissolution. Using this equation the value of θ for a particular experiment can be derived from the rate constant k' used in the numerical modelling to fit the data. From this it is possible to modify the dissolution equation further as follows:

$$-\frac{\partial[HCO_3^-]}{\partial y} = k_1'([H^+]+(m-n)[PHTH]) \tag{4.79}$$

If the adsorption is modelled in terms of total phthalic acid, and it is assumed that adsorption is Langmuirian then:

$$\theta = \frac{K_L[PHTH]}{1+K_L[PHTH]} \tag{4.80}$$

In order to test that the behaviour is indeed Langmuirian equation (4.80) can be rearranged to:

$$\frac{1}{\theta} = 1+\frac{1}{K_L[PHTH]} \tag{4.81}$$

Therefore by plotting $1/\theta$ against 1/[PHTH], and the intercept should be 1, and the gradient will equal $1/K_L$ if this assumption is valid.

The plots of $1/\theta$ against 1/[R], where R represents either PHTH or HOMO respectively, are shown in figures 4.17 and 4.18 below. The values of θ are derived by

altering the value of the effective rate constant k' until the best fit for the experimental points is obtained by the numerical modelling using the BI method, since $k_1' = k_1 \times \theta$ and k is known from experiments with mineral acid in the absence of inhibitor, then θ can be deduced.

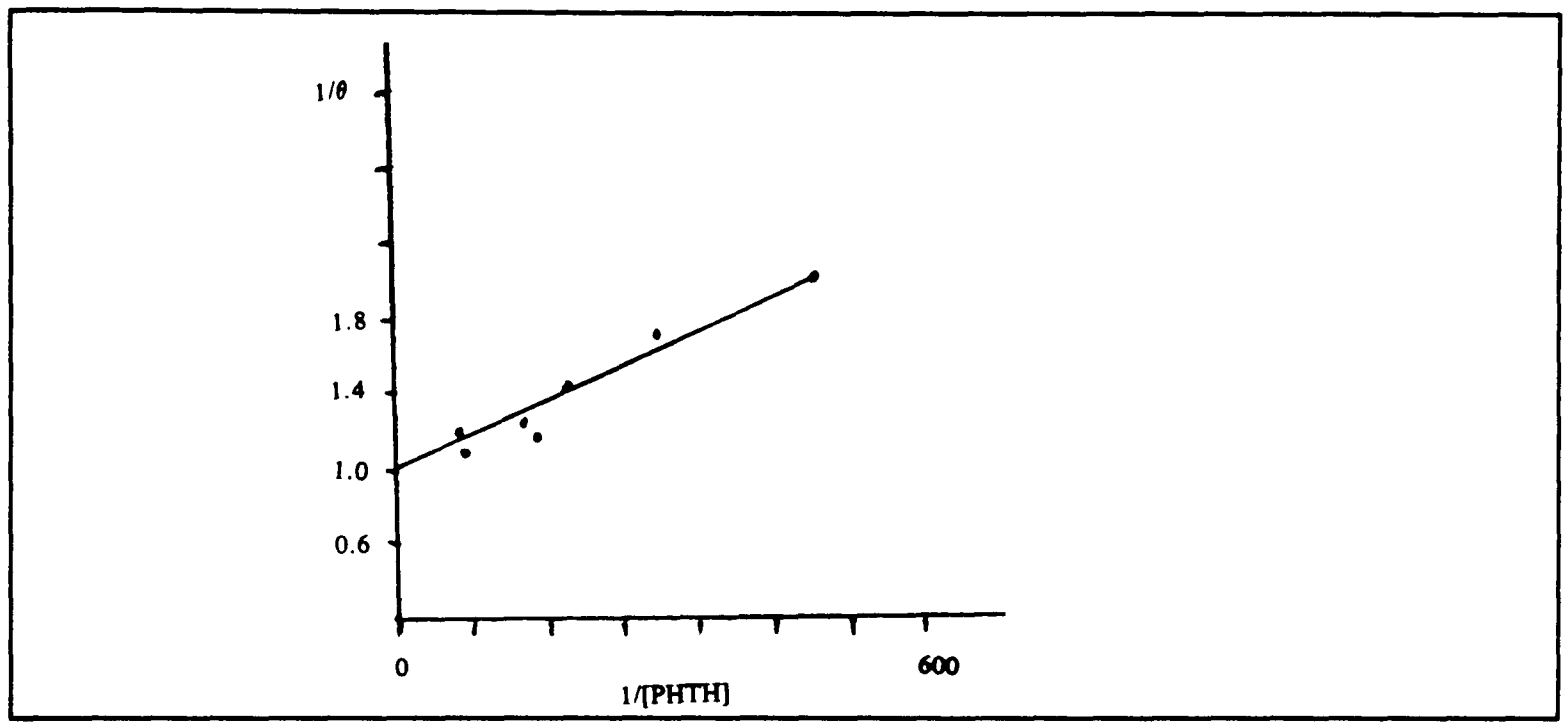

Figure 4.17: The plot of 1/θ against 1/[Phth^{2-}] for phthalic acid.

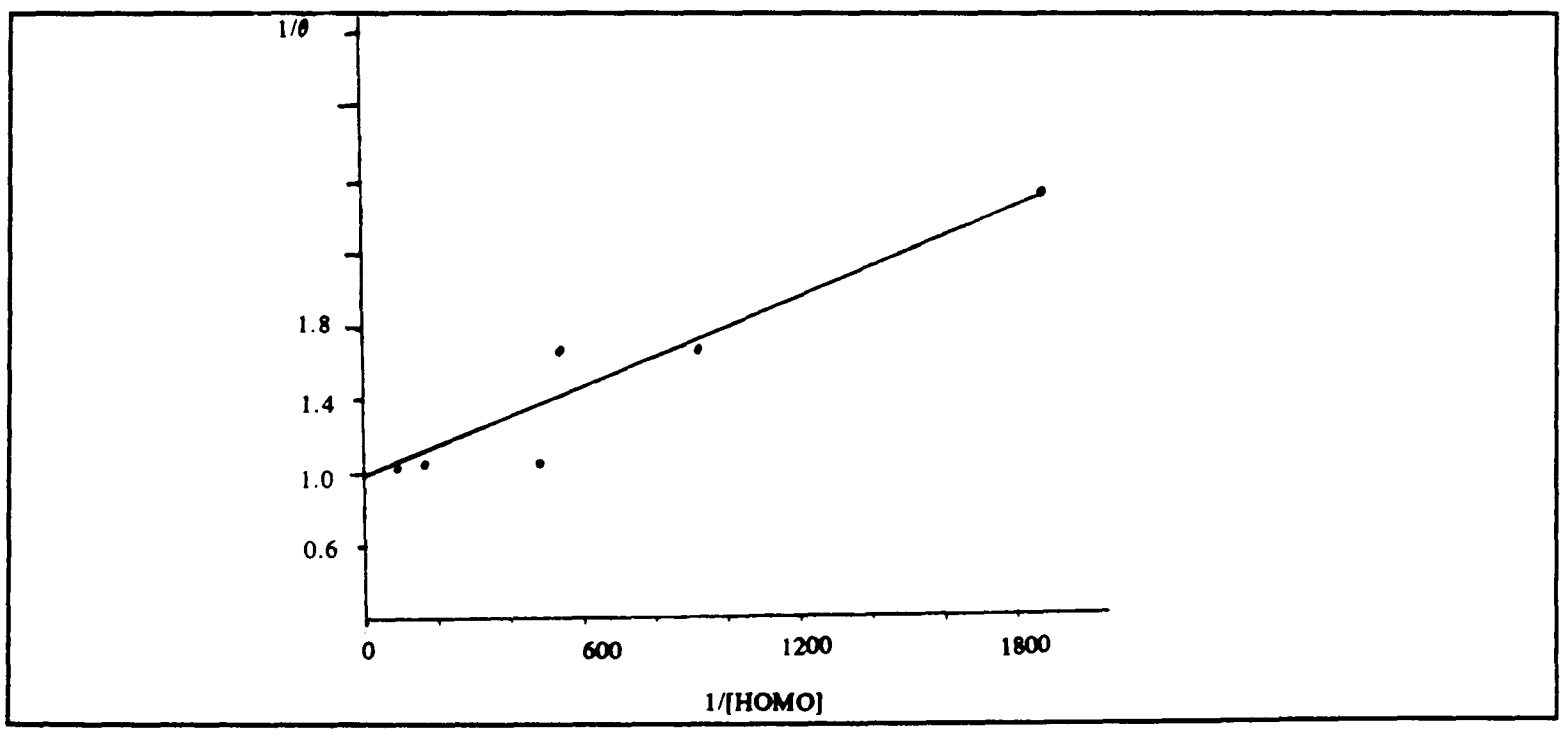

Figure 4.18: The plot of 1/θ against 1/[Homo^{2-}] for homo-phthalic acid.

As can be seen these plots are linear thus showing that the adsorption is Langmuirian.

The full results are summarised below in tables 4.1 and 4.2.

Table 4.1 The Results for Phthalic Acid

[PHTH] $\times 10^{-3}$/ mol dm^{-3}	pH	θ	$[PHTH]^{-1}$ / dm^3mol^{-1}	θ^{-1}	(2-n)
1.79 (±0.01)	3.01	0.50 (± 0.10)	559	2.0	1.7
4.41 (±0.01)	2.67	0.70 (± 0.05)	227	1.43	1.6
3.28 (±0.01)	2.86	0.60 (± 0.10)	305	1.7	1.6
5.38 (±0.01)	3.99	0.85 (± 0.02)	186	1.18	1.6
5.92 (±0.01)	2.56	0.80 (± 0.03)	169	1.25	1.6
12.0 (±0.1)	2.44	0.85 (± 0.02)	83.3	1.18	1.7
11.2 (±0.01)	2.48	0.90 (± 0.02)	89.4	1.11	1.7

Table 4.2 The Results for Homo-Phthalic Acid

[HOMO] $\times 10^{-3}$ / mol dm^{-3}	pH	θ	$[HOMO]^{-1}$ / dm^3 mol^{-1}	θ^{-1}	(2-n)
1.85 (±0.01)	3.23	0.60 (± 0.10)	540	1.67	1.7
1.08 (±0.01)	3.43	0.60 (± 0.10)	925	1.67	1.7
2.01 (±0.01)	2.82	0.85 (± 0.02)	498	1.18	1.7
11.0 (±0.1)	2.53	0.96 (± 0.01)	90.8	1.04	1.9
5.43 (±0.01)	2.99	0.82 (± 0.02)	184	1.22	1.8
0.562 (±0.001)	3.61	0.40 (± 0.10)	1780	2.5	1.6

From figures 4.17 and 4.18 the K_L values for the adsorption of these inhibitors on calcite can be determined (phthalic acid $K_L = 604 \pm 20 dm^3\ mol^{-1}$ and homo-phthalic acid $K_L = 1250 \pm 50 dm^3\ mol^{-1}$).

4.4.5 Discussion

As discussed in section 4.3, the previous work on maleic, fumaric and various tartaric acids concluded that inhibition was caused by the dianion, and the relative inhibition order was related to the inter-carboxylic distance in the dianion. It is of interest to compare the relative strength of inhibition of the dianions of these acids with those of phthalic and homo-phthalic acids. Note however that an important difference is that here the modelling was done in terms of the total acid concentration rather than the concentration of the dianion. Consequently the values for phthalic and homo-phthalic acid are not directly comparable, but do provide maximum values of what the values of the Langmuirian equilibrium constant would be for the dianion. The comparison of the K_L values for homo-phthalic and phthalic acid with those from literature is made in Table 4.3.

Table 4.3 Comparing K_L for Various Inhibitors

Acid	K_L / $dm^3\ mol^{-1}$
maleic acid [144]	4800
meso-tartaric acid [145]	1400
homo-phthalic acid (total)	1250
phthalic acid (total)	604

Alternatively it is possible to compare the acids in terms of the value of the effective rate constants for the dissolution of calcite at low pH would be for a concentration of acid of 2×10^{-2} mol dm^{-3}. This is given in Table 4.4.

Table 4.4 Comparing the Effective Rate Constants for the Dissolution of Calcite in the Presence of a Variety Small Molecules

Acid	k_1' / cm s^{-1}
maleic acid [144]	0.0004
homo-phthalic acid	0.0017
meso-tartaric acid [145]	0.0023
phthalic acid	0.0030
d & *l* tartaric acid [145]	0.011
fumaric acid [144]	0.025

Inspection of tables 4.3 and 4.4 give an overall order of:

maleic acid $>>$ homo-phthalic acid $\approx$ *meso*-tartaric acid $>$ phthalic acid $>$ *d* & *l* tartaric acid $>>$ fumaric acid

If it is the dianion which adsorbs for phthalic and homo-phthalic acid then as is extremely likely, then this relative order may be explained in terms of the inter-carboxylic acid distance. For phthalic acid this value is found from its disodium salts to be 3.74 Å

(calculated from the x-ray crystallography data [151]). For homo-phthalic the inter-carboxylic acid distance is not rigid, but from crystallographic data can be estimated to be in the order of 5.10 Å in its preferred conformer [152]. So comparing with the relevant inter-Ca^{2+} distances of 4.04 Å and 4.99 Å, it is obvious that the size of the phthalic acid dianion is smaller than the shortest distance compatible with the calcite [100] surface. This is possibly part of the reason why phthalic acid is not such a strong inhibitor as maleic acid or even *meso*-tartaric acid. Also there will be some steric hinderance to adsorption by the large benzene ring.

Homo-phthalic acid seems to have an inter-carboxylic acid distance closer to that of the larger Ca^{2+} - Ca^{2+} separation. If adsorption occurs at the shortest Ca^{2+}- Ca^{2+} distance then the energy of the slight conformational change required must be similar to that for *meso*-tartaric acid given their very similar inhibitory powers.

4.5 A Polymeric Inhibitor - Polyacrylic Acid

4.5.1 Introduction

Polyacrylic acid is one of the two major commercial scale inhibitors [53]. The other is polymaleic acid. Polymaleic acid (molecular weight 1082) has been studied previously at low pH by Unwin and Compton [53]. The latter used the channel flow method, and observed that the dissolution reaction of calcite in the presence of polymaleic acid initially had a rate constant which was similar to that caused by mineral acid at the same pH. However after approximately 30 minutes or more this reaction rate decreased and it was concluded that time was needed for inhibition to occur. This was attributed to the polymer requiring to take a specific conformation in order to adsorb

and so block dissolution. The slow rate of this conformational change is related to the highly sterically hindered structure of polymaleic acid [53]. This can be seen by comparing the monomer structure of polymaleic acid with that of polyacrylic acid as show in figure 4.19 below.

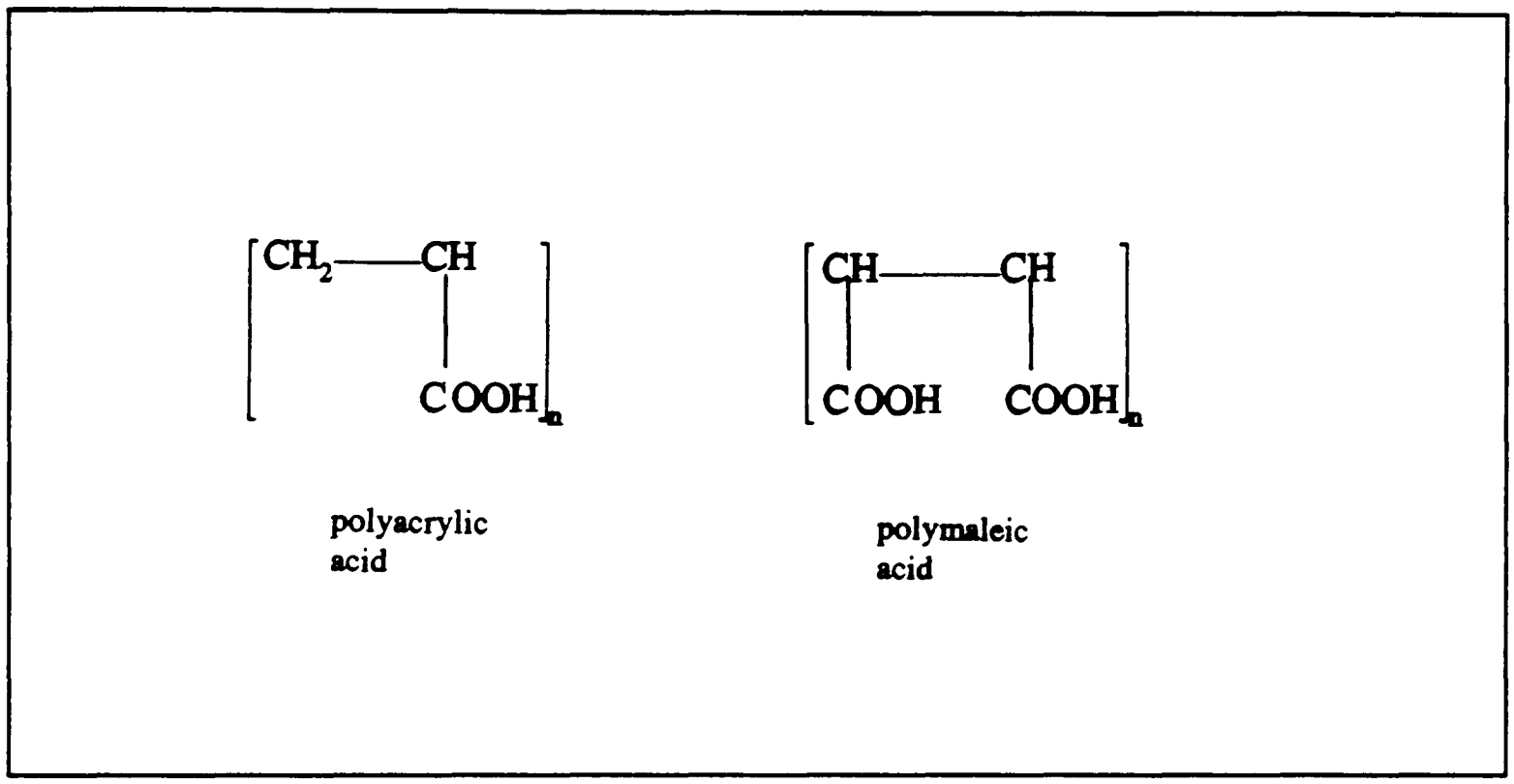

Figure 4.19: The structures of the monomers of polyacrylic and polymaleic acids.

By studying polyacrylic acid, not only is the other major industrial inhibitor examined but also this hypothesis can be tested to some extent. As can be seen below in figure 4.19 polyacrylic acid is considerably less sterically hindered than polymaleic acid. It is then possible that it could adopt a conformation suitable to adsorb on the surface much more rapidly and so reach full inhibition faster. As the molecular weights are not too dissimilar, with the lowest molecular weight polyacrylic acid available being 2000 as compared to 1082 for polymaleic acid, if there are significant differences this could be attributed to true structural differences rather than just molecular weight effects.

4.5.2 Experimental Approach to the dissolution of Calcite in the Presence of Polyacrylic Acid

4.5.2.1 *The Molecular Weight Distributions of the Polymers Studied.*

In this study three different molecular weight polymers were used. The molecular weight distributions are shown below (figures 4.20 to 4.22). The 2000 M.W. polymer was analyzed by Aldrich [154] and the other two by F.M.C. [153]. These weight distributions were obtained in two different ways. For the 2000 M.W. polymer, gel permeation chromatography was used. However for the other two samples, HPLC (High Pressure Liquid Chromatography) was used. In all cases the number of molecules (represented by arbitrary units) is shown against molecular weight in the figures (4.20 to 4.22).

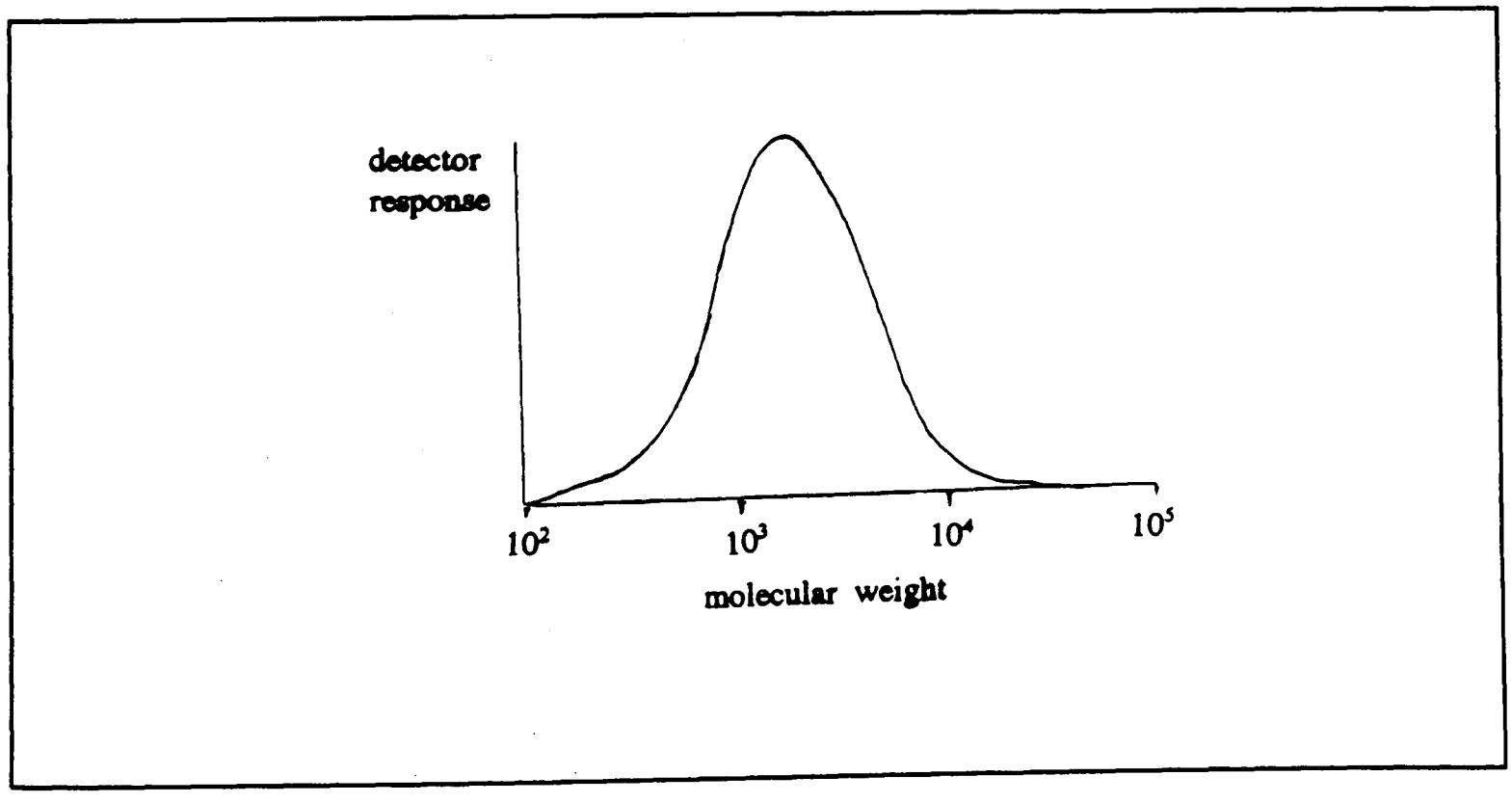

Figure 4.20: The molecular weight distribution for polyacrylic acid M.W. 2000.

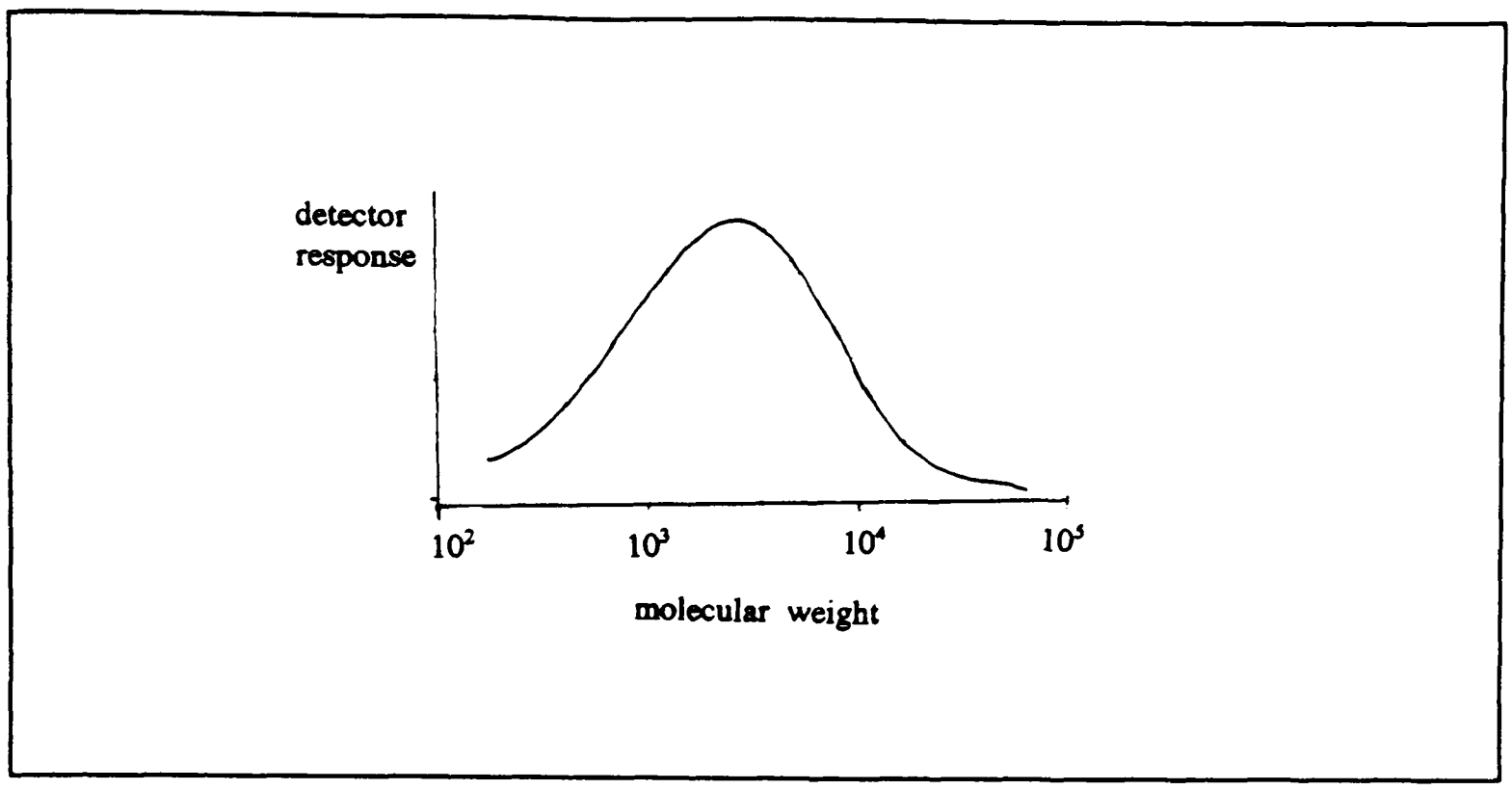

Figure 4.21: The molecular weight distribution for polyacrylic acid M.W. 4800.

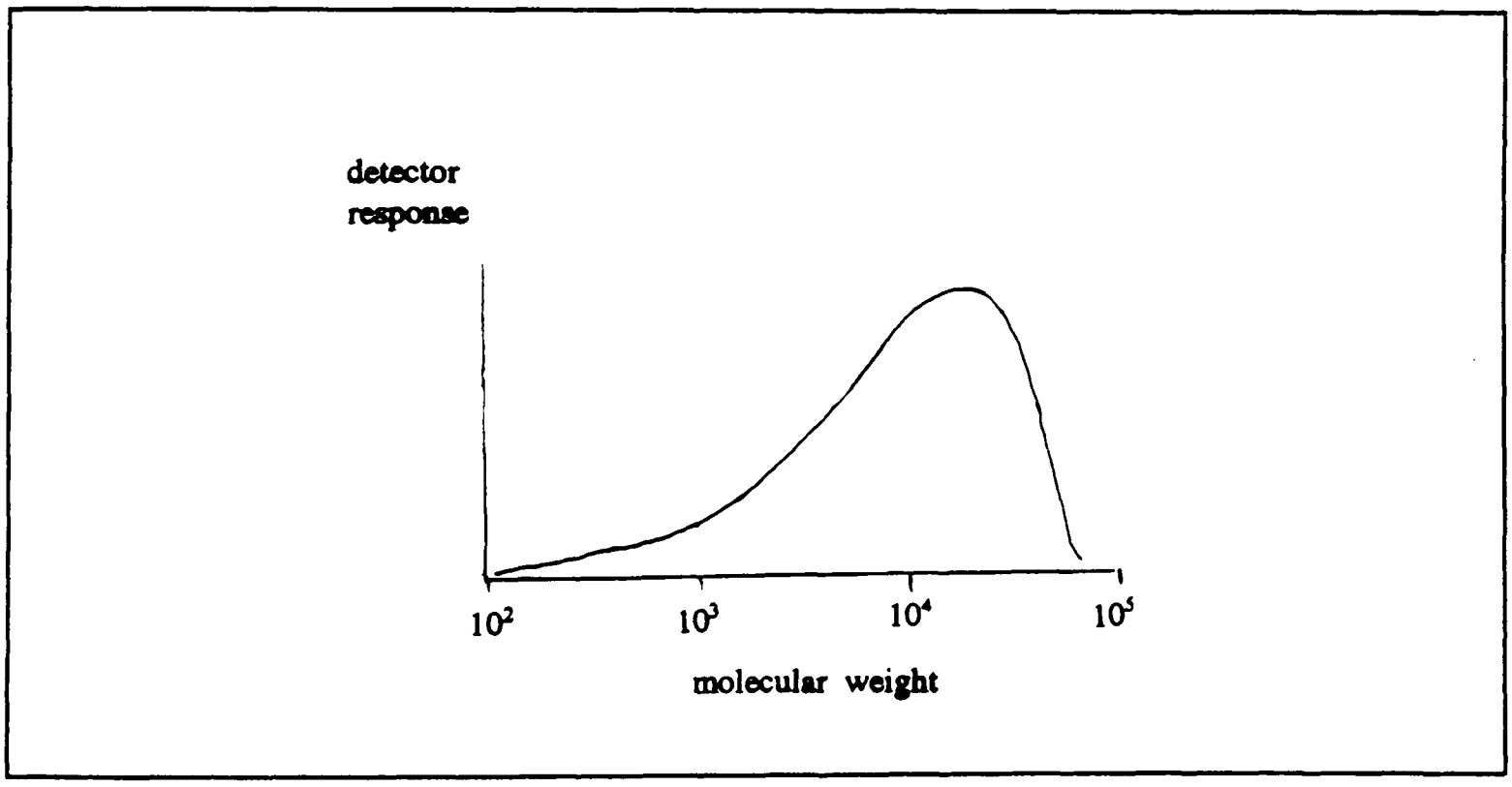

Figure 4.22: The molecular weight distribution for polyacrylic acid M.W. 14800.

The polymer of 2000 M.W. is in the form of the free acid, but the other two molecular weights were provided in the form of solutions of the acid neutralized with NaOH. This means that for the higher two molecular weights the solutions have to be

acidified before investigating their effect at low pH. Note that the molecular weight distributions refer to the neutralized polymer rather than the free acid form.

4.5.2.2 *Preliminary Rotating Disc Experiments of Proton Reduction in the Presence of Polyacrylic acid.*

As with phthalic and homo-phthalic acid it was necessary to determine if all the protons reaching a potentiostat detector electrode are reduced. That is both 'free' *and* those transported to the electrode by the polymer are measured. In order to do this rotating disc experiments were performed. Examination of the linearity of the plot of limiting current (I_{LIM}) against $\omega^{1/2}$ (ω is rotation speed), after the component of the limiting current due to 'free' H^+ as derived from pH, can establish whether the dissociation reactions are rapid enough to enable them to be considered insignificant in the modelling.

Once the contribution to limiting current due to 'free' H^+ is subtracted then, for polyacrylic acid (PAA) the Levich equation is modified to:

$$I_{LIM} = 1.554 F \omega^{1/2} \nu^{-1/6} A D_{PAA}^{2/3} (m-n)[PAA^{n-}] \tag{4.82}$$

where m is the average total number of protons on the fully polyacrylic acid molecule (ie. 27.6 on average for M.W. 2000), n is the number of protons per molecule which are 'free' in solution, as obtained from the solution pH. The value of m is calculated by dividing the total average molecular weight by the weight of a monomer unit.

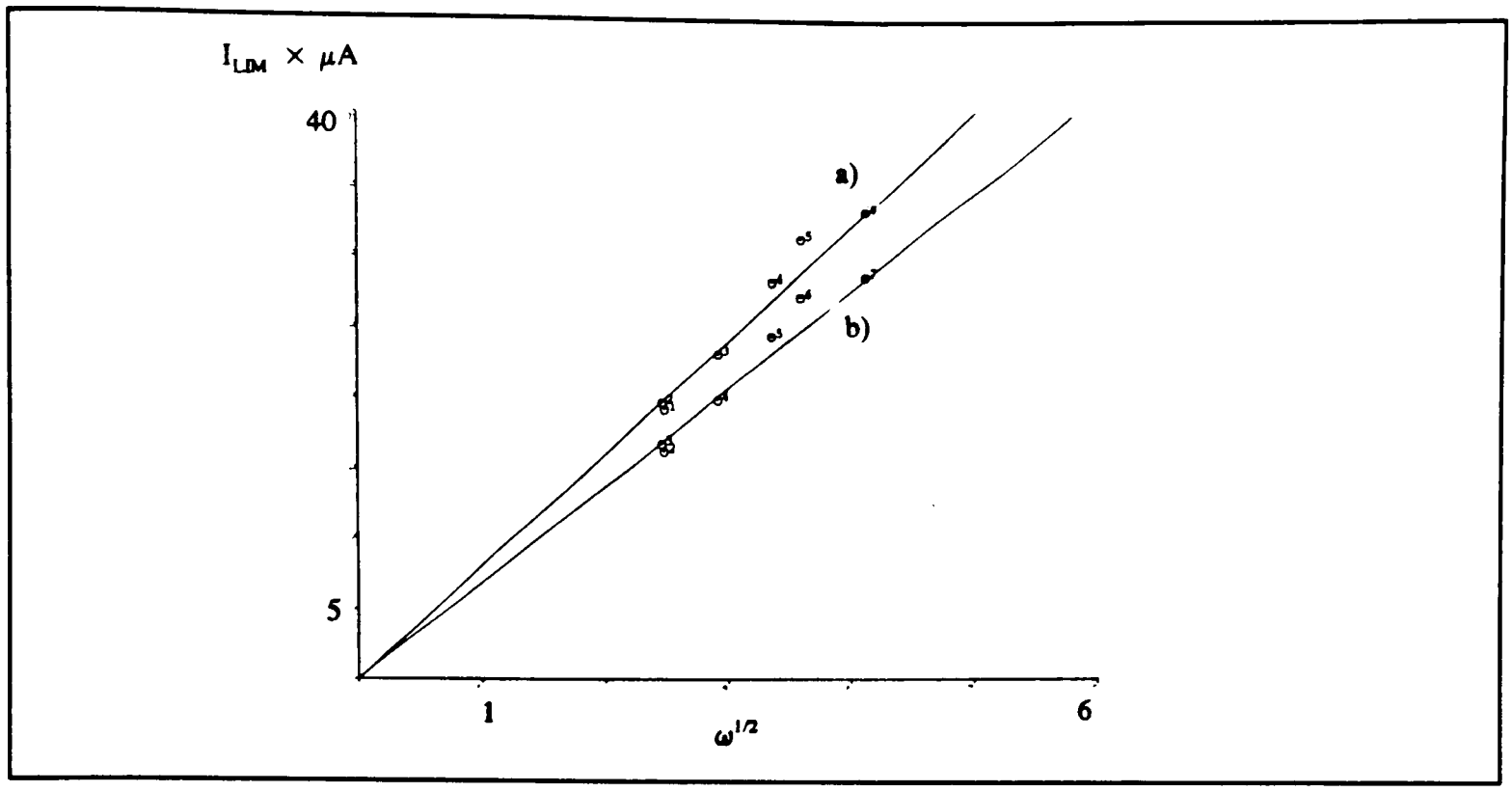

Figure 4.23: A Levich plot of I_{Lim} against $(\omega)^{1/2}$ for polyacrylic acid (M.W. 2000) of concentration 1.92× 10^{-5} mol dm^{-3} and initial solution pH 4.16. Where (a) The total I_{Lim}, and (b) shows the I_{Lim} with the contribution due to 'free' H^+ subtracted.

As can be seen from figure 4.23 above the Levich plot is linear and thus justifies the assumption that all the protons are equally reduced at the electrode, with the necessary dissociation reactions being rapid enough to be ignored.

4.5.2.3*Investigation of Polyacrylic Acid by Potentiometric Titration.*

It was also deemed necessary to determine whether all of the protons on the acid groups on the polymer chain (*m*) are *titratable*, that is that they are available for reaction at the electrode and/or calcite surfaces. This was ascertained by potentiometric titration of solution of the acid. An example of the results of such a titration is shown in figure 4.24 below.

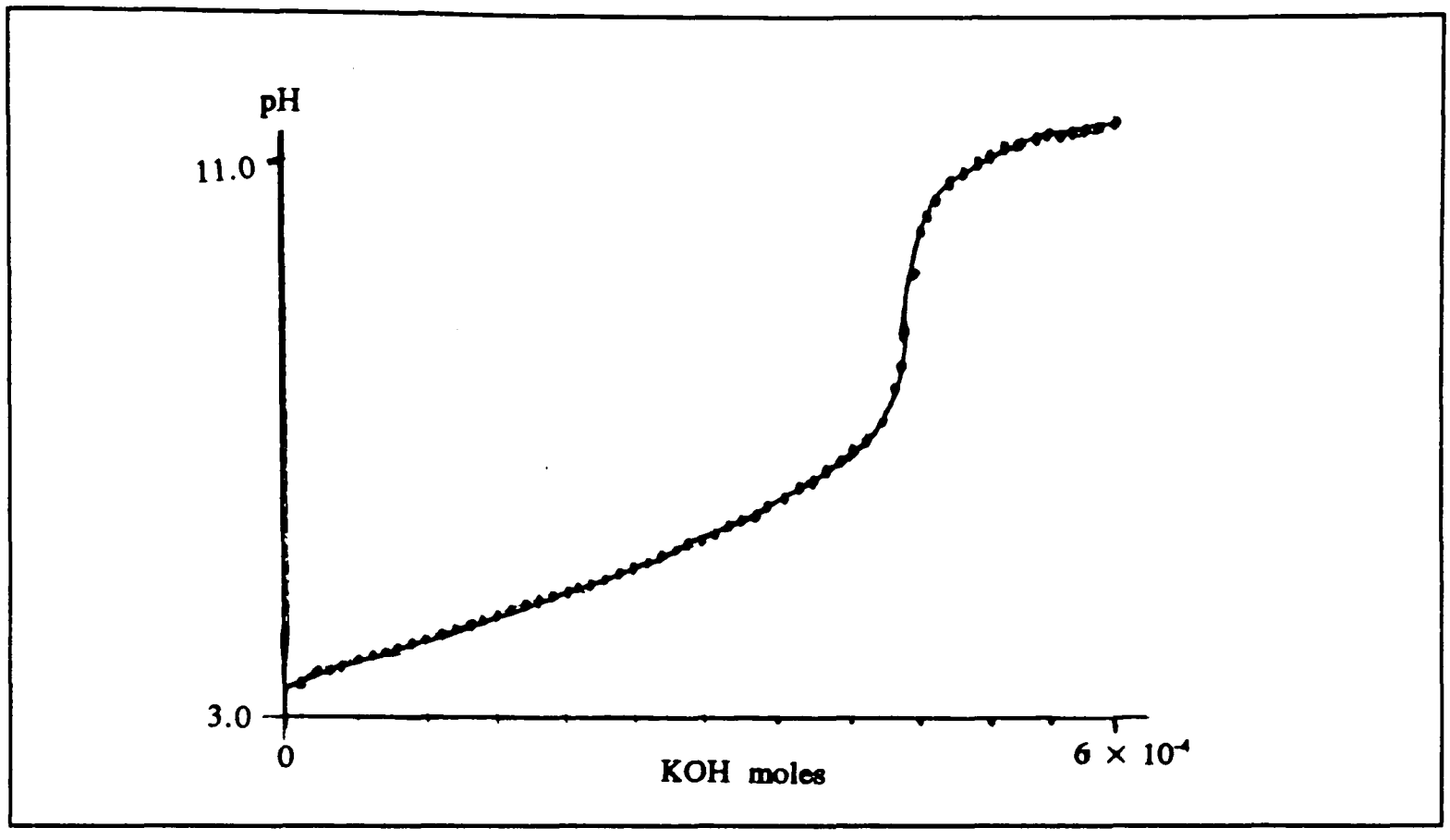

Figure 4.24: The potentiometric titration of 1.57 × 10^{-4} mol dm^{-3} polyacrylic acid (M.W. 2000) with 1.01 × 10^{-3} mol dm^{-3} KOH.

As can be seen for the potentiometric titration of polyacrylic acid there is only one inflection point. This is normal for polymeric acids since, as the number of acid groups on one molecule gets bigger so these acid groups will increasingly interact with each other [155]. This curve also shows the high buffering ability of polyacrylic acid in the range 4 to 6.4, as established by Gregor *et al.* [156]. The curve does show that all the H^+ is titratable as calculated from the end point.

In contrast polymaleic acid, shows one end point and also has all its protons titratable, but does not have a buffered region.

4.5.2.4 *Calculating the Effective diffusion Coefficient for the Transport of Protons by Polyacrylic Acid.*

It has been shown from these potentiometric titrations described above that all of the H^+ is titratable. Also the rotating disc experiments showed that all the protons, both 'free' and bound, react at the electrode, when the electrode is held at a potential consistent with the total reduction of H^+. Hence it is possible to use the modified Levich equation (4.82) and the results of the rotating disc experiments, to calculate the effective diffusion coefficient for the transport of protons to the surface by polyacrylic acid (PAA). This was calculated to be $D_{PAA} = 1.1\ (\pm\ 0.1) \times 10^{-6}$ cm s^{-1} for 2000M.W.. This value is comparable with literature values of 1.77×10^{-6} cm s^{-1} for 5000 M.W. polyacrylic acid and 1.16×10^{-6} cm s^{-1} for 160000 M.W. polyacrylic acid [157]. From this experimental value of the diffusion coefficient, $D_{PAA} = 1.1 \times 10^{-6}$ cm s^{-1}, it is now possible to model the transport of polyacrylic acid in a channel flow cell and hence study the effect of its presence on the dissolution of calcite.

4.5.3 The Theory for the dissolution of Calcite in the Presence of Polyacrylic Acid

From the previous two sections it has been shown that all of the protons on polyacrylic acid are titratable and can be detected at a detector electrode held at a potential such that all H^+ ions reaching it will be reduced. Also it can be calculated that polyacrylic acid (PAA) of M.W. 2000 has an average of 27.6 protons per molecule. As each of these protons can dissociate near the calcite surface and react to cause

dissolution, this can be considered as:

$$PAA^{n-} \rightleftharpoons PAA^{m-} + (m-n)H^{+} \tag{4.83}$$

$$(m-n)H^{+} + CaCO_3 \longrightarrow (m-n)Ca^{2+} + (m-n)HCO_3^{-}$$

where m is the average number of protons on the polymer chain, n is the number of 'free' protons per molecule of polyacrylic acid, and k_1' is the effective heterogeneous rate constant. Or overall:

$$PAA^{n-} + CaCO_3 \xrightarrow{k_1'} PAA^{m-} + (m-n)Ca^{2+} + (m-n)HCO_3 \tag{4.85}$$

As the protonation/deprotonation reactions are at equilibrium the convective-diffusion equation for polyacrylic acid is:

$$0 = D_{PAA}\frac{\partial^2[PAA^{n-}]}{\partial y^2} - v_0\left(1-\frac{(y-h)^2}{h^2}\right)\frac{\partial[PAA^{n-}]}{\partial x} \tag{4.86}$$

Again channel flow cell experiments using amperometric detection was used to monitor the dissolution. The detector electrode monitored both 'free' H^+ and protons transported to the detector by polyacrylic acid. Under these conditions the boundary conditions for polyacrylic acid are similar to those for phthalic acid as outlined in section 4.4 above. Except that the term $(m\text{-}n)$ replaces $(2\text{-}n)$, and D_{PAA} replaces D_{PHTH}. the matrix elements formulated for the channel flow cell experiments are exactly as those derived for phthalic acid above.

4.5.4 Results

First experiments were carried out on solutions of polyacrylic acid (M.W. 2000) of varying concentrations (2×10^{-5} to 2×10^{-4}mol dm^{-3}). It was seen that, unlike the polymaleic acid case investigated by Unwin and Compton [2], there was no long initial period necessary for inhibition. The time scale for inhibition to commence was on approximately the same time scale as that needed to perform a measurement: at the most one or two minutes. The limiting currents measured for the same flow rates varied no more than experimental error with time ($\pm 3\%$), and showed no systematic trends. This lack of a kinetic threshold to inhibition was attributed to the greater flexibility of the polyacrylic acid chain as compared to the fairly rigid and more sterically hindered polymaleic acid chain[2]. The former would be more readily able to adopt a configuration necessary for adsorption.

Initially it was postulated that, as for molecular inhibitors, the inhibition occurred via Langmuirian adsorption of the polymer on the calcite surface. This assumption was tested by means of fitting the experimental detector current/flow rate data for these experiments (see table 4.4) with an effective rate constant. This effective rate constant k_1' is related to the 'true' rate constant k_1 by the surface coverage, θ, where:

$$k_1' = k_1(1-\theta) \tag{4.87}$$

θ will vary with the concentration of inhibitor, and the θ value for each concentration is obtained from the effective rate constant (see figures 4.25 and 4.26) which best fits the experimental data. The results of this initial fitting is given in table 4.5 below.

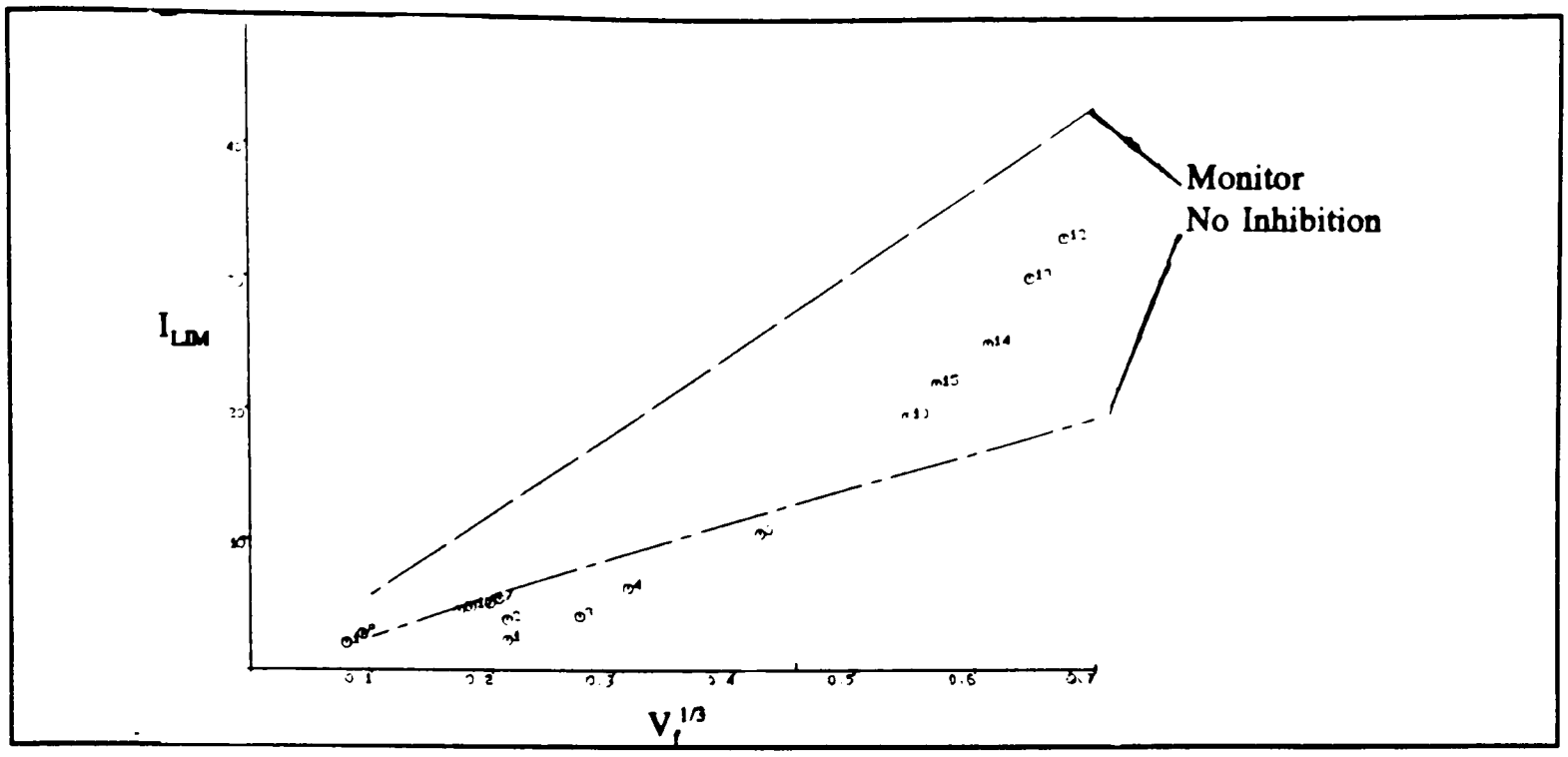

Figure 4.25: An example of the BI fit for polyacrylic acid with no added calcium, (9.2 × 10^{-5} mol dm^{-3} PAA) showing the increased inhibition at high flow rates. In this case no adequate fit could be obtained.

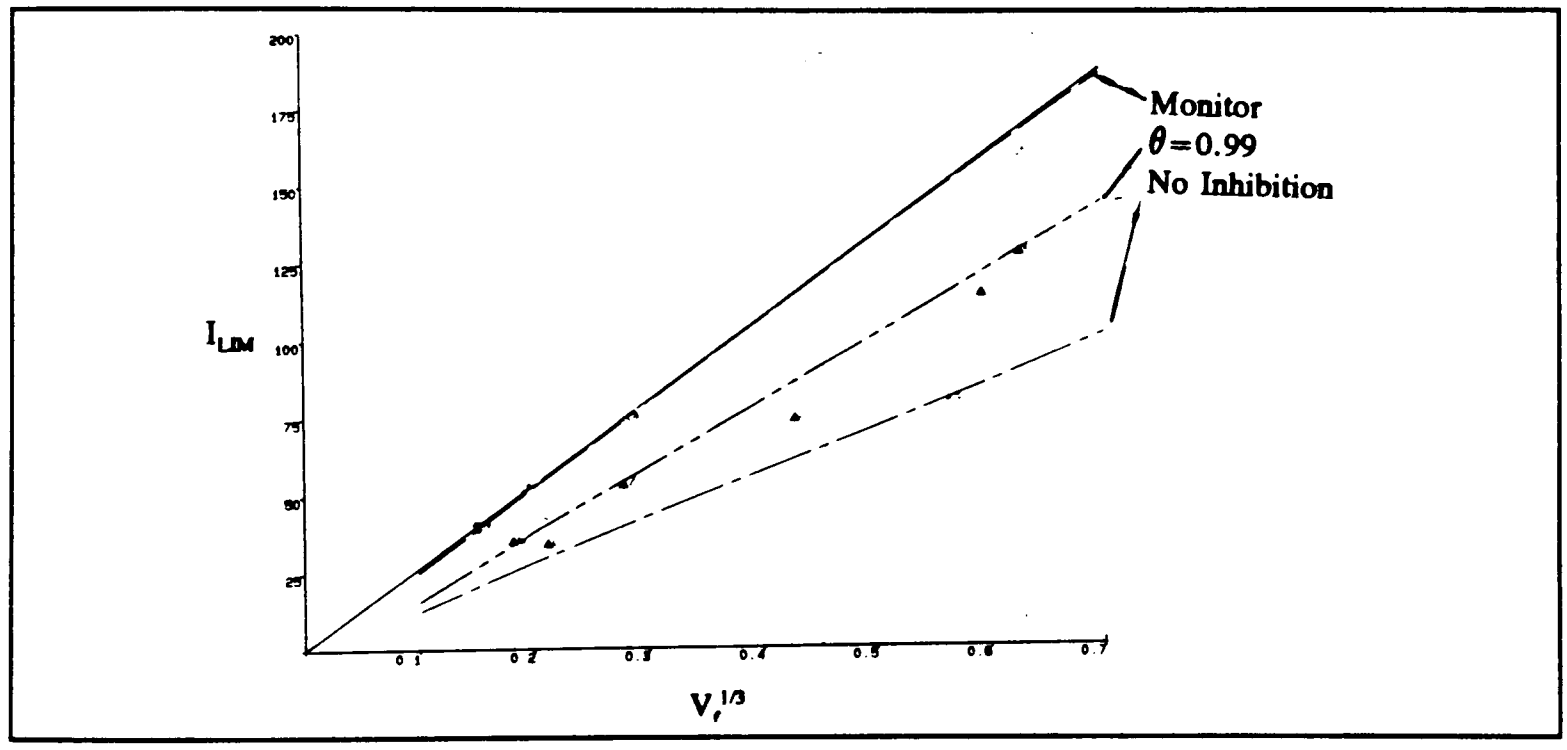

Figure 4.26: An example of a BI fit at higher concentration of polyacrylic acid (0.505 × 10^{-3} mol dm^{-3}). In this case θ = 0.99, which fits the whole flow rate range.

The assumption that simple Langmuirian adsorption can explain the inhibition is obviously not justified since for low concentrations, there is considerable curvature in the experimental data, with no inhibition present at low flow rates (for example see figure 4.25). For low concentrations this is the value of θ which is shown in the table is that which best fits the experimental data at high flow rates.

Table 4.4 Values for θ for initial Experiments on PAA (M.W.2000)

[PAA] / 10^{-3} mol dm^{-3}	pH (bulk)	θ	*m-n*
3.21 (±0.01)	2.84	0.99 (± 0.01)	26.2
1.496 (±0.005)	3.09	0.99 (± 0.01)	26.2
0.800 (±0.002)	3.18	0.99 (± 0.01)	25.9
0.703 (±0.002)	3.22	0.98 (± 0.01)	25.8
0.505 (±0.002)	3.26	0.99 (± 0.01)	25.6
0.404 (±0.002)	3.34	0.99 (± 0.01)	25.6
0.178 (±0.001)	3.52	0.90 (± 0.02)*	25.0
0.163 (±0.001)	3.36	0.60 (± 0.10)*	24.9
0.092 (±0.001)	3.36	0.00	25.6

NOTE: 1) The values of θ marked with a * corresponds to the cases where the best fit for high flow rate has been used to calculate the value of θ (see text).

2) The value of *m-n* is calculated from the number of 'free' protons in solution from the pH, by subtracting this value from the total number of protons available on the polyacrylic acid (ie. 27.6 × [PAA]), and then dividing the number by the concentration of polyacrylic acid [PAA]. Thus *m-n* is the number of protons still bound to each polymer chain before any reaction of the polymer with $CaCO_3$.

The full set of results are summarised in Table 4.5. As can be seen from the table in most cases there is full inhibition. However between [PAA]=0.4 mol cm^{-3} and [PAA]=0.19 mol cm^{-3} there is no inhibition at all at low flow rates.

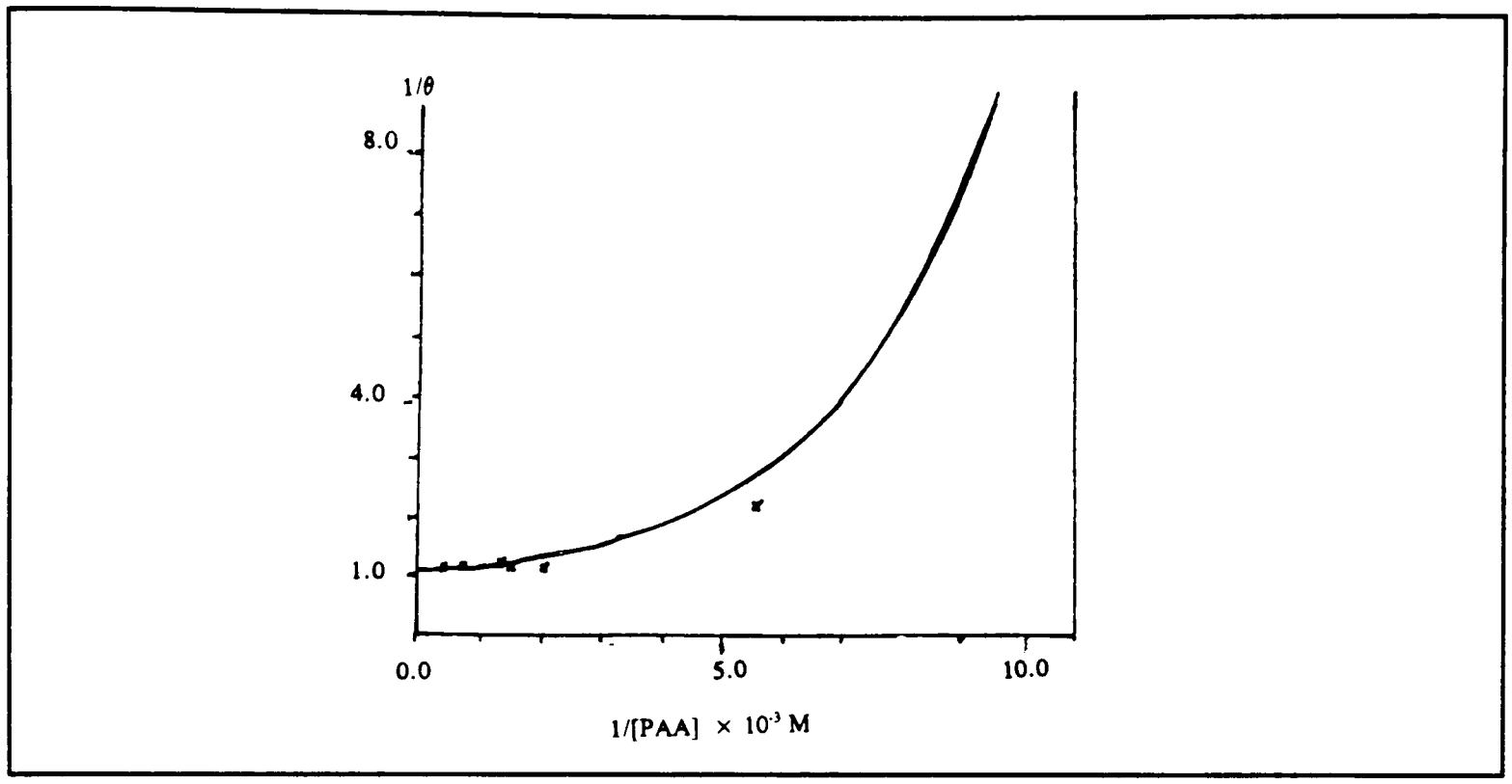

Figure 4.27: The plot of 1/θ against 1/[PAA] in order to investigate if adsorption is of a simple langmuirian manner.

In Figure 4.27, $1/\theta$ is plotted against 1/[PAA] as outlined in section 4.4.4. The plot of $1/\theta$ against 1/[PAA] is not linear, but at low concentrations the value of $1/\theta$ quickly approaches infinity (θ quickly approaches zero or no inhibition). Thus the inhibition is not Langmuirian. Also for low concentrations where very little inhibition occurs the fit is not a unique fit for the whole flow rate range. This indicates that the above theory does not adequately in explain the action of polyacrylic acid on the calcite surface. Therefore the simple model of Langmuirian adsorption of the polymer is not applicable.

4.5.5 The Effect of Background added Calcium on Inhibition by Polyacrylic acid (M.W. 2000)

It was postulated that perhaps background levels of calcium were in some way connected with the inhibition in the presence of polyacrylic acid. This suggestion fitted the observed increase in inhibition with flow rate for low concentrations of the polymer, since when the flow rate increases so does dissolution of calcite, and hence the levels of calcium released into solution. In order to explore the exact processes occurring, background Ca^{2+} in the form of calcium chloride was added to solutions of polyacrylic acid, and these solutions used to investigate the inhibition of the dissolution of calcite. Initially experiments were conducted with just background Ca^{2+} and a HCl solution, to see if Ca^{2+} had any inhibitory properties itself at low pH. As can be seen from figure 4.28 there was no sign of any inhibition by Ca^{2+}; the results obtained are exactly those

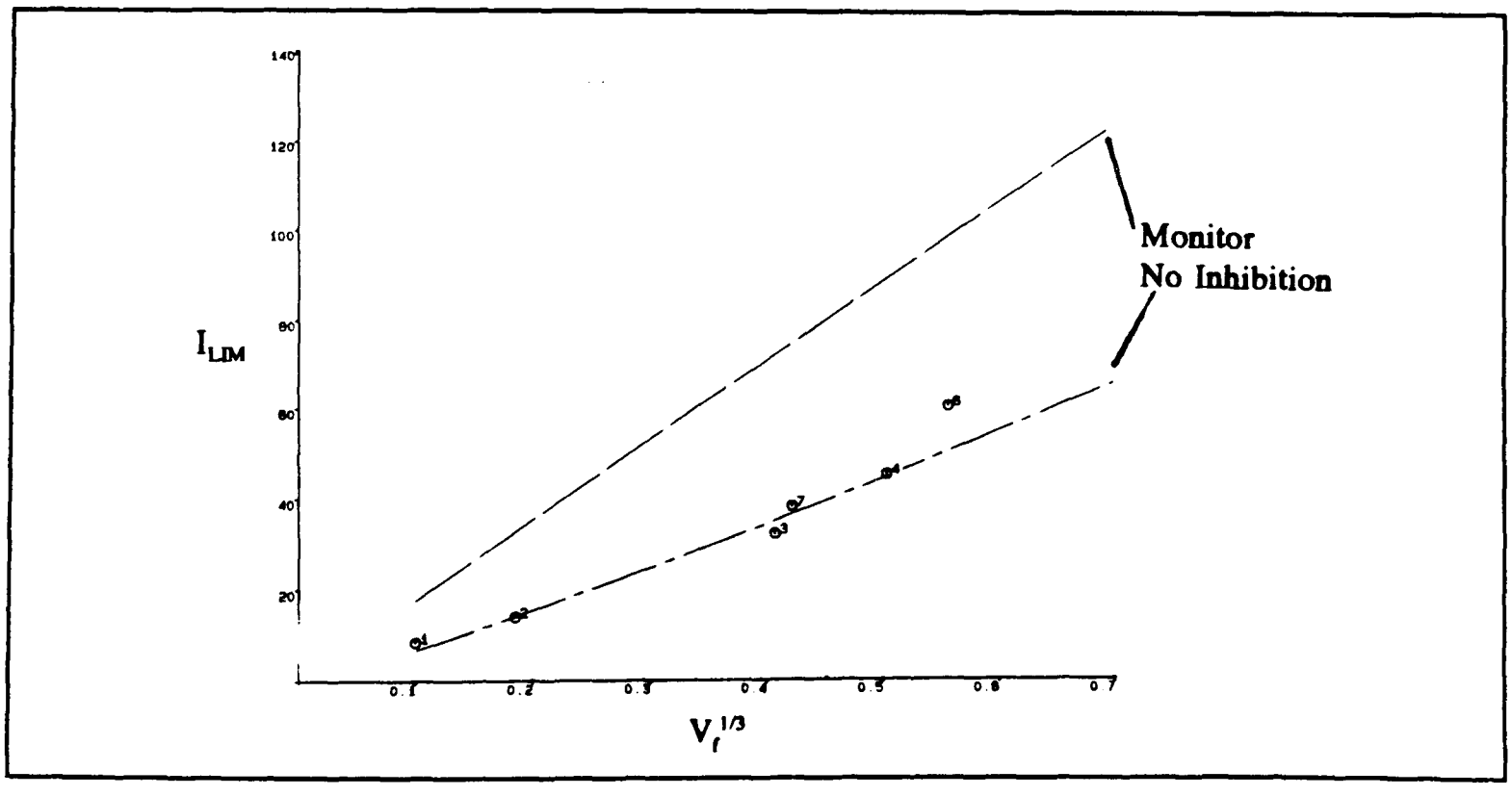

Figure 4.28: A comparison of the results obtained with an pH 3.40 solution containing background Ca^{2+} (10×10^{-3} M) and those expected for a solution of mineral acid at the same pH. (w=0.245 cm, X_{crys} = 0.580 cm and X_{el} = 0.292 cm)

predicted fusing the backwards implicit finite difference method, for a solution of HCl at the same pH with both solutions having 0.5 mol dm^{-3} KCL as background electrolyte.

Next background calcium was added to a solution of polyacrylic acid the inhibition by polyacrylic acid was seen to increase dramatically as shown in figure 4.29 below.

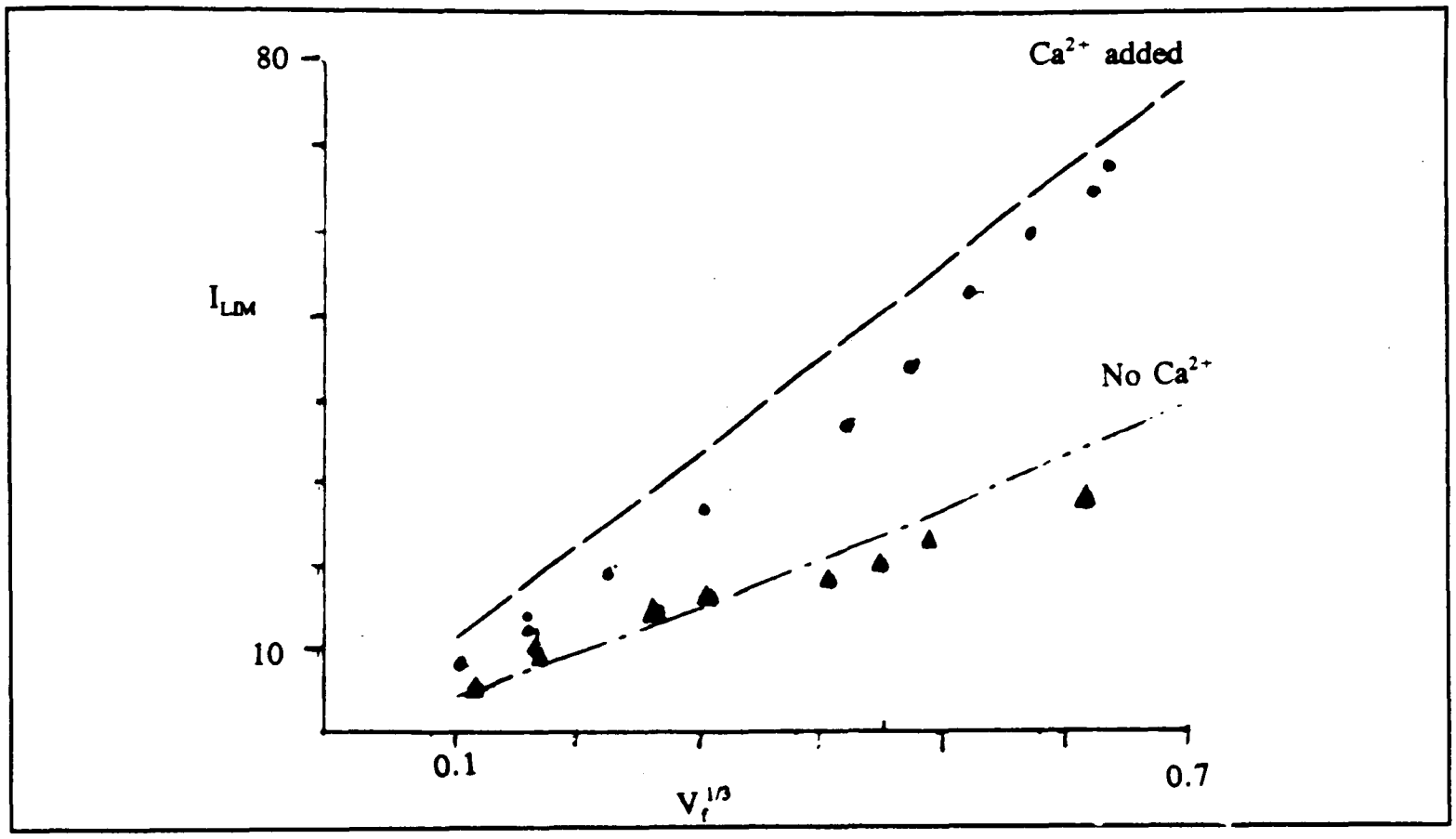

Figure 4.29: A comparison of the detector electrode limiting current variation with flow rate for two identical concentrations of polyacrylic acid (9.1× 10^{-5} mol dm^{-3}) a) with no added Ca^{2+} and, b) with 1 × 10^{-3} mol dm^{-3} added Ca^{2+}. (w=0.245 cm, X_{crys} = 0.580 cm and X_{el} = 0.292 cm).

As can be seen in this plot, without added Ca^{2+} the experimental points follow the same curve as if no inhibition is taking place, that is the same level of hydrogen ions (as measured by limiting current I_{LIM}) is measured as is modelled with $k'=k$, that is $\theta=0$. However when there is Ca^{2+} in a solution of the *same* concentration of polyacrylic acid, inhibition is enhanced, and a higher level of H^+ is detected than if modelled with $k'=k$. From this it can be clearly seen that calcium has an enhancing effect on the inhibition of calcite dissolution by polyacrylic acid.

4.5.5.1 *Modelling the Inhibition by Polyacrylic acid in the Presence of Added Ca^{2+}*

It was postulated that calcium forms a complex with polyacrylic acid, and it is this complex which adsorbs on the surface and causes the inhibition. Thus:

$$x\mathrm{Ca}^{2+} + \mathrm{PAA} \overset{K_{eq}}{\rightleftharpoons} \mathrm{Ca}_x\mathrm{PAA} \tag{4.88}$$

where K_{eq} is the equilibrium constant for the formation of the complex and can be defined as:

$$K_{eq} = \frac{[\mathrm{complex}]}{[\mathrm{Ca}^{2+}]^x[\mathrm{PAA}^{n-}]} \tag{4.89}$$

Assuming this complex adsorbs on the surface in a Langmuirian manner then:

$$\theta^{-1} = 1 + K_L^{-1}[\mathrm{complex}]^{-1} \tag{4.90}$$

These two equations can be combined to give:

$$\theta^{-1} = 1 + \frac{K_L^{-1}K_{eq}^{-1}}{[\mathrm{Ca}^{2+}]^x[\mathrm{PAA}^{n-}]} \tag{4.91}$$

If the substitution :

$$y = [\mathrm{PAA}^{n-}]\left(\frac{1}{\theta} - 1\right) \tag{4.92}$$

is used then equation (4.91) can be rewritten as:

$$\log y = -\log(K_L K_{eq}) - x\log[\mathrm{Ca}^{2+}] \tag{4.93}$$

It follows that a plot of log y against log $[Ca^{2+}]$ should be linear with a slope of $-x$ and an intercept of -log $(K_L K_{eq})$.

In order to test this complex model it is necessary to accurately know the concentration of Ca^{2+} at the surface, and know how it is affected by the dissolution of calcite. This is deduced by the appropriate modelling, and the relevant matrix elements are derived in the next section.

4.5.5.2*The Boundary Conditions for Ca^{2+}*

The boundary conditions for Ca^{2+} can be written as follows.

(i) *Upstream of the Crystal*

The concentration of all species are equal to those present in the bulk solution entering the flow cell:

$$x = 0, \quad 0 < y < 2h, \quad [Ca^{2+}] = [Ca^{2+}]_{bulk} \tag{4.94}$$

(ii) *Zone of the Crystal*

At the surface of the crystal the flux is given by the rate law for dissolution of calcite.

$$0 < x \leq x_c, \quad y = 0, \quad D_{Ca^{2+}} \frac{\partial [Ca^{2+}]}{\partial y} = -k_1([H^+] + (m-n)[PAA^{n-}]) \tag{4.95}$$

(iii) *The Far wall of the Flow Cell.*

On the channel wall opposite the crystal, there is no flux so:

$$0 < x \leq x_{c+e}, \quad y = 2h, \quad \frac{\partial [Ca^{2+}]}{\partial y} = 0 \tag{4.96}$$

(iv) *Downstream of the Crystal*

Over any gap between the crystal and detector, and on the far wall (see above) there is no flux so the boundary condition as in equation (4.96). Such a condition also

operates at the detector electrode surface for the case of Ca^{2+}, which is electroinactive at the potentials used for the H^+ reduction:

$$x_c < x \leq x_{c+e}, \quad y = 0, \quad \frac{\partial[Ca^{2+}]}{\partial y} = 0 \tag{4.97}$$

4.5.5.3 *The Matrix Elements for Ca^{2+}*

We next examine the approximate form of the transport equations to be solved subject to the above boundary conditions. Previous work [158] has shown that Ca^{2+} ions bind to PAA, but only under extreme conditions induced by neutralizing PAA with $Ca(OH)_2$. Accordingly solution coupling of Ca^{2+} and PAA may be neglected. At the levels of background Ca^{2+} and the bulk pH's used in this work it has been established that the possible interaction of Ca^{2+} with HCO_3^- and CO_3^{2-} are not relevant to the modelling [2,53]. As there are no homogeneous reactions involving Ca^{2+} then the convective-diffusion equation for calcium is:

$$0 = D_{Ca}\frac{\partial[Ca^{2+}]}{\partial y} - v_0\left(1 - \frac{(y-h)^2}{h^2}\right)\frac{\partial[Ca^{2+}]}{\partial x} \tag{4.98}$$

If A represents Ca^{2+} let:

$$g^A = \frac{[Ca^{2+}]}{[H^+]_{bulk}} \tag{4.99}$$

(i) *The Matrix Elements for Ca^{2+} in solution*

Then applying the equation (4.99) above to equation (2.66) from Chapter 2, gives the following general equation describing Ca^{2+} concentration in the channel:

$$g^{A}_{j,k} = -\lambda^{A}_{j} g^{A}_{j-1,k+1} + (2\lambda^{A}_{j} + 1) g^{A}_{j,k+1} - \lambda^{A}_{j} g^{A}_{j+1,k+1} \qquad j = 2,3..J\text{-}2 \quad (4.100)$$

If this is written in the form:

$$d^{A}_{j} = a^{A}_{j} g^{A}_{j-1,k+1} + b^{A}_{j} g^{A}_{j,k+1} + c^{A}_{j} g^{A}_{j+1,k+1} \qquad (4.101)$$

then:

$$d^{A}_{j} = g^{A}_{j,k} \qquad j=2,3,\ldots J\text{-}2 \quad (4.102)$$

$$a^{A}_{j} = -\lambda a^{A}_{j} \qquad j=2,3,\ldots J\text{-}2 \quad (4.103)$$

$$b^{A}_{j} = 2\lambda^{A}_{j} + 1 \qquad j=2,3,\ldots J\text{-}2 \quad (4.104)$$

$$c^{A}_{j} = -\lambda^{A}_{j} \qquad j=2,3,\ldots J\text{-}2 \quad (4.105)$$

The matrix elements for the other species are unaltered from those used earlier, and defined in section 4.4.3..

(ii) *The Matrix Elements for Ca^{2+} at the Crystal Surface.*

The boundary condition (4.95) for flux of Ca^{2+} at the surface of the calcite crystal can be rearranged to give:

$$g^{A}_{0,k+1} = g^{A}_{1,k+1}\left(1 - \frac{\Delta y\, k_1 (g^{H}_{0,k} + (m-n) g^{PAA}_{0,k})}{D_{Ca^{2+}}}\right)^{-1} \qquad (4.106)$$

At the crystal surface equation (4.100) c_1 and d_1 are as for the centre of the channel but:

$$j=1 \quad (4.107)$$

$$a_1^{\Lambda} = 0$$

$$b_1^{\Lambda} = \lambda_1^{\Lambda} + 1 - \frac{\lambda_j^{\Lambda}\Delta y\left(g_{0,k}^{H} + (m-n)g_{0,k}^{PAA}\right)}{D_{Ca^{2+}}}$$

(iii) *The Matrix Elements for Ca^{2+} at the Far Wall of the Channel.*

At the far wall of the channel (the wall opposite the reactive surface, either electrode or calcite crystal) the flux of all species is zero, this modifies the matrix elements for all species as stated in section 4.3.2.3above.

(iv) *The Matrix elements for Ca^{2+} at the Detector Electrode surface*

Ca^{2+} is inactive at the electrode so there is a no flux condition here and the matrix elements are analogous to for the crystal surface except that:

(4.108)

$$a_1^{\Lambda} = 0$$

$$b_1^{\Lambda} = \lambda_1^{\Lambda} + 1$$

4.5.5.4*Results with added Calcium.*

Experiments were performed to study the dissolution of calcite in the presence of polyacrylic acid with background calcium present. Figures 4.30 and 4.31 show the experimental data for two of the experiments performed, the data for the full range of experiments is tabulated in Table 4.6.

An average value of Ca^{2+} at the surface can be calculated by including Ca^{2+} in the BI modelling, and from this it can be determined if the amount of calcium generated at the surface is a significant amount compared to that in the bulk. The BI method

calculates values for the concentration of Ca^{2+} for each of the surface grid points over the calcite crystal. These are then averaged for the whole crystal surface. The contribution to this surface Ca^{2+} concentration depends on the amount of background Ca^{2+}. For example in the experiment shown below in figure 4.30, the background Ca^{2+} concentration is 93.56×10^{-3} mol dm^{-3}, at a flow rate of 0.001 cm^3 s^{-1} the average surface concentration is 94.60×10^{-3}, and at a flow rate of 0.343 cm^3 s^{-1} the average surface concentration is 94.77×10^{-3} mol dm^{-3}. Alternatively for a background Ca^{2+} concentration of 9.717×10^{-3} mol dm^3 (figure 4.31), at flow rate 0.001 cm^3 s^{-1} the average surface concentration is 9.84 mol dm^{-3}, and at a flow rate of 0.343 cm^3 s^{-1} the average surface concentration is 10.39×10^{-3} mol dm^{-3}.

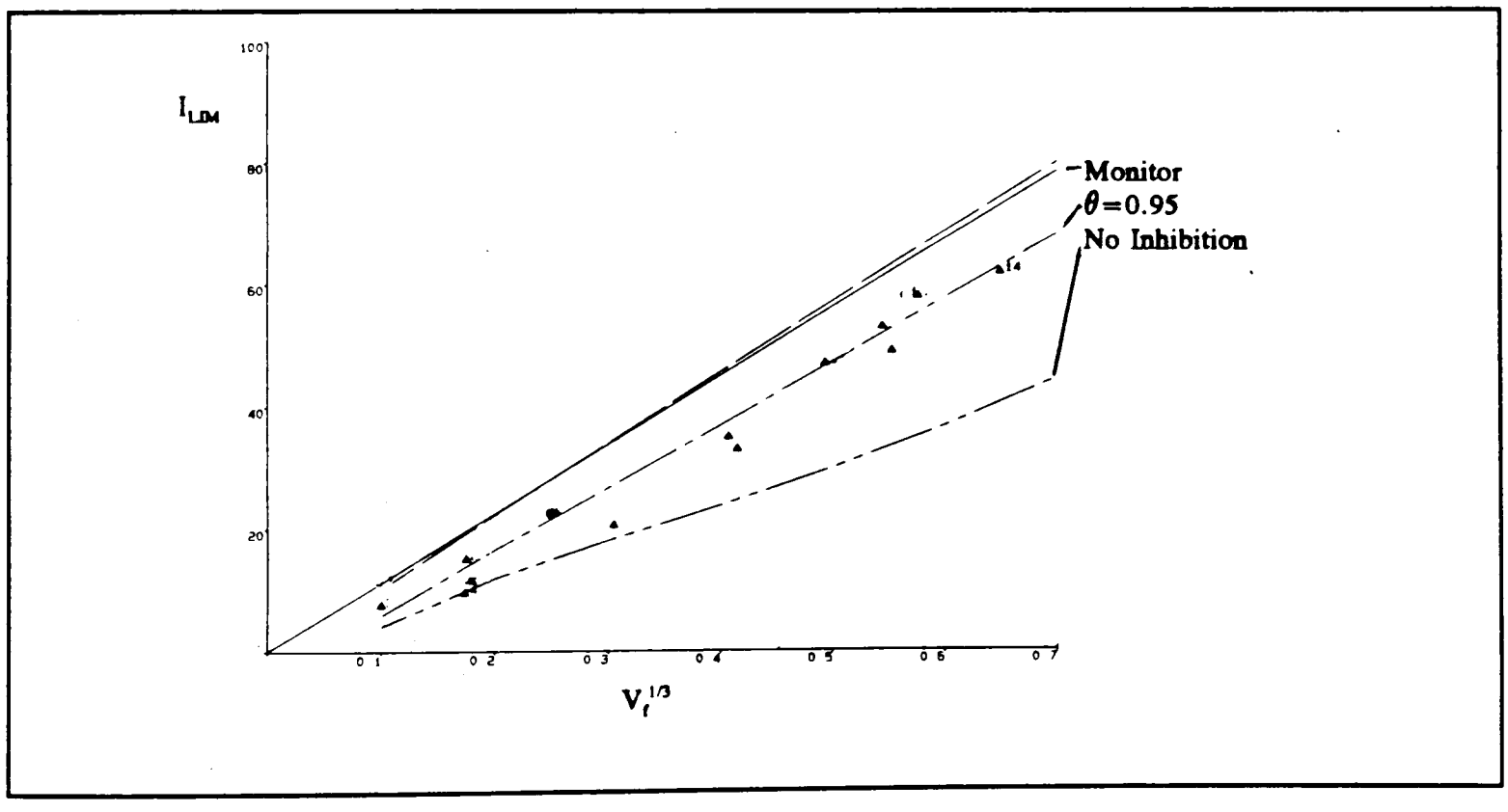

Figure 4.30: The BI fit for the dissolution of calcite with a pH 3.30 solution of 0.0918×10^{-3} mol dm^{-3} polyacrylic acid with a background Ca^{2+} level of 93.56×10^{-3} mol dm^{-3}, $\theta = 0.95$. ($w = 0.248$, $X_{crys} = 0.544$ and $X_{el} = 0.295$).

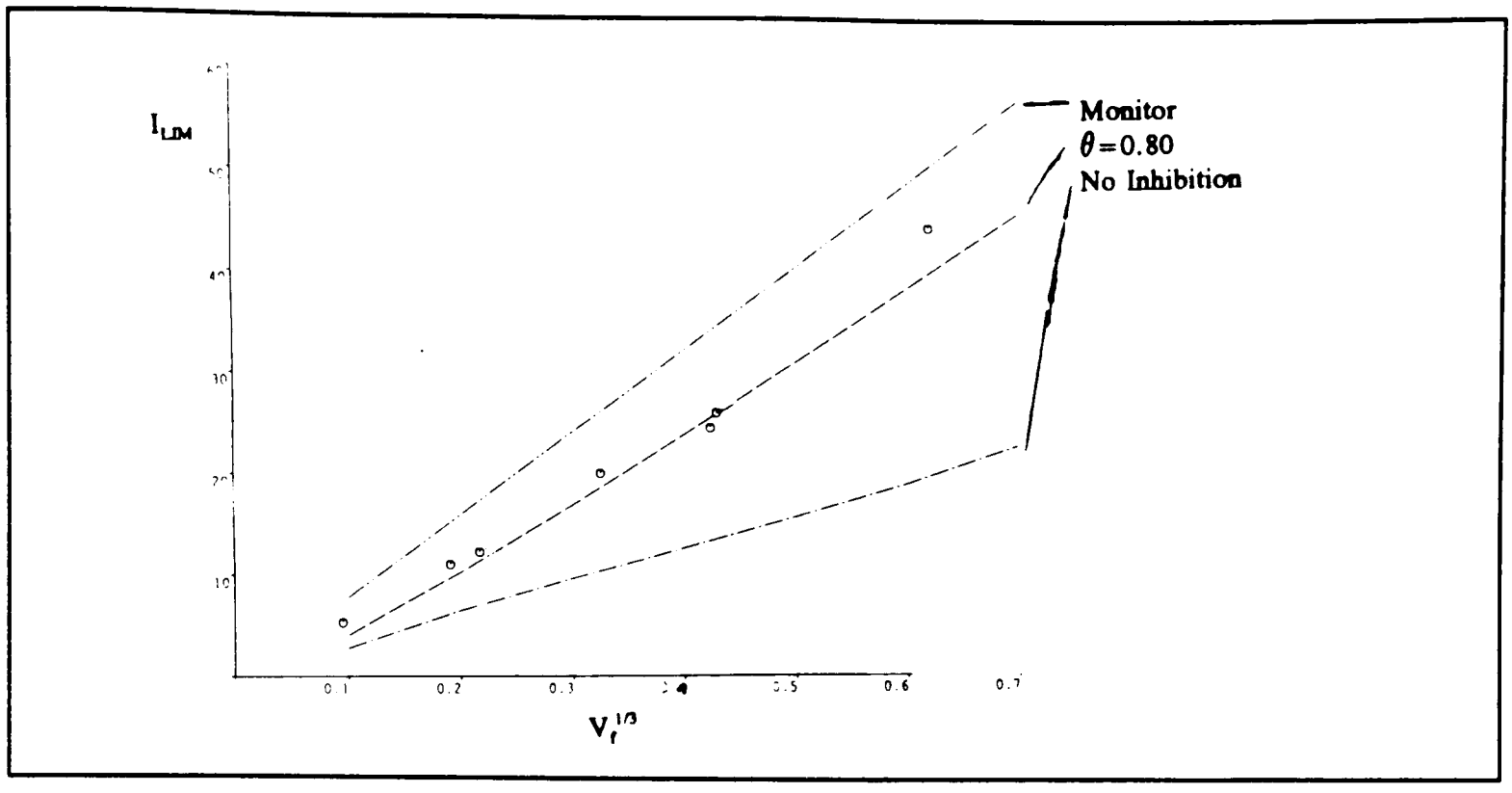

Figure 4.31: The BI fit for the dissolution of calcite with a pH 3.25 solution of 0.046 × 10^{-3} mol dm^{-3} polyacrylic acid with a background Ca^{2+} level of 9.71 × 10^{-3} mol dm^{-3}, θ = 0.80. (w= 0.248, X_{crys}=0.544 and X_{el}=0.295).

Figures 4.30 and 4.31 above show the variation of current measured at the detector electrode with flow rate for two concentrations of both polyacrylic acid and background calcium. Also shown is theoretically predicted behaviour modelled using the BI method using the parameters as quoted in the figure legends. As can be clearly seen, with background added calcium the theoretical behaviour fits for all the flow rates. This good fit was seen in all of the concentrations of polyacrylic acid studied, unlike without background Ca^{2+}. This ability to obtain a unique BI fit for the data with added Ca^{2+} supports the hypothesis that the increase in inhibition with flow rate for low polyacrylic acid solutions without added Ca^{2+}, is due to the generation of Ca^{2+} at the surface.

Below are tabulated the results for the inhibition of calcite dissolution in the presence of polyacrylic acid with additional background Ca^{2+} (Table 4.6). Only values of θ equal or less than 0.95 were considered to be reliable, as when the inhibition is greater than this, θ is very sensitive to small changes in the measurements. Thus the errors in θ become unacceptably large due to the experimental errors above this value.

Table 4.5 The results for Polyacrylic acid (M.W.2000) Inhibited Dissolution of Calcite in the Presence of Background Added Calcium

[PAA] / 10^{-3} mol dm^{-3}	$[Ca^{2+}]_{added}$ / 10^{-3} mol dm^{-3}	$[H^+]$ / 10^{-3} mol dm^{-3}	θ*	pH
0.0918 (±0.001)	1.04 (±0.01)	0.54 (±0.06)	0.50 (±0.10)	3.27
0.0918 (±0.001)	93.6 (±0.1)	0.49 (±0.04)	0.95 (±0.01)	3.31
0.089 (±0.001)	0.898 (±0.002)	0.37 (±0.03)	0.80 (±0.03)	3.43
0.089 (±0.001)	4.49 (±0.01)	0.66 (±0.06)	0.90 (±0.02)	3.18
0.177 (±0.001)	3.90 (±0.01)	0.50 (±0.06)	0.80 (±0.03)	3.30
0.177 (±0.001)	9.71 (±0.01)	0.69 (±0.06)	0.80 (±0.03)	3.16
0.177 (±0.001)	4.53 (±0.01)	0.53 (±0.06)	0.80 (±0.03)	3.28
0.177 (±0.001)	4.51 (±0.01)	0.46 (±0.05)	0.95 (±0.01)	3.34
0.046 (±0.001)	9.72 (±0.01)	0.56 (±0.06)	0.80 (±0.03)	3.25
0.046 (±0.001)	0.045 (±0.002)	0.87 (±0.08)	0.80 (±0.03)	3.06
0.023 (±0.001)	0.013 (±0.002)	0.87 (±0.08)	0.70 (±0.1)	3.06

*See Appendix 5, the discussion of errors.

The data in Table 4.5 was then analyzed by a plot of log y against log $[Ca^{2+}]$ (section 4.5.5.1) to test the complex formation and adsorption theory as outlined above. This leads to figure 4.32 below.

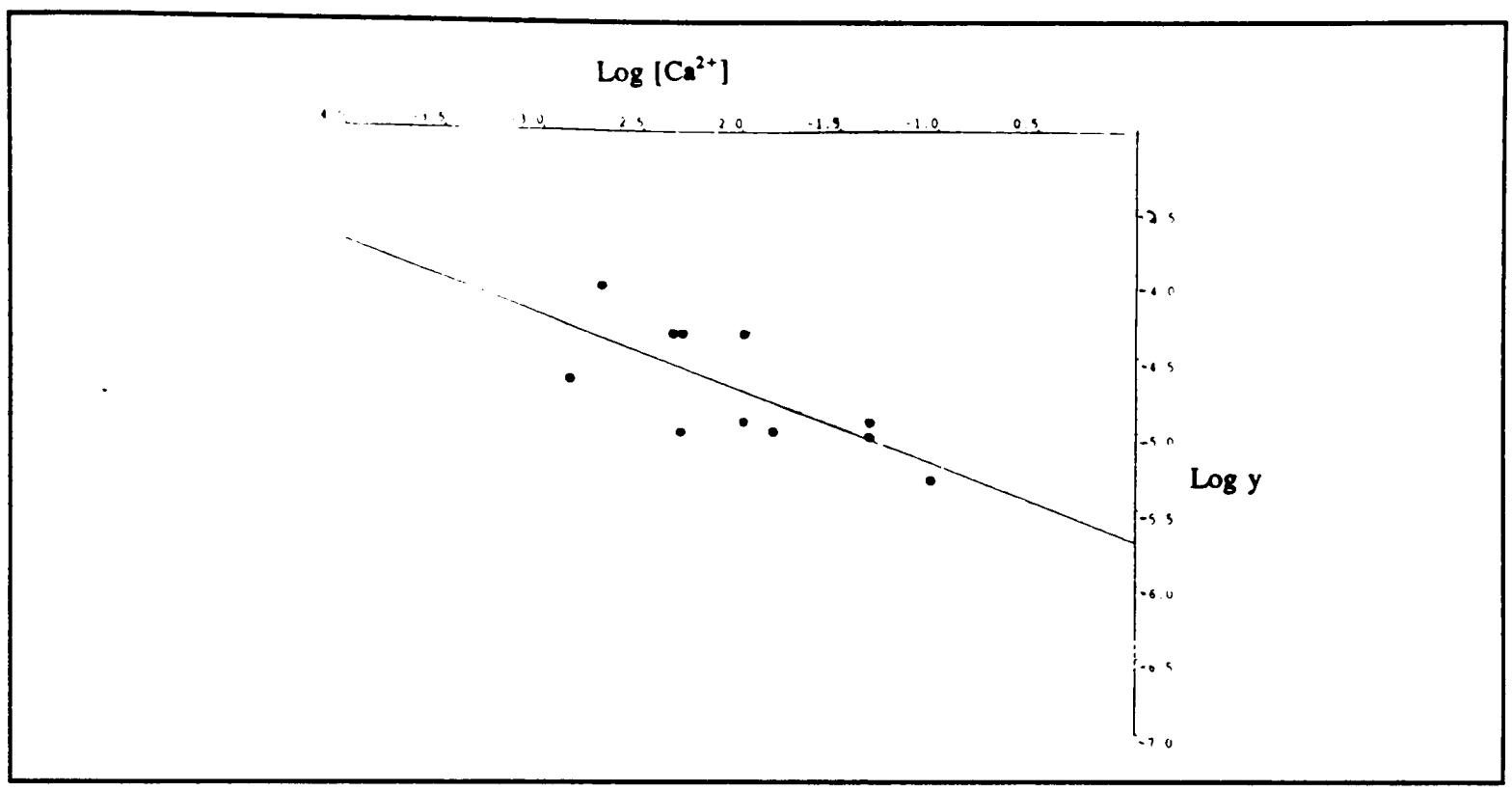

Figure 4.32: The plot of log y against log[Ca^{2+}] (with polyacrylic acid M.W. 2000) to test if the complex formation model is valid.

As can be seen this plot is linear so supports the calcium complex theory as proposed earlier in this section. The plot does have an increased error over the raw data, which is as expected as the individual errors in the experimental data are multiplied in the analysis. However from this plot it is possible to measure the gradient x which is a measure of the number of Ca^{2+} ions which combine each polyacrylic acid chain. In this case the line yields a value of $x = 0.49$, when analyzed by a least squares fit. This suggests that approximately two polyacrylic acid chains react with each calcium ion. The chemical probability of this result adds confidence to the analysis, and supports the underlying theory.

The next step is to further investigate the general validity of this theory with different molecular weight polyacrylic acid polymers.

4.5.6The Effect of the Molecular Weight of Polyacrylic Acid on the Inhibition of Calcite Dissolution

Using two other molecular weight polyacrylic acid molecules allows investigation of the effect of the molecular weight on inhibition of calcite dissolution. Solutions of Antiprex (4800 M.W.) covering the range 1×10^{-6} to 2×10^{-5} mol dm^{-3}, and Narlex (14800 M.W.) covering the range 3×10^{-6} to 2×10^{-5} mol dm^{-3}, were used in the channel flow cell experiments. The names of these two molecular weight versions are commercial names which will be used here for ease of differentiating between different molecular weight polyarcylic acid polymers. The solutions were made up with background electrolyte concentrations of 0.5 mol dm^{-3} KCl, and had background added Ca^{2+} of between 1×10^{-1} and 1×10^{-3} mol dm^{-3}.

Examples of the BI fit for each of these molecular weights are shown in figures 4.33 and 4.34.. As can be seen they fit adequately over the whole flow rate range. This good fit is seen throughout all the experiments conducted. Higher concentrations of polymer could not be studied since the amount of H_2 generated at the detector electrode was enough to give bubbles of H_2 gas at the electrode which interfered with flow through the cell.

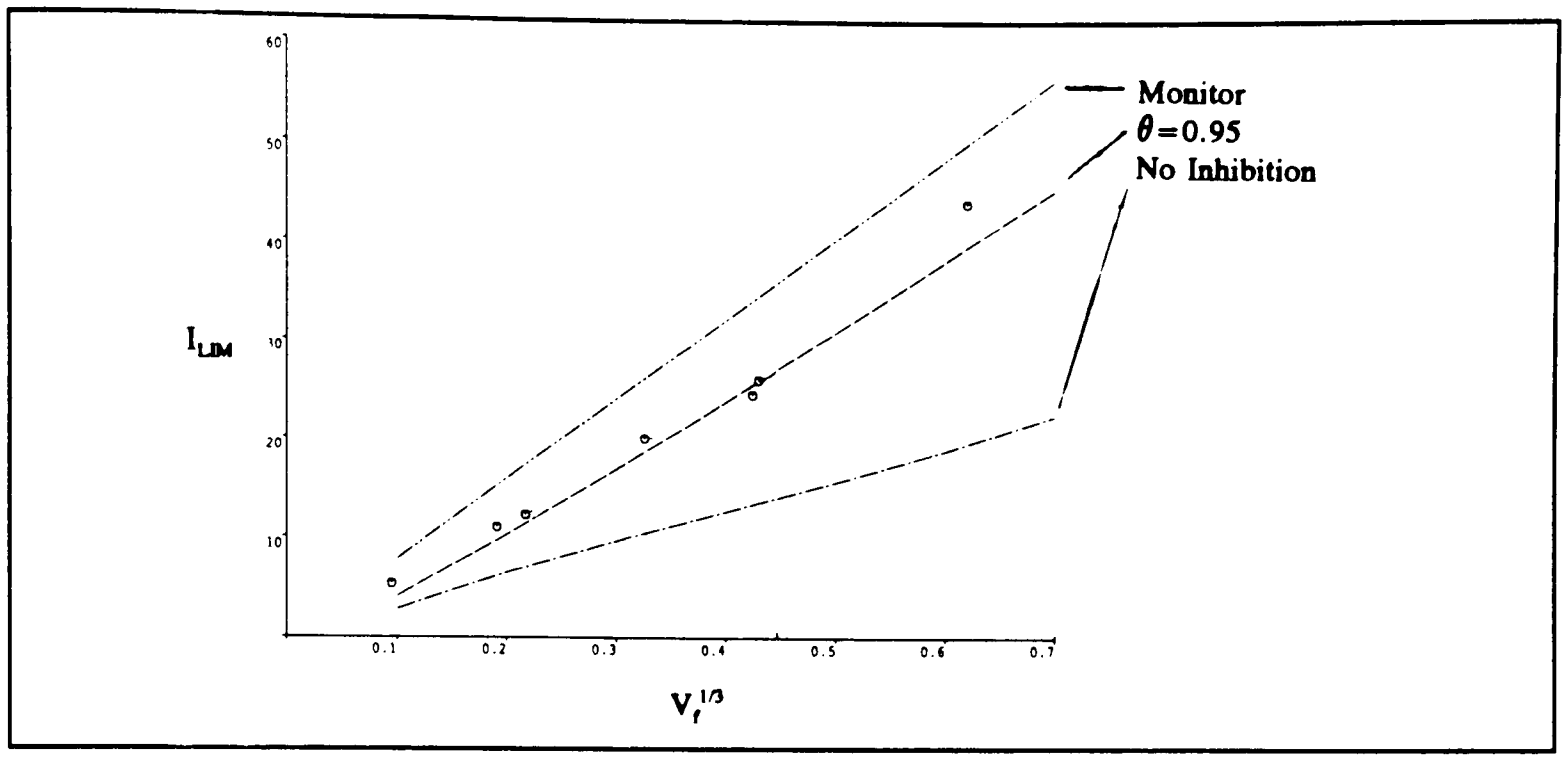

Figure 4.33: The BI fit for the dissolution of calcite in the presence of Antiprex (2.6 × 10^{-5} mol dm^{-3}) with 5.49 × 10^{-3} mol dm^{-3} Ca^{2+}, θ = 0.95. (w=0.306 cm, X_{crys} = 0.645 cm and X_{el} = 0.175 cm)

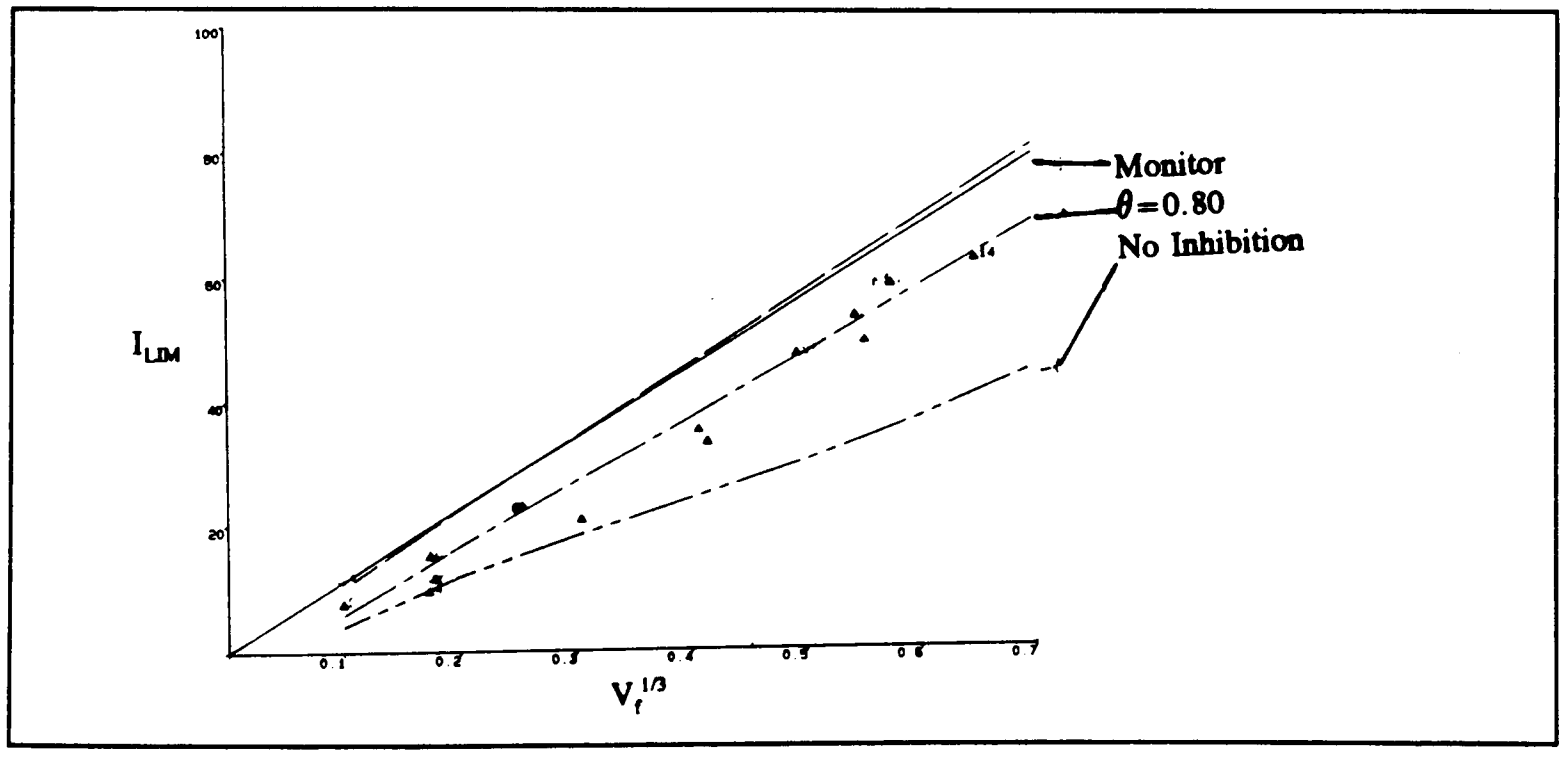

Figure 4.34: The BI fit for the dissolution of calcite in the presence of Narlex (3.6 × 10^{-6} mol dm^{-3}), with 88.09 × 10^{-6} mol dm^{-3} Ca^{2+}, and θ = 0.80. (w=0.306 cm, X_{crys} = 0.645 cm and X_{el} = 0.175 cm)

The full analysis of the experimental data for these two polymers is given in Tables 4.7 and 4.8 below.

Table 4.7 The Results for Antiprex (M.W. 5000)

[Anti] / 10^{-5} mol dm^{-3}	[Ca^{2+}] / 10^{-3} mol dm^{-3}	[H^+] / 10^{-3} mol dm^{-3}	θ	pH
2.58 (± 0.05)	2.20 (± 0.005)	0.54 (± 0.06)	0.70 (± 0.1)	3.27
2.58 (± 0.05)	54.9 (± 0.05)	0.60 (± 0.06)	0.95 (± 0.01)	3.22
1.29 (± 0.02)	9.23 (± 0.005)	0.18 (± 0.02)	0.80 (± 0.03)	3.74
1.29 (± 0.02)	2.00 (± 0.005)	0.74 (± 0.08)	0.75 (± 0.05)	3.13
0.11 (± 0.005)	98.9 (± 0.05)	0.75 (± 0.08)	0.60 (± 0.1)	3.12

Table 4.8 The Results for Narlex (M.W. 15000)

[Nar] / 10^{-6} mol dm^{-3}	[Ca^{2+}] / 10^{-3} mol dm^{-3}	[H^+] / 10^{-3} mol dm^{-3}	θ	pH
3.62 (± 0.05)	88.1 (± 0.05)	0.20 (± 0.02)	0.80 (± 0.03)	3.70
15.5 (± 0.1)	1.37 (± 0.005)	0.14 (± 0.02)	0.80 (± 0.03)	3.85
3.87 (± 0.05)	1.02 (± 0.005)	0.51 (± 0.06)	0.80 (± 0.03)	3.29
7.73 (± 0.06)	9.27 (± 0.005)	0.13 (± 0.02)	0.80 (± 0.03)	3.89
18.7 (± 0.1)	1.54 (± 0.005)	0.069 (± 0.005)	0.90 (± 0.02)	4.16

The model which was proposed for the 2000 M.W. polymer and, which fitted so well, is then tested for these two molecular weights. Equation (4.93) was examined again with y being defined in equation (4.92) in terms of [PAA]. However in this case PAA is either Antiprex or Narlex. Again a plot of log y against log $[Ca^{2+}]$ should again be linear if the model applies.

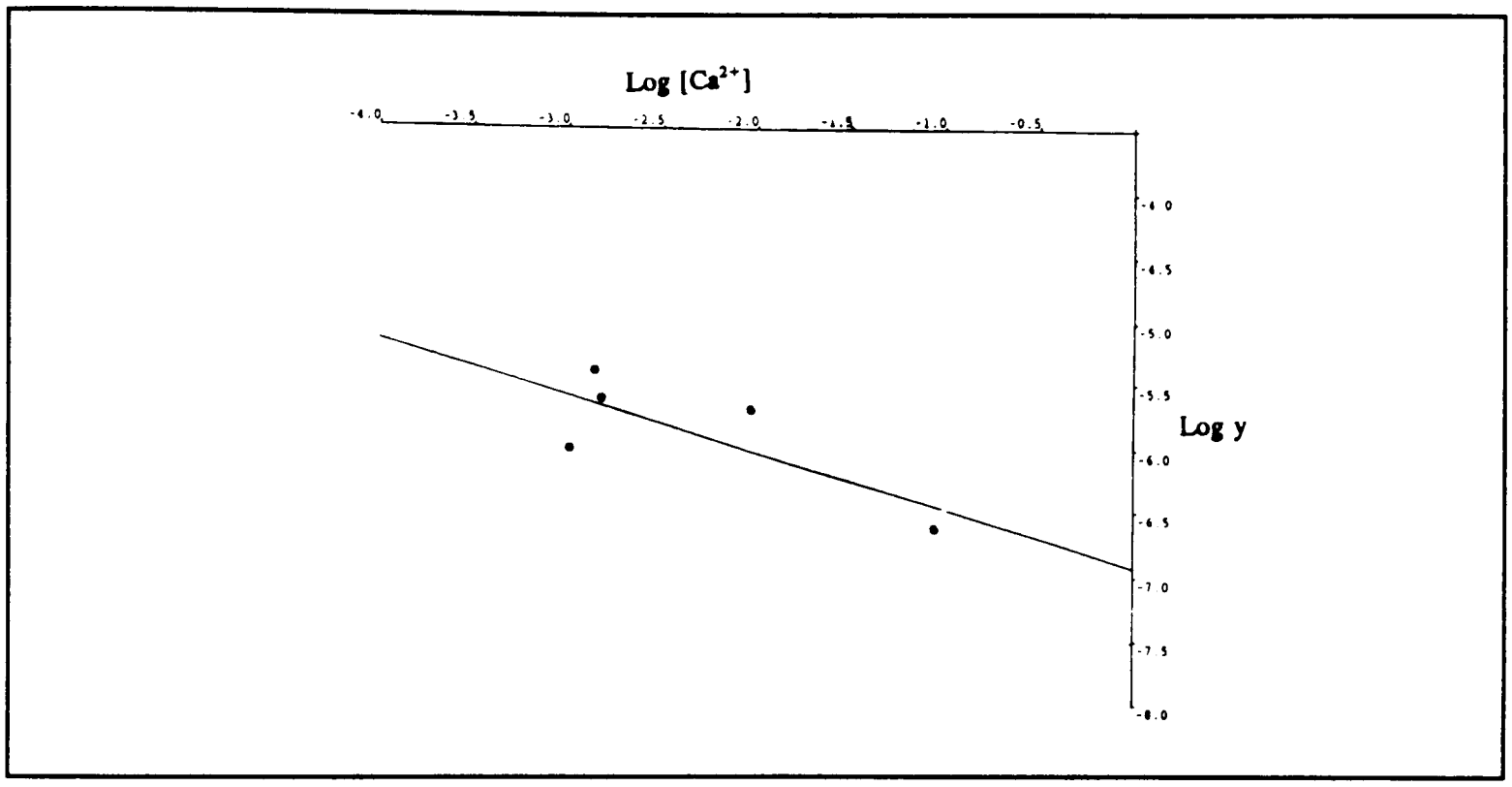

Figure 4.35 The plot of log y against log $[Ca^{2+}]$ for Antiprex.

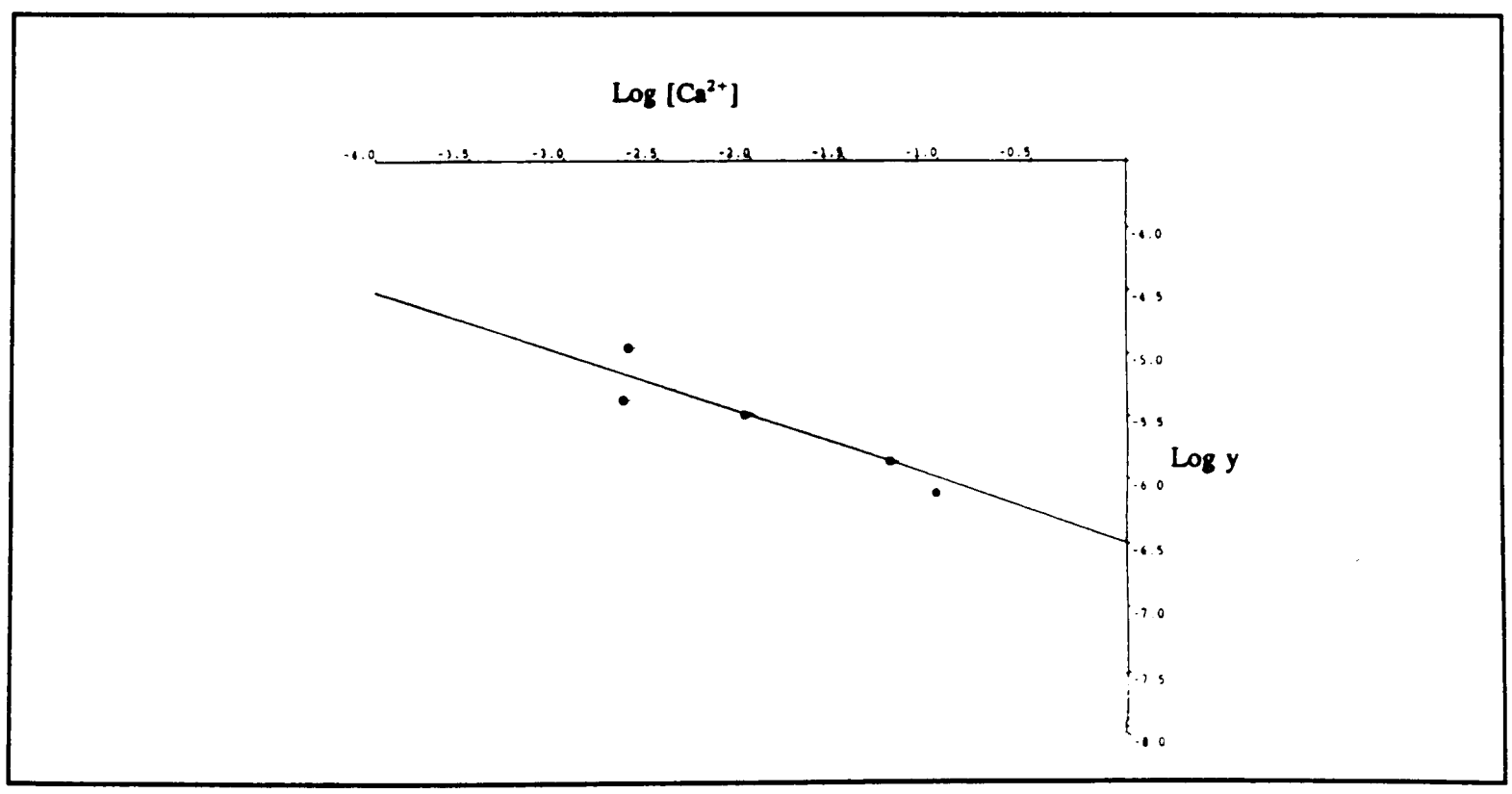

Figure 4.36 The plot of log y against log $[Ca^{2+}]$ for Narlex.

Above in figures 4.35 and 4.36 are the plots of log [Ca^{2+}] against log *y* for Antiprex and Narlex. As can be seen there seems to be a linear relationship. This supports the complex formation theory postulated earlier. It follows that the same theory is valid for all three molecular weights, which provides further strong conformation of the proposed theory. Again the gradient yields a measure of x, or the number of Ca^{2+} ions which combine with each polyacrylic acid chain. In these cases the values of x are 0.48 and 0.44 respectively for Antiprex and Narlex. This, as in section 4.5.5.3, suggests two polymer chains are bound together by one Ca^{2+} ion.

In addition it follows from equation (4.93) the intercepts of these plots is equal to -log $K_{eq}K_L$). Thus for 200 M.W. polyacrylic acid $K_{eq}K_L = 5.09 (\pm 0.08) \times 10^{-5}$, for Antiprex $K_{eq}K_L = 31.1 (\pm 0.5) \times 10^{-5}$, and for Narlex $K_{eq}K_L = 52 (\pm 1) \times 10^{-5}$. These values will be further discussed in section 4.5.8 below.

4.5.7 The Effect of Other Divalent Cations on the Inhibition of Calcite by Polyacrylic Acid

In order to test whether the inhibition enhancing effect noted above was specific to Ca^{2+}, experiments were carried out with magnesium, Mg^{2+} and barium, Ba^{2+} as the added cation. These were carried out with the 2000 molecular weight polymer (2×10^{-5} to 5×10^{-4} mol dm^{-3}), with background added Mg^{2+} (5×10^{-2} to 1×10^{-3} mol dm^{-3}) or alternatively Ba^{2+} (5×10^{-4} to 9×10^{-3}).

These experiments were modelled using the BI method and analyzed using the same complexation theory as used for calcium. In this case instead of the surface

concentration of calcium being used the background concentration of the relevant cation was used. Examples of two of the fits are given below in figures 4.36 and 4.37.

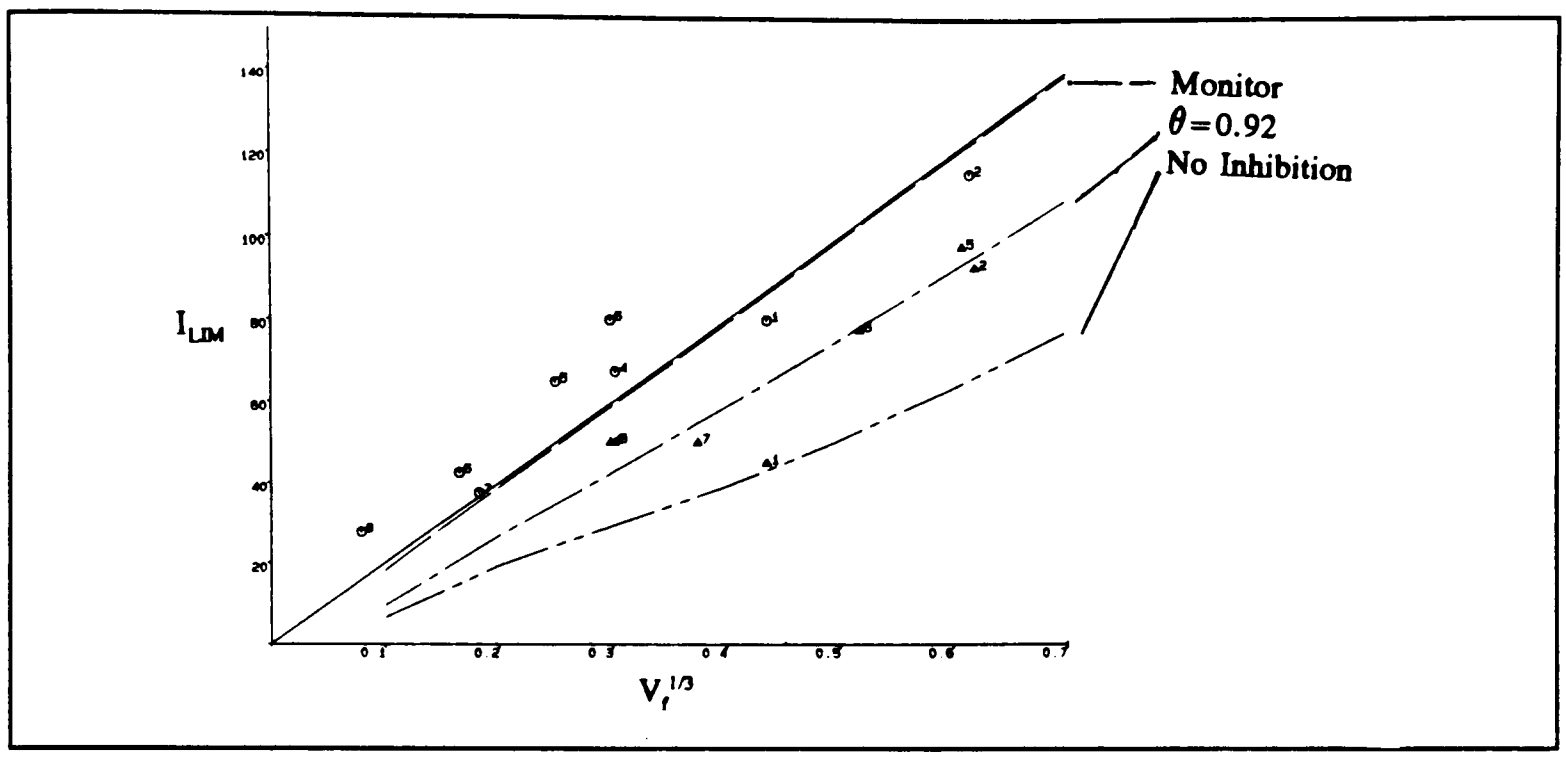

Figure 4.37: The BI fit for the dissolution of calcite in the presence of polyacrylic acid (M.W. 2000) 2.9 × 10^{-5} mol dm^{-3} with added background Mg^{2+} 4.95 × 10^{-2} mol dm^{-3}. (w=0.187, X_{crys}=0.566 and X_{el}=0.228), with θ=0.92.

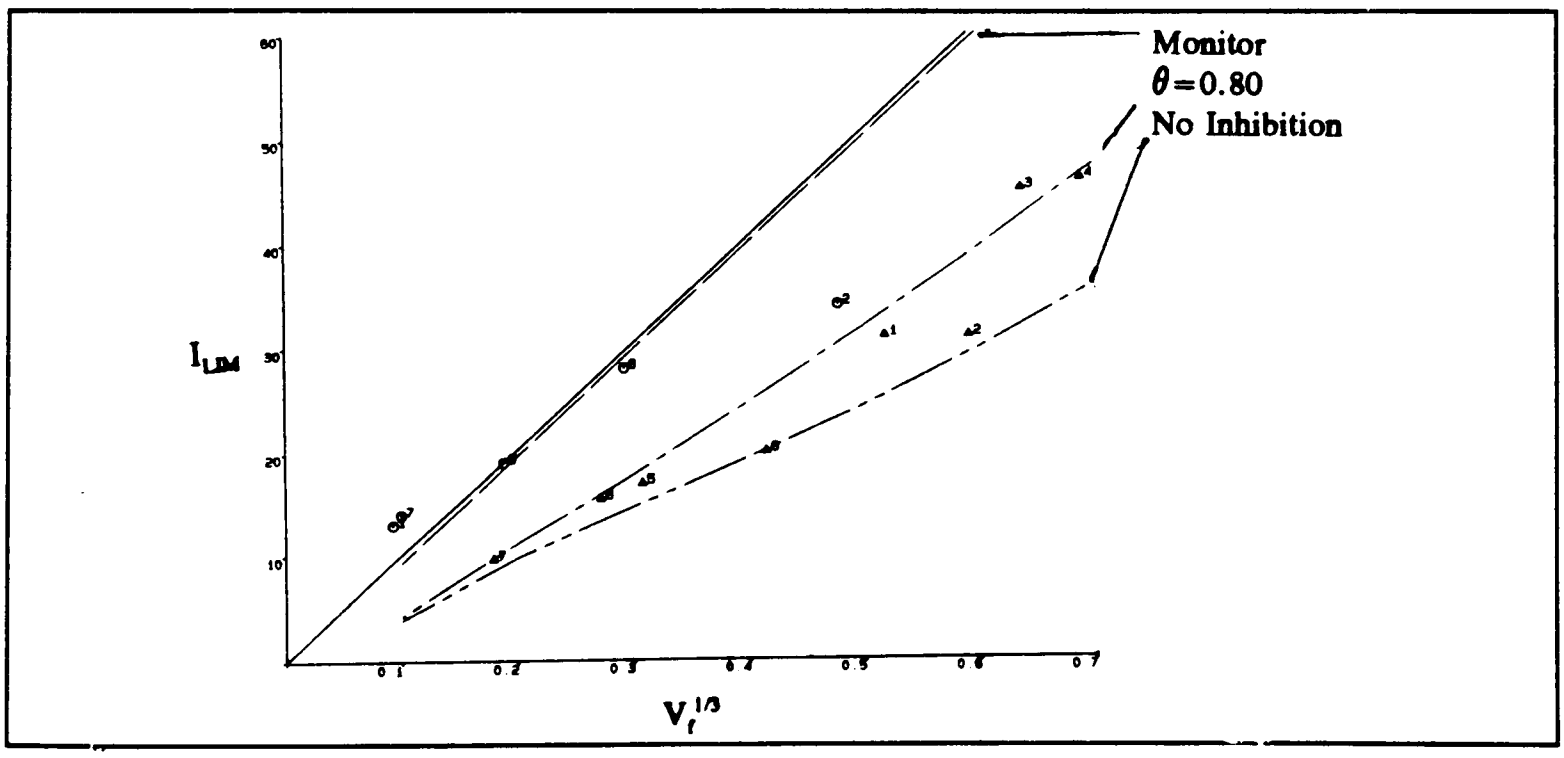

Figure 4.38: The BI fit for the dissolution of calcite in the presence of polyacrylic acid (M.W. 2000) 3.1 × 10^{-5} mol dm^{-3} with added background Ba^{2+} 4.88× 10^{-4} mol dm^{-3}. (w=0.131, X_{crys}=0.564 and X_{el}=0.131) with θ= 0.80.

These examples again show that the BI theory produces a good fit over the whole flow rate range. The full set of results are tabulated below in tables 4.9 and 4.10.

Table 4.9 The Results for 2000 M.W.polyacrylic acid with added background Magnesium

[PAA] / 10^{-3} mol dm^{-3}	[Mg^{2+}] / 10^{-3} mol dm^{-3}	[Ca^{2+}] / 10^{-3} mol dm^{-3}	θ	pH
0.053 (±0.001)	18.5 (±0.05)	0.22 (±0.005)	0.90 (±0.02)	3.75
0.12 (±0.005)	2.54 (±0.005)	0.53 (±0.005)	0.60 (±0.05)	3.57
0.10 (±0.005)	1.33 (±0.005)	0.20 (±0.005)	0.90 (±0.02)	3.64
0.029 (±0.001)	49.5 (±0.05)	1.66 (±0.005)	0.92 (±0.02)	2.71
0.052 (±0.001)	5.04 (±0.005)	0.43 (±0.005)	0.60 (±0.05)	2.85
0.058 (±0.001)	1.97 (±0.005)	0.712(±0.005)	0.90 (±0.02)	3.05

Table 4.10 The Results for Polyacrylic Acid M.W.2000 with Added Background Barium

[PAA] / 10^{-3} mol dm^{-3}	[Ba^{2+}] / 10^{-3} mol dm^{-3}	[Ca^{2+}] / 10^{-3} mol dm^{-3}	θ	pH
0.031 (±0.001)	0.49 (±0.005)	0.060 (±0.005)	0.80 (±0.05)	3.50
0.054 (±0.001)	9.43 (±0.005)	0.48 (±0.005)	0.90 (±0.02)	3.27
0.027 (±0.001)	0.79 (±0.005)	0.086 (±0.005)	0.90 (±0.02)	3.80
0.50 (±0.005)	0.99 (±0.005)	0.085 (±0.005)	0.3 (±0.10)	3.28
0.091 (±0.001)	9.43 (±0.01)	0.48 (±0.005)	0.90 (±0.02)	3.42

The next step was to apply the complex theory for Ca^{2+} and to see if it also fits for these two cations. In order to do this plots of log *y* against log $[M^{2+}]$ were used, where $[M^{2+}]$ is either $[Mg^{2+}]$ or $[Ba^{2+}]$ respectively. This plot will be linear if the theory fits. It is not possible to include Ca^{2+} in the modelling unless either, it can be shown that variation in the inhibitory power with cation is insignificant, or a value for K_{eq} alone (as opposed to $K_{eq}K_L$) for the Ca^{2+} cation complex could be isolated. If the variation with

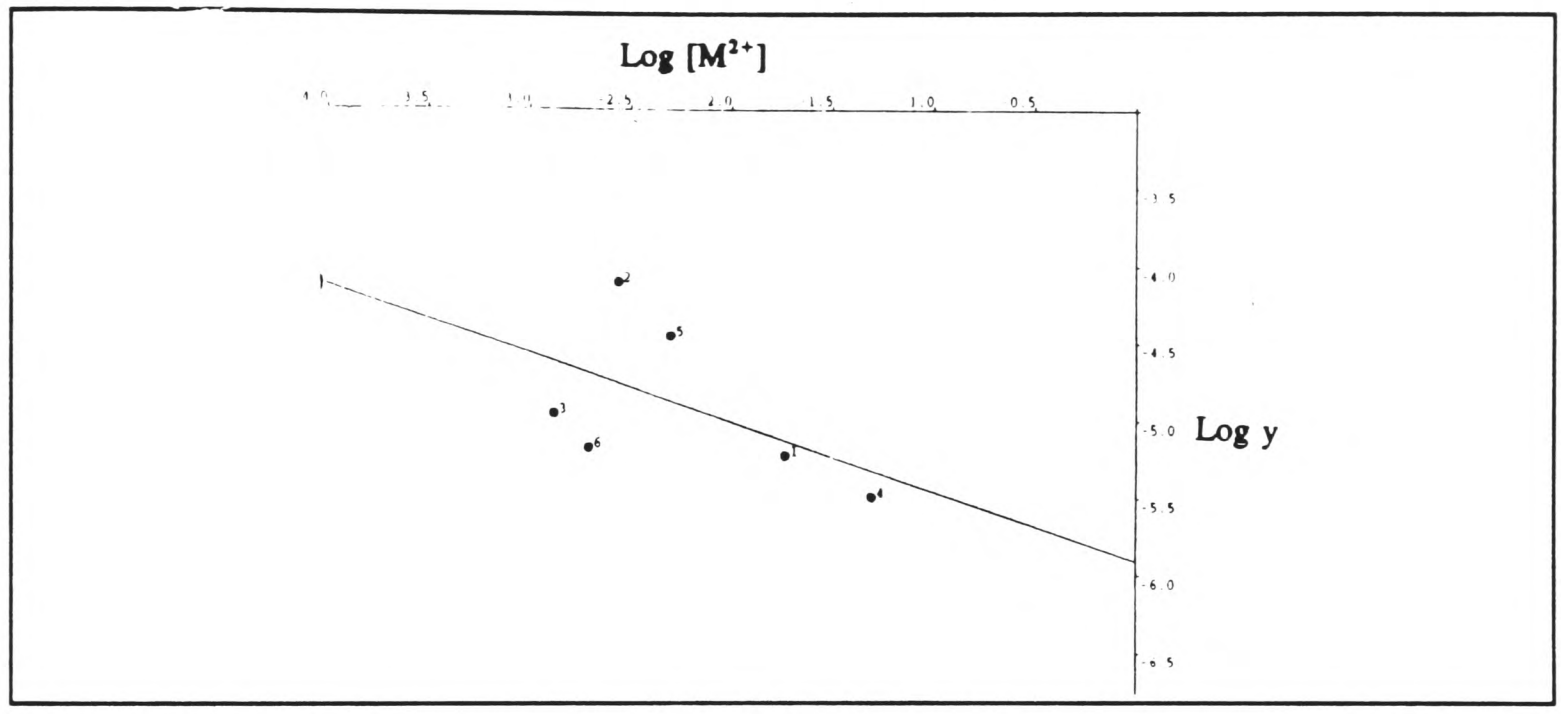

Figure 4.39: The plot of log y against log [Mg2+] for polyacrylic acid molecular weight 2000.

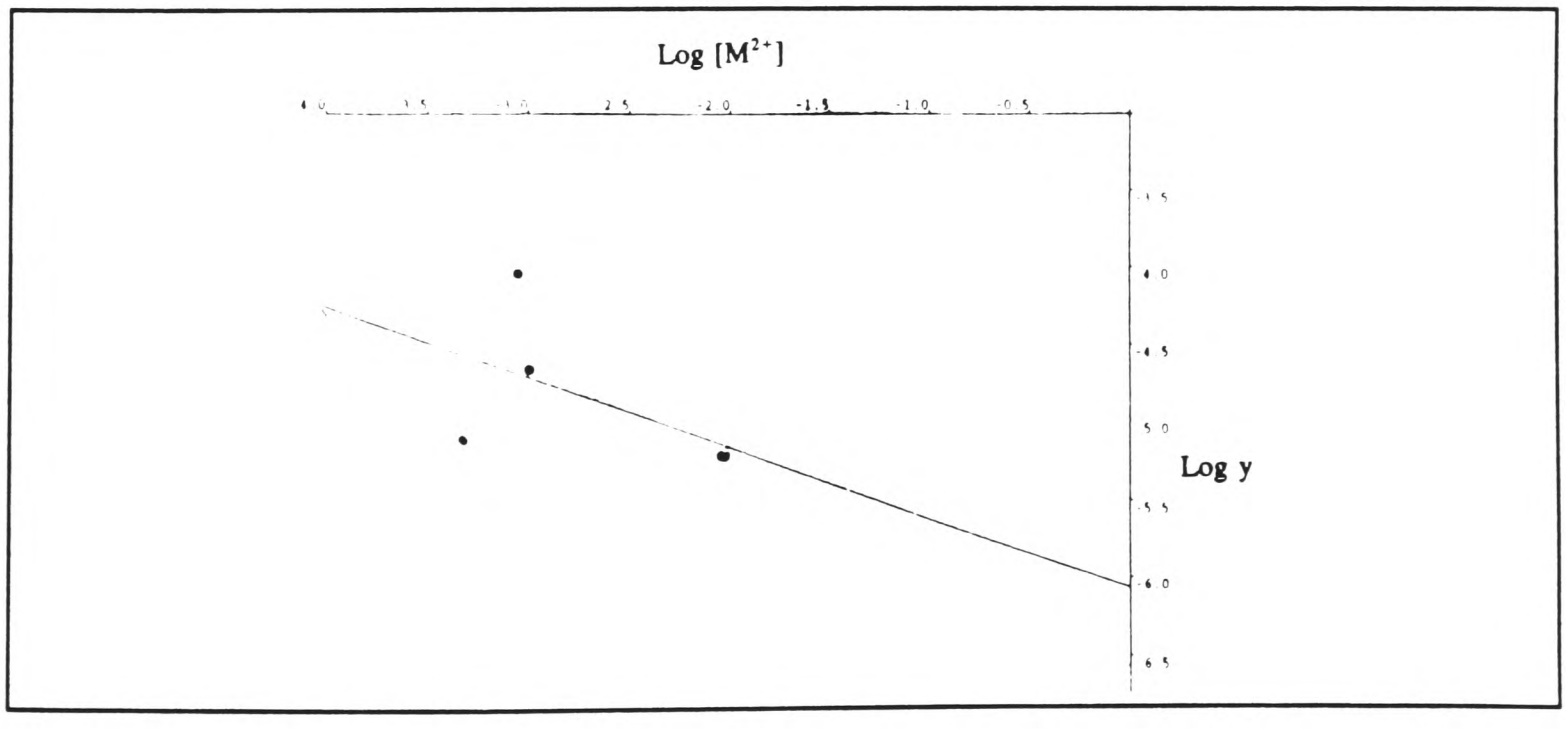

Figure 4.40: The plot of log y against log $[Ba^{2+}]$ for polyacrylic acid molecular weight 2000.

cation is insignificant this would be seen from the plots of log y against log $[M^{2+}]$, and then the data might be reanalysed using the total cation concentration. Hence these plots of log y against log $[M^{2+}]$ are shown in figures 4.39 and 4.40 below.

As can be seen these two plots are approximately linear though with a degree of scatter at low cation concentrations, which is as would be expected as this is the region where the influence of Ca^{2+} produced at the surface would become most significant. The gradients of these lines yield values for x of 0.49 for Mg^{2+} and 0.47 for Ba^{2+}. Again each metal ion complexes with approximately two polyacrylic molecules.

If the intercepts of these two plots (4.39 and 4.40) are taken and the values of $K_{eq}K_L$ obtained they are 8.13 ($\pm$ 0.2) $\times$ 10^5 for Mg^{2+} and 11.80 ($\pm$ 0.2) $\times$ 10^5 for Ba^{2+}. These values compare with 5.09 ($\pm$ 0.08) $\times$ 10^5 for 2000 M.W. polyacrylic acid with added Ca^{2+}. The values are close, but not within the estimated errors, so all three cations are not equivalent. This means that it is not possible to reanalyse the results including the effect of Ca^{2+} produced at the surface and hence reduce the errors at low added background cation concentrations.

4.5.8 Discussion

The value of K_LK_{eq} can be taken as a measure of the relative inhibitory strength of each complex, as used in the previous section. In particular it is possible to calculate from the value of $K_{eq}K_L$, the amount of inhibitor in grams needed per litre of solution to produce a specific surface coverage, given the known concentration of background calcium present. A coverage of 50%, and two calcium concentrations were chosen (1×10^{-4} M and 1×10^{-1} M) these representing no added calcium, and calcium added in large quantities.

These values of $K_{eq}K_L$ and the amount of polyacrylic acid needed for 50% coverage are tabulated in the following two tables, Table 4.11 which compares the three different molecular weights, and Table 4.12 which compares the three different cations.

Table 4.11 $K_L K_{eq}$ for different Molecular Weights of Polyacrylic acid and the grams per litre needed for a coverage of 50%

Molecular Weight (M.W.)	Cation	$K_L K_{eq}$ / $(mol/dm^{-3})^{-x}$	x	milligrams/litre of PAA needed for $\theta = 0.5$	
				$[Ca^{2+}]=$ 1×10^{-1} mol dm^{-3}	$[Ca^{2+}]=$ 1×10^{-4} mol dm^{-3}
2,000	Ca	5.09 ($\pm$0.01) $\times 10^5$	0.49 ($\pm$0.03)	12.43	392.9
4,800	Ca	31.10 ($\pm$0.04) $\times 10^5$	0.48 ($\pm$0.06)	5.08	160.8
14,800	Ca	52.36 ($\pm$0.06) $\times 10^5$	0.44 ($\pm$0.06)	9.06	286.5

Table 4.11 $K_L K_{eq}$ for Polyacrylic acid with different Divalent Cations

Molecular Weight (M.W.)	Cation	$K_L K_{eq}$ / $(mol/dm^{-3})^{-x}$	x	PAA needed for $\theta = 0.5$ ($[M^{2+}] = 1 \times 10^{-1}$ mol dm^{-3})	
				mg L^{-1}	moles L^{-1}
2,000	Ca^{2+}	5.09 ($\pm$0.01) $\times 10^5$	0.49 ($\pm$0.03)	12.43	6.07×10^{-6}
2,000	Mg^{2+}	8.13 ($\pm$0.02) $\times 10^5$	0.49 ($\pm$0.06)	7.78	3.80×10^{-6}
2,000	Ba^{2+}	11.79 ($\pm$0.04) $\times 10^5$	0.47 ($\pm$0.03)	5.36	2.50×10^{-6}

Comparing the number of grams needed to create equal surface coverage from Table 4.11 gives the inhibitory strength for different molecular weights of polymer. From this it is apparent that the effectiveness of inhibition increases with molecular weight from 2,000 to 4,800 (to Antiprex) followed by a subsequent drop between 4,800 and 14,800 (Antiprex to Narlex). The area each chain can cover increases with increasing chain length, so it might be expected that inhibition would also increase with chain length.

A maximum adsorption of polyacrylic acid with chain length has been observed previously [159, 160] in studies investigating the affect of sodium polyacrylic as a stabiliser $CaCO_3$ slurries. The decrease in adsorption after this molecular weight is thought to be due to the polymer being able to adopt a more coiled structure in solution as its chain length increases. A more coiled chain could possibly adopt a less 'flat' conformation on the surface and hence give less coverage per gram of polymer [159,160].

A combination of these two effects, would explain the results observed in this work. Possible coverage increases with increasing chain length, but also a more coiled conformation is adopted. So there are two counterbalancing phenomena which may explain the observed maximum.

As seen in Table 4.12 both Mg^{2+} and Ba^{2+} have a greater effect on the inhibition of polyacrylic acid than Ca^{2+}, this increase though is relatively small. However the number of grams of polyacrylic acid needed for 50% coverage, is approximately half as many with both Ba^{2+} and Mg^{2+}, as with Ca^{2+} as the added cation.

4.6 Conclusions

In comparing the relative strength of monomeric inhibitors with polyacrylic acid the situation is complicated as for monomeric inhibitors the value measured is K_L where as for polyacrylic acid it is a combined term $K_L K_{eq}$. However again (as in tables 4.11 and 4.12), the number of grams per litre of the specific inhibitor needed to give a surface coverage of 50% may be calculated from the experimental results to allow comparison with polyacrylic acid. Table 4.13 tabulates these values for the previously studied small inhibitors (maleic acid, *meso*-tartaric acid, phthalic acid, and homo-phthalic acid) and also polymaleic acid.

Table 4.13 Comparison the inhibition strength in terms of the number of grams of inhibitor needed to effect 50% coverage, for various inhibitors.

Inhibitor	M.W.	K_L	milligrams / litre of inhibitor needed for $\theta=0.5$
Maleic acid	116	4,800	24
meso- Tartaric acid	148	1,400	105
Homo-phthalic acid	180	1,250	144
Phthalic acid	166	604	275
Polymaleic acid	1082	2200	491
Polyacrylic acid ($[Ca^{2+}]= 1 \times 10^{-1}$ mol dm^{-3})	2,000	N/A	12
Polyacrylic acid ($[Ca^{2+}]= 1 \times 10^{-4}$ mol dm^{-3})	4800	N/A	160
Polyacrylic acid ($[Ca^{2+}]= 1 \times 10^{-1}$ mol dm^{-3})	4,800	N/A	5

From the above table with low concentrations of background calcium for polyacrylic acid it is possible to give an overall inhibition order of:

maleic acid > *meso*-tartaric acid ~ homo-phthalic acid > polyacrylic acid > phthalic acid > polymaleic acid.

The polymers seem to be generally less efficient inhibitors than the monomers on a weight needed for equal coverage basis. Also polyacrylic acid for all three molecular weights studied is a more efficient inhibitor than polymaleic acid (M.W. 2200).

If it is assumed that none of the inhibitors show any alteration in behaviour with high levels of background calcium, then for $[Ca^{2+}]=1 \times 10^{-1}$ mol dm^{-3} a different inhibition order would be seen:

polyacrylic acid > maleic acid > *meso*-tartaric acid ~ homo-phthalic acid > phthalic acid > polymaleic acid.

So for the 2000 M.W. polymer with this much added background calcium, PAA is a more efficient inhibitor on the weight needed for a specific coverage than even maleic acid.

From the previous discussion of the relative inhibitory strength with molecular weight, it is seen that the 2000 M.W. polymer is the *weakest* inhibitor of the various molecular weights. Also it has been seen from the discussion comparing the three divalent cations that the complexes formed with calcium are the *weakest* inhibitors. Therefore as this order holds with the weakest combination of molecular weight and cation, then even for the other molecular weights and/or cations, polyacrylic acid would still cause the strongest inhibition of all the inhibitors.

Given the situations in which scale inhibitors typically applied it is quite likely that there will be high concentrations of calcium and other divalent cations present. So this result could be of some significance.

Overall in this chapter it has been shown that then channel flow cell method is capable of giving reliable kinetic information about the inhibition of calcite dissolution. Specific conclusions were drawn for simple monomeric inhibitors; inhibition strength can still be explained simply in terms of molecular size and shape. Significantly it has also been shown that polyacrylic acid adsorbs on the calcite surface via the formation of a complex with divalent cations, with approximately two polymer chains binding to each cation. In addition, investigating the overall efficiency of inhibition it is seen that polyacrylic acid is a more efficient inhibitor in terms of weight of inhibitor needed than polymaleic acid. Further when there are high background concentrations of divalent cations in solution polyacrylic acid is the most efficient in terms of weight of inhibitor needed of all of the inhibitors studied at low pH so far.

CHAPTER 5

THE KINETICS OF CALCITE DISSOLUTION AT HIGH pH (> 7)

5.1 Introduction

This chapter deals with the deduction of the heterogeneous kinetics describing the dissolution and precipitation of calcium carbonate at high pH (> 7). There has been a considerable body of previous work studying the dissolution of calcite at high pH, as outlined in chapter 1. However these studies suffered from the lack of well defined hydrodynamics, and frequently a lack of control over surface morphology. In order to distinguish between previously suggested rate laws for high pH dissolution it is necessary to over cover these experimental limitations. It is also necessary to be able to predict behaviour for each candidate rate law, therefore enabling the evaluation of the validity of these rate laws by comparison with reliable experimental data. All of these requirements are achieved by use of the channel flow cell, and the Backwards Implicit (BI) finite difference numerical method for theoretical modelling.

Then, as none of the rate laws existing in the literature are found to adequately describe the dissolution kinetics over the very wide range of experimental conditions used, a new rate law with a sound mechanistic rationale is developed which accurately describes all observed experimental data.

5.2 Experimental details

The method used to investigate calcite dissolution at high pH in this chapter, is the channel flow cell as outlined in Chapter 3. Solution is flowed through a rectangular duct, under laminar flow conditions via a gravity feed, and over the surface of a calcite crystal (Iceland Spar) which is flush in the wall of the channel. Immediately downstream is an electrochemical detector, in this case a pH micro electrode. The pH response is measured on a Jenway 3030 pH meter, which is switched to the mV scale. The mV response with flow rate, as determined by capillary diameter and height of the reservoir above the outlet, is recorded.

The well defined flow (Chapter 2) permits modelling of the convection/diffusion processes within the cell. Then the BI method can be used to compute the solution profiles of H^+, Ca^{2+}, and other solution species, for each investigated rate equation and experiment, therefore allowing prediction of the experimental detector response and its flow rate dependence. This allows comparison of theory and experiment, from which mechanistic information can be obtained. Typical dimensions of the cell parameters were outlined in Chapter 3.

5.3 Kinetics

In general the dissolution of calcite occurs by the following reactions.

$$H^+ + CaCO_3 \rightarrow Ca^{2+} + HCO_3^- \quad (5.1)$$

$$CaCO_3 + H_2CO_3 \rightarrow Ca^{2+} + 2HCO_3^- \quad (5.2)$$

$$CaCO_3 + H_2O \rightarrow Ca^{2+} + HCO_3^- + OH^- \quad (5.3)$$

At high pH equation (5.1) can be ignored as it has minimal influence over the reaction. Also under the conditions adopted reaction (5.2) is eliminated by the absence of dissolved carbon dioxide in the bulk solution, due to vigorous degassing with argon. So equation (5.3) is the only important surface reaction.

However it is also necessary to consider the following homogeneous solution kinetics at high pH,

$$CO_3^{2-} + H_2O \rightleftharpoons HCO_3^- + OH^- \quad (5.4)$$

$$H^+ + OH^- \rightleftharpoons H_2O \quad (5.5)$$

in order to accurately investigate the surface and solution speciation, and reaction kinetics.

5.4 Theory

In this section theory will be derived which relates the potentiometric response of a pH electrode in the flow system to the mechanism of dissolution/precipitation reaction taking place at the calcite surface. It predicts the influence of solution flow rate and flow geometry. This allows the prediction of experimental response for a given theory, thus enabling the testing of the validity of the latter. The problem is complicated

as in the low pH case discussed in the previous chapter, by the necessity to include the solution equilibria (5.4), (5.5) as well as the heterogeneous reaction (5.3)

The steady state convective-diffusion equation describing the distribution of Ca^{2+} ions in the channel flow cell is

$$\frac{\partial[Ca^{2+}]}{\partial t} = 0 = D_{Ca^{2+}} \frac{\partial^2[Ca^{2+}]}{\partial y^2} - v_x \frac{\partial[Ca^{2+}]}{\partial x} \tag{5.6}$$

where D_{Ca} is the diffusion coefficient of Ca^{2+}, x and y are the coordinates in the channel flow cell, and v_x is the solution in the x-direction. This last term is given by

$$v_x = v_o(1 - (h-y)^2/h^2) \tag{5.7}$$

where v_o is the solution velocity in the centre of the channel and h is the channel half-height.

The boundary conditions are as follows:

(i) *Upstream of the Crystal*

The Ca^{2+} concentration was that present in the bulk solution entering the flow cell:

$$x = 0, \quad 0 < y < 2h, \quad [Ca^{2+}] = [Ca^{2+}]_{bulk} \quad \& \quad [CO_3^{2-}] = 0 \tag{5.7}$$

(ii) *Zone of the Crystal*

At the surface of the crystal the flux of Ca^{2+} entering the solution was given by the appropriate rate law for the dissolution/precipitation reaction. The exact form of this is the will be discussed later. At present the net dissolution flux will be considered

as some function, f, of the concentrations of Ca^{2+} and CO_3^{2-} at the Outer Helmholtz Plane:

$$0 < x < x_c\ ,\quad y = 0\ ,\quad D\frac{\partial[Ca^{2+}]}{\partial y} = f\{[Ca^{2+}]_o, [CO_3^{2-}]_o, K_{sp}\} \tag{5.9}$$

where K_{sp} is the solubility product of $CaCO_3$. There was an additional no-flux condition at the channel wall opposite the crystal:

$$0 < x < x_c\ ,\quad y = 2h\ ,\quad D\frac{\partial[Ca^{2+}]}{\partial y} = 0 \tag{5.10}$$

where x_c is the length of the crystal.

(iii) *Downstream of the Crystal*

Over the surface of the pH electrode and over the gap between the crystal and the detector a no-flux condition operated:

$$x > x_c\ ,\quad y = 0\ ,\quad D\frac{\partial[Ca^{2+}]}{\partial y} = 0 \tag{5.11}$$

and again at the channel wall:

$$x > x_c\ ,\quad y = 2h\ ,\quad D\frac{\partial[Ca^{2+}]}{\partial y} = 0 \tag{5.12}$$

As outlined in Chapter 2 and discussed previously in Chapter 4 for low pH (< 4) dissolution, the BI method [113] can be used to solve transport problems in channel electrodes. The method involved only vector calculations where the vectors describe concentrations in the y-direction for different values of x. The calculation proceeded 'downstream', each vector enabling the calculation of the next, starting from the vector defining the boundary conditions specified for upstream of the crystal. It can be seen that the computation of $[Ca^{2+}]$ as a function of x and y throughout the flow cell could be

readily achieved in this way if the quantities $[Ca^{2+}]_o$ and $[CO_3^{2-}]_o$ in equation (5.9) were known. However as this was not the case, the following procedure was followed:

(i) In the zone of the crystal the values of $[Ca^{2+}]_o$ and $[CO_3^{2-}]_o$ from the 'preceding' vector were used as an initial guess to enable the calculation of Ca^{2+} along the vector of interest.

(ii) Next reactions (5.4) and (5.5) were assumed to be at equilibrium so that

$$a_H \cdot a_{OH^-} = K_w \tag{5.13}$$

and

$$\frac{a_H \cdot [CO_3^{2-}]}{[HCO_3^-]} = K_{a2} \tag{5.14}$$

where K_{a2} is the (mixed) second dissociation constant of carbonic acid [11]. The equilibrium assumption was justified by the values of pH measured close to the electrode surface (*vide infra*) together with the known [162] rate constant for the reaction

$$OH^- + HCO_3^- \xrightarrow{k=6\times10^9 M^{-1}s^{-1}} H_2O + CO_3^{2-} \tag{5.15}$$

Moreover if it is assumed that Ca^{2+}, HCO_3^- and CO_3^{2-} have similar diffusion coefficients then stoichiometric dissolution of $CaCO_3$ implies that at each point in space,

$$[Ca^{2+}] - [Ca^{2+}]_{bulk} = [CO_3^{2-}] + [HCO_3^-] \tag{5.16}$$

Also since dissolution must preserve electro-neutrality,

$$2[Ca^{2+}] - 2[Ca^{2+}]_{bulk} = 2[CO_3^{2-}] + [HCO_3^-] + [OH^-] - [OH^-]_{bulk} \tag{5.17}$$

where $[\ ]_{bulk}$ denotes bulk concentrations and it has been assumed that $[OH^-] \gg [H^+]$.

Equations (5.13), (5.14), (5.16) & (5.17) could be combined to give

$$\left([Ca^{2+}] - [Ca^{2+}]_{bulk} + \frac{K_w}{\gamma_{OH^-} a_{H^+,bulk}}\right)\frac{a_{H^+}^2}{K_2}$$

$$+ \left(a_{H^+,bulk}^{-1} - K_2^{-1}\right)\frac{K_w a_{H^+}}{\gamma_{OH^-}} - \frac{K_w}{\gamma_{OH^-}} = 0 \qquad (5.18)$$

where γ_{OH^-} is the activity coefficient of OH^-. This is a quadratic equation in a_{H+} which, knowing $[Ca^{2+}]$ from (i), was solved to give a_{H+} along the vector of interest.

(iii) a_{H+} then, in combination with equations (5.14) and (5.16), permitted the deduction of $[HCO_3^-]$ and $[CO_3^{2-}]$ along the same vector.

The new values of $[HCO_3^-]_o$ and $[CO_3^{2-}]_o$ thus generated were used to provide improved values for equation (5.9) and the steps in (i) to (iii) were repeated until all concentrations had converged. Typically this required about five iterations to give concentrations correct to six significant figures.

(iv) Having used the above procedure to find the concentration profiles in the zone of the crystal, the vector describing the $[Ca^{2+}]$ profile along the downstream edge of the crystal was used to provide a 'starting' vector for the zone downstream of the crystal. The calculation in this zone proceeded without the need for iteration; a_{H+} was calculated from $[Ca^{2+}]$ via equation (5.18) and hence the other concentrations were deduced.

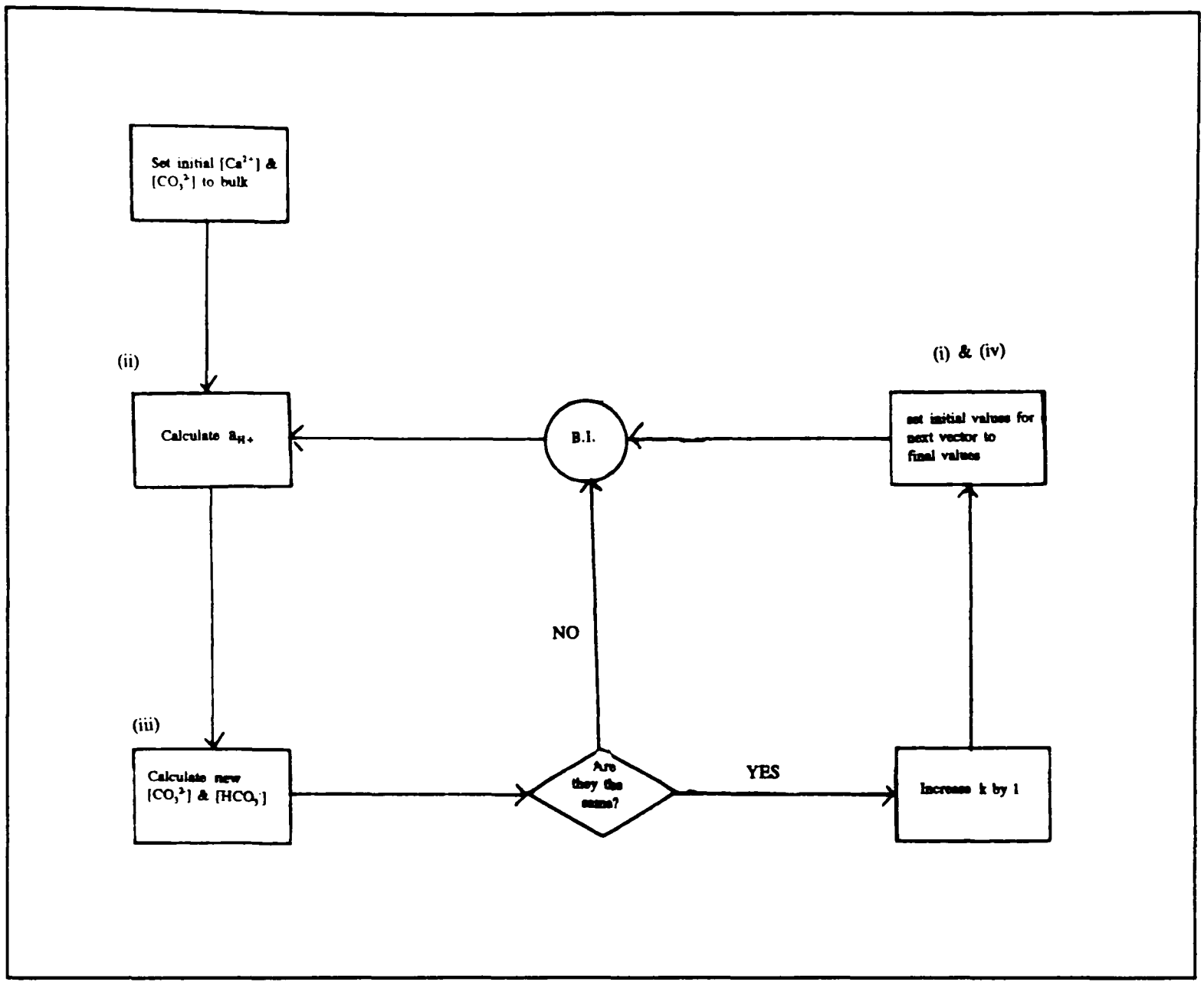

Figure 5.1 Flow chart showing the strategy for calculating the concentrations of the species in the flow cell using BI, with an iterative method to find a_{H+}.

Having calculated the speciation throughout the channel cell in the above manner the H^+ activity was averaged over the surface of the pH sensor and thus the dependence of the measured pH on the proposed rate law (equation (5.9)) and flow rate for a defined channel geometry was deduced. The following thermodynamic quantities, pertaining to 25°C, were assumed in this modelling:

(a) $K_w = 1.008 \times 10^{-14}$ mol^2 dm^{-6} [163].

(b) $K_{a2} = 1.409 \times 10^{-10}$ mol dm^{-3}. This was deduced using the value of Harned and Scholes at infinite dilution [164]. With this value corrected for the ionic strength at which the experiments described below were conducted (0.5 mol dm^{-3}), with the activity

coefficients for CO_3^{2-} and HCO_3^- as measured by Walker *et al.* [165]. These activity coefficient values agree almost exactly with those predicted by the Davies equation [166]

$$\log \gamma = -Az^2\left(\frac{I^{1/2}}{1 + I^{1/2}} - 0.2I\right) \tag{5.19}$$

where z is the charge on the ion, I is the ionic strength of the solution and A is a constant dependent on temperature and dielectric constant of the solvent, which for water at 25°C is 0.509.

(c) $\gamma_{OH^-} = 0.69$. This was predicted by the Davies equation (5.19) for an ionic strength of 0.5 M.

(d) $K_{sp} = 6.26 \times 10^{-8}$ mol^2 dm^{-6}. This was deduced from the experimental value of Inskeep and Bloom [75] corrected for the activity coefficients of Ca^{2+} and CO_3^{2-} at 0.5 mol dm^{-3}. The activity coefficient of Ca^{2+} was calculated from the Davies equation and that of CO_3^{2-} was an experimental value [165]. The value of K_{sp} closely agrees with that measured by Sjöberg [167]. Table 5.1 lists other literature values of the calcium carbonate solubility product.

(e) The diffusion coefficient of Ca^{2+} ions D = 7.93×10^{-6} cm^2 s^{-1}. This was calculated from the ionic conductivity of Ca^{2+} [168] using the Einstein relation [169] after converting into ionic mobility. This was in good agreement with the value of 7.4×10^{-6} cm^2 s^{-1} obtained by Sjörberg [64]. This result was obtained from chemistatic rotating disc experiments on Iceland spar in 0.7 M KCl solutions, with slow rotation speeds so that the rate of dissolution varied linearly with rotations speed indicating that the reaction was diffusion controlled (at least as far as could be detected by a remote pH electrode measuring bulk solution changes). Other work in the literature assumed an arbitrary value of 1×10^{-5} cm^2 s^{-1} [16,56].

Table 5.1. Solubility Product of Calcite

Reference	$K_{sp} = [Ca^{2+}][CO_3^{2-}]$ /mol^2 dm^{-6}	Ionic Strength /mol dm^{-3}	Temperature /°C
Inskeep & Bloom [75]	$3.35 \pm 0.15 \times 10^{-9}$	0	25
Jacobson & Langmuir [170]	3.80×10^{-9}	0	25
Plummer & Busenburg [171]	$3.31 \pm 0.15 \times 10^{-9}$	0	25
Sjöberg [167]	6.05×10^{-8}	0.7	20
Compton & Daly [72]	2.7×10^{-8}	0.3	25
Martynova *et al.* [172]	3.6×10^{-9}	0	25
Ghiringhelli & Bianucci [173]	2.9×10^{-9}	0	25
Krauskopf [166]	4.47×10^{-9}	0	25
Akin & Lagerwerff [174]	5.0×10^{-9}	0	25
Grèzes & Basset [175]	4.4×10^{-9}	0	25
Larson & Buswell [176]	4.55×10^{-9}	0	25
Millero *et al.* [177]	$3.47 \pm 0.24 \times 10^{-9}$	0	25
Nancollas & Reddy [24]	$4.7 \pm 0.3 \times 10^{-9}$	0	25
Frear & Johnston [178]	4.8×10^{-9}	0	25

Reference	$K_{sp} = [Ca^{2+}][CO_3^{2-}]$ /mol^2 dm^{-6}	Ionic Strength /mol dm^{-3}	Temperature /°C
Wolf *et al.* [179]	$3.4 \pm 0.7 \times 10^{-9}$	0	25
Langmuir [180]	$3.98 \pm 0.19 \times 10^{-9}$	0	25
Miller [181]	3.5×10^{-9}	0	25
Christ *et al.* [182]	$3.3 \pm 0.4 \times 10^{-9}$	0	20

Numerous equations, both empirical and mechanistic, for calcite dissolution/precipitation appear in the literature, as discussed in Chapter 1, and these are summarised in Table 5.2. Each of these rate laws was incorporated into the surface boundary condition in turn. To illustrate this the matrix elements for the Nancollas-Reddy equation are derived below.

5.4.1 Derivation of Matrix Elements

The Nancollas-Reddy rate law was incorporated into the surface boundary condition of the Backwards Implicit calculation as follows. According to Fick's first law the flux of calcium ions entering solution at the solid-liquid interface was given by

$$flux = D\frac{\partial g^{A}}{\partial y}\bigg|_{j=0} = -k_{NR} + \frac{k_{NR}}{K_{sp}} g^{A}_{0,k+1} g^{C}_{0,k+1} \qquad (5.20)$$

where D is the diffusion coefficient of calcium ions, k_{NR} is a rate constant, K_{sp} is the solubility product of calcite and $g^{A}_{j,k}$ is the concentration of Ca^{2+} ions and $g^{C}_{j,k}$ concentration of CO_3^{2-} ions at the point $x = k$, $y = j$.

Table 5.2. Literature Rate Laws for Calcite Dissolution/Precipitation

Reference	Net Dissolution Flux, J_{net}
Dorange and Guetchidjian [59][1]	$k_{DG}\left\{[Ca^{2+}]_{eq} - [Ca^{2+}]_o\right\}$
Sjöberg [167]	$k_S\left\{\sqrt{K_{sp}} - \sqrt{[Ca^{2+}]_o[CO_3^{2-}]_o}\right\}$
Plummer [55,57]	$k_P - k_P' a_{Ca^{2+}} a_{HCO_3^-}$
Nancollas and Reddy [24]; Inskeep and Bloom [75]	$k_{NR}\left\{1 - \frac{[Ca^{2+}]_o[CO_3^{2-}]_o}{K_{sp}}\right\}$
Davies and Jones [80,81]; Kazmierczak *et al.* [10]	$k_{DJ}\left\{\sqrt{K_{sp}} - \sqrt{\gamma_\pm^2[Ca^{2+}]_o[CO_3^{2-}]_o}\right\}^2$
Chiang and Donohue [95]; Reddy [32,46] & Reddy and Nancollas [183][2]	$k_{CD}\left\{[Ca^{2+}]_{eq}^2 - [Ca^{2+}]_o^2\right\}$

[1] $[Ca^{2+}]_{eq}$ is the equilibrium calcium ion concentration in a saturated solution of calcite [59].

[2] $\gamma_\pm$ is the mean ionic activity coefficient.

At the surface the differential term was approximated as follows

$$\left.\frac{\partial g^{A}}{\partial y}\right|_{j=0} = \frac{g^{A}_{1,k+1} - g^{A}_{0,k+1}}{\Delta y} \tag{5.18}$$

Equations (5.20) and (5.18) were combined to give

$$g^{A}_{0,k+1} = \frac{D g^{A}_{1,k+1} + \Delta y k_{NR}}{D + \Delta y \dfrac{k_{NR}}{K_{sp}} g^{C}_{0,k+1}} \tag{5.19}$$

At the crystal surface equation (2.66) gives

$$g^{A}_{1,k} = -\lambda_1 g^{A}_{0,k+1} + (2\lambda_1 + 1) g^{A}_{1,k+1} - \lambda_1 g^{A}_{2,k+1} \tag{5.20}$$

Substituting the surface concentration term (5.19) in equation (5.20) this becomes

$$d_1 = b_1 g^{A}_{1,k+1} + c_1 g^{A}_{2,k+1} \tag{5.21}$$

where

$$d_1 = g^{A}_{1,k} + \frac{\lambda_1 k_{NR} \Delta y}{D + \dfrac{k_{NR}}{K_{sp}} \Delta y g^{C}_{0,k+1}} \tag{5.22}$$

$$b_1 = \left(2 - \frac{D}{D + \dfrac{k_{NR}}{K_{sp}} \Delta y g^{C}_{0,k+1}} \right) \lambda_1 + 1 \tag{5.23}$$

$$c_1 = -\lambda_1 \tag{5.24}$$

Thus equation (5.21) incorporates the Nancollas-Reddy rate equation into the BI calculation which then proceeded as described above.

The other equations cited in Table 5.2 were converted into the surface boundary condition in a similar fashion. Plummer *et al.* [55] demonstrated that the Plummer

equation was effectively equivalent to the Nancollas-Reddy equation at high pH (see equation (1.21)). So only one of these equations needs to be considered.

There was a slight modification to the approach for rate laws with non-unity powers of calcium ion concentration (i.e. Sjöberg, Davies-Jones, Chiang-Donohue). To obtain an equivalent expression to equation (5.19) for $g^{A}_{0,k+1}$ would have involved solving a polynomial. This was avoided by using the (known) previous vector's surface concentration for the first calculation on a particular vector. Subsequent iterations used updated concentration values. Thus for the Sjöberg rate equation at the crystal surface the flux was

$$J = D\left(\frac{g^{A}_{1,k+1} - g^{A}_{0,k+1}}{\Delta y}\right) = -k_S\sqrt{K_{sp}} + k_S\sqrt{g^{A}_{0,k}\, g^{C}_{0,k}} \tag{5.25}$$

which rearranges to

$$g^{A}_{0,k+1} = g^{A}_{1,k+1} + \frac{\Delta y k_S\left\{\sqrt{K_{sp}} - \sqrt{g^{A}_{0,k}\, g^{C}_{0,k}}\right\}}{D} \tag{5.26}$$

Substitution of equation (5.26) into equation (5.20) yielded equation (5.21) but with

$$b_1 = \lambda_1 + 1 \tag{5.27}$$

$$c_1 = -\lambda_1 \tag{5.28}$$

and, for the first iteration

$$d_1 = g^{A}_{1,k} + \frac{\lambda_1 \Delta y k_S\left\{\sqrt{K_{sp}} - \sqrt{g^{A}_{0,k}\, g^{C}_{0,k}}\right\}}{D} \tag{5.29}$$

but for subsequent iterations

$$d_1 = g^{A}_{1,k} + \frac{\lambda_1 \Delta y k_S\left\{\sqrt{K_{sp}} - \sqrt{g^{A}_{0,k+1}\, g^{C}_{0,k+1}}\right\}}{D} \tag{5.30}$$

Both the Dorange-Guetchidjian and Chiang-Donohue equations contain an equilibrium calcium ion concentration, $[Ca^{2+}]_{eq}$. This could be calculated for a given bulk calcium ion concentration since at equilibrium

$$K_{sp} = [Ca^{2+}]_{eq}[CO_3^{2-}]_{eq} \tag{5.31}$$

This together with equations (5.13), (5.14), (5.16) and (5.17) yielded the following quartic equation in $[CO_3^{2-}]_{eq}$

$$[CO_3^{2-}]_{eq}^{4} + \left(2[Ca^{2+}]_{bulk} - \frac{K_w}{\gamma_{OH^-} a_{H^+,bulk}} - \frac{K_w}{\gamma_{OH^-} K_{a2}}\right)[CO_3^{2-}]_{eq}^{3}$$

$$+ \left([Ca^{2+}]_{bulk}^{2} - 2K_{sp} - \frac{K_w}{\gamma_{OH^-} a_{H^+,bulk}}\right)[CO_3^{2-}]_{eq}^{2} \tag{5.32}$$

$$+ \left(\frac{K_w}{\gamma_{OH^-} a_{H^+,bulk}} - 2[Ca^{2+}]_{bulk}\right)K_{sp}[CO_3^{2-}] + (K_{sp})^2 = 0$$

Equation (5.32) was solved using the method of Grant and Hitchins as used in the NAG Library routine C02AEF. The solution so obtained when combined with equation (5.31) generated $[Ca^{2+}]_{eq}$.

The matrix elements for each rate law derived as described above are summarised in Tables 5.3 and 5.4.

Table 5.3. Matrix Elements for the Channel Cell

		d_j	a_j	b_j	c_j	u_j
$j=1$	crystal	see Table 5.4 & 5.5	-	see Table 5.4 & 5.5	$-\lambda_1$	$\hat{g}_{1,k+1}$
	downstream	$\hat{g}_{1,k}$	-	$\lambda_1 + 1$	$-\lambda_1$	$\hat{g}_{1,k+1}$
$j = 2, ..,J\text{-}2$		$\hat{g}_{j,k}$	$-\lambda_j$	$2\lambda_j + 1$	$-\lambda_j$	$\hat{g}_{j,k+1}$
$j = J\text{-}1$		$\hat{g}_{J-1,k}$	$-\lambda_{J-1}$	$\lambda_{J-1} + 1$	-	$\hat{g}_{J-1,k+1}$

Table 5.4 Surface Boundary Matrix Elements for Literature Rate Laws

Rate Equation	$g^{A}_{0,k+1}$	d_1	b_1
Dorange-Guetchidjan	$\frac{D g^{A}_{1,k+1} + \Delta y k_{DG} g^{A}_{sat}}{D + \Delta y k_{DG}}$	$g^{A}_{1,k} + \frac{\lambda_1 \Delta y k_{DG} g^{A}_{sat}}{D + \Delta y k_{DG}}$	$\left(2 - \frac{D}{D + \Delta y k_{DG}}\right)\lambda_1 + 1$
Sjöberg	$g^{A}_{1,k+1} + \frac{\Delta y k_S \left(\sqrt{K_{sp}} - \sqrt{g^{A}_{0,k} g^{C}_{0,k}}\right)}{D}$	$g^{A}_{1,k} + \frac{\lambda_1 \Delta y k_S \left(\sqrt{K_{sp}} - \sqrt{g^{A}_{0,k+1} g^{C}_{0,k+1}}\right)}{D}$	$\lambda_1 + 1$
Nancollas-Reddy	$\frac{D g^{A}_{1,k+1} + \Delta y k_{NR}}{D + \Delta y \frac{k_{NR}}{K_{sp}} g^{C}_{0,k+1}}$	$g^{A}_{1,k} + \frac{\lambda_1 k_{NR} \Delta y}{D + \frac{k_{NR}}{K_{sp}} \Delta y g^{C}_{0,k+1}}$	$\left(2 - \frac{D}{D + \frac{k_{NR}}{K_{sp}} \Delta y g^{C}_{0,k+1}}\right)\lambda_1 + 1$
Davies-Jones	$g^{A}_{1,k+1} + \frac{\Delta y k_S \left(\sqrt{K_{sp}} - \sqrt{g^{A}_{0,k} g^{C}_{0,k}}\right)^2}{D}$	$g^{A}_{1,k} + \frac{\lambda_1 \Delta y k_{DJ} \left(\sqrt{K_{sp}} - \sqrt{g^{A}_{0,k+1} g^{C}_{0,k+1}}\right)^2}{D}$	$\lambda_1 + 1$
Chiang-Donohue	$g^{A}_{1,k+1} + \frac{\Delta y k_{CD} \left\{\left(g^{A}_{sat}\right)^2 - \left(g^{A}_{0,k}\right)^2\right\}}{D}$	$g^{A}_{1,k} + \frac{\lambda_1 \Delta y k_{DG} \left\{\left(g^{A}_{sat}\right)^2 - \left(g^{A}_{0,k+1}\right)^2\right\}}{D}$	$\lambda_1 + 1$

5.5 Results

Experiments were conducted on solutions containing 0.5 mol dm^{-3} KCl and of varying bulk calcium ion concentrations of between 0 and 10^{-2} mol dm^{-3}. Figures 5.2 and 5.3 show some typical results in the form of plots of $[H^+]$, deduced from the detector pH electrode, as a function of solution flow rate. Clearly the solution pH decreases with flow rate. This is attributable to the fact that less surface reaction can take place for a given volume element of solution the faster it flows and the quicker its transit time over the crystal surface. Also at faster rates of flow, the perturbation of the solution concentrations from their bulk values is less and this will again have the effect of lowering the pH.

The data in plots such as Figures 5.2 and 5.3 were modelled using the theory presented above and with each of the rate laws in Table 5.2 in turn for equation (5.9) as a boundary condition. The fitting procedure involved varying the rate constant in each rate law for a given data set until the closest fit between model and experiment was achieved across the flow rate range. Examples of 'best fits' achieved with these rate laws are shown in Figures 5.2 and 5.3. Of the literature rate laws the Davies-Jones equation gave the best flow rate response. However this did not have a sound mechanistic basis since the model assumed that the positive and negative surface ion concentrations were equal (see Chapter 1) [184], which has been shown experimentally not to be the case on calcite [61,81]. None of the existing rate equations considered were found to give a satisfactory fit across the entire flow rate range for all of our sets of data, for different values of pH_{bulk} and $[Ca^{2+}]_{bulk}$. These rate laws seemed to breakdown first because of the wide range of conditions, especially of the rate of mass

transport, used in our flow cell experiments. Second, the pH detector electrode was

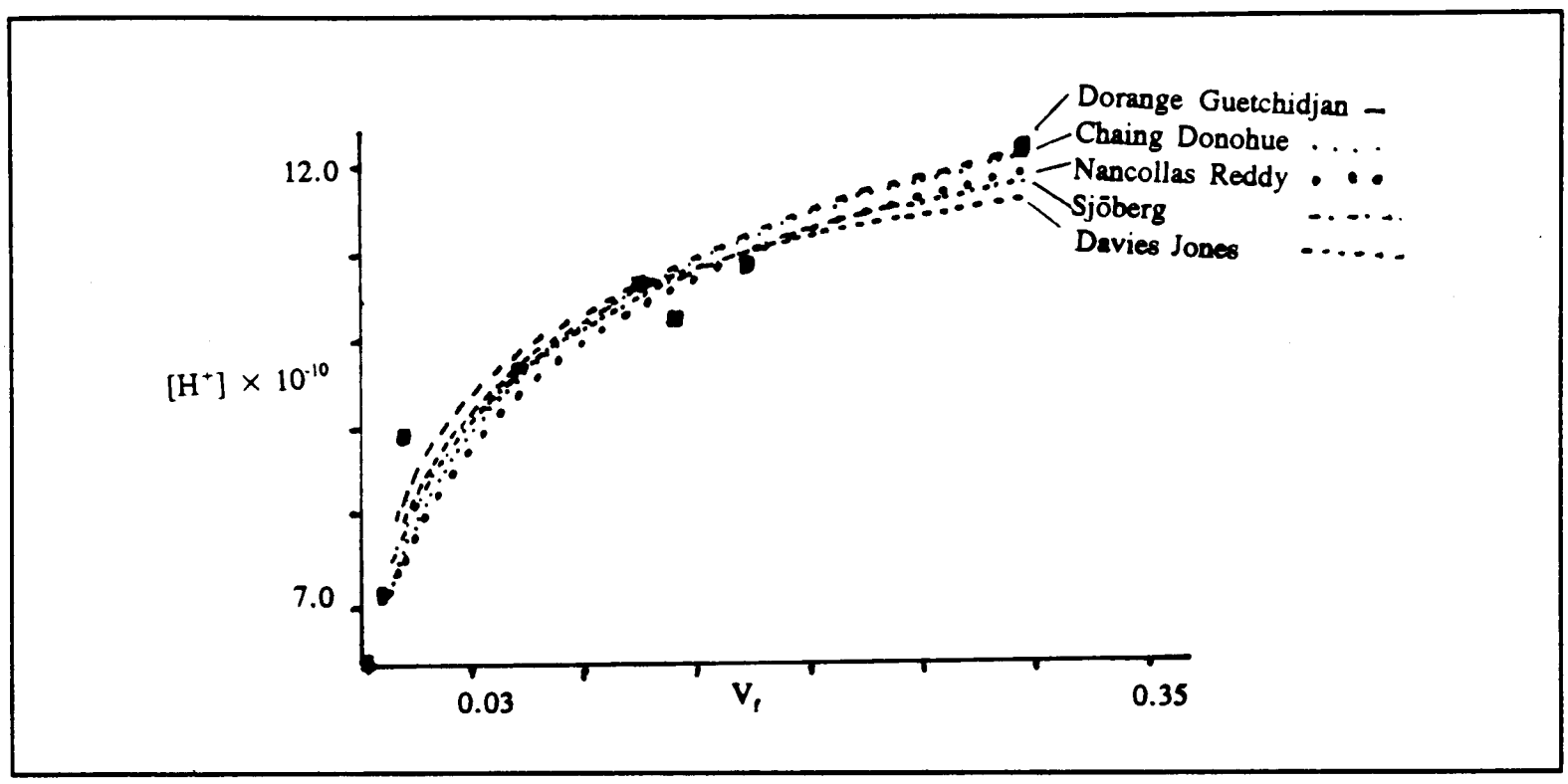

Figure 5.2. The flow rate dependence of the channel cell $[H^+]$ sensor for pH_{bulk} = 8.44 and $[Ca^{2+}]_{bulk}$ = 0. The dashed lines show the theoretical behaviour predicted using the literature rate laws listed in Table 5.2.

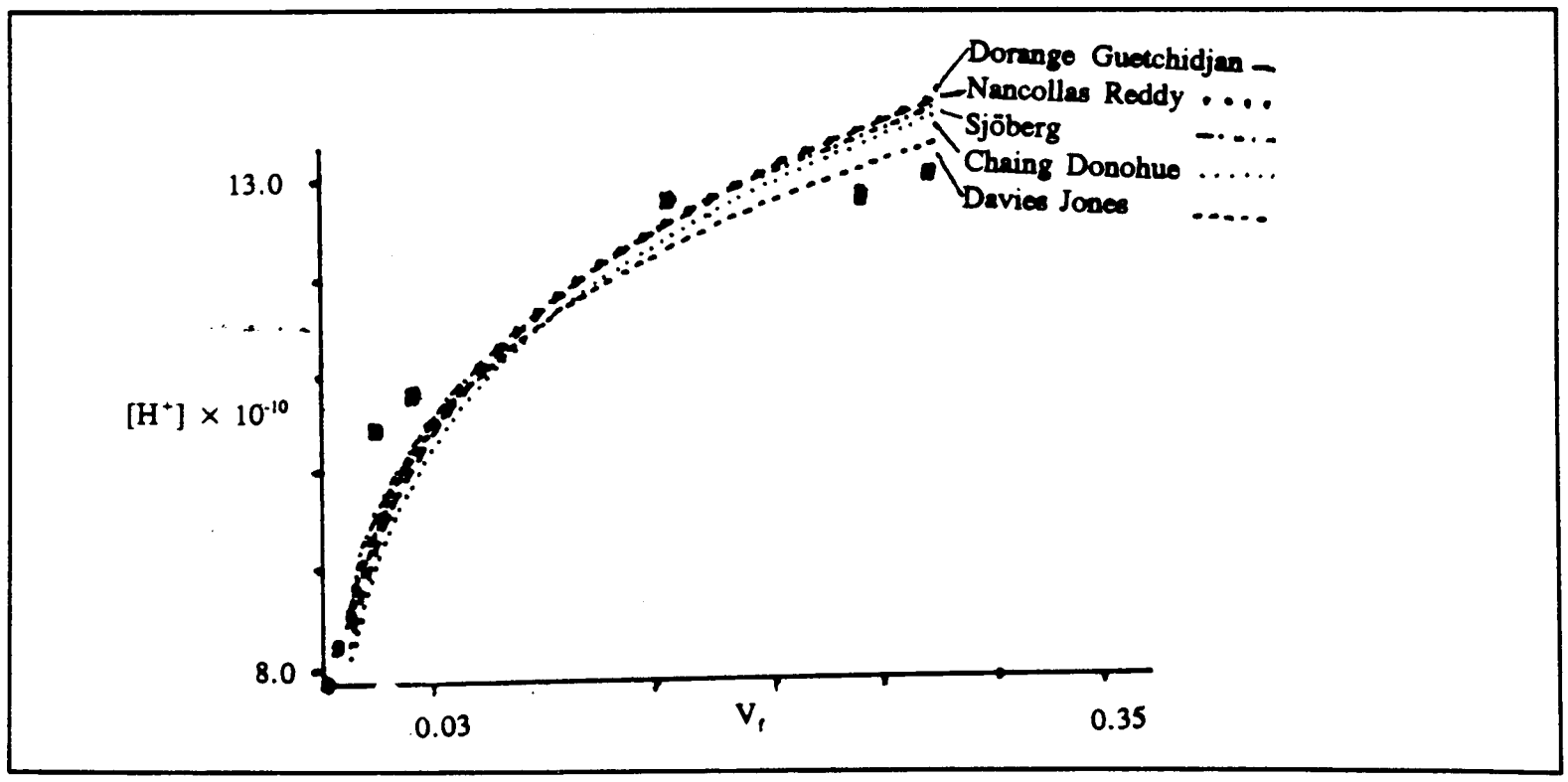

Figure 5.3. The flow rate dependence of the channel cell $[H^+]$ sensor for pH_{bulk} = 8.38 and $[Ca^{2+}]_{bulk}$ = 1.01 mM. The dashed lines show the theoretical behaviour predicted using the literature rate laws listed in Table 5.2.

positioned adjacent to the dissolving crystal, rather than the more remote, and insensitive, sensing typically used in other work. This, on account of the controlled hydrodynamics and theory given above, enabled the inference of the surface concentrations and thus the discrimination between candidate rate laws. It should be noted that the curvature of the experimental pH sensor plots was unique and differed from the response predicted by the existing rate laws.

Given the unsatisfactory assessment of the existing literature rate laws for calcite dissolution/precipitation a new, mechanistically rational approach was developed by adapting the surface reaction/molecule integration mechanism of Chiang and Donohue [95]:

$$Ca^{2+}_{(aq)} \rightleftharpoons Ca^{2+}_{(ads)} \tag{5.71}$$

$$CO_3^{2-}{}_{(aq)} \rightleftharpoons CO_3^{2-}{}_{(ads)} \tag{5.72}$$

$$Ca^{2+}_{(ads)} + CO_3^{2-}{}_{(ads)} \rightleftharpoons CaCO_3{}_{(ads)} \tag{5.73}$$

$$CaCO_3{}_{(ads)} \rightleftharpoons CaCO_3{}_{(lattice)} \tag{5.74}$$

The net dissolution rate can then be written as the balance between a forward dissolution term and a back precipitation term:

$$J_{net} = J_d - J_p \tag{5.75}$$

where,

$$J_d = k_d\left(1 - \theta_{Ca}\right)\left(1 - \theta_{CO_3}\right) \tag{5.76}$$

and

$$J_p = k_p \theta_{Ca} \theta_{CO_3} \tag{5.77}$$

where θ_A indicates the surface coverage of adsorbed A (A = Ca^{2+} or CO_3^{2-}) and k_d and k_p are rate constants for the dissolution and precipitation processes respectively. These

rate terms make no distinction over whether steps (5.73) or (5.74) are rate determining. The transition state of the rate determining step is, however, a neutral species and steps (5.71) and (5.72) are at equilibrium.

It is assumed that the adsorption of Ca^{2+} and CO_3^- ions follows the Langmuir isotherm:

$$\theta_A = \frac{K_A[A]_o}{1 + K_A[A]_o} \tag{5.78}$$

Further at equilibrium, $J_d = J_p$, and that under that condition $[Ca^{2+}]_o[CO_3^{2-}]_o = K_{sp}$. With these assumptions it can be deduced that

$$J_{net}/\text{mol cm}^{-2}\text{s}^{-1} = k_p K_{Ca} K_{CO_3} \left\{ \frac{K_{sp} - [Ca^{2+}]_o[CO_3^{2-}]_o}{(1 + K_{Ca}[Ca^{2+}]_o)(1 + K_{CO_3}[CO_3^{2-}]_o)} \right\} \tag{5.79}$$

where

$$k_d = k_p K_{Ca} K_{CO_3} K_{SP} \tag{5.80}$$

Equation (5.79) was used to interpret the experiments described above. The surface boundary matrix elements for this equation are shown in Table 5.5. As with the Sjöberg equation, combining equations (5.18) and (5.79) yielded a quadratic equation in $g^A_{0,k+1}$, i.e.

$$\begin{aligned} DK_{Ca}\left(g^{A}_{0,k+1}\right)^2 + \left\{ D - DK_{Ca}g^{A}_{1,k+1} + \frac{\Delta y k_p K_{Ca} K_{CO_3} g^{C}_{0,k+1}}{1 + K_{CO_3} g^{C}_{0,k+1}} \right\} g^{A}_{0,k+1} \\ - \left\{ Dg^{A}_{1,k+1} + \frac{\Delta y k_p K_{Ca} K_{CO_3} g^{C}_{0,k+1}}{1 + K_{CO_3} g^{C}_{0,k+1}} \right\} = 0 \end{aligned} \tag{5.81}$$

where as stated earlier (Chapter 4) g^A is the concentration of Ca^{2+} ions and g^C is the concentration of CO_3^- ions. Two methods of approach have been adopted to obtain an

expression for $g^{A}_{0,k+1}$. The first was to approximate all the concentration terms in equation (5.79) to be the same as the previous vector's concentrations in the first iteration and then update these on subsequent iterations. The second was to approximate just the numerator concentration terms to be the same as the previous vector's in the first iteration. Both approaches yielded identical numerical values for the calculated concentration profiles in the channel cell. The computer program used to solve the convective-diffusion equation with equation (5.79) as the surface boundary condition is listed in Appendix 4. The same fitting procedure used for the literature rate laws was used to fit equation (5.79) to the experimental data.

The level of agreement between theory and experiment can be seen from Figures 5.4-5.6which are typical: excellent agreement was seen over the entire flow rate range for all the experiments described above. Preliminary estimates of the three parameters in equation (5.79) were obtained by the examination of a data subset, including rate data measured for high bulk calcium levels. Under these latter conditions ($[Ca^{2+}]_{bulk} \approx 10^{-3}$ mol dm^{-3}) the surface calcium concentration was effectively fixed, as dissolution added relatively few Ca^{2+} ions and this enabled K_{CO3} to be estimated as 3×10^{7} cm^{3} mol^{-1}. Examination of the data measured with low levels of calcium present in bulk then revealed K_{Ca} to be no greater than 10^{6} cm^{3} mol^{-1}, i.e. the value of the product $K_{Ca}[Ca^{2+}]_{o}$ in the denominator of equation (5.79) was found to be small compared to unity for these cases.

Table 5.5. Surface Boundary Matrix Elements for Equation (5.79)

	Approach 1	Approach 2
$g_{0,}^{A}$	$g_{1,k+1}^{A} + \dfrac{\Delta y k_b K_{Ca} K_{CO_3}}{D}\left\{\dfrac{K_{sp} - g_{0,k}^{A} g_{0,k}^{C}}{\left(1 + K_{Ca} g_{0,k}^{A}\right)\left(1 + K_{CO_3} g_{0,k}^{C}\right)}\right\}$	$\dfrac{\left\{D g_{1,k+1}^{A} + \dfrac{\Delta y k_b K_{Ca} K_{CO_3} K_{sp}}{\left(1 + K_{Ca} g_{0,k}^{A}\right)\left(1 + K_{CO_3} g_{0,k}^{C}\right)}\right\}}{\left\{D + \dfrac{\Delta y k_b K_{Ca} K_{CO_3} g_{0,k+1}^{C}}{\left(1 + K_{Ca} g_{0,k}^{A}\right)\left(1 + K_{CO_3} g_{0,k}^{C}\right)}\right\}}$
d_1	$g_{1,k}^{A} + \dfrac{\lambda_1 \Delta y k_b K_{Ca} K_{CO_3}}{D}\left\{\dfrac{K_{sp} - g_{0,k}^{A} g_{0,k}^{C}}{\left(1 + K_{Ca} g_{0,k}^{A}\right)\left(1 + K_{CO_3} g_{0,k}^{C}\right)}\right\}$	$g_{1,k}^{A} = \dfrac{\left\{\dfrac{\lambda_1 \Delta y k_b K_{Ca} K_{CO_3} K_{sp}}{\left(1 + K_{Ca} g_{0,k}^{A}\right)\left(1 + K_{CO_3} g_{0,k}^{C}\right)}\right\}}{\left\{D + \dfrac{\Delta y k_b K_{Ca} K_{CO_3} g_{0,k+1}^{C}}{\left(1 + K_{Ca} g_{0,k}^{A}\right)\left(1 + K_{CO_3} g_{0,k}^{C}\right)}\right\}}$
b_1	$\lambda_1 + 1$	$1 + \lambda_1\left\{2 - \dfrac{D}{\left\{D + \dfrac{\Delta y k_b K_{Ca} K_{CO_3} g_{0,k+1}^{C}}{\left(1 + K_{Ca} g_{0,k}^{A}\right)\left(1 + K_{CO_3} g_{0,k}^{C}\right)}\right\}}\right\}$

All $g_{0,k}$ values are replaced by $g_{0,k+1}$ values on second and subsequent iterations. See Table 5.3 for other matrix elements.

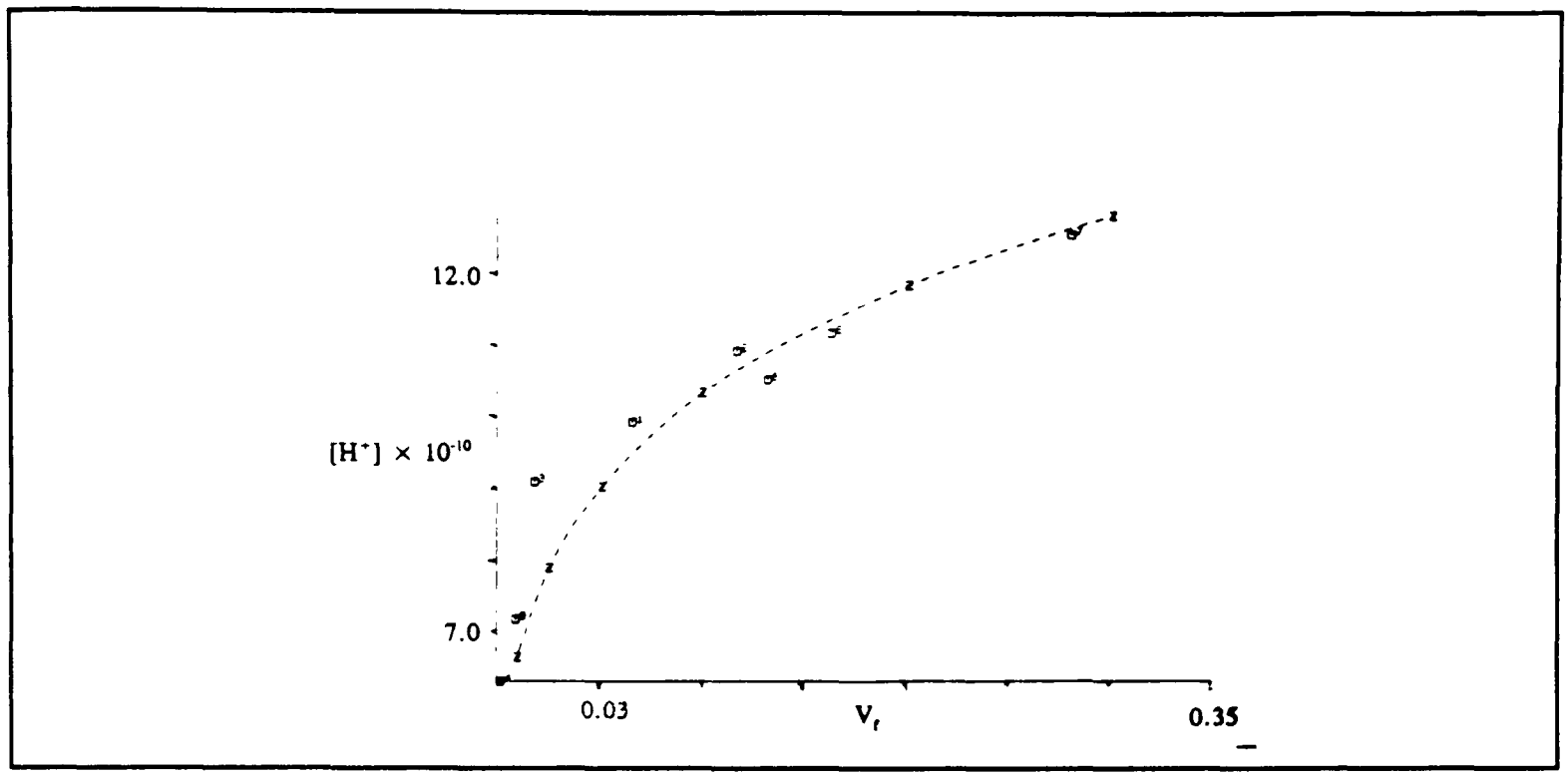

Figure 5.4. Flow behaviour of the detector pH electrode for $pH_{bulk}=8.44$ & $[Ca^{2+}]_{bulk}=0$. The line shows the behaviour predicted using equation (5.79) and parameters in Table 5.7 (Run C4).

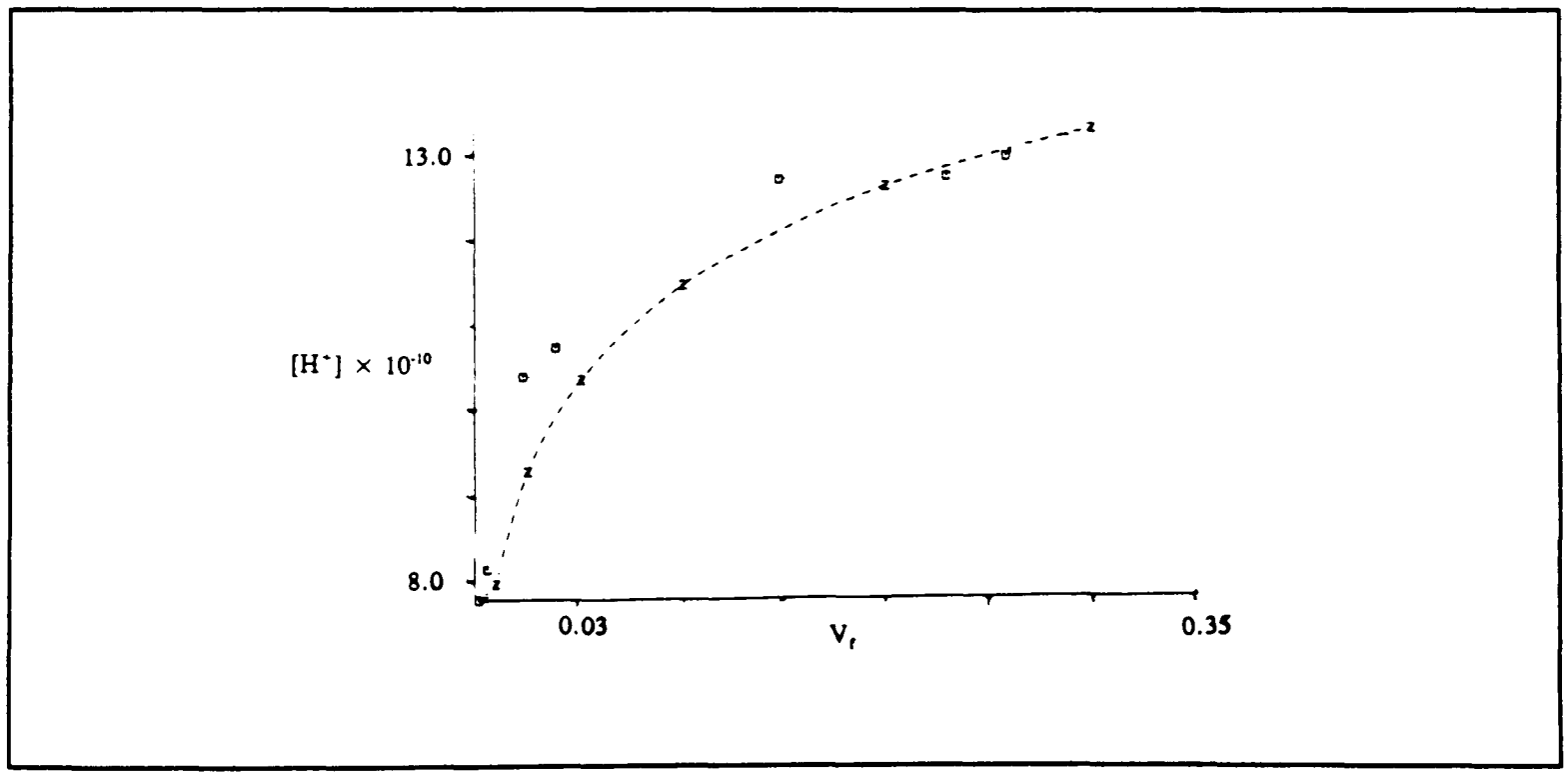

Figure 5.5. Flow behaviour of the detector pH electrode for $pH_{bulk}=8.66$ & $[Ca^{2+}]_{bulk}=0.102$ mM. The line shows the behaviour predicted using equation (5.79) & parameters in Table 5.7 (Run A10).

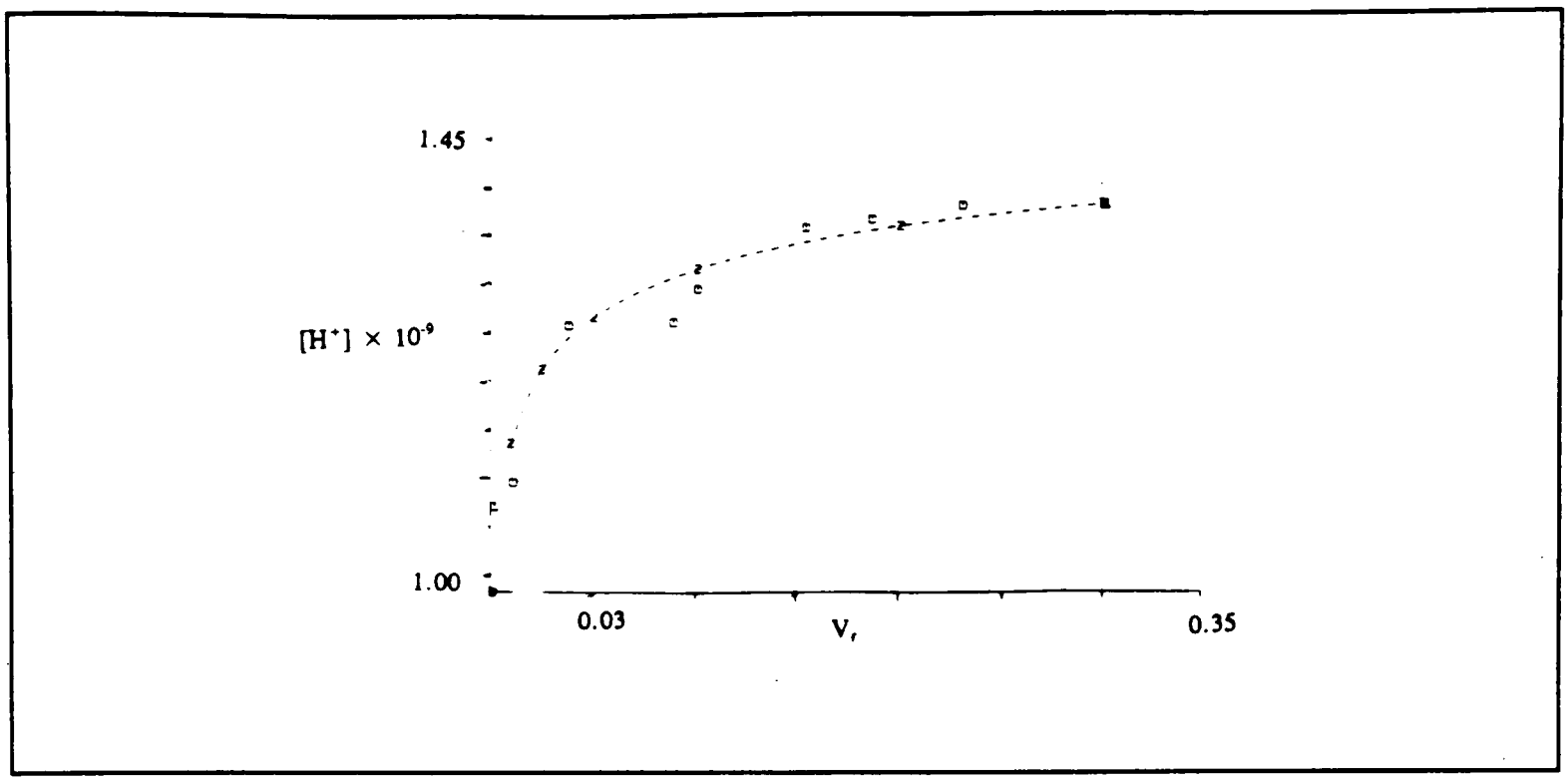

Figure 5.6. Flow behaviour of the detector pH electrode for $pH_{bulk}=8.80$ & $[Ca^{2+}]_{bulk}=1.4$ mM. The line shows the behaviour predicted using equation (5.79) & parameters in Table 5.7 (Run B4).

Table 5.6. Experimental Parameters for the Surface Reaction / Molecule Integration Model

un	$[Ca^{2+}]_{bulk}/\mu M$	pH_{bulk}	K_{CO3}/cm^3mol^{-1}	$k_pK_{Ca}K_{CO3}$ /$cm^4mol^{-1}s^{-1}$	
				$K_{Ca}=0$	$K_{Ca}=10^6$ cm^3mol^{-1}
B1	0	8.45	$3x10^7$	800	820
B2	0	8.70	$4.5x10^7$	675	685
B3	0	8.46	$3x10^7$	750	760
B4	0	8.44	$3x10^7$	930	950
B6	102	8.34	$3x10^7$	1140	1300
B7	204	8.57	$3x10^7$	990	1250
B8	1011	8.38	$3x10^7$	600	1200
B9	1065	8.53	$4.5x10^7$	720	1500
C2	5013	8.38	$3x10^7$	200	1200

Table 5.6 shows the best fits for the parameters k_p and K_{CO3} deduced from this subset of data with $K_{Ca} = 0$ in the denominator.

The rate information from the 36 separate experiments detailed in Table 5.7 were modelled using these mean values of $K_{CO3} = 3 \times 10^7$ cm^3 mol^{-1} and $K_{Ca} = 10^6$ cm^3 mol^{-1}. A mean value of $k_p K_{Ca} K_{CO3} = 727$ cm^4 mol^{-1} s^{-1} (standard deviation 430) was deduced from this complete set of data. This corresponded to an average precipitation rate constant $k_p = 2.42 \times 10^{-11}$ mol cm^{-2} s^{-1} (standard deviation $1.43\ 10^{-11}$).

Table 5.7. Analysis of the Full Set of Experimental Rate Data for Etched Surface with $K_{Ca} = 10^6$ cm^3 mol^{-1} and $K_{CO3} = 3 \times 10^7$ cm^3 mol^{-1}

Run	$[Ca^{2+}]_{bulk}$ /μM	pH_{bulk}	$k_p K_{Ca} K_{CO3}$ /cm^4 mol^{-1} s^{-1}
A1	0	8.74	380
A2	0	8.17	560
A3	0	8.44	550
A4	0	8.71	390
A5	0	8.80	270
A6	0	8.30	150
A7	10	8.51	780
A8	20.	8.77	130
A9	50	8.34	1250
A10	103	8.66	330
A11	103	8.42	510
A12	206	8.61	180
A13	0	8.44	640

Run	$[Ca^{2+}]_{bulk}$ /μM	pH_{bulk}	$k_p K_{Ca} K_{CO3}$ /cm^4 mol^{-1} s^{-1}
A14	100	8.30	100
B1	0	8.45	820
B2	0	8.70	670
B3	0	8.46	760
B4	0	8.44	950
B5	140	8.80	100
B6	102	8.34	1300
B7	204	8.57	1250
B8	1010	8.38	1200
B9	1070	8.53	1450
C1	0	8.60	610
C2	5013	8.38	1200
C3	0	7.93	120
C4	0	7.20	500
C5	0	8.74	900
C6	0	7.17	1700
C7	0	8.22	900
C8	0	7.59	900
C9	0	8.76	900
C10	0	7.22	900
C11	0	7.45	500
C12	0	8.74	900
D1	10000	8.48	1400

and a dissolution rate constant (as calculated from equation (5.80)) $k_d = 4.55 \times 10^{-11}$ mol cm^{-2} s^{-1} (standard deviation 2.7×10^{-11}). In addition, good agreement was seen between different calcite crystals: the runs given in Table 5.7 were based on five separate crystals. It may be concluded that equation (5.79) can adequately describe the kinetics of calcite dissolution/precipitation over a wide range of conditions and the merits of approaching the problem using the channel cell is evident. In particular, the existence of a well-defined and calculable hydrodynamic regime permits the sensitive interrogation of the dissolving interface using variable mass transport as a probe. This should be evident from Figures 5.7-5.13 which show the computed concentration profiles within the flow cell for all the kinetically significant species deduced using the mean parameters specified above and for a flow rate of 10^{-2} cm^3 s^{-1}.

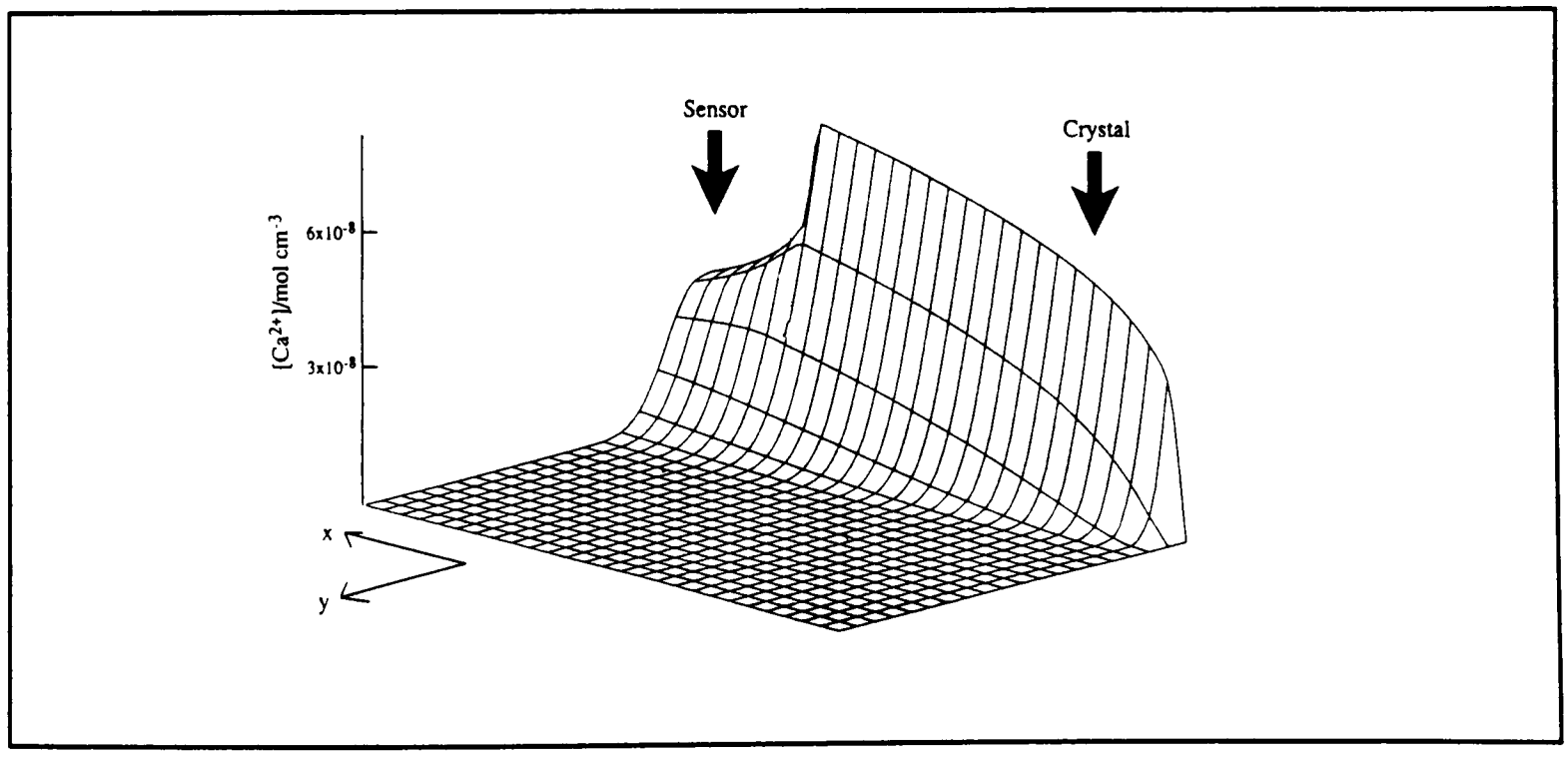

Figure 5.7. Computed concentration profile of Ca^{2+} in the channel cell calculated using the theoretical model and mean parameters described in the text together with the values of flow rate = 10^{-2} cm^3 s^{-1} and pH_{bulk} = 8.5.

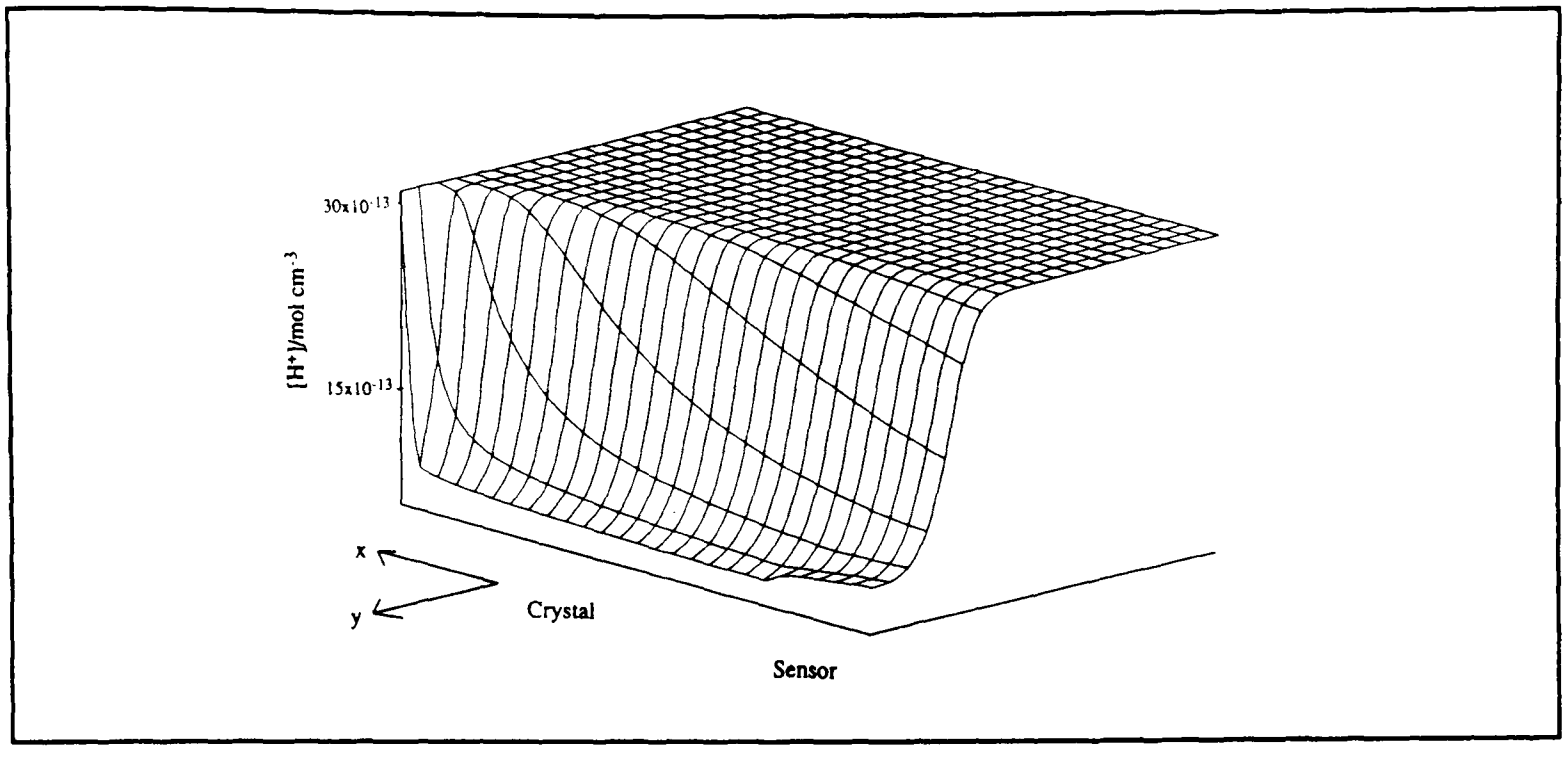

Figure 5.8. Computed concentration profile of H^+ in the channel cell calculated using the theoretical model and mean parameters described in the text together with the values of flow rate = 10^{-2} cm^3 s^{-1} and pH_{bulk} = 8.5.

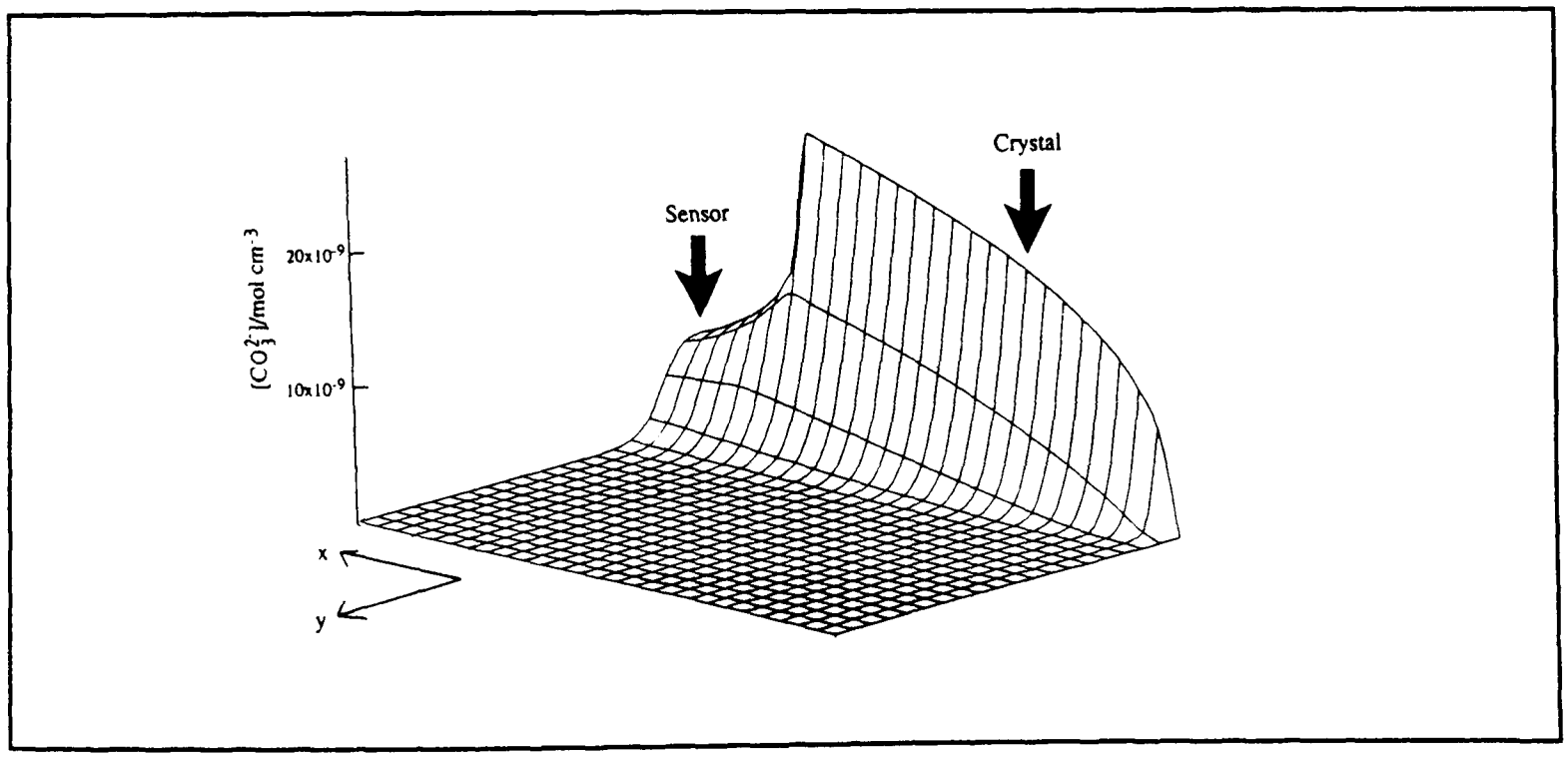

Figure 5.9. Computed concentration profile of CO_3^{2-} in the channel cell calculated using the theoretical model and mean parameters described in the text together with the values of flow rate = 10^{-2} cm^3 s^{-1} and pH_{bulk} = 8.5.

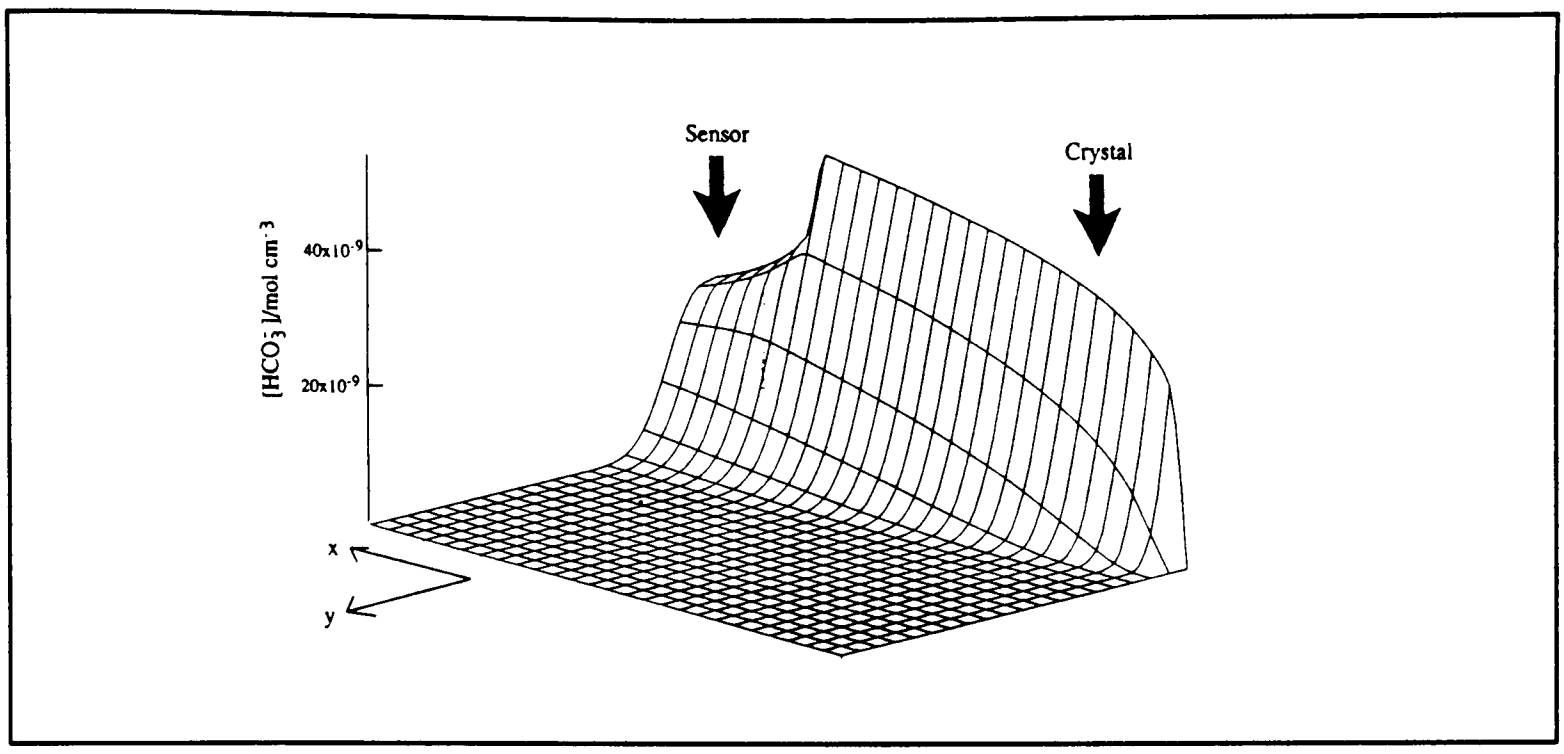

Figure 5.10. Computed concentration profile of HCO_3^- in the channel cell calculated using the theoretical model and mean parameters described in the text together with the values of flow rate = 10^{-2} cm^3 s^{-1} and pH_{bulk} = 8.5.

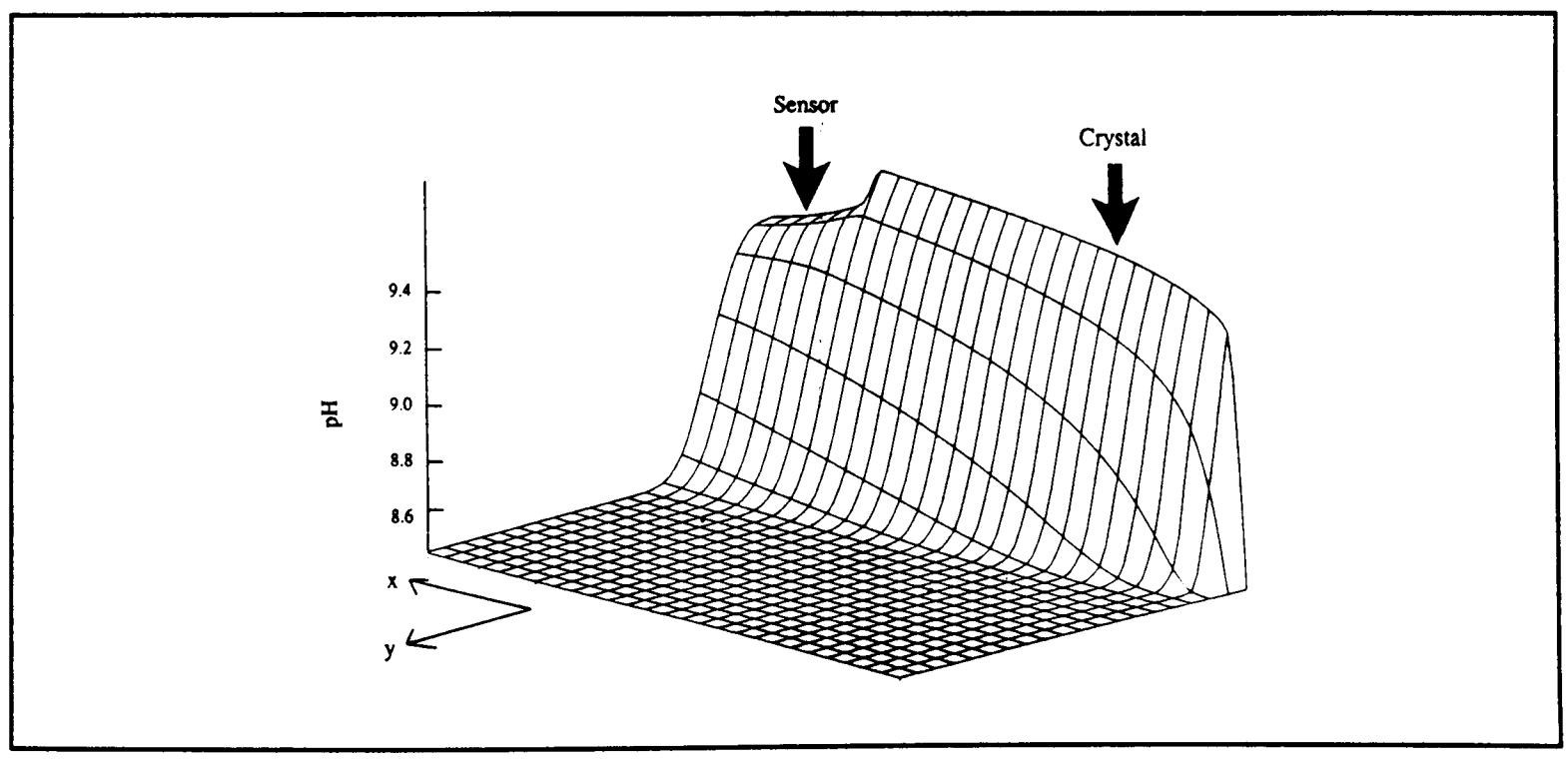

Figure 5.11. Computed contour plot of pH in the channel cell calculated using the theoretical model and mean parameters described in the text together with the values of flow rate = 10^{-2} cm^3 s^{-1} and pH_{bulk} = 8.5.

5.6 Discussion

The success of equation (5.79) in describing the calcite dissolution reaction under the widely differing conditions described in this chapter, strongly supports the surface reaction/ molecule integration mechanism as a correct description of the process under study.

It is interesting to consider some previous observations in the light of this possible mechanism. First Christoffersen and Christoffersen have pointed out that the rate of calcite growth/dissolution, as described by a Davies and Jones type rate equation, is strikingly independent of the saturated solution's ionic strength (from 0.01 M to 0.20 M) if the equation is written in terms of the activities of the solution species [10,68]. This is consistent with the electroneutral transition state predicted by the surface reaction/molecule integration mechanism. Second, streaming potential measurements of Thompson have shown that CO_3^{2-} and Ca^{2+}, but not HCO_3^-, are surface active on calcite [61]. This again is consistent with the proposed mechanism. Also the observation that $K_{Ca} < K_{CO3}$ is in line with the data of Thompson, and also with the electrophoresis measurements of Smith [81,185], which show calcite surfaces to bear a negative charge, except at high pCa values where they become positive. Moreover, it should be noted that equation (5.79) fitted the observed rate data over a wide range of conditions, including pCa. The fact that the surface charge is known to vary over these conditions [61,81,185] is additional evidence in favour of a neutral transition state. Third, House [60] has found previously used rate expressions to be inadequate and concluded there is no unique experimental growth curve. This points to the need to consider surface coverages of adsorbed ions in describing the calcite/water interface rather than solution

concentrations. Lastly, Huang *et al.* [186] have demonstrated, using calcite powder and Ca^{2+} ion selective electrodes, that the adsorption of Ca^{2+} ions fits the Langmuir isotherm with an adsorption constant of 1.80×10^6 cm^3 mol^{-1}. Similarly, Sjöberg [56] also concluded that the effect of Ca^{2+} ions on single crystal dissolution rates was due to Langmuirian adsorption with an adsorption constant of 1.32×10^6 cm^3 mol^{-1}. Both of these values of K_{Ca} are in excellent agreement with the value deduced from the fitting procedure described above. Langmuirian adsorption has also been recently noted for other divalent cations on calcite [186].

In conclusion, the channel flow cell has been successfully used to deduce the fundamental rate law - equation (5.79) - describing the dissolution/precipitation kinetics at high pH.

CHAPTER 6

THE EFFECT OF POLYACRYLICACID ON THE DISSOLUTION OF CALCITE AT HIGH pH (> 7).

6.1 Introduction

This chapter reports the investigation of the effect of the presence of polyacrylic acid on the dissolution of calcite at high pH, with the aim of advancing the knowledge gained from the work previously reported in Chapters 4 and 5.

In Chapter 4 the inhibition of dissolution of calcite at low pH in the presence of polyacrylic acid was studied. In this case it was shown that a complex formed between polyacrylic acid and Ca^{2+}, and it was this complex which adsorbed on the surface and caused the inhibition of dissolution.

Then in Chapter 5 the dissolution of calcite at high pH was examined. It was shown that none of the existing rate laws for this pH region fitted the experimental data sufficiently. A new mechanistically rational rate law was proposed, and shown to fit over the whole range of flow rates, pH and background Ca^{2+} concentrations studied [45].

It is of particular interest to study the effect of polyacrylic acid on the dissolution of calcite at high pH, because this pH region is more representative of the conditions in which the inhibitor is used commercially.

This chapter will draw together the conclusions of these two previous chapters. First the experimental technique will be outlined. Second the theory necessary to investigate the action of inhibitors at high pH will be introduced. Third results of experiments performed in the presence of polyacrylic acid will be reported. Finally these

results will be explained, drawing particular attention to the effects of background Ca^{2+} concentrations of polyacrylic inhibition.

6.2 Experimental details

The experimental set up used is analogous to that described in Chapter 5. Polyacrylic acid (M.W. 2000) solutions of varying concentrations (1×10^{-4} and 9×10^{-6} mol dm^{-3}), flow through the channel flow cell. The pH of these solutions was adjusted to between 7 to 9, by KOH and contained background KCl concentrations of 0.5 mol dm^{-3}. When background calcium was used calcium chloride was added to the solutions for the purpose. In parallel with each set of experiments, there was also at least one blank experiment in which there was background KCl in solution but no added polyacrylic acid or calcium chloride added. These experiments provided the value of $k_p K_{Ca} K_{CO3}$ for the associated polyacrylic acid experiments. The values of K_{Ca} and K_{CO3} were those as found previously in Chapter 5, that is $K_{Ca} = 1.0 \times 10^7 cm^3\ mol^{-1}$ and $K_{CO3} = 3.0 \times 10^7 cm^3\ mol^{-1}$.

6.3 Theory

The relevant calcite dissolution reaction is:

$$CaCO_3 + H_2O \rightarrow Ca^{2+} + HCO_3^- + OH^- \qquad (6.1)$$

and the following reactions occur in solution:

$$CO_3^{2-} + H_2O \rightleftharpoons HCO_3^- + OH^- \qquad (6.2)$$

$$H^+ + OH^- \rightleftharpoons H_2O \qquad (6.3)$$

Combining both the homogeneous and heterogeneous reactions and the theory for the dissolution of calcite as introduced in the previous chapters, the following rate equation can be derived:

$$J_{net}/\text{mol cm}^{-2}\text{s}^{-1} = k_p K_{Ca} K_{CO_3} \left\{ \frac{K_{sp} - [Ca^{2+}]_o [CO_3^{2-}]_o}{(1 + K_{Ca}[Ca^{2+}]_o)(1 + K_{CO_3}[CO_3^{2-}]_o)} \right\} \tag{6.4}$$

where

$$k_d = k_p K_{Ca} K_{CO_3} K_{SP} \tag{6.5}$$

with all symbols having the same meaning as in Chapter 5.

This mechanistically rational approach was developed by adapting the surface reaction/molecule integration mechanism of Chiang and Donohue [95]:

$$Ca^{2+}_{(aq)} \rightleftharpoons Ca^{2+}_{(ads)} \tag{6.6}$$

$$CO_3^{2-}{}_{(aq)} \rightleftharpoons CO_3^{2-}{}_{(ads)} \tag{6.7}$$

$$Ca^{2+}_{(ads)} + CO_3^{2-}{}_{(ads)} \rightleftharpoons CaCO_{3\ (ads)} \tag{6.8}$$

$$CaCO_{3\ (ads)} \rightleftharpoons CaCO_{3\ (lattice)} \tag{6.9}$$

This simply states that Ca^{2+} and CO_3^{2-} adsorb on the calcite surface, and then undergo reaction to form $CaCO_3$ which is adsorbed and then $CaCO_3$ is incorporated into the crystal lattice.

Within the above reaction scheme there are two modes of action by which an inhibitor might operate which can be envisaged. First the inhibitor might specifically adsorb at the growth site, and thus prevent the incorporation of $CaCO_3$ units into the crystal lattice (reaction (6.9)). This would cause a reduction in rate constants k_p and k_d. Second general adsorption of the inhibitor on the crystal surface might occur, so that the

adsorbed inhibitor would compete with adsorption of Ca^{2+} or CO_3^{2-} (reactions (6.6) and (6.7)). This would not only reduce the amount of Ca^{2+} or CO_3^{2-} on the surface and hence slow down the rate of growth, but would also reduce the number of empty adsorption sites free to receive calcium or carbonate ions dissolving from the lattice (reaction (6.8)).

In the latter case of general adsorption, the dissolution rate law would be modified depending on whether the inhibitor was negatively charged, and thus competed with CO_3^{2-} for adsorption sites, or whether it was positive and so competed with Ca^{2+}. Thus, in the case of a negatively charged inhibitor, the surface coverage of adsorbed CO_3^{2-} ions is given by

$$\theta_{CO_3} = \frac{K_{CO_3}[CO_3^{2-}]_o}{1 + K_{CO_3}[CO_3^{2-}]_o + K_I[I^-]_o} \tag{6.10}$$

where K_I is the adsorption equilibrium constant for the inhibitor, and $[I^-]_0$ is the concentration of inhibitor at the surface. This replaces equation (5.77) in the surface reaction/molecule integration scheme outlined in Chapter 5. From this, equation (6.4) may be modified so that the net dissolution flux, in the presence of negative inhibitors displaying Langmuirian adsorption, is given by:

$$J_{net}/\text{mol cm}^{-2}\text{s}^{-1} = k_p K_{Ca} K_{CO_3} \left\{ \frac{K_{sp} - [Ca^{2+}]_o[CO_3^{2-}]_o}{(1 + K_{Ca}[Ca^{2+}]_o)(1 + K_{CO_3}[CO_3^{2-}]_o + K_I[I^-]_o)} \right\} \tag{6.11}$$

An expression for the Langmuirian adsorption of a positive inhibitor was derived similarly:

$$J_{net}/\text{mol cm}^{-2}\text{s}^{-1} = k_p K_{Ca} K_{CO_3} \left\{ \frac{K_{sp} - [Ca^{2+}]_o[CO_3^{2-}]_o}{(1 + K_{Ca}[Ca^{2+}]_o + K_I[I^+]_o)(1 + K_{CO_3}[CO_3^{2-}]_o)} \right\} \tag{6.12}$$

Having these rate equation it is now possible to model the effect of any inhibitor on the dissolution of calcite using the Backwards Implicit finite difference method to solve the steady state convective-diffusion equation describing the distribution of Ca^{2+} ions in the channel flow cell:

$$\frac{\partial[Ca^{2+}]}{\partial t} = 0 = D_{Ca^{2+}} \frac{\partial^2[Ca^{2+}]}{\partial y^2} - v_x \frac{\partial[Ca^{2+}]}{\partial x} \tag{6.13}$$

where D_{Ca} is the diffusion coefficient of Ca^{2+}, x and y are the coordinates in the channel flow cell, and v_x is the solution in the x-direction (as defined in Chapter 5).

In order to model the expected behaviour for high pH dissolution in the presence of an inhibitor it is again necessary to derive matrix elements for the BI method.

6.3.1 Matrix Elements

Initially the boundary conditions have to be defined, and are as follows:

(i) *Upstream of the Crystal*

The Ca^{2+} concentration was that present in the bulk solution entering the flow cell:

$$x = 0, \quad 0 < y < 2h, \quad [Ca^{2+}] = [Ca^{2+}]_{bulk} \quad \& \quad [CO_3^{2-}] = 0 \tag{6.14}$$

(ii) *Zone of the Crystal*

At the surface of the crystal the flux of Ca^{2+} entering the solution was given by the rate law for the dissolution/precipitation reaction. As polyacrylic acid is negatively charged at high pH the first inhibitor rate equation (6.11) is the one of interest here.

$$0 < x < x_c\ ,\quad y = 0\ ,$$

$$-D\frac{\partial[Ca^{2+}]}{\partial y} = -k_p K_{CO_3} K_{Ca}\left\{\frac{K_{SP} - [Ca^{2+}]_0[CO_3^{2-}]_0}{(1 + K_{Ca}[Ca^{2+}])(1 + K_{CO_3}[CO_3^{2-}] + K_I[I^-])}\right\} \tag{6.15}$$

where x_c is the length of the crystal, and the other symbols are as defined earlier. The chemical nature of I^- will be discussed below.

(iii) *The Far Channel Wall*

There was a no-flux condition at the channel wall opposite the crystal:

$$0 < x < x_c\ ,\quad y = 2h\ ,\quad D\frac{\partial[Ca^{2+}]}{\partial y} = 0 \tag{6.16}$$

where x_c is the length of the crystal.

(iv) *Downstream of the Crystal*

Over the surface of the pH electrode and over the gap between the crystal and the detector a no-flux condition operated:

$$x > x_c\ ,\quad y = 0\ ,\quad D\frac{\partial[Ca^{2+}]}{\partial y} = 0 \tag{6.17}$$

and again at the channel wall:

$$x > x_c\ ,\quad y = 2h\ ,\quad D\frac{\partial[Ca^{2+}]}{\partial y} = 0 \tag{6.18}$$

Now the BI method [113] can be used to solve transport problems in channel electrodes. This involves an analogous procedure to Chapter 5 section 5.4. The only difference in the derived matrix elements are those at the surface, where the inhibitor interacts with the surface reaction.

From the inhibitor equation relevant for a negative inhibitor (6.11) the surface flux for the dissolution of calcite with such an inhibitor present is:

$$-D_{Ca}\frac{\partial g^{A}}{\partial y} = \frac{g^{A}_{1,k+1} - g^{A}_{0,k+1}}{\nabla y} = -k_p K_{CO_3} K_{Ca}\left\{\frac{K_{SP} - [Ca^{2+}]_0[CO_3^{2-}]_0}{(1+K_{Ca}[Ca^{2+}])(1+K_{CO_3}[CO_3^{2-}]+K_I[I^-])}\right\} \quad (6.19)$$

where A represents Ca^{2+}.

From this the matrix elements at the surface can be derived, with values for a^A, b^A, c^A and d^A respectively:

$$\begin{aligned} a^A &= 0 \\ b^A &= \lambda^A + 1 \\ c^A &= -\lambda^A \\ d^A &= g^A_{1,k} - \frac{\lambda^A \Delta y k_p K_{Ca} K_{CO_3}}{D_A}\left\{\frac{K_{SP} - g^A_{0,k+1} g^C_{0,k+1}}{(1+K_{Ca} g^A_{0,k+1})(1+K_{CO_3} g^C_{0,k+1} + K_I g^I_{0,k+1})}\right\} \end{aligned} \quad (6.20)$$

These values can then be used in modelling to investigate the strength of inhibition as measured by the value for K_I for the chosen inhibitor. This is performed by deriving $k_p K_{Ca} K_{CO3}$ from the parallel blank experiments, and using the values of K_{Ca} and K_{CO3} as found previously in Chapter 5, that is $K_{Ca} = 1.0 \times 10^7$ cm^3 mol^{-1} and $K_{CO3} = 3.0 \times 10^7$ cm^3 mol^{-1} thus the only unknown is K_I which can be found by substituting various values in until a 'best fit' for the experimental data is found.

6.4 Results

Initially the effect of polyacrylic acid (M.W. 2000) on the dissolution of calcite at high pH without any additional Ca^{2+} being added, was investigated. Ranges of polyacrylic acid concentrations between 4.9×10^{-4} to 4.0×10^{-6} mol dm^{-3} were used. Concentrations above this range were tried, but at such high levels the pH measured at the pH electrode were indistinguishable from those for the bulk solution (as shown in figure 6.1). That is at higher concentration dissolution was effectively totally stopped by the inhibitor.

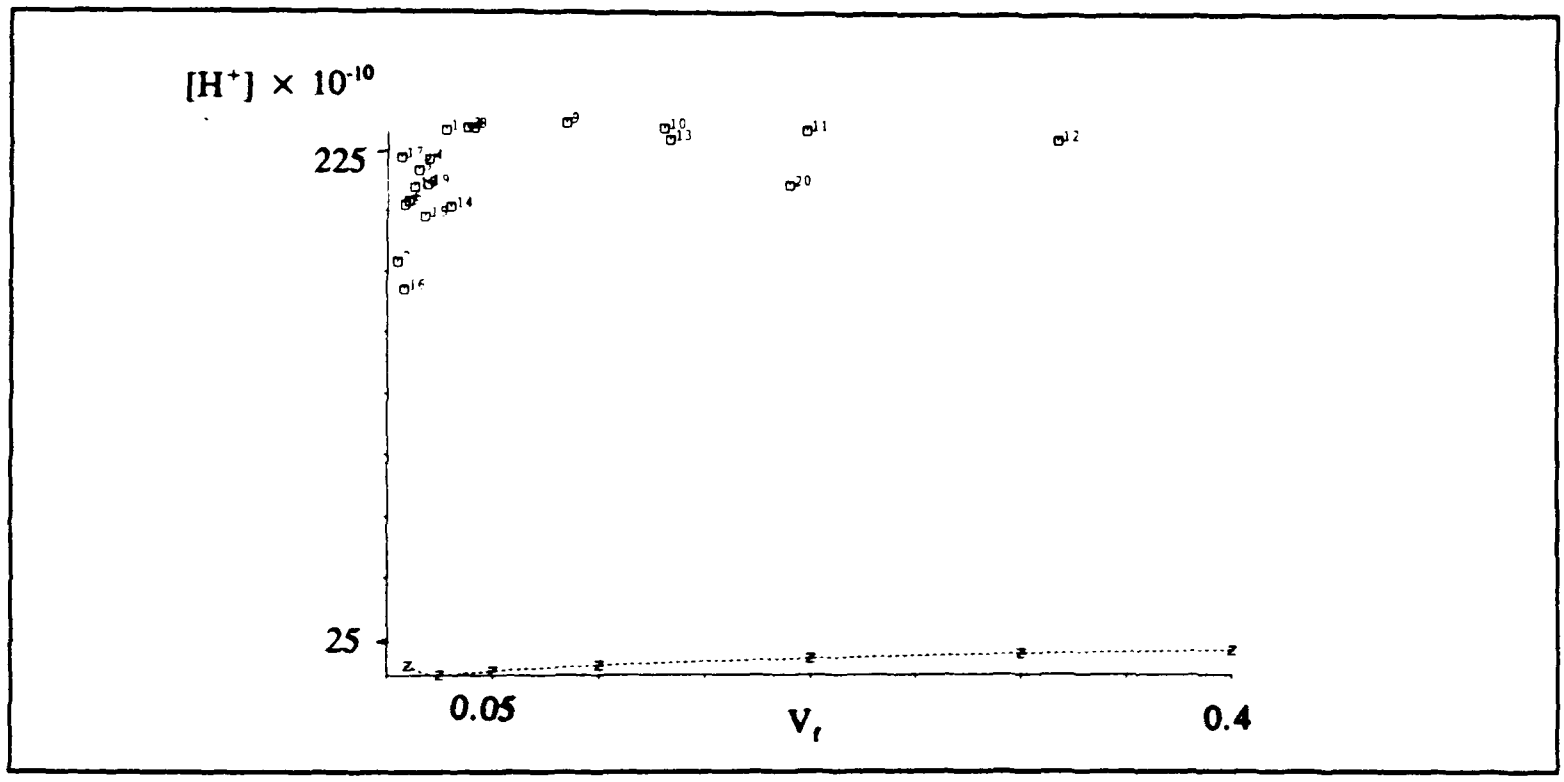

Figure 6.1:The flow rate behaviour for the dissolution of calcite at pH 7.69, with 4.9×10^{-4} mol dm^{-3} PAA. ($[H^+] = 2.04$ mol dm^{-3}) This shows that the $[H^+]$ measured at the detector electrode are those of the bulk, that is that inhibition is complete.

Figures 6.1 to 6.3 show the results for three typical experiments. The full details of the experiments are tabulated later in Table 6.1.

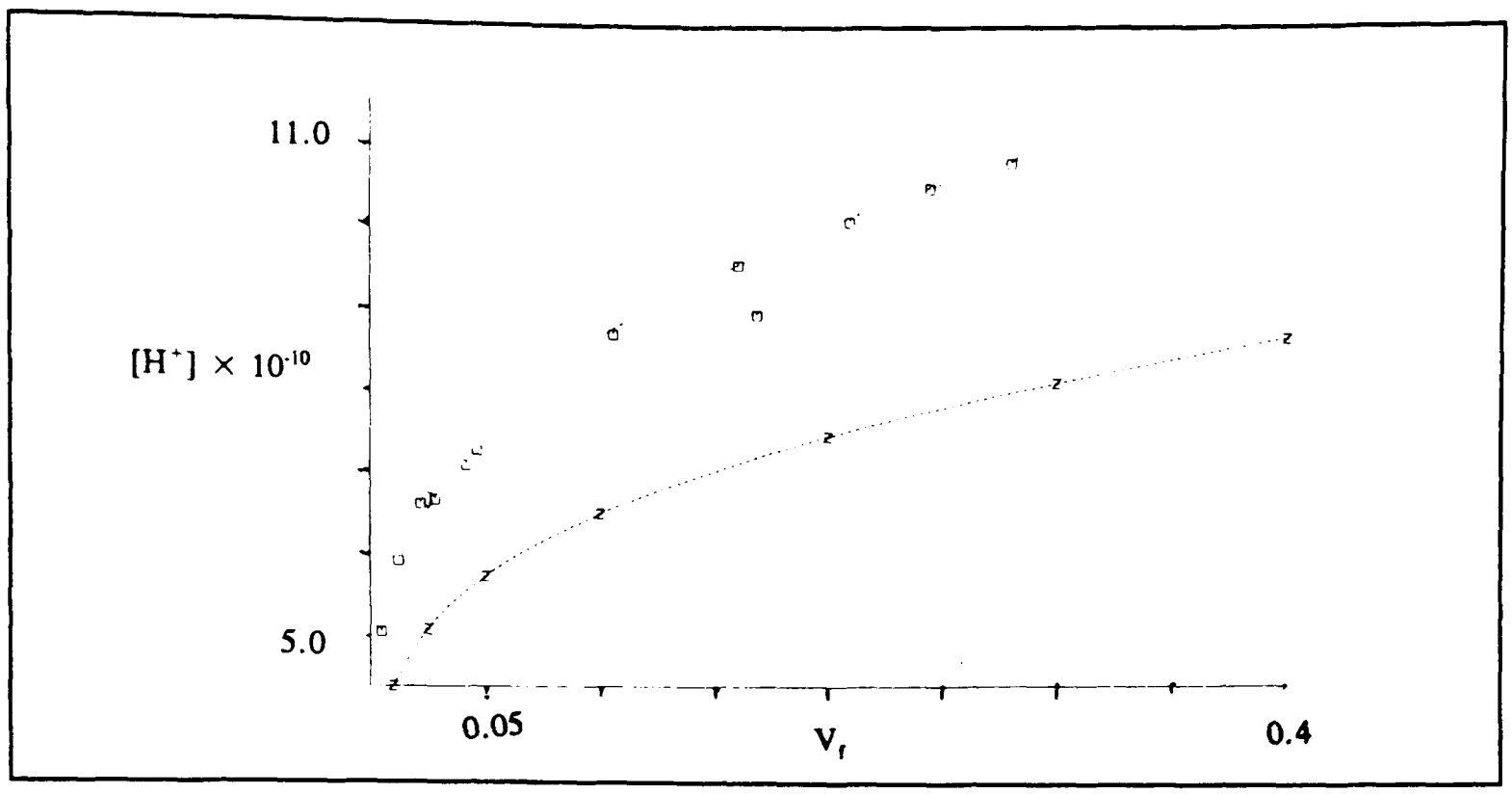

Figure 6.2 : A comparison of the behaviour predicted for dissolution of calcite at pH 7.17 with that observed for dissolution at this pH with a polyacrylic acid concentration of 1.0 × 10^{-5} mol dm^{-3} X_{crys}=0.978, gap=0.102, and X_{el}=0.318.

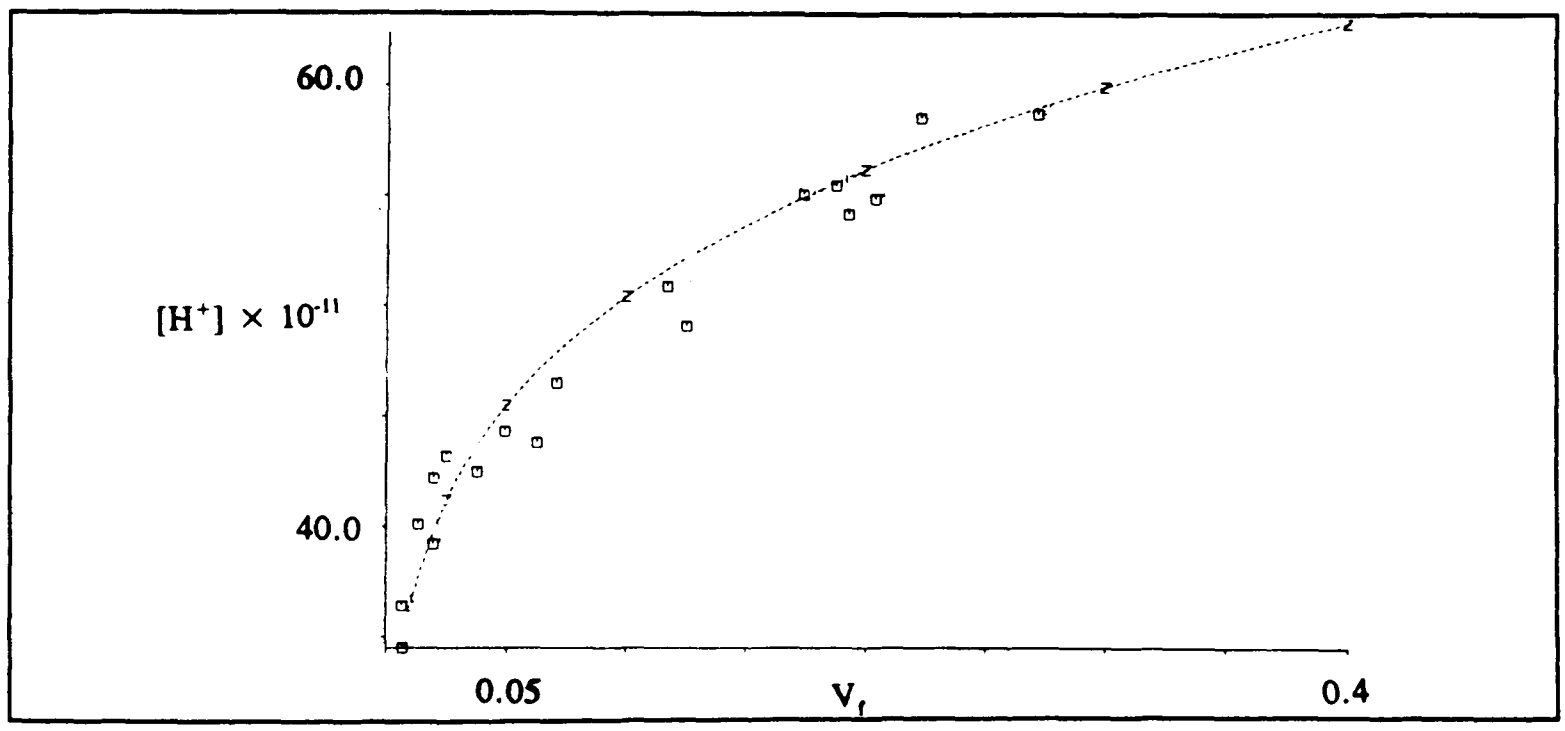

Figure 6.3 : A comparison of the behaviour predicted for dissolution of calcite at pH 8.47 with that observed for dissolution at this pH with a polyacrylic acid concentration of 4.0 × 10^{-6} mol dm^{-3} X_{crys}=0.978, gap=0.102, and X_{el}=0.318.

At the lower concentration it was hard to discern any appreciable difference from the pH variation with flow expected for a solution without polyacrylic acid at the same pH, so there was no inhibition (as shown in figure 6.3).

It was observed earlier (in Chapter 4) that the addition of background Ca^{2+} has an effect on the strength of inhibition of calcite dissolution at low pH. At low pH it was seen that a 2:1 polyacrylic acid to calcium complex was formed and adsorbs on the surface. For this to occur either the rate of dissolution has to be high enough, due to high PAA concentration and/or high flow rates, for enough Ca^{2+} to be generated at the surface to complex the surface PAA; alternatively there has to be enough Ca^{2+} in the bulk solution itself. Thus it is of interest to see if any such effect is observed at high pH.

A crucial difference is that the modelling for high pH dissolution already takes into consideration any levels of background Ca^{2+} added (see Chapter 5). Hence a series of experiments were performed with added background calcium in the range 9.0×10^{-6} to 9.0×10^{-4} mol dm^{-3}.

In order to model inhibition it was hypothesised that, as in the low pH case, a complex was formed between Ca^{2+} and polyacrylic acid:

$$x\,Ca^{2+} + PAA \rightleftharpoons Ca_xPAA_{(complex)} \tag{6.21}$$

with an equilibrium constant, K_{eq} :

$$K_{eq} = \frac{[Complex]}{[PAA][Ca^{2+}]^x} \tag{6.22}$$

If it is this complex which absorbs on the surface and causes inhibition, and it does so in a Langmuirian manner, then:

$$\theta^{-1} = 1 + K_L^{-1}[complex]^{-1} \tag{6.23}$$

where θ is the surface coverage, and K_L is the Langmuirian equilibrium constant of adsorption of the complex.

Using equation (6.11) $K_I[\,I\,]_0$ can be related to the concentrations of Ca^{2+} and polyacrylic acid by the equation:

$$K_I[I]_0 = K_L K_{eq}[PAA]_{tot}[Ca^{2+}]^x_{tot} \qquad (6.24)$$

where $[A]_{tot}$ is the total concentration of species A (A=PAA or Ca^{2+}) in solution, assuming the total concentration is much larger than the concentration of the species which are 'free'. Therefore there are two unknowns the pair (K_L K_{eq}) and x. To find values for $K_L K_{eq}$ the 'fits' that can be obtained by using the BI method, are compared for different fixed values of x. The equilibrium constant for each value of x are taken as those which fit the experimental data best.

It can be seen that the shapes of the curves for x = 0 or 1.0 do not fit the data well (figures 6.4 and 6.5), and that there is an effect caused by adding Ca^{2+} but the complex formed is not a simple one to one complex.

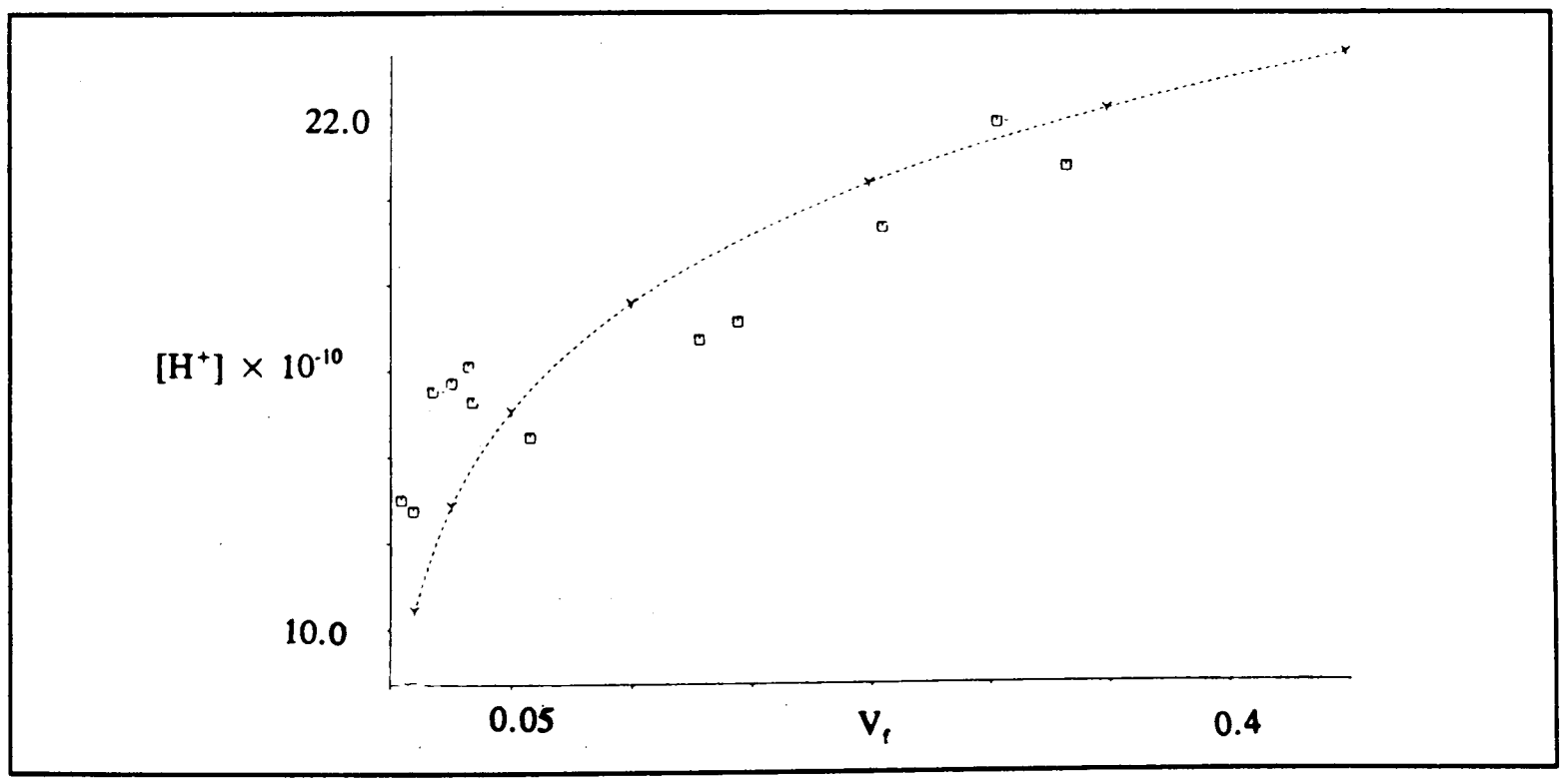

Figure 6.4: The best theoretical fit of the experimental data obtained with a solution where [PAA]= 9.7 × 10⁻⁶ mol dm⁻³ and [Ca²⁺]= 4.7 × 10⁻⁴ mol dm⁻³ (cell parameters as in figure 6.3) with a fixed x=0.0.

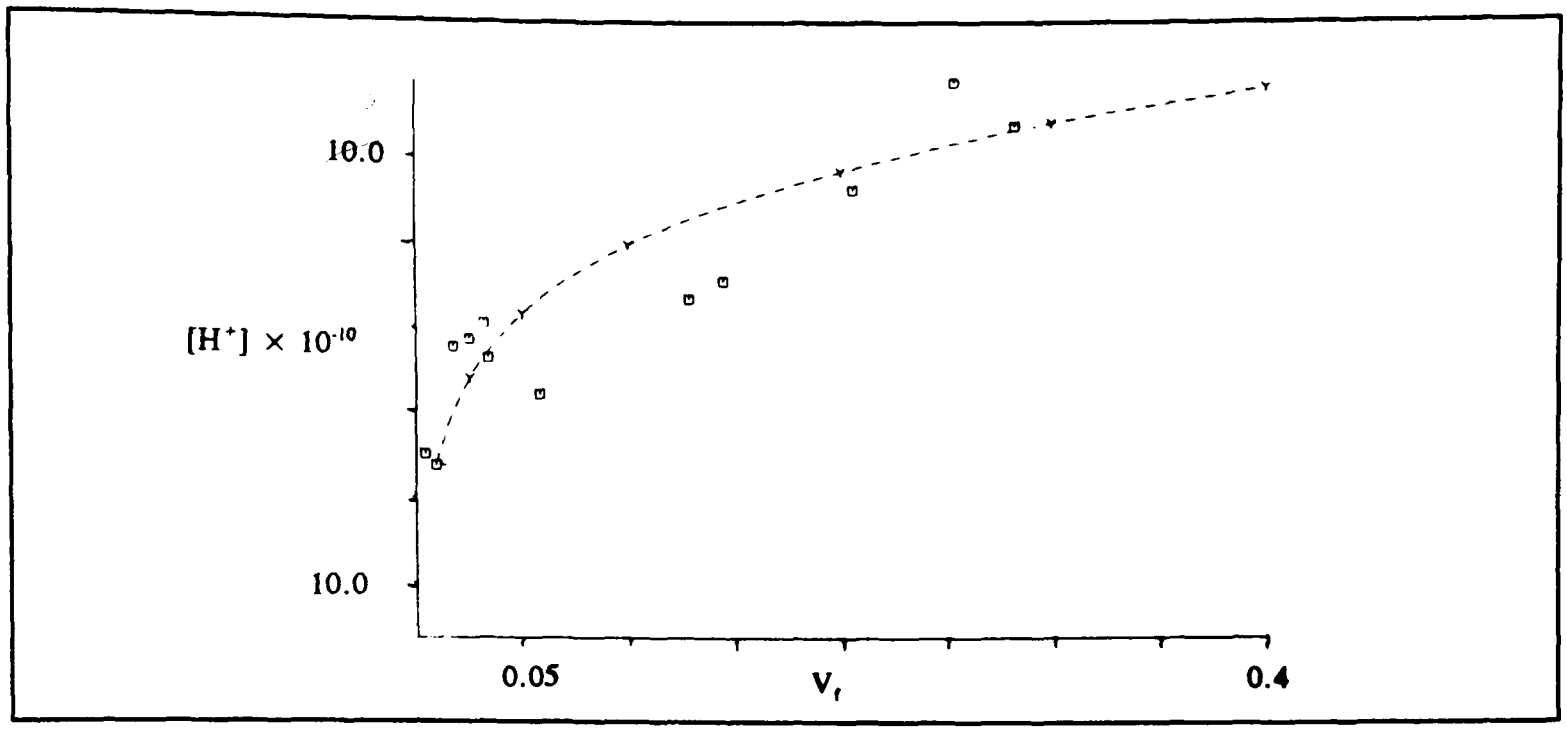

Figure 6.5: The best theoretical fit of the experimental data obtained with a solution where [PAA]= 9.7 × 10^{-6} mol dm^{-3} and [Ca^{2+}]= 4.7 × 10^{-4} mol dm^{-3} (cell parameters as in figure 6.3) with a fixed x=1.0.

These results lead to a closer examination of the values of x between these two limits. So the experimental results were fitted with values of x fixed to 0.25, 0.50 and 0.75, and the value of $K_{eq}K_L$ were obtained from those lines which fitted the data best. These fits are shown below in figures 6.6 to 6.11, and the values of $K_{eq}K_L$ are tabulated

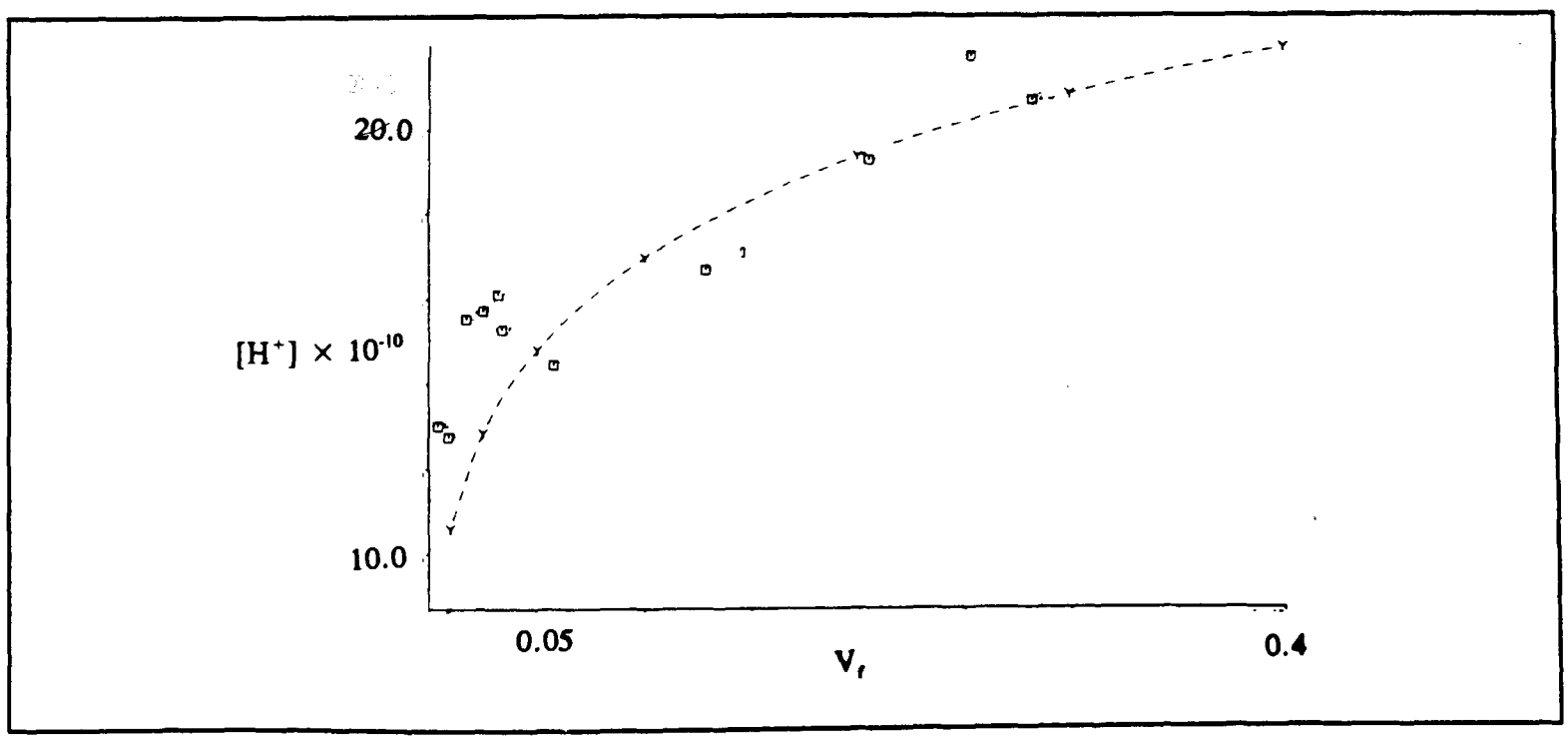

Figure 6.6: The best theoretical fit of the experimental data obtained with a solution where [PAA]= 9.7 × 10^{-6} mol dm^{-3} and [Ca^{2+}]= 4.7 × 10^{-4} mol dm^{-3} (cell parameters as in figure 6.3) with a fixed x=0.25.

for the whole range of experimental data in Table 6.1, where the values of Ca^{2+} quoted are the average surface concentration as obtained from the BI method. These values are used, as at high pH much lower levels of Ca^{2+} is needed to effect the inhibition, therefore the amounts of Ca^{2+} generated at the surface is comparable to that added, and so of significance.

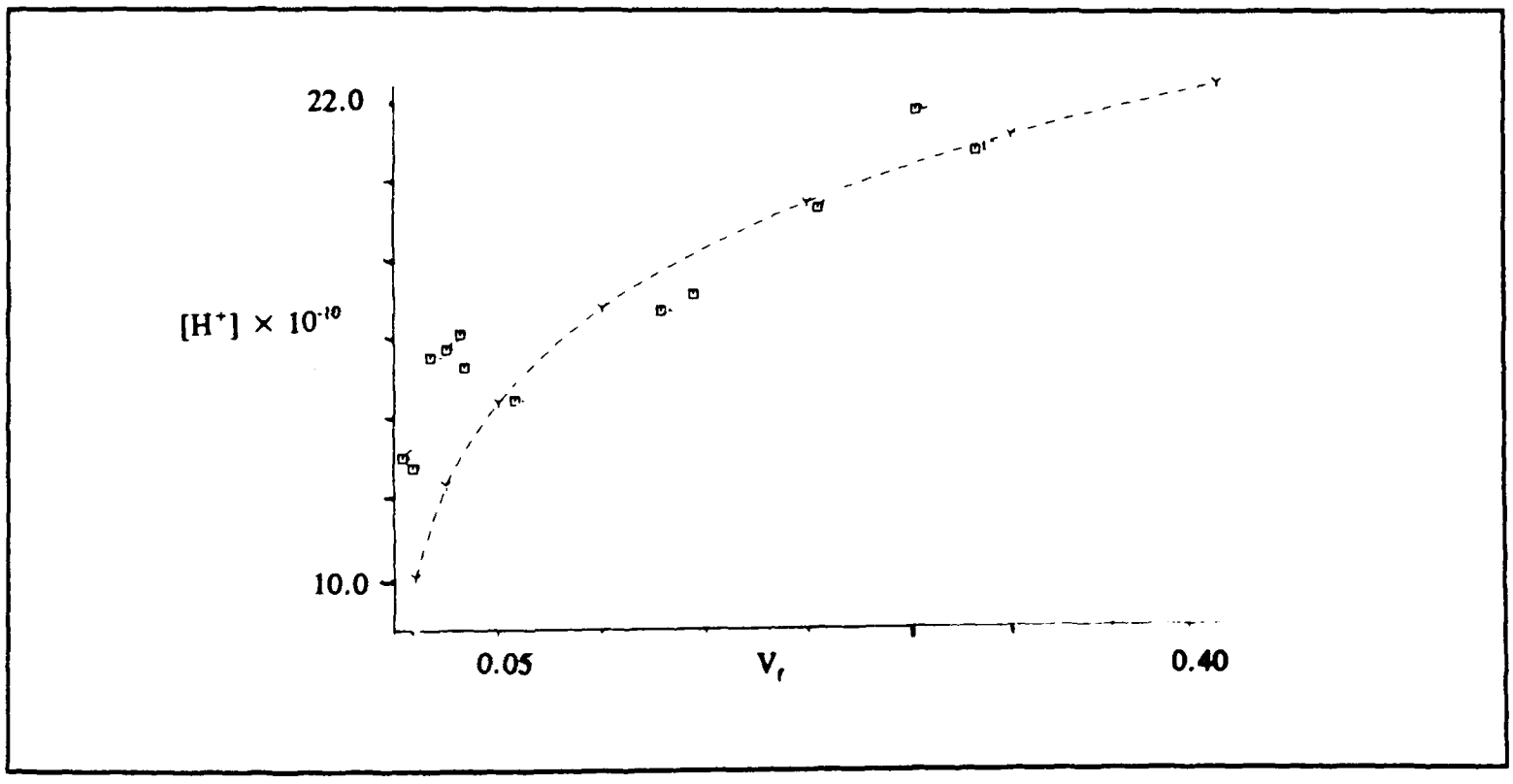

Figure 6.7: The best theoretical fit of the experimental data obtained with a solution where [PAA]= 9.7 × 10^{-6} mol dm^{-3} and [Ca^{2+}]= 4.7 × 10^{-4} mol dm^{-3} (cell parameters as in figure 6.3) with a fixed x=0.50.

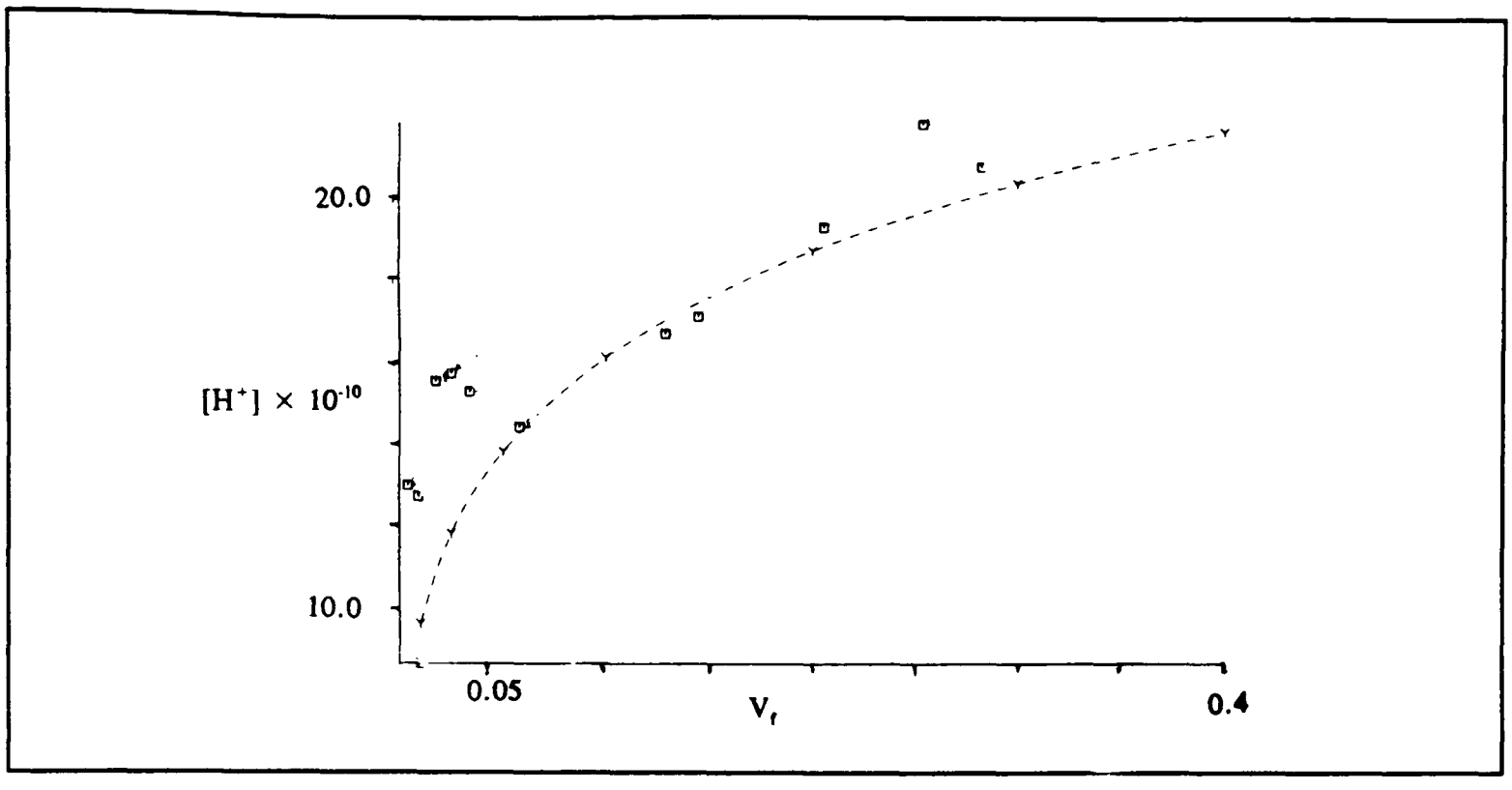

Figure 6.8: The best theoretical fit of the experimental data obtained with a solution where [PAA]= 9.7 × 10^{-6} mol dm^{-3} and [Ca^{2+}]= 4.7 × 10^{-4} mol dm^{-3} (cell parameters as in figure 6.3) with a fixed x=0.75.

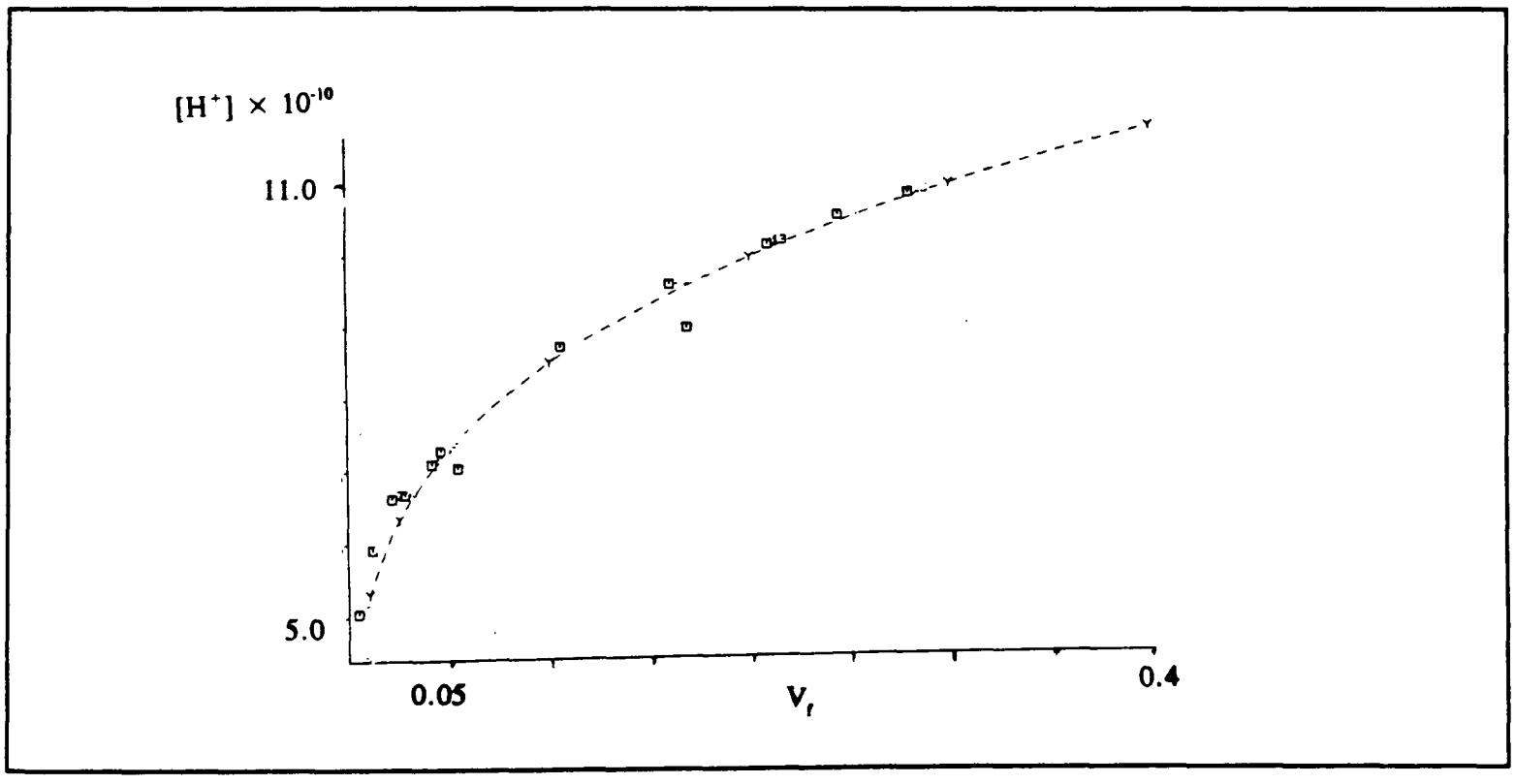

Figure 6.9: The best theoretical fit of the experimental data obtained with a solution where [PAA]= 1.0 × 10^{-5} mol dm^{-3} and no added Ca^{2+} (cell parameters as in figure 6.1) with a fixed x=0.25.

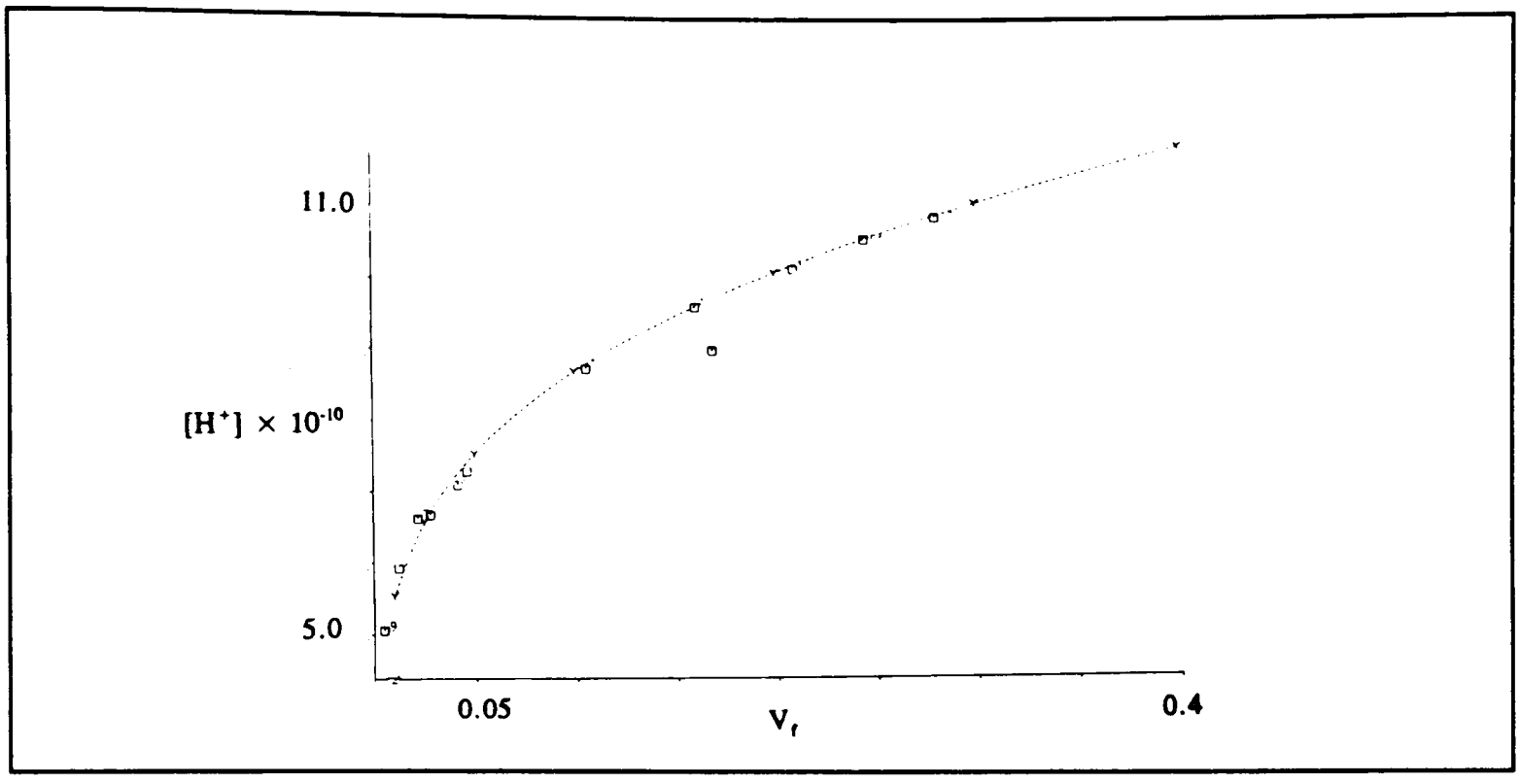

Figure 6.10: The best theoretical fit of the experimental data obtained with a solution where [PAA]= 1.0 × 10^{-5} mol dm^{-3} and no added Ca^{2+} (cell parameters as in figure 6.1) with a fixed x=0.50.

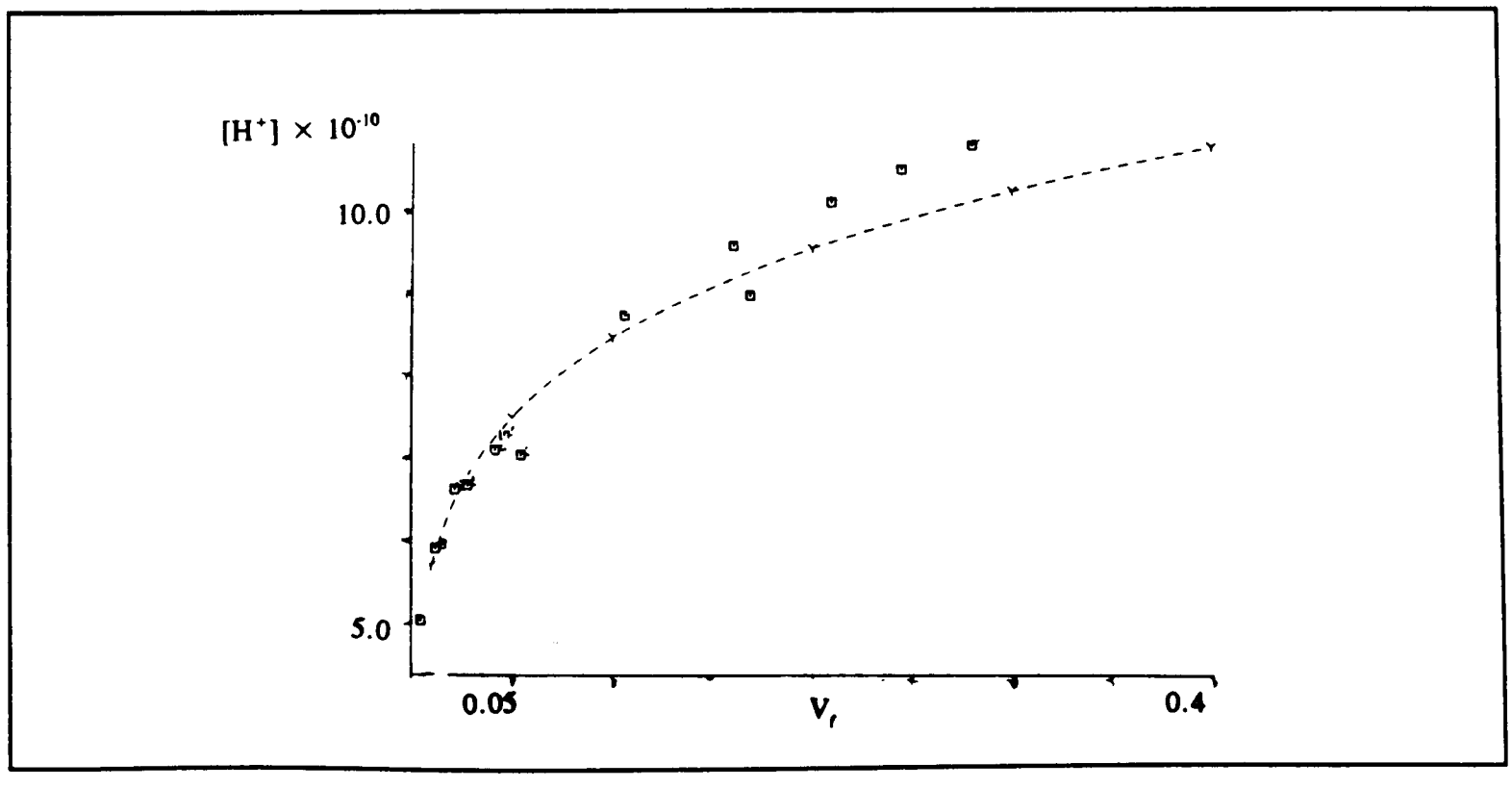

Figure 6.11: The best theoretical fit of the experimental data obtained with a solution where [PAA]= 1.0 × 10^{-5} mol dm^{-3} and no added Ca^{2+} (cell parameters as in figure 6.1) with a fixed x=0.75.

Table 6.1 The values of $K_{eq}K_L$ obtained from the best fits for the experimental data.

[PAA] / mol dm^{-3}	[Ca^{2+}] / mol dm^{-3}	$K_{eq}K_L$ / (mol dm^3)$^{(1+x)}$		
		$x = 0.25$	$x = 0.5$	$x = 0.75$
9.7 (±0.1) × 10^{-6}	4.7 (±0.1) × 10^{-4}	4.0 (± 0.5) × 10^3	1.5 (± 0.5) × 10^5	5.0 (± 0.5) × 10^6
9.7 (±0.1) × 10^{-6}	9.5 (±0.1) × 10^{-4}	2.0 (±0.5) × 10^4	7.0 (±0.5) × 10^5	2.5 (±0.5) × 10^7
1.9 (±0.1) × 10^{-5}	4.5 (±0.1) × 10^{-4}	7.0 (±0.5) × 10^3	2.0 (±0.5) × 10^5	2.0 (±0.5) × 10^7
4.8 (±0.1) × 10^{-5}	4.7 (±0.1) × 10^{-4}	5.0 (±0.5) × 10^3	2.0 (±0.5) × 10^4	2.5 (±0.5) × 10^6
4.9 (±0.1) × 10^{-5}	9.1 (±0.1) × 10^{-4}	2.0 (±0.5) × 10^3	7.0 (±0.5) × 10^4	2.5 (±0.5) × 10^6
9.7 (±0.1) × 10^{-5}	4.7 (±0.1) × 10^{-4}	5.0 (±0.5) × 10^3	2.0 (±0.5) × 10^5	7.0 (±0.5) × 10^6
1.0 (±0.1) × 10^{-5}	2.5 (±0.1) × 10^{-5}	5.0 (±0.5) × 10^3	8.0 (±0.5) × 10^5	3.0 (±0.5) × 10^6
2.0 (±0.1) × 10^{-5}	1.5 (±0.1) × 10^{-5}	7.0 (±0.5) × 10^3	1.0 (±0.5) × 10^6	1.7 (±0.5) × 10^6

It is important to remember that the values quoted above for calcium concentrations include the calcium generated at the surface. For the 1.0×10^{-5} and 2.0×10^{-5} polyacrylic acid solutions which have no added background calcium, these values refer only to Ca^{2+} generated at the surface as predicted from the theory.

However it was not possible to discern precisely between the three fractional values of x quoted above. If the means of the values of $K_{eq}K_L$ are taken, they are found to be: for $x = 0.25$ $K_{eq}K_L = 6.9 \times 10^3$ ($\pm$ 5.5×10^3) /(mol^{-1} dm^3)$^{(1+x)}$, for $x = 0.50$ $K_{eq}K_L =$ 4.2×10^5 ($\pm$ 3.6×10^5) /(mol^{-1} dm^3)$^{(1+x)}$ and for $x = 0.75$ $K_{eq}K_L = 9.2 \times 10^6$ ($\pm$ $8.7 \times$ 10^6)/(mol^{-1} dm^3)$^{(1+x)}$. This does show an increase in the size of the error relative to the mean with increasing x.

6.5 Discussion

These experiments show that at high pH, as at low pH, it is a complex between Ca^{2+} and polyacrylic acid which adsorbs on the calcite surface and causes inhibition. The exact ratio of cation to polymer in the complex formed at high pH could not be distinguished, but it was deduced that this was between zero and one. This compares to low pH where the ratio was approximately 0.5 cations to each polymer chain.

Another important observation is that inhibition is complete at a lower level of added polymer. This is because different kinetics occur at high pH as opposed to low pH. At low pH the dissolution reaction is that with H^+, which has a much faster rate than at high pH where the reaction is with H_2O. It is also significant that much lower background levels of added background Ca^{2+} are needed at high pH, to cause the inhibition to be enhanced and totally 'shut off' the dissolution reaction. These levels of background Ca^{2+} needed are comparable to the levels of Ca^{2+} generated at the surface.

Thus polyacrylic acid inhibits at high pH and that it does so via the formation of a complex with Ca^{2+} ions. This is of special interest as it is likely that in most 'natural' or 'industrial' settings there will be 2+ cations present. Therefore any estimates of the strength of inhibition of calcite dissolution by polyacrylic acid, which are gained in the laboratory in the absence of background levels of 2+ cations, could be significant underestimates. This could have possible consequences, particularly in situations such as liming acid lakes, when polyacrylic acid is often used as a dispersant and its inhibitory properties ignored [161].

6.6 Conclusions

The work in this chapter has built on the work in Chapter 4, where inhibition of calcite dissolution in the presence of polyacrylic acid was studied under conditions of low pH. In addition the conclusions in Chapter 5 concerning the mechanism of dissolution at high pH has been modified to describe the action of an inhibitor which competes with CO_3^{2-} for a surface adsorption site.

Again the channel flow cell method has been shown to be capable of giving reliable kinetic information on the inhibition of calcite dissolution. Using the conclusions from these previous chapters it has been possible to discern that as at low pH, it is a complex between Ca^{2+} and polyacrylic acid which adsorbs on the surface at high pH, and causes the inhibition observed.

6.7 Final Overall Conclusions

Throughout this work the channel flow cell has been used to probe the surface kinetics of calcite dissolution, and with the use of the backwards implicit finite difference method, it has been possible to draw conclusions about the mechanisms which are occurring. This has been achievable both at low and high pH, although very different kinetics occur under these two regimes.

At low pH (Chapter 4) further investigation was made of the effect of small molecules on the dissolution of calcite. The results supported the previous conclusions [91,145] concerning molecular shape and the relative inhibitory strength. The effect of polyacrylic acid on dissolution at low pH was also investigated, and it was seen that inhibition occurred via the formation of a complex with Ca^{2+}, with the stoichiometry of two polyacrylic chains for each Ca^{2+}. On further investigation it was seen that this need for the formation of a complex before adsorption on the surface did not seem to be affected by the chain length (or molecular weight) of the polymer. Also it was seen that at low pH other divalent cations was as (or more) efficient as Ca^{2+} in the formation of a suitable complex.

If it is assumed that none of the small molecules or polymaleic acid [2] have any similar enhancement of inhibition then the overall strength of inhibition of all the molecules studied by the channel flow cell method at low pH is:

polyacrylic acid > maleic acid > *meso*-tartaric acid ~ homo-phthalic acid

> phthalic acid > polymaleic acid.

Thus in conditions when there are significant concentrations of di-valent cations in solution polyacrylic acid is the strongest inhibitor. Further work to verify that the

assumption that di-valent cations do not affect the inhibitory strength of the other inhibitors would be useful. Although the lack of any deviation from the predicted behaviour at low inhibitory strength and high flow rate for these molecules does indicate that the assumption is valid. Thus as under natural or industrial conditions it would seem normal for there to be background Ca^{2+} or other di-valent cations present; for such conditions polyacrylic acid is the strongest inhibitor.

At high pH investigation was made of a number of rate equations which had been previously proposed. It was seen that none of these adequately fitted the experimental data over the whole range of flow rates, pH's and background Ca^{2+} levels. So a new mechanistically rational rate law was proposed and shown to accurately predict experimental behaviour.

This rate law for high pH dissolution of calcite was then modified to describe the behaviour in the presence of inhibitors, and applied to the case of high pH dissolution in the presence of polyacrylic acid. Again it was seen that polyacrylic acid, as at low pH adsorbs on the surface of calcite via the formation of a complex with Ca^{2+}. Further study could be performed in the future to investigate the effect of molecular weight and other cations as at low pH. It would be of interest to see if there is a similar maximum in the strength of inhibition with molecular weight, particularly as high molecular polyacrylic acids are much more soluble at these pH's.

Another area that would be of considerable interest would be to investigate whether any other polymers form a complex before adsorbing on the surface of calcite, in particular whether an analogous mechanism occurs in natural systems for example with polysaccharides.

In conclusion the channel flow cell has provided quantitative information on the dissolution of calcite. By probing surface concentrations the precise mechanisms involved in the inhibition of dissolution by a number of molecules have been examined. Finally it has been possible to distinguish between different proposed mechanisms, which helps to determine exactly which reactions are important in calcite dissolution.

APPENDIX 1

ADSORPTION OF FOREIGN SPECIES ON CALCITE

The table below lists many of the literature reports on the effect of various species on calcite dissolution/precipitation kinetics, their adsorption on, and coprecipitation with, calcite and distribution coefficients, etc.

Table A1.1. The Adsorption of Various Species on Calcite

Inhibitor	Technique	Conclusions	Reference
Am	equil^{m}, powder, radio-tracer	Am rapidly & strongly adsorbed.	[188]
various cations	diss, powder, $P_{CO2} \approx 1$, titration	Effectiveness of inhibitor $Pb^{2+} > La^{3+} > Y^{3+} > Sc^{3+} > Cd^{2+} > Cu^{2+} > Au^{3+} > Zn^{2+} > Ge^{4+} > Mn^{2+} > Ni^{2+} = Ba^{2+} = Mg^{2+} = C$ o^{2+}	[189]
Ba^{2+}, Sr^{2+}, Cd^{2+}, Mn^{2+}, Zn^{2+}, Co^{2+}, Ni^{2+}	equil^{m}	M^{2+}-Ca^{2+} exchange on cation specific surface sites. Sorption was in sequence $Cd > Zn \geq Mn > Co > Ni \gg Ba = Sr$.	[190]
Ba^{2+}	ppt, seeded growth	Partition coefficient independent of ppt^{n} rate.	[191]
Ba^{2+}	single crystal & powder	Atomic absorption & ESCA study of Ba^{2+} sorption; conclude Ca^{2+}-Ba^{2+} exchange & Langmuirian adsorption.	[192]
Be^{2+}, Mg^{2+}, Sr^{2+}, Ba^{2+}	powder	Kinetics of aragonite to calcite transformation - inhibited by $Be^{2+} > Mg^{2+} > Sr^{2+} > Ba^{2+}$.	[193]
Cd^{2+}	equil^{m}, powder, atomic adsorption	< 1 μmol g^{-1}, linear adsorption isotherm; higher $[Cd^{2+}]$ gave $CdCO_3$ ppt.	[194]

Inhibitor	Technique	Conclusions	Reference
Co^{2+}	powder, radio-tracer	Co^{2+} adsorption occurred but no $CoCO_3$ surface phase formed. Ca^{2+} & Mg^{2+} compete with Co^{2+} for adsorption sites.	[195]
Cu^{2+}	equilibration in distilled & sea water, powder, atomic spect^{y}	Conclude that a coppt. is formed in distilled water, but surface ppt^{n} of $CuCO_3$ occurred in seawater.	[196]
Cu^{2+}	Cu^{2+} detection in calcite	VIS & IR reflectance spectroscopy.	[197]
Cu^{2+}	diss, powder, free drift, conductivity	Cu^{2+} strongly inhibits.	[198]
Cu^{2+}, Pb^{2+}, Zn^{2+}, Cd^{2+}	-	extraction	[199]
Mg^{2+}, SO_4^{2-}	ppt, powder	Enhanced solubility. Langmuirian adsorption.	[174]
Mg^{2+}	ppt, chemo-stat, $P_{CO2}=10^{-2.5}$	Amount of Mg^{2+} incorporated into overgrowth independent of ppt^{n}. rate.	[25]
Mg^{2+}	diss, single crystal, free-drift, conductivity	Inhibition by Mg^{2+}, due to surface adsorption.	[200]
Mg^{2+}, Ba^{2+}, Zn^{2+}	diss, free-drift, atomic abs^{n}	Adsorption occurred. New phases found with Ba & Zn. No new phase with Mg.	[201]
Mg^{2+}, PO_4^{3-}	diss, powder & single crystal, free-drift & pH-stat	Mg^{2+} exhibited Langmuirian adsorption. Phosphate inhibits at very low concentrations.	[56]
Mg^{2+}, Sr^{2+}	ppt, seeded growth, pH-stat	Incorporation of M^{2+} independent of precipitation rate.	[76]

Inhibitor	Technique	Conclusions	Reference
Mg^{2+},	ppt, single crystal, Auger	Langmuirian adsorption of Mg^{2+}. Surface $[Mg^{2+}]/[Ca^{2+}]$ determined.	[202-204]
Mg^{2+}	powder & single crystal, radio-tracer	Adsorption of Mg^{2+}. Surface $[Mg^{2+}]/[Ca^{2+}]$ determined.	[205-209]
Mg^{2+}, Co^{2+}, Ni^{2+}, Fe^{2+}	equil^{m}, powder, radio-tracer	Adsorption of M^{2+}. Surface $[M^{2+}]/[Ca^{2+}]$ determined.	[210]
Mg^{2+}	powder, streaming potentials	Adsorption of Mg^{2+}.	[211]
Mg^{2+}, Sr^{2+}	ppt, free-drift, atomic abs^{n}	With Mg^{2+}, $CaCO_3$ precipitated as spherulites, which aged to aragonite and distorted magnesian calcite. Sr^{2+} produced no change of habit.	[212]
Mg^{2+}	ppt, seeded growth, free drift, atomic abs^{n} & titration	Inhibition due to Langmuirian adsorption of Mg^{2+}.	[213]
Mg^{2+}	equil^{m}, X-ray diffraction	Kinetics of aragonite to calcite transformation, inhibited by Mg^{2+}.	[214]
Mg^{2+}	ppt, seeded growth, chemo-stat	Strong inhibition at sea water concentrations.	[215]
Mg^{2+}	ppt, atomic abs^{n}	Distribution coefficient of Mg^{2+} in calcite.	[216]
Mg^{2+}	ppt, seeded growth, chemo-stat	P_{CO2} has significant effect on $MgCO_3$ incorporation.	[217]
Mg^{2+}	ppt, seeded growth, chemo-stat	Distribution coefficient of Mg^{2+} in calcite overgrowths.	[218]

Inhibitor	Technique	Conclusions	Reference
Mg^{2+}, Mn^{2+}, Ni^{2+}, Cr^{3+}, F^-	ppt, free-drift	Only Mg^{2+} & Mn^{2+} showed substantial inhibition.	[219]
Mn^{2+}, Fe^{2+}	ppt, seeded-growth, chemo-stat	Distribution coefficients.	[220]
Mn^{2+}	ppt, seede-growth, chemo-stat	Increased inhibition as $[Mn^{2+}]/[Ca^{2+}]$ increased and Ω decreased.	[79]
Mn^{2+}	equil^m, powder, radio-tracer	Mn^{2+} exchanges with 1 - 2 layers of Ca^{2+}.	[221]
Na^+, K^+	ppt	$[Na^+]/[Ca^{2+}]$ and $[K^+]/[Ca^{2+}]$ ratios in calcite independent of pH & solution $[Ca^{2+}]$. Na^+ & K^+ thought to be incorporated at interstitial sites.	[222]
Sc^{3+}	diss, radio-tracer	Adsorption at active sites.	[223]
Sr^{2+}	ppt, seeded growth, free-drift, AA	Distribution coefficients.	[224]
Zn^{2+}	ppt, free-drift, titration	Inhibition and partial coppt^n.	[225]
Zn^{2+}	ppt, free-drift, titration & radio-tracer	Distribution coefficients.	[226]
Zn^{2+}	equil^m	Zn^{2+}-Ca^{2+} exchange in surface adsorption layer. Freundlich, Lanmuir-Freundlich, 2 part Langmuir isotherms.	[227]

Inhibitor	Technique	Conclusions	Reference
uranyl, UO_2^{2+}	equil^m	Uranyl ion found to adsorb due to formation of hydroxy-carbonato species. Maximum extent of adsorption dependent on $[UO_2^{2+}]$.	[228]
various	ppt, pH-stat	Inhibition $Fe^{2+} > ATP > P_3O_7^{5-} > P_2O_7^{4-} > (PO_3)_6^{6-} > Zn^{2+} >$ $ADP > Ce^{3+} > Pb^{2+} >$ carbamyl phosphate $> Fe^{3+} > PO_4^{3-} > Co^{2+} > Mn^{2+} > Be^{2+} >$ β-glycerophosphate $> Ni^{2+} > Cd^{2+} >$ phenylphosphate $> Ba^{2+} >$ citrate $>$ AMP $> Sr^{2+} > SO_4^{2-} > Mg^{2+}$	[229]
phosphate, silica, NO_3^-, organics	diss, powder, pH-stat	Significant inhibition by PO_4^{3-}. Little or no effect by NO_3^-, silica or organics at sea water concentrations.	[230]
phosphate	ppt, seeded growth, pH-stat	Inhibition dependent on $[HPO_4^{2-}]$ & $[PO_4^{3-}]$.	[78]
phosphate	ppt, free-drift, seeded growth	Inhibition found to be dependent on Ω.	[231]
orthophosphate	equil^m, free-drift & chemo-stat	Phosphate uptake not affected by $[Mg^{2+}]$. or $[F^-]$. Elovichian chemisorption theory used.	[232]
phosphate & glycerophosphate	ppt, seeded growth	50% inhibition at 16 μM & 2 μM for glycero- and ortho-phosphate. Langmuirian adsorption observed.	[46]
orthophosphate	ppt, seeded growth, chemo-stat	Inhibition determined by $[PO_4^{3-}]$.	[77]
phosphate	diss, pH-stat	Phosphate ions strongly adsorbed.	[27]

Inhibitor	Technique	Conclusions	Reference
phosphate	equil^{m}	At low phosphate concentration PO_4^{3-} exchanged with surface CO_3^{2-}. At higher concentration, HPO_4^{2-} is adsorbed with accompanying counterion(s) as neutral species following Freundlich isotherm.	[233]
phosphonates	ppt, seeded growth, free-drift	Inhibition at μM levels. Langmuirian adsorption observed.	[46]
diphosphonates	ppt, pH-stat	Powerful inhibitors at 10^{-7} mol dm^{-3}. Langmuirian adsorption found.	[234]
SeO_3^{2-}	equil^{m}, isotope tracer method, pH7.0-9.5	SeO_3^{2-} exchanged with CO_3^{2-}; SO_4^{2-} & PO_4^{2-} decreased SeO_3^{2-} adsorption but was unaffected by Mg^{2+}, implying anion specific adsorption sites.	[235]
benzenehexacarboxylic and benzene-1.3.5-tricarboxylic acids	ppt, chemo-stat, pH8.50	Benzenehexacarboxylic acid follows Langmuirian adsorption isotherm; benzene-1,3,5-tricarboxylicacid - little effect.	[236]
stearic acid, octadecylamine, octdecanol, cholesterol	ppt, Langmuir trough	Crystallisation of $CaCO_3$ under compressed Langmuir monolayers of organic species.	[237-239]
stearic acid & albumin	powder, free-drift	Stearic acid and albumen form monolayers on surface.	[240]
amino acids, sugars, proteins, acetate, malate, pyruvate, citrate, succinate	ppt	Ppt^{n} greatly inhibited by citrate, malate, pyruvate, glycylglycineand glycogen. Some of the others affect $CaCO_3$ crystal type formed.	[241]
palmitic acid	diss, powder, free drift	S-shape adsorption isotherms. Mg^{2+} ions greatly decreased fatty acid adsorption.	[242]

Inhibitor	Technique	Conclusions	Reference
maleic acid	diss, channel	Langmuirian adsorption of maleic acid dianion.	[91]
tartaric acid	diss, channel	Langmuirian adsorption of tartaric acid dianion. Meso-tartarate more potent isomer.	[92]
α,ω-dicarboxylates	ppt	Effect of species on calcite morphology.	[244]
polyvinyl sulponate (PVS) & polyglutamic acid (PGA)	ppt	PVS no effect. PGA slight effect.	[243]
polymaleic acid	diss, channel	Dissolution rate slowly decreased with time as PMA adsorbed.	[2]

ppt - precipitation; diss - dissolution; equil^{m} - equilibrium;
AA - atomic absorption spectroscopy.

APPENDIX 2

THE THOMAS ALGORITHM

The Thomas algorithm [131], is a simplified form of Gaussian elimination and is an efficient method for the solution of tridiagonal matrix systems. The matrix equation to be solved is written as

$$\{d\} = [T]\{u\} \tag{A2.1}$$

The algorithm operates by factorising the tridiagonal matrix $[T]$ into two bidiagonal matrices $[T_L]$ and $[T_U]$

$$[T] = [T_L][T_U] \tag{A2.2}$$

A solution is then found for the vector $\{f\}$ in

$$[T_L]\{f\} = \{d\} \tag{A2.3}$$

and $\{f\}$ is used to give a final solution

$$[T_U]\{u\} = \{f\} \tag{A2.4}$$

Since

$$[T_L]^{-1}\{d\} = \{f\} \qquad [T_U]\{u\} = [T_L]^{-1}\{d\} \tag{A2.5}$$

thus

$$([T_L][T_U])\{u\} = \{d\} \tag{A2.6}$$

The matrix $[T]$ of $(J\text{-}1)\text{x}(J\text{-}1)$ elements can be written as

$$[T] = \begin{bmatrix} b_1 & c_1 & 0 & & & & & \\ a_2 & b_2 & c_2 & 0 & & & & \\ & \ddots & \ddots & \ddots & & & & \\ & & \ddots & \ddots & \ddots & & & \\ & & 0 & a_j & b_j & c_j & 0 & \\ & & & & \ddots & \ddots & \ddots & \\ & & & & & \ddots & \ddots & \ddots \\ & & & & & 0 & a_{J-2} & b_{J-2} & c_{J-2} \\ & & & & & & 0 & a_{J-1} & b_{J-1} \end{bmatrix} \tag{A2.7}$$

On factorisation $[T]$ takes the form

$$[T] = [T_L][T_U] = \begin{bmatrix} \alpha_1 & & & & & 0 \\ \alpha_2 & \alpha_2 & & & & \\ & \ddots & \ddots & & & \\ & & \ddots & \ddots & & \\ & & & \alpha_{J-2} & \alpha_{J-2} & \\ 0 & & & & \alpha_{J-1} & \alpha_{J-1} \end{bmatrix} \begin{bmatrix} 1 & \beta_1 & & & 0 \\ & 1 & \beta_2 & & \\ & & \ddots & \ddots & \\ & & & \ddots & \ddots \\ & & & & 1 & \beta_{J-2} \\ 0 & & & & & 1 \end{bmatrix} \tag{A2.8}$$

where α_j and β_j are to be determined.

By equating the left- and right-hand sides of the equation $[T] = [T_L]\,[T_U]$, the the following relations are obtained

$$\alpha_1 = b_1 \tag{A2.9}$$

$$\beta_1 = \frac{c_1}{\alpha_1} \tag{A2.10}$$

$$\alpha_j = b_j - a_j\beta_{j-1} \qquad j = 2,3\ldots J\text{-}1 \tag{A2.11}$$

$$\beta_j = \frac{c_j}{\alpha_j} \qquad j = 2,3\ldots J\text{-}2\ (a_j \neq 0) \tag{A2.12}$$

After obtaining α_j and β_j, the equation for $\{f\}$ is solved

$$[T_L]\{f\} = \{d\} \tag{A2.13}$$

where the elements f_j of $\{f\}$ are given by

$$f_1 = \frac{d_1}{\alpha_1} \tag{A2.14}$$

$$f_j = \frac{(d_j - a_j f_{j-1})}{\alpha_j} \qquad j = 2,3\ldots J\text{-}1 \tag{A2.15}$$

$\{f\}$ is then used to determine the elements u_j of $\{u\}$

$$u_{J-1} = f_{J-1} \tag{A2.16}$$

$$u_j = f_j - \beta_j u_{j+1} \qquad j = 1,2\ldots J\text{-}2 \tag{A2.17}$$

By this procedure the matrix equation $[T]\{u\} = \{d\}$ is solved for $\{u\}$.

APPENDIX 3

THE POTENTIOSTAT

The potentiostat is a device which actively maintains the potential difference between the working (WE) and reference (RE) electrodes at a given value by altering the voltage between the working and counter (CE) electrodes, as necessary. In other words, it forces whatever current is necessary through the WE so that the required potential is achieved. The potentiostat's design is based on the operational amplifier. The ideal operational amplifier has several useful features

(a) Infinite input impedance, i.e. the inverting (-) and non-inverting (+) inputs draw no current from the voltage sources (can be 10^5 - 10^{14} Ω).

(b) Zero output impedance, i.e. the output voltage remains constant irrespective of the current drawn (limits typically 5 - 100 mA).

(c) Infinite gain, A, i.e. any voltage difference between the inputs, drives the output to the limit deliverable by the power supply. (Typically $A = 10^4$ - 10^8 for d.c. signals).

$$E_{out} = -A(E_- - E_+) \qquad \text{(A3.1)}$$

(d) Infinite bandwidth, i.e. it can respond to a change in voltage with infinite speed or respond to a signal of any frequency. (Typical unity-gain bandwidths, 100 Hz - 100 MHz).

In most applications the operational amplifier is stabilised by feeding back part of its output to the inverting input (negative feedback). In this mode of operation the two inputs are forced to have the same potential. Booster amplifiers (non-inverting, usually low gain) are included, permitting the attainment of larger currents and voltages than would have otherwise been accessible.

APPENDIX 4

THE COMPUTER PROGRAMS

4.1 PAAABI - low pH dissolution

This section lists the computer program which uses the Backwards Implicit Finite Difference method to model the dissolution of calcite in the channel flow cell, at low pH in the presence of polyacrylic acid. This program is an example of the programs used to model low pH dissolution of calcite. It uses the surface kinetics and surface boundary conditions as described in chapter 4.

```
      REAL*8 LH(3000),LB(3000),LP(3000),LA(3000)
      REAL*8 GB(3000),GP(3000),GH(3000),GA(3000)
      REAL*8 BH(3000),BB(3000),BP(3000),BA(3000)
      REAL*8 DOFH(3000),DOFB(3000),
     +   DOFP(3000),DOFA(3000)
      REAL*8 SUMH,BHA,BPAA,SUMP,ILIMP1,
     +   ILIMH1,KN1,BX,PX
      REAL*8 KHCO3,H,KEHCO3,KN,MSUBN,
     +   THETA,RH,RB,RP,RA
      REAL*8  CONSTH(3000),CONSTB(3000),
     +   SF,ILIMH2,ILIMP2
      REAL*8 SURCONCH,XEL,XE,XEM,TOTL,BCA
      CHARACTER*1  ANS,st
      INTEGER  S

      COMMON  NY
      F=9.648456E4
      DD  = 0.60D0
      DH  = 7.6000000000000E-5
      DP  = 1.1000000000000E-6
      DB  = 1.0000000000000E-5
      DA  = 7.9300000000000E-6

      KHCO3   = 19.0D0
      KEHCO3  = 3.06000000000E-7
      KN      = 0.0430D0
      KN1     = 0.0430D0

C     KHCO3  =0.D0
C     KEHCO3=0.0D0
C     KN   = 0.0D0

C     KN1  = 0.0D0

      IANS=1
```

```
      PRINT*,'Value of kn ?'
      READ*,KN
C     KN = 0.0430D0

      PRINT*,'Value of theta ie. surface coverage'
      READ*,THETA

C     THETA = 0.0D0

      PRINT*,'All dimensions of length in cm'
      PRINT*,'Size of Grid X'
      READ*,NX

C     NX= 500

      PRINT*,'Size of Grid Y'
      READ*,NY

C     NY = 200

      PRINT*,'Volume flow rate'
      READ*,V

C     V = 1.00000000000000E-3
      PRINT*,'[H+] mM/cm3'
      READ*,BHA

C     BHA = 1.000000000000000E-6
      BHA=BHA*1.0E-6

      PRINT*,'BULK [PAA] mol/cm3'
      READ*,BPAA
C     BPAA = 0.0D0
      BPAA=BPAA*1.0E-6
      PRINT*,BPAA

      PRINT*,'Height of channel (2h)'
      READ*,TWOH

      PRINT*,'width of electrode(w)'
      READ*,w    C  w = 0.40d0

      PRINT*,'Length of crystal'
      READ*,XE

      XE = 0.40d0

      PRINT*,'Lenght of detector'
      READ*,XEL
      TOTL=XEL+XE
      C  TOTL = 0.80d0

**********Calculate m-n

      C  MSUBN=((BPAA*26.7)-BHA)/BPAA

      PRINT*,'m-n?'
      READ*,MSUBN

      C  MSUBN = 1.0D0

      PRINT*,'Bulk[Ca]?'
      READ*,BCA
      BCA=BCA*1e-3
```

```
*********MONITOR ELECTRODE PRESENT
      PRINT*,'MONITOR ELECTRODE PRESENT Y/N?'
      READ 11,ANS
11    FORMAT(A1)
      IF (ANS.EQ.'Y') THEN
         IANS=2
         PRINT*,'MONITOR ELECTRODE LENGTH'
         READ*,XEM

      ENDIF
*******NX,DX AND DY

      DELX  = XE/DBLE(NX)
      DELY  = TWOH/DBLE(NY)
      NXT   = NINT(TOTL/DELX)
      KN    = (1.0d0 - THETA)*KN
      KN1=KN
      H  = TWOH/2.0d0

*****CALCULATION  OF LAMBDA

      RH  =(DH*DELX*TWOH*TWOH*TWOH*DD)/
     +   (6.0D0*V*DELY*DELY*DELY)

      RP  =(DP*DELX*TWOH*TWOH*TWOH*DD)/
     +   (6.0D0*V*DELY*DELY*DELY)

      RB  =(DB*DELX*TWOH*TWOH*TWOH*DD)/
     +   (6.0D0*V*DELY*DELY*DELY)

      RA  =(DA*DELX*TWOH*TWOH*TWOH*DD)/
     +   (6.0D0*V*DELY*DELY*DELY)

      DO 10 J=1,NY-1
        LH(J)  = RH/(DBLE(J)*(TWOH-(DBLE(J)*DELY)))
        LP(J)  = RP/(DBLE(J)*(TWOH-(DBLE(J)*DELY)))
        LB(J)  = RB/(DBLE(J)*(TWOH-(DBLE(J)*DELY)))
        LA(J)  = RA/(DBLE(J)*(TWOH-(DBLE(J)*DELY)))
10    CONTINUE

*****LOOP FOR CALCULATING SHIELDING
******FACTORS

      DO 333 S = 1,IANS

       IF (S.EQ.1) THEN

        KN = KN*1.0d0
        KN1 = KN1*1.0D0
       ELSE
        KN = 0.0000d0
        KN1 = 0.0D0

       ENDIF

******DEFINE BULK CONCENTRATIONS

      DO 15 J = 1,NY-1
        GH(J)  = 1.0D0
        GB(J)  = 0.0D0
        GP(J)  = BPAA/BHA
        GA(J)  = BCA/BHA

15    CONTINUE
```

```
******SET CURRENT TOTALS

      SUMH = 0.0D0
      SUMP = 0.0D0
      AVEH = 0.0D0
      AVEP = 0.0D0
      AVEB = 0.0D0
      AVEA = 0.0D0

*******K LOOP OVER CRYSTAL

      DO 30 K = 1,NX

*******CALCULATE HOMOGENEOUS RATES

      DO 131 J =1,NY-1
         CONSTH(J) = (((KHCO3*GH(J)*GB(J))/
     +      ((KEHCO3/BHA)+GB(J)+GH(J)))
     +      *((LH(J)*DELY*DELY)/DH))

         CONSTB(J) = (((KHCO3*GH(J)*GB(J))/
     +      ((KEHCO3/BHA)+GB(J)+GH(J)))
     +      *((LB(J)*DELY*DELY)/DB))

131   CONTINUE

******SPECIES H+

      BX = LH(1)/(1.0D0 +((DELY*KN)/DH))

      BH(1) = (2.0d0*LH(1)) + 1.0d0 - BX
      BH(NY-1) = LH(NY-1)+1.0D0

      DO 221 J = 1,NY-1
        DOFH(J) = GH(J) - CONSTH(J)
221   CONTINUE

*******CALL BI ROUTINE

      CALL BI(GH,LH,DOFH,BH)

*******SPECIES PAA

      PX = (DP*LP(1))/(DP + (KN1*DELY*MSUBN))

      BP(1) = 2.0D0*LP(1) + 1.0d0 - PX
      BP(NY-1) = LP(NY-1)+1.0D0

      DO 223 J = 1,NY-1
        DOFP(J)=GP(J)
223   CONTINUE

*******CALL BI ROUTINE

      CALL BI(GP,LP,DOFP,BP)

*******SPECIES HCO3-

      BB(1) = LB(1) + 1.0D0
      BB(NY-1) = LB(NY-1)+1.0D0

      DOFB(1) = GB(1)+(((LB(1)*KN*DELY*DH)/
     +   (DB*(DH +(KN*DELY))))*GH(1))
     +   +(((LB(1)*KN1*DELY*DP*MSUBN)/
     +   (DB*(DP + (KN1*DELY*MSUBN))))*GP(1))
     +   - CONSTB(1)
```

```
      DO 222 J = 2,NY-1
        DOFB(J)=GB(J)  - CONSTB(J)
222   CONTINUE

*******CALL BI ROUTINE

      CALL BI(GB,LB,DOFB,BB)
      BA(1) = LA(1) + 1.0D0
      BA(NY-1) = LA(NY-1)+1.0D0
      DOFA(1) = GA(1)+(((LA(1)*KN*DELY*DH)
     +   /(DA*(DH+(KN*DELY))))*GH(1))
     +   +(((LA(1)*KN1*DELY*DP*MSUBN)/
     +   (DA*(DP + (KN1*DELY*MSUBN))))*GP(1))

      DO 224 J = 2,NY-1
        DOFA(J)=GA(J)
224   CONTINUE

*******CALL BI ROUTINE

      CALL BI(GA,LA,DOFA,BA)

******CALCULATE SURFACE CONCENTRATIONS

      SURCONCH = DH*GH(1)/(DH  + (KN*DELY))
      SURCONCP = DP*GP(1)/(DP  +
     +      (KN1*DELY*MSUBN))
      SURCONCB =GB(1)+(DELY*KN*GH(1)*DH)
     +   /(DB*((DELY*KN)+DH))
     +   +((KN1*DELY*DP*MSUBN*GP(1))
     +   /(DB*((DELY*KN1*MSUBN)+DP)))
      SURCONCA =GA(1)+(DELY*KN*GH(1)*DH)/
     +   (DA*((DELY*KN)+DH))
     +   +((KN1*DELY*DP*MSUBN*GP(1))
     +   /(DA*((DELY*KN1*MSUBN)+DP)))

      AVEH = AVEH + SURCONCH
      AVEP = AVEP + SURCONCP
      AVEB = AVEB + SURCONCB
      AVEA = AVEA + SURCONCA
*******K LOOP CONTINUE

30  CONTINUE

**********************************
***** DOWNSTREAM *****
**********************************

      DO 90 K = NX+1,NXT

*******CALCULATE HOMOGENEOUS RATES

      DO 132 J =1,NY-1
       CONSTH(J) = (((KHCO3*GH(J)*GB(J))/
     +   ((KEHCO3/BHA)+GB(J)+GH(J)))
     +   *((LH(J)*DELY*DELY)/DH))

       CONSTB(J) = (((KHCO3*GH(J)*GB(J))/
     +   ((KEHCO3/BHA)+GB(J)+GH(J)))
     +   *((LB(J)*DELY*DELY)/DB))

132   CONTINUE
```

```
******SPECIES H+

      BH(1) = 2.0D0*LH(1) + 1.0D0
      BH(NY-1) = LH(NY-1) + 1.0D0

      DO 321 J = 1,NY-1
        DOFH(J) = GH(J) - CONSTH(J)
321   CONTINUE

*******CALL BI ROUTINE

      CALL BI(GH,LH,DOFH,BH)

******SPECIES HCO3-

      BB(1) = LB(1) + 1.0D0
      BB(NY-1) = LB(NY-1) + 1.0D0

      DO 322 J = 1,NY-1
       DOFB(J) = GB(J) - CONSTB(J)
322   CONTINUE

*******CALL BI ROUTINE

      CALL BI(GB,LB,DOFB,BB)

*******SPECIES PAA

      BP(1) = 2.0D0*LP(1) + 1.0D0
      BP(NY-1) = LP(NY-1) + 1.0D0

      DO 323 J = 1,NY-1
        DOFP(J) = GP(J)
323   CONTINUE

*******CALL BI ROUTINE

      CALL BI(GP,LP,DOFP,BP)

*******CALCULATE FLUXES AT ELECTRODE FOR
*******H+ AND PAA

      SUMH = SUMH + GH(1)
      SUMP = SUMP + GP(1)

******K LOOP CONTINUE

90    CONTINUE

******OUTPUT DATA

      PRINT*,S
      AVEH = (AVEH*BHA*1.00E3)/DBLE(NX)
      PRINT*,'AVE H+=',AVEH
      AVEB = (AVEB*BHA*1.00E3)/DBLE(NX)
      PRINT*,'AVE HCO3-=',AVEB
      AVEP =(AVEP*BHA*1.00E3)/DBLE(NX)
      PRINT*,'AVE PAA=',AVEP
      AVEA =(AVEA*BHA*1.00E3)/DBLE(NX)
      PRINT*,'AVE Ca2+=',AVEA
      AVEH =0.0D0
      AVEP =0.0D0
      AVEB =0.0D0
      AVEA =0.0D0
      TOTL = XELM+XE
      NXT = NINT(TOTL/DELX)
```

```
      IF (S.EQ.1) THEN


        PRINT 940,KN
        ILIMH1 = (F*SUMH*W*DH*BHA*DELX)/DELY
        ILIMP1 = (MSUBN*F*SUMP*W*DP*BHA*DELX)
     +      /DELY


      ELSE


        ILIMH2 =(F*SUMH*W*DH*BHA*DELX)/DELY
        ILIMP2 =(MSUBN*F*SUMP*W*DP*BHA*DELX)
     +    /DELY


      ENDIF


****** SHIELDING FACTOR LOOP CONTINUE

      TOTL=XE+XEM
      NXT  = NINT(TOTL/DELX)


333   CONTINUE


****** CALCULATE SHIELDING FACTOR


      IF (ANS.EQ.'Y') THEN
        SF = (ILIMH1+ILIMP1)/(ILIMH2+ILIMP2)
      ENDIF


      PRINT 900,SF,ILIMH1,ILIMH2
      PRINT 910,ILIMP1,ILIMP2
      PRINT 920,V,TWOH,THETA
      PRINT 930,BHA,BPAA
      PRINT*,'****************************************'
      PRINT 950,ILIMP1+ILIMH1,ILIMP2+ILIMH2
      PRINT*,'****************************************'


900   FORMAT (X,'SF=',F10.6,/,X,'ILIMH1=',E11.4,X,
     +     'ILIMH2=',E11.4)
910   FORMAT (X,'ILIMP1='E11.4,X,'ILIMP2='E11.4)
920   FORMAT (X,'VF =',F6.3,X,2xH =',E11.4,X,
     +  'Theta =',F6.3)
930   FORMAT (X,'Bulk H+ =',E11.4,X,'BulkPAA
     +   =',E11.4)
940   FORMAT(X,F7.4)
950   FORMAT(X,'ILIM KNnot =0',E11.4,3X,
     +  'ILIM KN=0',E11.4)
      STOP
      END


************************************

****** BI SUBROUTINE *****

************************************


      SUBROUTINE BI(G,L,DOF,B)


      COMMON NY
      REAL*8 L(3000),G(3000),DOF(3000),A(3000)
      REAL*8 B(3000),C(3000),AL(3000),BE(3000),F(3000)
******* CALCULATE A, B AND C
        DO 200 J=1,NY-1
        A(J)=-L(J)
        C(J)=-L(J)
200   CONTINUE
      DO 240 J=2,NY-2
        B(J)=2.0d0*L(J)+1.0d0
240   CONTINUE
```

```
******CALCULATE ALPHA AND BETA
      AL(1)=B(1)
      BE(1)=C(1)/AL(1)
      DO 400 J=2,NY-1
         AL(J)=B(J)-A(J)*BE(J-1)
         BE(J)=C(J)/AL(J)
400   CONTINUE

******CALCULATE f(j) VALUE
     F(1)=DOF(1)/AL(1)

     DO 500 J=2,NY-1
       F(J)=(DOF(J)-A(J)*F(J-1))/AL(J)
500  CONTINUE

******CALCULATE u(j) VALUES
     G(NY-1) = F(NY-1)

     DO 600 J = NY-2,1,-1
       G(J) = F(J)-BE(J)*G(J+1)
600  CONTINUE
           RETURN
         END
```

4.2 BIBCN - high pH dissolution

This section lists the computer program which uses the Backwards Implicit Finite Difference method to model the dissolution of $CaCO_3$ in the channel cell, at high pH in the absence of inhibitors. This program uses the surface kinetics described in Chapter 5, as defined by the rate equation (5.79) and the surface boundary matrix elements as given in Table 5.5 (Approach 1).

```
C   DISSOLUTION OF CaCO3 -
C   BCN EQUATION
C
*****************************************
C   EQUILIBRIUM ASSUMED AT
C   EACH POINT
C   FOR HIGH pH (pH>8) ONLY


C   IMPLICIT DOUBLE PRECISION
C   (A-H,O-Z)

 REAL *8 LA(0:3000),LB(0:3000),
+ GA(0:3000,2),GB(0:3000,2),GC(0:3000,2),
+ H(0:3000,2),D(0:3000),B(0:3000),
+ GAOLD,GHOLD,GCOLD,SUM,SENH,AVG,
+ BCA,SUMCA
 REAL *8    KG,K1,KA1,KA2,KW,KSP,KCA,
+ KCO3
 LOGICAL CONV(4)
 CHARACTER DATFILE*28,HDAT*10,DF*1


 COMMON /BLOCKA/B,D,NX,NY/
+ BLOCKB/KG,K1,DELY
+ /BLOCKC/GA,H,KA1,KA2,KW,BOH,BCA,
+ KSP/BLOCKD/K,IT,NIT,CONV,PPM

C   FIXED VALUES
C   TWOH = 2h   DD = d   DA = DCa
C   XE = length of xtal
C   KA2 - 2nd H2CO3 dissociation consts.
C   GA=[Ca2+], GB=[HCO3-], GC=[CO32-]


 DA=7.93E-6
 KA2=1.409E-13
 KW=1.45E-20
 KSP=6.26E-14

 PRINT*,'All dimensions of length in cm'

 PRINT*,'Value of kKK?'
 READ*,KG
```

```
      PRINT*,'Value of KCa?'
      READ*,KCA
      PRINT*,'Value of KCO3?'
      READ*,KCO3
      PRINT*,'Size of Grid X'
      READ*,NX
      PRINT*,'Size of Grid Y'
      READ*,NY
      PRINT*,'Volume flow rate'
      READ*,V
      PRINT*,'Bulk pH'
      READ*,BPH
      PRINT*,'Bulk [Ca2+] /mM'
      READ*,BCA
      BCA=BCA*1.0E-6
      PRINT*,'Number of iterations'
      READ*,NIT
      PRINT*,'Convergence of surface [Ca2+] /ppm'
      READ*,PPM
      PRINT*,'Height of channel (2h)'
      READ*,TWOH
      PRINT*,'Width of channel (d)'
      READ*,DD
      PRINT*,'Length of crystal'
      READ*,XE
      PRINT*,'Distance from xtal to edge of sensor'
      READ*,GAP
      PRINT*,'Diameter of sensor'
      READ*,DIA
      PRINT*,'Datafile output of [H+]sensor? Y/N'
      READ'(A1)',DF

C     BULK [OH-]
      BOH=KW*(10**(BPH))*1.E3

C     DELTA X, DELTA Y
      DELX=XE/DBLE(NX)
      DELY=TWOH/DBLE(NY)

C     NDSTR is value of k at downstream limit
      NDSTR=INT((GAP+DIA)/DELX)+NX
      IGAP=INT(GAP/DELX)
C     CALCULATION OF LAMBDA(j) for Ca
      DO 10 J=1,NY-1
        LA(J)=DA*DELX*(TWOH**3)*DD/
     +    (6.0*V*(DELY**3)*DBLE(J)*
     +    (TWOH-DBLE(J)*DELY))
10    CONTINUE
      C SET GA(j,k&k+1)=bulk [Ca2+],
C     GB(j,k&k+1)=0, GC(j,k&k+1)=0
        DO 17 K=1,2
          DO 15 J=0,NY-1
            GA(J,K)=BCA
            GB(J,K)=0.0
            GC(J,K)=0.0
15        CONTINUE
17      CONTINUE
        SUMCA=BCA
        GAOLD=1.
        GHOLD=1.
        GCOLD=1.

C       Loop to increment to successive vectors over
C       crystal
```

```
      DO 30 K=0,NX-1

C     reset convergence flags

      CONV(1)=.FALSE.
      CONV(2)=.FALSE.
      CONV(3)=.FALSE.
C     Iterative loop until convergence is reached

      DO 20 IT=1,NIT

C **Set initial/final parameters for Ca & Calc
C  ** GA(j,k+1)
C  followed by BI calc & surface [Ca2+] calc

        D(1)=GA(1,1)+(LA(1)*DELY*KG/DA)
     +        *(KSP-GA(0,2)*GC(0,2))
     +        /((1+KCA*GA(0,2))
     +        *(1+KCO3*GC(0,2)))
        B(1)=LA(1)+1.
        B(NY-1)=LA(NY-1)+1.

        CALL BI(GA,LA)
        GA(0,2)=GA(1,2)+(DELY*KG/DA)
     +      *(KSP-GA(0,2)*GC(0,2))
     +     /((1+KCA*GA(0,2))*(1+KCO3*GC(0,2)))

C     Calc Surface [H+]
      CALL QUAD(0)

C           Calc Surface [CO32-]
      GC(0,2)=(GA(0,2)-BCA)/(1.0+H(0,2)/KA2)

C  Check convergence on surface data for Ca,H
C    & CO3

      CALL CONVCHK(1,GA,GAOLD)
      CALL CONVCHK(2,H,GHOLD)
      CALL CONVCHK(3,GC,GCOLD)
      IF(CONV(1).AND.CONV(2)
     +    .AND.CONV(3)) THEN
        IF(MOD(K,200).EQ.0.0)THEN
            PRINT*,'K=',K,' IT=',IT
        ENDIF
        GOTO21
      ENDIF

C     Put surface conc equal to old values
C          for convergence check
        GAOLD=GA(0,2)
        GHOLD=H(0,2)
        GCOLD=GC(0,2)
C     End of iterative loop
20    CONTINUE

C   Pick out mid-xtal [Ca2+] & [CO32-] values

21    IF(K.EQ.INT(NX/2)-1)THEN
        CAHALF=GA(0,2)
        CO3HALF=GC(0,2)
      ENDIF

C ** Put G(k+1) values as new G(k) values
```

```
      DO 27 J=0,NY-1
        GA(J,1)=GA(J,2)
        GC(J,1)=GC(J,2)
        H(J,1)= H(J,2)
27    CONTINUE

C  Running total of surface [Ca] over xtal
C    (K=0-NX)
      SUMCA=SUMCA+GA(0,2)

C  End of main K loop
30    CONTINUE

C  Get values at end of xtal

     CAEND=GA(0,2)
     CO3END=GC(0,2)

C **********************
C *** DOWNSTREAM  ***
C **********************

C    Sensor calcs in integer units of delx
C    IGAP calculated earlier

     IDIA=INT(DIA/DELX)
     IRAD=IDIA/2
     SUM=0.0
     AREA=0.0

     DO  100 K=NX,NX+IGAP+IDIA

C    CALC [Ca] downstream

     D(1)=GA(1,1)
     B(1)=LA(1)+1.0
     B(NY-1)=LA(NY-1)+1.0

     CALL BI(GA,LA)
     GA(0,2)=GA(1,2)
C      Downstream sensor ave  [H+] calc
C    Calc [H+] at upstream edge of sensor for
C    next loop
     IF (K.EQ.NX+IGAP-1) THEN
       CALL QUAD(0)
       H(0,1)=H(0,2)
     ENDIF
C  FOR K OVER SENSOR
     IF (K.GE.NX+IGAP
    +     .AND.K.LE.NX+IGAP+IDIA)
     THEN
       W=DBLE(IRAD**2-
    +    (NX+IGAP+IRAD-K)**2)
       IF (W.LT.0.0) THEN
         W=0.0
       ENDIF
       W=2.0*SQRT(W)
       AREA=AREA+W
C      Calc [H+] for next (ie k+1) value of K
       CALL QUAD(0)
       SUM=SUM+W*LOG10(H(0,1))
       H(0,1)=H(0,2)
     ENDIF
```

```
C  PUT [Ca](k+1) VALUES AS NEW [Ca](k)
   C    VALUES

        DO 50 J=0,NY-1
         GA(J,1)=GA(J,2)
50      CONTINUE

100   CONTINUE

      PRINT103,NX,NY,NIT
      PRINT104,PPM
      PRINT*,'Using Brown-Compton-Narramore
     +   equation'
      PRINT105,V,BPH
      PRINT106,KG,KCA,KCO3,KSP,
     +  BCA*1.0E6
      PRINT107,K1,KA1,KA2
      PRINT108,CAHALF,CO3HALF,
     +  CAEND,CO3END
      PRINT109,SUMCA/(DBLE(NX)+1)
103   FORMAT(1X,'Grid  Size: x ',I7,', y ',I7,
     +   'Max no itern',I3)
104   FORMAT  (1X,'Convergence of surface
     +    [Ca2+],[H+] & [CO3)2-]to ',F5.2,'ppm')
105   FORMAT  (1X,'Vf=',F5.3,'Bulk pH=',F5.2)
106   FORMAT  (1X,'kKK=',1PE9.3,'
     +    K(Ca,L)=',E9.3,'K(CO3,L)=',E9.3/1X,
     +    'Ksp=',E9.3,'[Ca2+]b=',0PF6.3,'mM')
107   FORMAT  (1X,'K1=',1PE9.3,'KA1=',E9.3,'
     +    KA2=',E9.3)
108   FORMAT  (1X,'Mid Crystal
     +    [Ca]o=',1PE9.3,' [CO3]o=',E9.3/1X,
     +    'End of Crystal [Ca]o=',E9.3,'
     +    [CO3]o=',E9.3)
109   FORMAT  (1X,'Average surface [Ca2+] over
     +     xtal =',1PE9.3)

 C AVERAGE  [H+] OVER SENSOR
  AVG=SUM/AREA
  SENH=10**AVG
  PRINT120,NX+IGAP,NX+IGAP+IDIA
  PRINT*,'Average sensor [H+]=',SENH
 C  write SENH to datafile
  IF(ICHAR(DF).EQ.89)THEN
     CALL NAME(HDAT,V)
     OPEN(3,FILE=HDAT,STATUS='NEW')
     WRITE(3,130)V,SENH
     CLOSE(3)
  ENDIF
  CLOSE(2)
     STOP

110   FORMAT(30(1X),E23.16)
120   FORMAT(1X,'Sensor between K=',I4,'and
     +   K=',I4)
130   FORMAT(F5.3,2X,1PE9.3)

     END

     SUBROUTINE  BI(G,L)
   C To calculate concentrations  of one vector
   C using the Backward Implicit Finite Difference
   C Method
     REAL  *8 L(0:3000),G(0:3000,2),U(0:3000),
    +   D(0:3000),A(0:3000),B(0:3000),C(0:3000),
    +   AL(0:3000),BE(0:3000)F(0:3000)
     COMMON  /BLOCKA/B,D,NX,NY
```

```
C  SET VALUES OF D (ie d(j)), A, B, C

      DO 200 J=1,NY-1
        A(J)=-L(J)
        C(J)=-L(J)
200   CONTINUE
      DO 220 J=2,NY-1
        D(J)=G(J,1)
220   CONTINUE
      DO 240 J=2,NY-2
        B(J)=2*L(J)+1.
240   CONTINUE

C     CALCULATE ALPHA AND BETA

      AL(1)=B(1)
      BE(1)=C(1)/AL(1)
      DO 400 J=2,NY-1
        AL(J)=B(J)-A(J)*BE(J-1)
        BE(J)=C(J)/AL(J)
400   CONTINUE

C     CALCULATE f(j) VALUES

      F(1)=D(1)/AL(1)
      DO 500 J=2,NY-1
        F(J)=(D(J)-A(J)*F(J-1))/AL(J)
500   CONTINUE

C     CALCULATE u(j) VALUES

      U(NY-1)=F(NY-1)
      DO 600 J=NY-2,1,-1
        U(J)=F(J)-BE(J)*U(J+1)
600   CONTINUE

C     u(j) values are new G(j,k+1) values

      DO 650 J=1,NY-1
        G(J,2)=U(J)
650   CONTINUE

700   RETURN
      END


      SUBROUTINE QUAD(J)
C     To solve quadratic equation for [H+]
      IMPLICIT REAL *8 (A-H,O-Z)
      REAL *8 GA(0:3000,2),H(0:3000,2),
     +   A,B,C,ROOT(2),BCA
      REAL *8 KA1,KA2,KW,KSP
      COMMON /BLOCKC/GA,H,KA1,KA2,KW,
     +   BOH,BCA,KSP

C     SOLVE QUADRATIC FOR [H+]

      A=(GA(J,2)-BCA+BOH)/KA2
      B=BOH-KW/KA2
      C=-KW
      ROOT(1)=SQRT(B*B-4.0*A*C)
      ROOT(2)=(-B-ROOT(1))/(2.0*A)
      ROOT(1)=(-B+ROOT(1))/(2.0*A)

C FIND POSITIVE ROOT

      IF (ROOT(1).GE.0.0.
     +   AND.ROOT(2).GE.0.0)
     +   PRINT*,'2 +veROOTS',ROOT
```

```
      IF (ROOT(1).LT.0.0.
     +    AND.ROOT(2).LT.0.0)
     +    PRINT*,'2 -ve +ROOTS',ROOT


       H(J,2)=MAX(ROOT(1),ROOT(2))
         RETURN
         END



      SUBROUTINE  CONVCHK(I,G,GOLD)
     C  To check for convergence in iterative loop
      REAL *8 G(0:3000,2),GOLD
      LOGICAL  CONV(4)
      COMMON  /BLOCKD/K,IT,NIT,CONV,PPM
      CHARACTER*5  ION(4)
      DATA  ION/'Ca2+','H+','CO3--','HCO3-'/
      IF (GOLD.EQ.0.0.
     +       AND.G(0,2).EQ.0.0)THEN
           PRINT*,'ZERO  CHECK CONV
     +          K=',K,ION(I)
       ELSE


       P=1000000.0*(MAX(GOLD,G(0,2))
     +     -MIN(GOLD,G(0,2)))/
     +     MAX(GOLD,G(0,2))
```

```
       IF (P.LT.PPM) CONV(I)=.TRUE.
        IF (P.GE.PPM.AND.IT.EQ.NIT) THEN
        PRINT100,ION(I),P,K
        ENDIF
       ENDIF
       RETURN
  100  FORMAT(1X,'SURFACE  [',A5,']
     +   converged to ',F12.3,'ppm'+,3(1X),'K=',I4)
        END



        SUBROUTINE  NAME(HDAT,V)
      C To provide name for output  file relating to
      C   flow rate
      IMPLICIT REAL *8(A-H,O-Z)
      CHARACTER*1  DGT1,DGT2,HDAT*10


      IV=INT(V*100.)
      ITENS=INT(V*10)
      DGT1=CHAR(ITENS+48)
      IUNITS=MOD(IV,10)
      DGT2=CHAR(IUNITS+48)
      HDAT='TEMP'//DGT1//DGT2//'.DAT'


      RETURN
      END
```

APPENDIX 5

ERRORS

Every physical measurement is subject to a degree of uncertainty. This uncertainty can only be decreased so far, there is always an *error* associated with any measurement. Or as stated by T.J.Hannagan [245]; 'All scientific measurements are to some degree inaccurate, either because no measuring device can record an exact reading or because of the experimenters inability to read the index accurately'. It is crucial to determine the size of this error, otherwise the result is of unknown reliability and hence totally worthless.

Various types of errors can occur, errors due to the scientist, due to the instrumentation and random errors. One can attempt to eliminate the first. By the choice of appropriate methods and equipment, the second can be *minimized*. The third of these categories of errors, cannot be eliminated or possibly even reduced. Random errors can however be estimated from the *variation* in experimental results, when all necessary precautions are taken. This is why it is necessary to perform multiple experiments, and why the results are more statistically accurate when there are more experiments involved in the determination.

A5.1 Sources of Instrumental Errors

There are a variety of sources of instrumental error in the experiments in this work. The errors associated with the making of solutions are probably the main sources of error. These derive from the error in the weighing of samples. There is also an error associated with the making of solutions in volumetric flasks. Further dilution increases the errors with an additional error deriving from the use of a pipette. Whilst these errors are quite small they are significant, and in combination they do propagate to produce a much larger error overall. Therefore the lower the concentration of the species the greater the error associated with its calculated concentration in solution.

Other errors are associated with the calibration of equipment. A major possible calibration error comes with the calibration of pH electrodes. First it is necessary to ensure the buffers used are accurate. This was done by always using fresh solution and ensuring it had not been standing in the laboratory for too long. Second it is important to calibrate the pH electrodes with the correct choice of buffers, i.e. choosing buffers so that their pH's *surround* the pH region of interest in the experiments. Then it is also essential that the calibration is performed at a time close to the experiments and under similar environmental conditions (i.e. temperature). Similar precautions were taken with all other calibrations performed. Additionally at low pH, where detection occurs by amperometric detection of H^+ reduction, there are errors associated with the potentiostat, and the chart recorder on which the reduction wave was recorded.

Other measurement errors concern the determination of the dimensions of the flow cell itself.

A5.2 Errors of Method

The errors of method considered here are those associated with the 'fitting' of experimental data with theoretical predictions by the Backwards Implicit finite difference method. As can be seen from any of the fitted experimental data in this work there are random errors in the experimental data. This random variation means that there is a limit to how precisely it is possible to differentiate between different candidate fits. This is particularly important for the low pH determinations, as can be seen from figure 1.

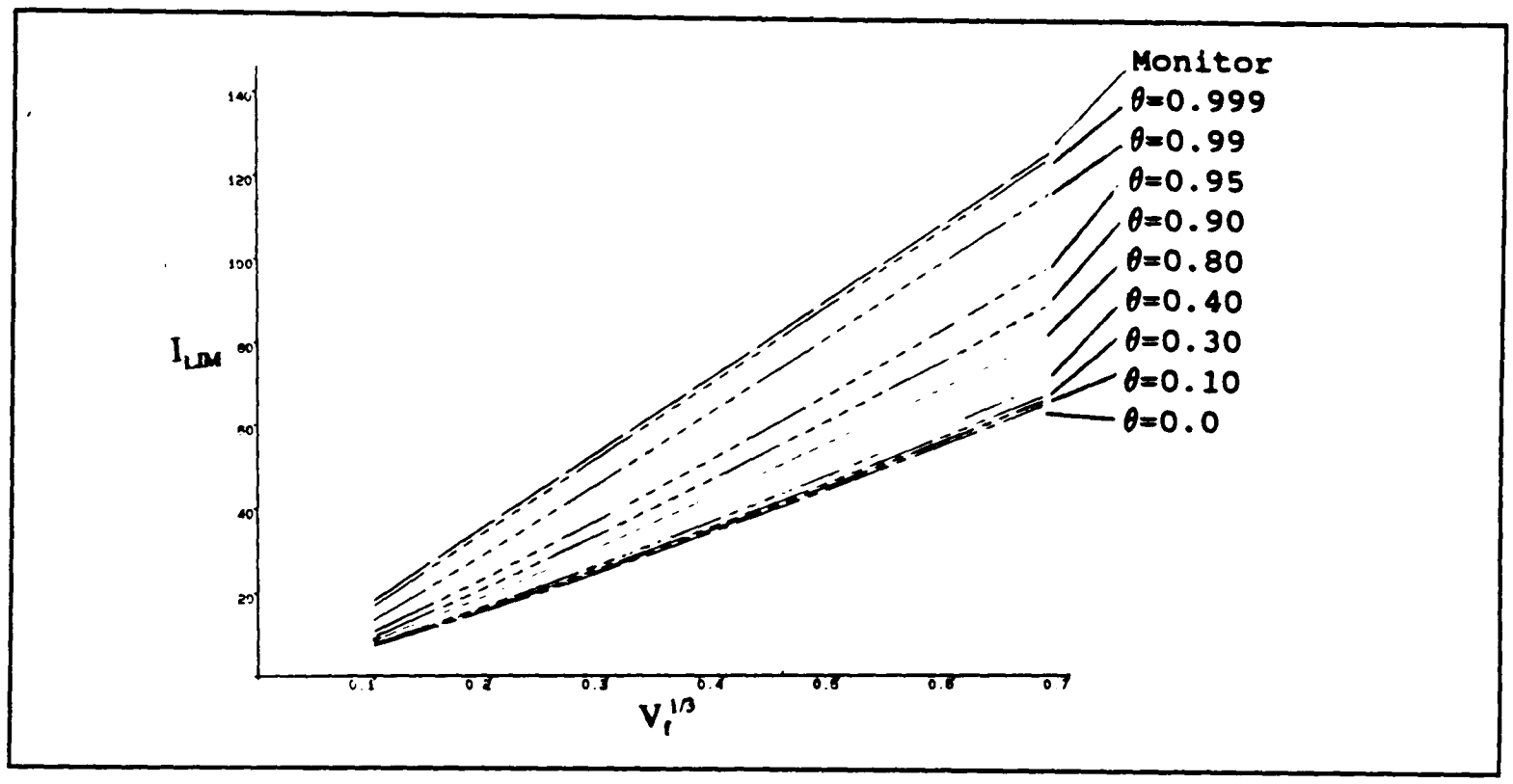

Figure 1: The BI predictions of I_{LIM} against $V_f^{1/3}$ for the same experimental conditions with different values of θ.

For low values of θ, the surface coverage, the BI method predicts that the curves fall very close to each other. However at high values of θ the curves fall much further apart. Thus it may seem that it would be possible for instance to differentiate between $\theta=0.99$ and $\theta=0.999$. However at these high degrees of inhibition a wide range of values of θ fall into the area within experimental variation of results, and it is best to consider the inhibition to be approximately total.

It is for this reason that the experiments analyzed in Chapter 4 were limited to those where the data was fitted with a value of θ less than 0.95 in order to avoid a spurious claim of accuracy.

A5.3 The Combination of Errors.

All sources of error need to be considered in determing the size of the error for a particular determination. These errors combine or 'propagate' to give the overall error as quoted in this work. The propagation of errors has to be considered thoroughly when considering parameters which are derived from other experimentally determined parameters. In particular in Chapter 4 section 4.5.5.4 and the values of $K_{eq}K_L$, are obtained from a plot of log [Ca^{2+}] against a derived parameter. This latter parameter itself contains a variable which is calculated from analysis of the experimental results.

APPENDIX 6

DERIVING K_a'S FROM POTENTIOMETRIC TITRATIONS

In Chapter 4 it was necessary to derive the K_a's for homo-phthalic acid from measured potentiometric titration curves. The method employed was the method of Skoog and West [148]. In which the expected potentiometric titration curves for different concentrations of a polyfunctional acid with an alkali of known strength are predicted given candidate values for K_1 and K_2, where K_1 and K_2 are defined as the equilibrium constants for the dissociation reactions:

$$H_2A + H_2O \overset{K_1}{\rightleftharpoons} H_3O^+ + HA^- \tag{A6.1}$$

$$HA^- + H_2O \overset{K_2}{\rightleftharpoons} H_3O^+ + A^{2-} \tag{A6.2}$$

The predicted curves are then compared with the experimental curves.

In deriving the titration curve two further expressions are needed. First the total concentration, C_T equals the sum of the three species:

$$C_T = [H_2A] + [HA^-] + [A^{2-}] \tag{A6.3}$$

Also a charge balance requires that:

$$[H^+] = [HA^-] + 2[A^-] + [OH^-] \approx [HA^-] + 2[A^-] \tag{A6.4}$$

The latter simplification assumes that in acidic solutions the concentration of hydroxide ions is negligible.

From these expressions the concentrations of all of the species in solution can be calculated to be:

$$[H_2A] = \frac{C_T}{1 + \frac{K_1}{[H^+]} + \frac{K_1K_2}{[H^+]^2}} \quad \text{(A6.5)}$$

$$[HA^-] = \frac{C_T}{\frac{[H^+]}{K_1} + 1 + \frac{K_2}{[H^+]}} \quad \text{(A6.6)}$$

$$[A^{2-}] = \frac{C_T}{\frac{[H^+]^2}{K_1K_2} + \frac{[H^+]}{K_2} + 1} \quad \text{(A6.7)}$$

From this speciation the initial pH of a solution of an acid can be calculated.

To calculate the first equivalent point on a potentiometric titration curve, first the concentration of HA^- at this point has to be calculated. At this point [148] the species HA^- acts as though amphiprotic, hence the H^+ concentration can be found by:

$$[H^+] = \sqrt{\frac{K_1K_2[HA^-] + K_1K_W}{[HA^-] + K_1}} \quad \text{(A6.8)}$$

where K_W the solubility product for water.

The second equivalent point occurs when twice as many moles of base have been added as there were moles of acid at the start of the titration. At this point A^{2-} is the dominant species in solution. Assuming that the concentration of hydroxide is approximately equal to the concentration of HA^- then from the following relationship:

(A6.9)

$$\frac{K_W}{K_2} = \frac{[OH^-][HA^-]}{[A^{2-}]}$$

the OH^- concentration at the second equivalent point can be calculated. Hence the pH.

These three points can be used initially to narrow down the possible dissociation constants for the acid in question. Then the pH values between these points can be calculated.

There are five equations ((A6.3), (A6.4), (A6.5), (A6.6) and (A6.7)) which describe the speciation of the acid at all times. Examining the parameters in these equations it can be deduced that there are only four unknowns as: the value of C_T is known, as is the concentration of OH^- at any given point, and the values of the K_a's are set to those being investigated. Hence with five equations and four unknowns, the simultaneous equations can be solved to give the values of the unknowns which are $[H_2A]$, $[HA^-]$, $[A^{2-}]$, and pH.

Then by comparing the predicted potentiometric titration curves for the candidate dissociation constants, the values of the K_a's are determined to be those which give the closest agreement with experiment.

REFERENCES

1. D.M.Dawson and A.M.Pritchard *Inst. Chem. Eng. Symp. Ser.*, 86 435 (1984).
2. P.R.Unwin and R.G.Compton *J. Chem. Soc. Faraday Trans.*, 86 1572 (1990).
3. J.C.Jamieson *J. Phys. Chem.*, 21 1385 (1953).
4. A.Boguski *Chem. Ber.*, 9 1442 (1876).
5. A.Boguski and T.Kajander *Chem. Ber.*, 10 34 (1877).
6. W.Spring *Z. Phys. Chem.*, 1 209 (1887).
7. W.Spring *Z. Phys. Chem.*, 2 13 (1888).
8. E.Brunner *Z. Phys. Chem.*, 47 79 (1904).
9. P. Van Cappelen, J.F. Gaillard, and C.Rabouille in 'Interactions of C, N, P and S Biogeochemical Cycles and Global Change', Ed. R.Wollest, F.T.Macenise, and L.Chou. Springer-Verlag Berlin, Heidelberg, 1993. pp.401.
10. T.F.Kazmierczak, M.B.Tomson, and G.H.Nancollas *J. Phys. Chem.*, 86 103 (1982).
11. W.Stumm and J.J.Morgan 'Aquatic Chemistry', 2nd Edition, Wiley, New York, 1981.
12. P.E.Cloud in 'Chemical Oceanography' Vol 2. Ed. J.P.Diley and G.Skirrow. Academic Press, New York, 1965. pp.127.
13. R.A.Berner 'Principles of Chemical Sedimentology', M^{c}Graw-Hill, New York, 1971.
14. E.L.Sjöberg and D.T.Rickard *Chem. Geol.*, 49 405 (1985).
15. J.E.Myroic and J.L.Carer *Earth Processes and Landforms.*, 15 413 (1990).
16. D.Buhmann and W.Dreybrodt *Chem. Geol.*, 48 189 (1985).
17. D.Buhmann and W.Dreybrodt *Chem. Geol.*, 53 109 (1985).

18. J.Baumann, D.Buhmann, W.Dreybrodt, and H.D.Shultz *Chem. Geol.*, 53 219 (1985).

19. G.Howells 'Acid Rain and Acid Waters', Ellis Horwood, London, 1990.

20. M.Cresser and A.Edwards 'Freshwater Acidification', Cambridge University Press, 1987.

21. M.M.Reddy, L.N.Plummer, and E.Busserbey *Geochim. Cosmochim. Acta*, 45 1281 (1981).

22. D.Arder, S.Emerson and C.Reiner *Geochim. Cosmochim. Acta*, 53 2831 (1989).

23. J.W.Morse *Am. J. Sci.*, 274 97 (1974).

24. G.H.Nancollas and M.M.Reddy *J.Colloid Interface Sci.*, 37 824 (1971).

25. S.Zhong and A.Mucci *Chem. Geol.*, 78 283 (1989).

26. J.W.Morse and R.C.Berner 'Chemical modelling in Aqueous systems', Ed E.A. Jenne, *Am. Chem. Soc. Symp. Ser.*, 93 499 (1979).

27. R.C.Berner and J.W.Morse *Am. J. Sci.*, 274 108 (1974).

28. P.F.Chester 'Acid Lakes in Scandanavia: The evolution of Understanding' CEGB report (1986).

29. H.Svendrup and I.Bjerle *Valter*, 38 59 (1982).

30. K.B. Krauskorf 'Introduction to Geochemistry', McGraw-Hill, New York 1979.

31. S.Woodin and U.Skita *New Scientist* 125 50(1990).

32. M.M. Reddy, *Verh. Internat. Verein. Limnol.*, 19 429 (1975).

33. R.G.Compton, K.L.Pritchard, and P.R.Unwin *Frshwater Biol.*, 22 285 (1989).

34. M.Wallin and I.Berle *Geochi. Cosmochim. Acta*, 53 1171 (1989).

35. J.Gribbin *New Scientist*, 188 32 (1988).

36. R.P.Wayne 'Chemistry of Atmospheres' Oxford Scince publications, Oxford 1985.

37. K.Lund, H.S.Fogler, C.C.M^{c}Cure, and J.W.Ault *Chem. Eng. Soc.* 30 825 (1975).

38. H.S.Weichers, P.Sturrock and G.V.R.Marais *Water Res.*, 9 835 (1975).

39. D.H.Caldwell, W.B.Lawrence *Ind. Eng.Chem.*, 45 535 (1953).

40. G.M.Fair, J.C.Geyer, and D.A.Okun 'Elements of Water Supply and Wastewater Disposal' Wiley, New York. (1971) pp 474-483.

41. M.N.Elliot *Desalinination*, 8 221 (1970).

42. J.P.Rank *Desalination*, 6 75 (1969).

43. J.Christoffersen and M.R.Christoffersen *J.CrystalGrowth*, 100 203 (1990).

44. D.Husson and S.Steinberg *Desalination*, 147 128 (1983).

45. Z.Amjad and J.Hooley *Desalination*, 111 496 (1986).

46. M.M. Reddy *J. Crystal Growth*, 41 287 (1977).

47. Z.V.Morgan *Oil Gas J.*,49 102 (1959).

48. W.K.Burton, N.Cabrera, and F.C.Frank *Phil. Trans. Roy. Soc. London*, A243 295 (1951).

49. P.Bennema *J.CrystalGrowth*, 69 182 (1984).

50. J.M.Thomas and G.D.Renshaw *Trans. Faraday Soc.*, 61 791 (1965).

51. D.Rickard and E.L.Sjöberg *Am. J. Sci.*, 283 815 (1983).

52. J.W.Morse in Reviews in Mineralogy II "Carbonates: Mineralogy and Chemistry" Ed. R.J.Reeder, Minearalogy Soc. America., 1985,

53. R.G.Compton and P.R.Unwin *Phil. Trans. Roy. Soc. London*, A330 1 (1990).

54. E.L.Sjöberg and D.T.Rickard *Chem. Geol.*, 42 119 (1984).

55. L.N.Plummer, D.L.Parkhurst, and T.M.L.Wigley *Am. Chem. Soc. Symp. Ser.*, 93, 537 (1979).

56. E.L.Sjöberg *Stockholm Cont. Geol.*, 32 1 (1978).

57. L.N.Plummer, T.M.L.Wigley,and D.L.Parkhurst *Am. J. Sci.* 278 179 (1978).

58. M.M.Reddy and G.H.Nancollas *J. Colloid Interface Sci.*, 36 166 (1971).

59. G.Dorang and A.Gurtchidjan *C. R. Acad. Sci. Paris*, 286c 159 (1978).

60. W.A.House *J. Chem. Soc. Faraday Trans.1*, 77 341 (1981).

61. D.W.Thompson and P.G.Pownall *J. Colloid Interface Sci.*, 131 74 (1985).

62. G.E.Cassford, W.A.House, and A.D.Pethybridge *J. Chem. Soc. Faraday Trans. 1*, 79 1617 (1983).

63. M.M.Reddy and G.H.Nancollas *J. Crystal Growth*, 35 33 (1976).

64. E.L.Sjöberg and D.T.Richard *Geochim. Cosmochim. Acta*, 48 485 (1984).

65. R.G.Compton and P.J.Daly *J. Colloid Interface Sci.*, 1 159 (1984).

66. L.Chou, R.M.Garrels, and R.Wollast *Chem. Geol.* 78 269 (1989).

67. H.N.S. Wiechers, P. Sturrock and G.V.R. Marais *Water Res.*, 9 835 (1975).

68. L.N.Plummer and T.M.L.Wigley *Geochim. Cosmochim. Acta*, 40 191 (1976).

69. C.V.King and C.L.Liu *J. Am. Chem. Soc.*, 55 1928 (1933).

70. C.A.Kaye *J. Geol.*, 65 35 (1957).

71. R.G.Compton, P.J.Daly and W.A.House *J. Colloid Interface Sci.*, 113 12 (1986).

72. R.G.Compton and P.J.Daly *J. Colloid Interface Sci.*, 115 493 (1987).

73. E.L.Sjöberg *Geochim. Cosmochim. Acta*, 40 191 (1970).

74. W.Dreybrodt and D.Buhmann *Chem. Geol.*, 40 107 (1991).

75. W.P.Inskeep and P.R.Bloom *Geochim. Cosmochim Acta*, 49 2165 (1985).

76. A. Mucci and J.W. Morse *Geochim. Cosmochim. Acta*, 47 217 (1983).

77. A. Mucci *Geochim. Cosmochim. Acta*, 50 2255 (1986).

78. E.A. Burton and L.M. Walter *Geochim. Cosmochim. Acta*, 54 797 (1990).

79. E.L. Dromgoole and L.M. Walter *Geochim. Cosmochim. Acta*, 54 2991 (1990).

80. C.W. Davies and A.L. Jones *Discuss. Faraday Soc.*, 5 103 (1949).

81. C.W. Davies and A.L. Jones *Trans. Faraday Soc.*, 51 812 (1955).

82. T. Foxall, G.C. Peterson, H.M. Rendall and A.L. Smith *J. Chem. Soc., Faraday Trans. I*, 75 1034 (1979).

83. A.E. Nielsen 'Kinetics of Precipitation', Pergamon, Oxford, 1964.

84. A.E. Nielsen *J. Crystal Growth*, 67 289 (1984).

85. S.Stipp and M.F.Hochella *Geochim. Cosmochim. Acta*, 55 1723 (1991).

86. P.E. Hillner and A.J.Gratz *Geology*, 20 359 (1992).

87. P. Van Cappelen, L.Cahtel, W.stumm and P.Wersin *Geochim. Cosmochim. Acta*, 57 305 (1993).

88. P.R. Unwin D. Phil. Thesis, Oxford University, 1989.

89. P.Harriott *Am. Inst. Chem. Eng. J.*, 8 93 (1962).

90. T.K.Sherwood, R.L.Pigford and C.R.Wilke 'Mass Transfer' M°Graw-Hill, Tokyo, 1975.

91. R.G. Compton, K.L. Pritchard, P.R. Unwin, G. Grigg, P. Silvester, M. Lees and W.A. House *J. Chem. Soc. Faraday Trans. I*, 85 4335 (1989).

92. A.J. Barwise, R.G. Compton and P.R. Unwin *J. Chem. Soc. Faraday Trans.*, 86 137 (1990).

93. C.A. Brown, D.Phil. Thesis, Oxford University 1992.

94. R.G.Compton, C.T.Walker, P.R.Unwin and W.A.House *J. Chem. Soc. Faraday Trans.*, 86 849 (1990).

95. P.Chaing and M.D. Donohue *J. Colloid Interface Sci.*, 122 230 (1988).

96. K.B. Oldham and C.G. Zoski in 'Comprehensive Chemical Kinetics', Eds. C.H. Bamford and R.G. Compton, Vol. 26, p. 92.

97. A. Fick *Philosophical Magazine*, 10 30 (1855).

98. A. Fick *Poggendorf's Annalen der Physik und Chemie*, 94 59 (1855).

99. C.M.A.Brett and A.M.C.F.Oliveira Brett in 'Comprehensive Chemical Kinetics', Eds. C.H. Bamford and R.G. Compton, Vol. 26, p. 356.

100. K.B. Oldham and C.G. Zoski in 'Comprehensive Chemical Kinetics', Eds. C.H. Bamford and R.G. Compton, Vol. 26, p. 113.

101. Southampton Electrochemistry Group, 'Instrumental Methods in Electrochemistry', Ellis Horwood, Chichester, 1985, p. 26.

102. H.J.M. Hanley (ed.), 'Transport Phenomena in Fluids', Dekker, New York, 1969.

103. K.B. Oldham and C.G. Zoski, in 'Comprehensive Chemical Kinetics', Eds. C.H. Bamford and R.G. Compton, Vol. 26, p. 122.

104. R.B. Bird, W.E. Stewart and E.N. Lightfoot 'Transport Phenomena', Wiley, New York, 1960, p. 47.

105. V.G. Levich 'Physicochemical Hydrodynamics', Prentice-Hall, Englewood Cliffs, 1962, p. 32.

106. J.S. Newman, 'Electrochemical Systems', Prentice-Hall, Englewood Cliffs, 1962.

107. B.A. Coles and R.G. Compton *J. Electroanal. Chem.*, 144 87 (1983).

108. V.G. Levich 'Physiochemical Hydrodynamics', Prentice-Hall, Englewood Cliffs, 1962, pp. 60-78.

109. J.B. Flanagan and L. Marcoux *J. Phys. Chem.*, 78 718 (1974).

110. K.achi, K.Tahuda and H.Malusudu *J. Electoanal. Chem.*, 217 33 (1987).

111. V.G. Levich 'Physicochemical Hydrodynamics', Prentice-Hall, Englewood Cliffs, 1962, pp. 112-116.

112. M.A. Lévêque *Ann. Mines Mem. Ser. 12*, 13 201 (1928).

113. R.G. Compton and M.B.G. Pilkington *J. Chem. Soc. Faraday Trans. I*, 84 2155 (1988).

114. P.R. Unwin and R.G. Compton in 'Comprehensive Chemical Kinetics', Ed R.G. Compton, Vol. 29, p. 182.

115. P.R. Unwin and R.G. Compton *J. Electroanal. Chem.*, 245, 287 (1988).

116. J.L. Anderson and S. Moldoveanu *J. Electroanal. Chem.*, 179, 107 (1984).

117. K.B. Oldham *J. Electroanal. Chem.*, 122, 1 (1981).

118. P. Pastore, F. Magno, I. Lavagnini and C. Amatore *J. Electroanal. Chem.*, 301, 1 (1991).

119. M.R. Goldman and L.R. Barrett *Trans. Inst. Chem. Eng.*, 47, T29 (1969).

120. A.A. Wragg *Electrochim. Acta*, 16, 373 (1971).

121. R. Alkire and A.A. Mirarefi *J. Electrochem. Soc.*, 124, 1043 (1977).

122. D. Britz 'Digital Simulation in Electrochemistry', 2nd Edition, Springer-Verlag, Berlin Heidelburg, 1988.

123. J. Crank and P. Nicolson *Proc. Cambridge Phil. Soc.*, 43, 50 (1947).

124. S. Moldoveanu and J.L. Anderson *J. Electroanal. Chem.*, 175, 67 (1984).

125. S.G. Weber and W.C. Purdy *Anal. Chim. Acta*, 100, 531 (1978).

126. P. Laasonen *Acta Math.*, 81, 309 (1949).

127. R.G. Compton, A.C. Fisher, R.G. Wellington, D. Bethell and P. Lederer *J. Phys. Chem.*, 95, 4749 (1991).

128. R.G. Compton, R. Barghout, J.C. Eckland, A.C. Fisher, A.M. Bond and R. Colton *J. Phys. Chem.*, 97 1661 (1993).

129. R.G. Compton, A.C. Fisher and G.H.W. Sanders *Electroanal.*, 5 615 (1993).

130. R.G. Compton, A.C. Fisher and R.A. Spackman *Electroanal.*, 4 167 (1992)

131. L. Lapidus and G.F. Pinder 'Numerical Solution of Partial Differential Equations in Science and Engineering', Wiley, New York, 1982.

132. R.C. Weast 'Handbook of Chemistry and Physics',55th Edition, Chemical Rubber Company, Cleveland, 1975.

133. M. Stackelburg, M. Pilgram and V. Toome *Z. Elektrochem.*, 57, 342 (1953).

134. G.J. Janz in 'Reference Electrodes', Eds. D.J.G. Ives & G.J. Janz, Academic Press, 1961, p. 205.

135. J.M. Lamarche, J. Persello and Alain Foissy *Ing. Eng. Chem. Prod. Res. Dev.*, 22 123 (1983).

136. Yu.B. Vassiliev, V.S.Bagotzky, N.V.Osetrova and A.A.Mikhailova *J.Electroanal. Chem.*, 189 311 (1985).

137. Yu.B. Vassiliev, V.S. Bagotzky, N.V. Osetrova, O.A. Khazova and N.A. Mayora *J. Electroanal.Chem.*, 189 271 (1985).

138. Yu.B. Vassiliev, V.S. Bagotzky, O.A. Khazova and N.M. Mayorova *J.Electroanal.Chem.*, 189 295 (1985).

139. L.P. Hammett *J.Am.Chem.Soc.*, 46 7 (1924).

140. J. O'M. Bochris, I.A. Immor and A.K.M.s.Auz *J.Phys.Chem.*, 61 879 (1957).

141. S.B. Brummer, J.I.Ford and M.J.Turner *J.Phys.Chem.*, 61 3424 (1965).

142. K. Stulik and V. Hora *J.Electroanal. Chem.*, 70 253 (1976).

143. A.M. Baruzzii, E.P.M. Leiva and M.C. Giordano *J.Electroanal.Chem.*, 189 257 (1985).

144. R.G. Compton, K.L. Pritchard, P.R. Unwin, G.Grigg, P. Silvester, M. lees, and W.A. House *J. Chem Soc., Faraday Trans. I.*, 85 4335 (1989).

145. A.J. Barwise, R.G. Compton and P.R. Unwin *J. Chem. Soc., Faraday Trans.*, 86 137 (1990).

146. W.J. Hamer, G.D. Pinching and S.F. Acree, *J. Research Nat. Bur. Standards*, 35, 539 (1945) & W.J. Hamer and S.F. Acree, *ibid.*, 35, 381 (1945), in G. Kortüm, W. Vogel and K. Andrussow, 'Dissociation Constants of Organic Acids in Aqueous Solution', IUPAC, Butterworths, London, 1961.

147. 'Dictionary of Organic Compounds', Vol 1. Ed. J.Buckingham. Chapman and Hall, New York (1982).

148. D.A. Skoog and D.M. West 'Fundamentals of Analytical Chemistry' Holt-Sanders International, New York 1976.

149. C.R. Wilkie and P. Chang *Am. Inst. Chem. Eng. J.*, 1 264 (1955).

150. K.S.Krishman and G.S.Laddhu, *Ind.Chem. Eng*, 7 83 (1965).

151. O. Ermer, *Helv. Chim. Acta*, 64, 1902 (1981).

152. M.P. Gupta and M. Sahu *Acta Cryst. (B)*, 27 2464 (1971).

153. Private communication from Ciba-Geigy Industrial additives.

154. Private communication from Aldrich Ltd.

155. W. Kern *Z. physik. Chem. [A]*, 181 249 (1938).

156. H.P.Gregor, L.B. Luttinger and E.M. Loebl *J. Phys. Chem.*, 59 34 (1955).

157. R.Sartorio, V.Vitagliano, G.Guardino and O.Ortona *J. Sol. Chem.*, 16 935 (1987).

158. Z. Wojtczak *Kocziki Chemii*, 42 1319 (1968).

159. J.M. Lamarche, J. Persello and A. Folssy *Ind. Eng. Chem. Prod. Res. Dev.*, 22 123 (1983).

160. G.M.Lindquist R.A.Stratton *J.Colloid Inter.Sci.*, 55 45 (1976).

161. T. Sato and R. Ruch, 'Stabalization of Colloidal Dispersions by polymer Adsorption' in 'Surfactant Science' 9 Marcel Delker, New York 1980.

162. D.N. Hague, 'Fast Reactions', Wiley-Interscience, London, 1971, p. 84.

163. D.D. Perrin, 'Dissociation Constants of Inorganic Acids and Bases in Aqueous Solution', IUPAC, Butterworths, London, 1969, p. 213.

164. H.S. Harned and S.R. Scholes, *J. Am. Chem. Soc.*, 63, 1706 (1941).

165. A.C. Walker, U.B. Brar and J. Johnston, *J. Am. Chem. Soc.*, 49, 1235 (1929).

166. K.B. Krauskopf, 'Introduction to Geochemistry', McGraw-Hill, New York, 1967, p. 74.

167. E.L. Sjöberg, *Geochim. Cosmochim. Acta*, 40, 441 (1976).

168. G.W.C. Kaye and T.H. Laby, 'Tables of Physical and Chemical Constants', Longmans.

169. P.W. Atkins, 'Physical Chemistry', 2nd Edition, Oxford Unviersity Press, Oxford, 1982.

170. R.L. Jacobson and D. Langmuir, *Geochim. Cosmochim. Acta*, 38, 301 (1974).

171. L.N. Plummer and E. Busenberg, *Geochim. Cosmochim. Acta*, 46, 1011 (1982).

172. O.I. Martinova, L.G. Vasina and S.A. Pozdnyakova, *Dokl. Akad. Nauk SSSR*, 205, 1110 (1971).

173. L. Ghiringhelli and G. Bianucci, *Ann. Idrol.*, 1, 36 (1963).

174. G.W. Akin and J.V. Lagerwerff, *Geochim. Cosmochim. Acta*, 29, 353 (1965).

175. G. Grèzes and M. Basset, *C.R. Hebd. Seances Acad. Sci.*, 260, 869 (1965).

176. T.E. Larson and A.M. Buswell, *J. Am. Water Works Ass.*, 34, 1667 (1942).

177. F.J. Millero, P.J. Milne and V.L. Thurmond, *Geochim. Cosmochim. Acta*, 48, 1141 (1984).

178. G.L. Frear and J. Johnston, *J. Am. Chem. Soc.*, 51, 1082 (1929).

179. M. Wolf, O. Breitkopf and R. Puk, *Chem. Geol.*, 76, 291 (1989).

180. D. Langmuir, *Geochim. Cosmochim. Acta*, 32, 835 (1968).

181. J.P. Miller, *Am. J. Sci.*, 250, 161 (1952).

182. C.L. Christ, P.B. Hostetler and R.M. Siebert, *J. Res. U.S. Geol. Surv.*, 2, 175 (1974).

183. M.M. Reddy and G.H. Nancollas, *Desalination*, 12, 61 (1973).

184. W.A. House, in 'Comprehensive Chemical Kinetics', Ed. R.G. Compton, Vol. 28, Chap. 3.

185. A.L. Smith, *J. Colloid Interface Sci.*, 55, 525 (1976).

186. Y.C. Huang, F.M. Fowkes, T.B. Lloyd and N.D. Sanders, *Langmuir*, 7, 1742 (1991).

187. J.E. Gebhardt and D.W. Fuerstenau, *Colloids and Surfaces*, 7 221 (1983).

188. P.M. Shanbhag and J.W. Morse, *Geochim. Cosmochim. Acta*, 46, 241 (1982).

189. S.G. Terjesen, O. Erga and S.G. Thorsen, *Chem. Eng. Sci.*, 14, 277 (1961).

190. J.M. Zachara, C.E. Cowan and C.T. Resch, *Geochim. Cosmochim. Acta*, 55, 1549 (1991).

191. N.E. Pingatore and M.P. Eastman, *Chem. Geol.*, 45, 113 (1984).

192. G.M. Bancroft, J.R. Brown and W.S. Fyfe, *Chem. Geol.*, 19, 131 (1977).

193. M.E. McLester, D.F. Martin and W.H. Taft, *J. Inorg. Nucl. Chem.*, 32, 391 (1970).

194. P. Papadopoulos and D.L. Rowell, *J. Soil Sci.*, 39, 23 (1988).

195. W.A. Kornicker, J.W. Morse and R.N. Damasceno, *Chem. Geol.*, 53, 229 (1985).

196. M.L. Franklin and J.W. Morse, *Ocean Sci. Eng.*, 7, 147 (1982).

197. S.J. Gaffey and K.L. Reed, *Econ. Geol.*, 82, 195 (1987).

198. O. Erga and S. Terjesen, *Acta Chem. Scand.*, 10, 872 (1956).

199. W.F. Pickering, *Water Air Soil Poll.*, 20, 299 (1983).

200. D. Buhmann and W. Dreybrodt, *Chem. Geol.*, 64, 89 (1987).

201. P. Kaushansky and S. Yariv, *Appl. Geochem.*, 1, 607 (1986).

202. J.W. Morse, A. Mucci, L.M. Walter and M.S. Kaminsky, *Science*, 205, 904 (1979).

203. A. Mucci, J.W. Morse and M.S. Kaminsky, *Am. J. Sci.*, 285, 289 (1985).

204. A. Mucci and J.W. Morse, *Am. J. Sci.*, 285, 306 (1985).

205. P. Brättler, P. Möller and U. Rösick, *Earth Planetary Sci. Lett.*, 14, 50 (1972).

206. P. Möller and G. Werr, *Radiochimica Acta*, 18, 144 (1972).

207. P. Möller, *J. Inorg. Nucl. Chem.*, 35, 395 (1973).

208. P. Möller and P.P. Parekh, *Marine Chem.*, 3, 63 (1975).

209. C.S. Sastri and P. Möller, *Chem. Phys. Lett.*, 26, 116 (1974).

210. V. Koß and P. Möller, *Z. Anorg. Allg. Chem.*, 410, 165 (1974).

211. P. Möller and G. Rajagopalan, *Z. Phys. Chem., Neue Folge*, 94, 297 (1975).

212. M.M. Reddy and G.H. Nancollas, *J. Crystal Growth*, 35, 33 (1976).

213. M.M. Reddy and K.K. Wang, *J. Crystal Growth*, 50, 470 (1980).

214. J.L. Bischoff and W.S. Fyfe, *Am. J. Sci.*, 266, 65 (1968).

215. R.A. Berner, *Geochim. Cosmochim. Acta*, 39, 489 (1975).

216. A. Katz, *Geochim. Cosmochim. Acta*, 37, 1563 (1973).

217. E.A. Burton and L.M. Walter, *Geochim. Cosmochim. Acta*, 55, 777 (1991).

218. A. Mucci, R. Canuel and S. Zhong, *Chem. Geol.*, 74, 309 (1989).

219. O. Söhnel and J.W. Mullin, *J. Crystal Growth*, 60, 239 (1982).

220. E.L. Dromgoole and L.M. Walter, *Chem. Geol.*, 81, 311 (1990).

221. V. Koß and P. Möller, *Inorg. Nucl. Chem. Lett.*, 10, 849 (1974).

222. M. Ishikawa and M. Ichikuni, *Chem. Geol.*, 42, 137 (1984).

223. I. Nestaas and S.G. Terjesen, *Acta Chem. Scand.*, 23, 2519 (1969).

224. N.E. Pingatore and M.P. Eastman, *Geochim. Cosmochim. Acta*, 50, 2195 (1986).

225. A. Glasner and D. Weiss, *J. Inorg. Nucl. Chem.*, 42, 655 (1980).

226. A. Tsutsu and H.D. Holland, *Geochim. Cosmochim. Acta*, 30, 439 (1966).

227. J.M. Zachara, J.A. Kittrick and J.B. Harsh, *Geochim. Cosmochim. Acta*, 52, 2281 (1988).

228. J.W. Morse, P.M. Shanbhag, A. Saito and G.R. Choppin, *Chem. Geol.*, 42, 85 (1984).

229. H.J. Meyer, *J. Crystal Growth*, 66, 639 (1984).

230. J.W. Morse, *Am. J. Sci.*, 274, 638 (1974).

231. W.A. House, *J. Colloid Interface Sci.*, 119, 505 (1987).

232. J. de Kanel and J.W. Morse, *Geochim. Cosmochim. Acta*, 42, 1335 (1978).

233. T. Suzuki, S. Inomata and K. Sawada, *J. Chem. Soc., Faraday Trans. I*, 82, 1733 (1986).

234. A.G. Xyla and P.G. Koutsoukos, *J. Chem. Soc., Faraday Trans. I*, 83, 1477 (1987).

235. C.E. Cowan, J.M. Zahara and C.T. Resch, *Geochim. Cosmochim. Acta*, 54, 2223 (1990).

236. Z. Amjad, *Langmuir*, 3, 224 (1987).

237. S. Mann, B.R. Heywood, S. Rajam and J.D. Birchall, *Proc. R. Soc. Lond. A*, 423, 457 (1989).

238. S. Rajam, B.R. Heywood, J.B.A. Walker, S. Mann, R.J. Davey and J.D. Birchall, *J. Chem. Soc., Faraday Trans.*, 87, 727 (1991).

239. B.R. Heywood, S. Rajam and S. Mann, *J. Chem. Soc., Faraday Trans.*, 87, 735 (1991).

240. E. Suess, *Geochim. Cosmochim. Acta*, 34, 157 (1970).

241. Y. Kitano and D.W. Hood, *Geochim. Cosmochim. Acta*, 29, 29 (1965).

242. R.W. Lahann and R.C. Campbell, *Geochim. Cosmochim. Acta*, 44, 629 (1980).

243. S. Sarig and F. Kahana, *J. Crystal Growth*, 35, 145 (1976).

244. S. Mann, J.M. Didymus, N.P. Sanderson, B.R. Heywood and E.J.A. Samper, *J. Chem. Soc., Faraday Trans.*, 86, 1873 (1990).

245. T.J. Hannagan in 'Mastering Statistics' Macmillan, Basingstoke, 1986 pp20.